

**Al-Co-Ce Glass Forming Alloys and Their  
Corrosion Behaviour**

**Chunling Li**

Thesis submitted for the degree of

Doctor of Philosophy

Faculty of Engineering

University of Nottingham

July 2014

## Abstract

There is growing interest in Al-TM (transition metal)-RE (rare earth) amorphous alloys because of the combination of good mechanical properties and corrosion resistance that can be achieved. However, the high critical cooling rate required to form the amorphous structure leads to difficulties in generating bulk material in the amorphous form and more recently there has been greater interest in producing amorphous Al-TM-RE alloys as surface layers. In the present study, three types of solidification processes namely wedge mould casting, laser surface melting (LSM) and large area electron beam (LAEB) surface melting were used to fabricate Al-Co-Ce alloys with the compositions of  $\text{Al}_{88.0}\text{Co}_{6.0}\text{Ce}_{6.0}$ ,  $\text{Al}_{87.4}\text{Co}_{7.9}\text{Ce}_{4.7}$  and  $\text{Al}_{86.0}\text{Co}_{7.6}\text{Ce}_{6.4}$  (at.%) in both crystalline and amorphous form. The solidification of an Al-33Cu (wt.%) alloy (eutectic composition) was also studied to provide data on solidification velocities and cooling rates based on the well-known relationship for lamellar eutectic spacing.

The microstructures formed by different processes were investigated by scanning electron microscopy, energy dispersive X-ray spectroscopy, image analysis and X-ray and glancing angle X-ray diffraction. In particular, LAEB surface melting was found to be able to provide a sufficiently high solidification velocity for the generation of an amorphous layer on the remelted surface of bulk crystalline Al-Co-Ce alloys. The effects of LAEB treatment parameters, the lengthscale of the starting microstructures, and laser pretreatment on the development of the amorphous layer were systematically investigated. Results show the formation of Al-Co-Ce amorphous layer under some suitable LAEB treatment parameters.

Experimental results also show that the higher cathode voltage and more LAEB pulses of irradiation improved homogenisation of the multiphase crystalline starting material. However, excessive LAEB pulses caused localised crystallisation of the treated layer. The high cooling rate of the LAEB process also resulted in cracking of the treated layer. However, the cracking was largely reduced by laser pretreatment due to the greatly refined microstructure of the as-cast alloy. Laser pretreatment also increased the extent of homogenisation and amorphisation generated by the subsequent LAEB treatment.

The temperature field generated by the multi-pulse LAEB treatment was also numerically simulated through a finite difference method, and compared with experimental findings on both Al-Ce-Co alloys and an Al-Cu eutectic. The numerical simulation results were generally consistent with the experimental results.

The corrosion behaviour of Al-Co-Ce glass forming alloys formed by different solidification processes in 3.5 wt.% NaCl solution was studied through potentiodynamic polarisation tests. Results show that Al-Co-Ce amorphous layer had an enhanced corrosion resistance compared to the alloy in the crystalline form, although cracking in the amorphous layer greatly influenced the effectiveness of the amorphous layer protecting the substrate.

## Preface

This thesis is submitted for the degree of Doctor of Philosophy at the University of Nottingham. The research work was carried out under the supervision of Dr. K.T. Voisey and Professor D.G. McCartney in the Faculty of Engineering.

It is certified that the work presented in this thesis is original, and suitable references are made to any work from the literature or carried out elsewhere.

The list of publications from the work presented in this thesis is presented here:

[1] C.L. Li, J.W. Murray, K.T. Voisey, A.T. Clare, D.G. McCartney, Amorphous layer formation in an Al-Co-Ce alloy using electron beam melting and laser microstructural refinement, Proceedings of 26<sup>th</sup> International Conference on Surface Modification Technologies, Lyon France, 2012, 283-292.

[2] C.L. Li, J.W. Murray, K.T. Voisey, A.T. Clare, D.G. McCartney, Amorphous layer formation in  $\text{Al}_{86}\text{Co}_{7.6}\text{Ce}_{6.4}$  glass-forming alloy by large-area electron beam irradiation, Applied Surface Science, 280 (2013) 431-438.

[3] C.L. Li, J.W. Murray, K.T. Voisey, A.T. Clare, D.G. McCartney, Effect of prior laser microstructural refinement on the formation of amorphous layer in an  $\text{Al}_{86}\text{Co}_{7.6}\text{Ce}_{6.4}$  alloy, Applied Surface Science, 289 (2014) 230-236.

[4] C.L. Li, J.W. Murray, K.T. Voisey, A.T. Clare, D.G. McCartney, Corrosion behaviour of  $\text{Al}_{87.4}\text{Co}_{7.9}\text{Ce}_{4.7}$  amorphous layer prepared by large area electron beam irradiation, Applied Surface Science, under review.

Chunling Li

July 2014

## **Acknowledgements**

I would like to express my deepest gratitude to my supervisors, Dr Katy Voisey and Professor Graham McCartney. It would not have been possible to complete this thesis without their continuous support and guidance during my PhD studies. Dr. Voisey who helped me at all stages of this thesis with her excellent guidance, patience, enthusiasm and encouragement. I also greatly benefited from Professor McCartney's valuable comments on my project and thesis writing. Besides my supervisors, I also wish to thank my internal assessor, Professor Philip Shipway for his valuable suggestions on my project.

In addition, I also acknowledge the technical assistance I have received from Mr Keith Dinsdale, Dr Deen Zhang, Dr Nigel Neate, Mr Mark Roe and Mr Stuart Branston. I also would like to offer my special thanks to Dr Adam Clare and Mr James Murray for providing the electron beam machine and helping me prepare a great number of samples.

My greatest appreciation goes to my colleagues and friends in Nottingham. They are Hao Chen, Xuanli Luo, Matthew Moles, Xiaoling Liu, Kanika Barman, Majid Hashemzadeh, Taiwo Abioye, et al., whose support and friendship made me go through the new life and studies in the UK. I shall cherish the memory of working and studying with them.

I would also like to thank my parents and younger brother. They were always supporting me and encouraging me with their unconditional love. Finally, I would like to thank my husband, Shuangqing Sun. He was always there cheering me up.

## List of abbreviations

Al-TM-RE: Al-transition metal-rare earth  
APS: air plasma spray  
BSE: back scattered electron  
CCC: chromate conversion coating  
CGDS: cold gas dynamic spray  
CPR: corrosion penetration rate  
CPVC: critical pigment volume concentration  
EDS: energy dispersive X-ray spectroscopy  
GAXRD: glancing angle X-ray diffraction  
GFA: glass forming ability  
HAP: hazardous air pollutants  
HPS: high-energy plasma spraying  
HVAF: high velocity air flame  
HVOF: high velocity oxygen flame  
ICP-OES: inductively coupled plasma optical emission spectrometry  
KM: kinetic metallisation  
LAEB: large area electron beam  
LEHCPEB: low energy, high current, pulsed electron beam  
LPPS: low pressure plasma spray  
LSM: laser surface melting  
LSM-LAEB: laser surface melting-large area electron beam  
MA: mechanical alloying  
Mm: misch metal  
OCP: open circuit potential  
PTFE: polytetrafluoroethylene  
PTS: pulsed thermal spray  
PVC: pigment volume concentration  
PVD: physical vapour deposition  
SE: secondary electron  
SEM: scanning electron microscopy  
VOC: volatile organic compound  
VPS: vacuum plasma spray  
XRD: X-ray diffraction

# Table of contents

<b>CHAPTER 1 INTRODUCTION .....</b>	<b>1</b>
<b>CHAPTER 2 LITERATURE REVIEW .....</b>	<b>4</b>
<b>2.1 Introduction .....</b>	<b>4</b>
<b>2.2 Conventional coating system for corrosion protection of high strength aluminium alloys.....</b>	<b>4</b>
2.2.1 Alclad layer .....	5
2.2.2 Pre-treatment layers .....	6
2.2.3 Primer layers.....	8
2.2.4 Topcoat.....	9
<b>2.3 Novel coating systems for corrosion protection of high strength aluminium alloys.....</b>	<b>9</b>
2.3.1 Sol-gel coatings .....	10
2.3.2 Plasma polymerised coatings.....	11
2.3.3 Multifunctional amorphous alloy coating.....	12
<b>2.4 Al-TM (transition metal)-RE (rare earth) amorphous alloys.....</b>	<b>13</b>
2.4.1 Introduction .....	13
2.4.2 Glass forming ability (GFA).....	15
2.4.3 Glass formation range.....	16
2.4.4 Microstructure of Al-TM-RE nanocrystalline/amorphous alloy coatings	18
2.4.5 Corrosion behaviour of Al-TM-RE amorphous alloys and coatings .....	20
<b>2.5 Preparation of bulk amorphous alloys, powders, coatings and surface layers.....</b>	<b>26</b>
2.5.1 Bulk amorphous alloys .....	26
2.5.2 Coatings.....	27
2.5.3 Surface layers .....	35
2.5.4 Powders .....	38
<b>2.6 Large area electron beam surface melting .....</b>	<b>41</b>
2.6.1 Physical foundation .....	41
2.6.2 Applications.....	42
2.6.3 Numerical simulation of temperature field and stress field .....	44
<b>2.7 A summary of the literature review .....</b>	<b>45</b>
2.7.1 Research gap.....	45
2.7.2 Objectives of the research project.....	47
<b>CHAPTER 3 MATERIALS AND EXPERIMENTAL METHODS .....</b>	<b>48</b>
<b>3.1 Materials.....</b>	<b>48</b>
<b>3.2 Wedge mould casting.....</b>	<b>49</b>
<b>3.3 Laser surface melting (LSM) treatment.....</b>	<b>53</b>
<b>3.4 Large area electron beam (LAEB) surface melting treatment.....</b>	<b>54</b>
3.4.1 LAEB surface melting .....	54

3.4.2	Sample temperature measurement.....	57
<b>3.5</b>	<b>Characterisation .....</b>	<b>57</b>
3.5.1	Sample preparation.....	57
3.5.2	Optical microscopy.....	59
3.5.3	Scanning electron microscopy (SEM) and energy dispersive X-ray spectroscopy (EDS).....	60
3.5.4	X-ray diffraction analysis (XRD).....	61
3.5.5	Micro-hardness testing .....	62
3.5.6	Image analysis.....	62
<b>3.6</b>	<b>Corrosion testing.....</b>	<b>64</b>
3.6.1	Sample preparation.....	64
3.6.2	Potentiodynamic polarisation test.....	66
<b>CHAPTER 4 CHARACTERISATION OF SOLIDIFICATION</b>		
<b>CONDITIONS USING AN AL-CU EUTECTIC ALLOY .....</b>		
<b>4.1</b>	<b>Introduction .....</b>	<b>68</b>
<b>4.2</b>	<b>Experimental characterisation of Al-Cu eutectic solidification in different processes .....</b>	<b>70</b>
4.2.1	Wedge mould casting .....	70
4.2.2	Laser surface melting (LSM).....	72
4.2.3	Large area electron beam (LAEB) treatment.....	78
<b>4.3</b>	<b>Solidification velocity calculation.....</b>	<b>83</b>
4.3.1	Wedge mould casting and laser surface melting.....	83
4.3.2	LAEB treatment.....	83
<b>4.4</b>	<b>Discussion .....</b>	<b>85</b>
4.4.1	Effect of the process parameters on the solidification velocity .....	85
4.4.2	Cooling rate of LAEB treated alloy.....	88
<b>4.5</b>	<b>Summary .....</b>	<b>92</b>
<b>CHAPTER 5 WEDGE MOULD CASTING AND LASER SURFACE</b>		
<b>MELTING OF AL-CO-CE ALLOYS .....</b>		
<b>5.1</b>	<b>Introduction .....</b>	<b>93</b>
<b>5.2</b>	<b>Wedge mould casting of Al-Co-Ce alloys .....</b>	<b>94</b>
5.2.1	SEM results .....	94
5.2.2	EDS results.....	99
5.2.3	XRD results .....	102
5.2.4	Phase fraction .....	104
5.2.5	Micro-hardness of different regions in the as-cast alloy 3.....	105
5.2.6	Metal flakes in the split of wedge mould.....	107
<b>5.3</b>	<b>Overlapped multi-track laser surface melting of Al-Co-Ce alloy 3 ...</b>	<b>108</b>
5.3.1	SEM results .....	108
5.3.2	EDS results.....	111
5.3.3	XRD results .....	112
<b>5.4</b>	<b>Discussion .....</b>	<b>112</b>
5.4.1	Wedge mould casting .....	112

5.4.2	Laser surface melting.....	119
<b>5.5</b>	<b>Summary .....</b>	<b>120</b>
<b>CHAPTER 6 LAEB TREATMENT OF AL-CO-CE ALLOYS.....</b>		<b>121</b>
<b>6.1</b>	<b>Introduction .....</b>	<b>121</b>
<b>6.2</b>	<b>Effect of LAEB treatment parameters .....</b>	<b>122</b>
6.2.1	Effect of number of pulses.....	122
6.2.2	Effect of cathode voltage.....	128
<b>6.3</b>	<b>Effect of as-cast alloy original microstructures .....</b>	<b>133</b>
6.3.1	Microstructure characterisation .....	133
6.3.2	Glancing angle XRD results .....	135
<b>6.4</b>	<b>Effect of laser microstructural refinement.....</b>	<b>136</b>
6.4.1	Surface morphology .....	137
6.4.2	Cross sectional morphology .....	139
6.4.3	Cracking .....	141
6.4.4	Phase transformation .....	142
<b>6.5</b>	<b>Formation of craters and particles.....</b>	<b>144</b>
<b>6.6</b>	<b>Discussion .....</b>	<b>146</b>
6.6.1	General formation mechanism of the amorphous layer .....	146
6.6.2	Homogenisation.....	146
6.6.3	Amorphisation .....	149
6.6.4	Crystallisation.....	150
6.6.5	Cracking .....	151
6.6.6	Formation of craters and particles .....	153
<b>6.7</b>	<b>Summary .....</b>	<b>154</b>
<b>CHAPTER 7 NUMERICAL SIMULATION OF MULTI-PULSE LAEB IRRADIATION PROCESS.....</b>		<b>156</b>
<b>7.1</b>	<b>Introduction .....</b>	<b>156</b>
<b>7.2</b>	<b>Mathematical model.....</b>	<b>159</b>
7.2.1	Heat transfer equation.....	159
7.2.2	Heat source .....	164
7.2.3	Latent heat .....	166
7.2.4	Physical and thermal properties of alloys .....	167
7.2.5	Programme flow chart .....	169
<b>7.3</b>	<b>Results.....</b>	<b>170</b>
7.3.1	Validation of code .....	170
7.3.2	Estimation of heat transfer coefficient.....	172
7.3.3	Number of LAEB pulses and equivalent initial temperature .....	176
7.3.4	Modelling results of Al-Cu alloy .....	180
7.3.5	Modelling results of Al-Co-Ce alloy 3 .....	186
<b>7.4</b>	<b>Discussion .....</b>	<b>195</b>
7.4.1	Features of the heat source .....	195
7.4.2	Thickness of the remelted layer and the homogenised layer .....	197
7.4.3	Melting time and homogenisation .....	200

7.4.4	Solidification velocity/cooling rate and initial temperature.....	203
7.4.5	Solidification velocity/cooling rate and cathode votage.....	206
<b>7.5</b>	<b>Summary .....</b>	<b>207</b>
<b>CHAPTER 8 CORROSION BEHAVIOUR OF AL-CO-CE ALLOY WITH DIFFERENT MICROSTRUCTURES .....</b>		<b>209</b>
<b>8.1</b>	<b>Introduction .....</b>	<b>209</b>
<b>8.2</b>	<b>AA2024 and alclad 2024.....</b>	<b>210</b>
8.2.1	Characterisation of AA 2024 and alclad 2024.....	210
8.2.2	Potentiodynamic polarisation tests .....	214
8.2.3	Corrosion morphologies .....	215
<b>8.3</b>	<b>Al-Co-Ce alloy with different microstructures .....</b>	<b>221</b>
8.3.1	Potentiodynamic polarisation test.....	221
8.3.2	Corrosion morphologies .....	223
<b>8.4</b>	<b>Discussion .....</b>	<b>235</b>
8.4.1	Corrosion behaviour of AA2024, pure Al and alclad 2024 .....	235
8.4.2	Corrosion behaviour of as-cast, LSM and LAEB treated Al-Co-Ce alloy .....	238
8.4.3	Corrosion behaviour of LSM-LAEB treated amorphous alloys (crack-free) .....	241
<b>8.5</b>	<b>Summary .....</b>	<b>248</b>
<b>CHAPTER 9 CONCLUSIONS.....</b>		<b>250</b>
<b>CHAPTER 10 FUTURE WORK .....</b>		<b>255</b>
<b>REFERENCES .....</b>		<b>257</b>
<b>APPENDIXES .....</b>		<b>270</b>
<b>Appendix 1</b>	<b>ICP-OES results of as-cast Al-Co-Ce alloys .....</b>	<b>270</b>
<b>Appendix 2</b>	<b>DSC measurement .....</b>	<b>272</b>
<b>Appendix 3</b>	<b>Laser flash measurement .....</b>	<b>274</b>
<b>Appendix 4</b>	<b>Programme code of numerical simulation.....</b>	<b>275</b>
<b>Appendix 5</b>	<b>Repeated scans of OCP and potentiodynamic polarisation tests 281</b>	

## Chapter 1 Introduction

Because of the highly different microstructure compared to the crystalline alloy, and its favourable properties, the amorphous alloy has attracted enormous attention and stimulated widespread research enthusiasm. In 1987, an amorphous phase with good ductility was first discovered in Al-Ni-Si and Al-Ni-Ge alloy systems [1, 2], which triggered a large body of research on the ternary ductile amorphous alloys, including Al-EM-LM (EM=early transition metal, LM=late transition metal) and Al-LM-RE (RE=rare earth metal) alloys. These alloys containing above 80 at.% Al are exemplified by Al-Zr-Cu, Al-Zr-Ni and Al-Nb-Ni [2], Al-(Fe, Co, Ni or Rh)-(Ce, Gd or Y) [3] and Al-(Fe, Co, Ni, Cu)-(Y, La, Ce) [4, 5].

The above Al-TM-RE (TM=transition metal) alloys were found to have outstanding mechanical properties. Their tensile fracture strength and Vickers micro-hardness greatly exceed those of conventional crystalline aluminium alloys [6]. Meanwhile, Al-TM-RE amorphous alloys also exhibit good bending ductility due to the high content of aluminium [7]. The favourable corrosion resistance is another advantage of the Al-TM-RE amorphous alloys [8]. First of all, the lack of defects such as grain boundaries, dislocations and precipitates makes these amorphous alloys a good barrier to prevent pitting corrosion. In addition, their corrosion resistance properties are tunable with the concentration of TM and RE elements [9]. Another important mechanism of corrosion protection of amorphous alloy is the active corrosion inhibition [10]. These amorphous alloys can release  $Ce^{3+}$ ,  $Y^{3+}$  and  $Gd^{3+}$  ions, which are good corrosion inhibitors for the aluminium alloys.

With a combination of good mechanical properties and corrosion resistance, Al-TM-RE amorphous alloys have been extensively studied from various perspectives, especially the Al-(Fe, Co, Ni, Cu)-(Y, La, Ce) alloys systems. However, the high critical cooling rate required to achieve the amorphous state of this alloy system limits the dimensions of bulk samples. To date, the maximum dimension of bulk Al-based amorphous alloys achieved is still around 1 mm in diameter [7]. Therefore, there is interest in using surface modification techniques to generate coatings or films of these amorphous materials.

High strength aluminium alloys are a family of commercial aeronautical alloys. However, these alloys are susceptible to various types of local corrosion including pitting, intergranular corrosion, exfoliation corrosion and stress corrosion cracking [11, 12]. To date, many corrosion prevention methods have been developed and applied for these aluminium alloys such as cladding, anodising, corrosion protection compounds, and conversion coatings, etc. Each of these methods has different corrosion prevention mechanisms and drawbacks. For instance, alclad layers usually have limited protection range when the layers are scratched, and chromate conversion coatings have been gradually phased out due to the toxicity to the environment and carcinogenicity to human beings [13]. A new environmentally friendly, good corrosion resistant, long-lifespan corrosion prevention method is therefore desired.

In this context, the Al-TM-RE amorphous alloys, could be considered to have potential if applied as thin layers. Scully et al. [14] have prepared an Al-Co-Ce nanocrystalline/amorphous coating by pulsed thermal spray (PTS) and high velocity oxy-fuel spray (HVOF) technologies. The effects of metallurgical,

physical and geometrical factors on corrosion behaviour were investigated [15]. However, the characterisation of nanocrystalline/amorphous alloys is still insufficient, especially the transformation process of material microstructure from the crystalline to amorphous form. In addition, the effect of material microstructure defects, such as cracks, compositional heterogeneity, recrystallised particles, on the corrosion properties is also not clear. Therefore, there is interest to conduct further work on this topic, which is particularly beneficial to the development and application of amorphous alloy surface coating and other surface treated layers.

In this research project, the Al-Co-Ce glass forming alloys with three different compositions in both crystalline and amorphous forms were investigated. Wedge mould casting, laser surface melting (LSM) and large area electron beam (LAEB) surface treatment were used to prepare materials. First, the solidification conditions of the sample preparation techniques were evaluated using an Al-Cu eutectic alloy. Second, the microstructures of the materials fabricated by different processes were characterised, and the relationship between the solidification conditions and structure established. In particular, the LAEB treatment in the generation of Al-Co-Ce amorphous layers was systematically investigated. The thermal history of LAEB treated alloys was also investigated using a numerical finite difference model. Third, the corrosion behaviour of Al-Co-Ce glass forming alloys with different microstructures was studied. Overall, the general aim of this work was to understand the process-microstructure-property relationship of the Al-Co-Ce glass forming alloys.

## **Chapter 2 Literature Review**

### **2.1 Introduction**

This chapter presents a review of the literature on the main contents studied in this thesis. The background of the project research is first presented. The conventional and novel coating systems for the corrosion protection of the high strength aluminium alloy (AA2024) are introduced, including the component layers of the conventional coating system, the new developed coating systems and their characteristics. Among the novel coating systems, the multifunctional amorphous alloy coating of Al-TM (transition metal)-RE (rare earth) is thought to be one of the most promising ones. Therefore, Al-TM-RE glass forming alloy and related coatings are also introduced in this chapter, including the glass forming ability and range, the microstructure of the coating, as well as the corrosion behaviour of the amorphous alloy and coatings. In addition, the preparation methods of the bulk amorphous alloy, powder, coating and surface layer are also presented in this chapter. As the most used technology in this thesis, the large area electron beam (LAEB) surface melting process is emphasised. At the end of this chapter, a summary of the literature review is given to present the research gap and the objectives of this research project.

### **2.2 Conventional coating system for corrosion protection of high strength aluminium alloys**

The typical corrosion protection coating system for the high strength aluminium alloys is comprised of four significantly different layers [16], as shown in **Figure**

2-1. The first layer that directly contacted with the substrate is the alclad layer, which is usually several percentages of the thickness of the substrate alloy. Aeronautical aluminium alloy sheet is usually supplied with an alclad layer already present to enhance the corrosion resistance. The second layer is a very thin pretreated layer such as an anodising layer (5-18  $\mu\text{m}$  in thickness) or chromate conversion coating (10-60 nm in thickness). The pretreated layer is applied to provide the corrosion protection and improve the adhesion between the alclad layer and the primer layer (the third layer). The primer layer (5-200  $\mu\text{m}$  in thickness) is the main provider of corrosion protection, which is comprised of a pigmented organic resin matrix enveloping the chromate or chromate-free inhibiting pigments. The topcoat is usually made of polyurethane with some special functional additives, which is the first defence exposed to the environment. The sections below summarise the main features and potential drawbacks of the above layers.

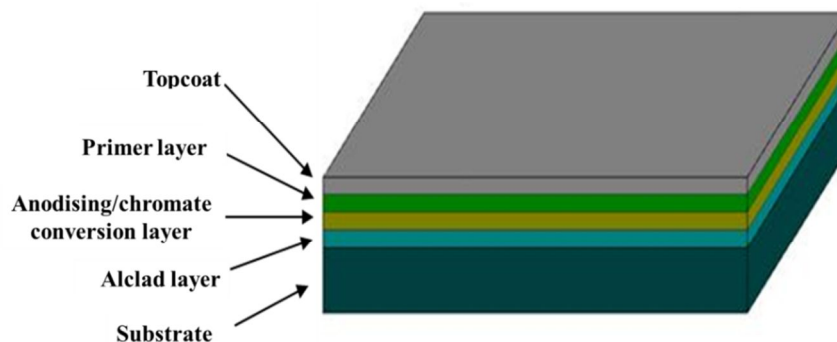


**Figure 2-1 Schematic of a typical corrosion protection system for the aluminium alloys (not drawn to scale).**

### 2.2.1 Alclad layer

In order to electrochemically protect the aluminium alloy, a thin layer of metallurgically bonded pure aluminium or aluminium alloy is coated on one or both surfaces of aluminium alloy [17]. Effective protection is attributed to the

potential difference between the substrate and cladding. The cladding alloy namely alclad is usually anodic to the substrate alloy. When the alclad product is in contact with the corrosive solution, the cladding, acting as the anode, will dissolve preferentially, thus protecting the substrate from corrosion. Therefore, it is important to select the cladding material with a suitable corrosion potential which is sufficiently anodic in order to electrochemically protect the substrate.

The open circuit potential (OCP) of the cladding layer is usually approximately 80 ~100 mV below that of the substrate metal [18], such as AA 2024-T3 which mainly contains Al, Cu, Mg and Zn. The small potential difference can only create a limited electrochemical throwing power [19], which results in the width of the scratch on the cladding layer that can be protected being only several millimetres. In addition, the pitting potential ( $E_{pit}$ ) of the cladding alloy is below that of underlying substrate metal. Therefore, accompanied by the favourable performance of sacrificial cathodic protection, the cladding layer also has a high self-corrosion rate [18]. This eventually deteriorates the corrosion protection performance of the cladding layer due to rapid consumption.

## **2.2.2 Pre-treatment layers**

### **2.2.2.1 Anodising coating**

Aluminium anodising is an electrochemical method in which the aluminium coated on the surface of the material is converted into aluminium oxide ( $Al_2O_3$ ) [17], i.e. anodised coating. Anodised coatings have a porous outer layer and a thin barrier layer adjacent to the interface of coating and substrate. The porous outer layer of the coating consists of close-packed cells of oxide,

predominantly hexagonal in shape, each of which contains a single pore [20] (**Figure 2-2**). In order to seal these pores and eliminate the path between the aluminium alloy substrate and the corrosive environment, the coating is sealed by treating it in slightly acidified hot water, deionized water, a hot dichromate solution, or a nickel acetate solution. Sealed anodised coatings are highly resistant to atmospheric and salt water attack. Some published work has also indicated that corrosion resistance of anodised coatings can be improved by the impregnation of polytetrafluoroethylene (PTFE) [20].

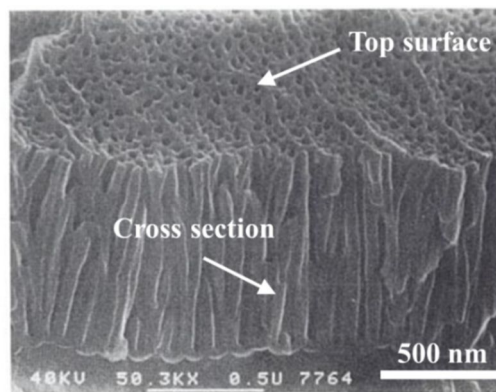


**Figure 2-2 Scanning electron micrograph showing cross section and surface of a sulphuric acid anodic coating [20].**

In general, the corrosion resistance of the anodised coatings is usually favourable in neutral or near neutral solutions. However, the quality of the anodised coating strongly depends on the anodising process due to the relatively complex process. In some cases, improper and insufficient cleaning prior to anodising results in the flaking of anodised coating from the substrate [17]. In addition, the cost of anodising is very high due to the great consumption of water and electric power.

#### **2.2.2.2 Chromate conversion coating**

Chromate conversion coating (CCC) can be an alternative to the anodising coating. CCC is formed by a chemical oxidation-reduction reaction between the suitable

reagent and the metallic surface, which differs from the electrochemical reaction in the process of anodising [17]. CCC is usually formed in an acidic solution containing one or more sources of hexavalent chromium. In order to activate the substrate surface, sodium fluoride (NaF) is usually added into the formation solution. Additionally, the formation of CCC is accelerated by some accelerators such as  $\text{Fe}[\text{CN}]_6^{3-}$  and  $\text{MoO}_4^{2-}$  [21]. The microstructure and composition of CCC have been investigated by many researchers. A two-layer structure is extensively accepted [22]. The top layer is a relatively thick porous layer which contains small pores and large defects. The lower layer is thin and dense which separates the top layer and the aluminium substrate.

Unfortunately, hexavalent chromium is a carcinogen to human beings [23, 24]. Due to the carcinogenicity of the hexavalent species, searching for a replacement for chromate conversion coatings has become an urgent issue to the application of aluminium alloys. Recently, corrosion researchers have developed organic-based conversion coatings [25] and rare earth-based conversion coatings [26].

### **2.2.3 Primer layers**

In most of the cases, the primer layer functions as the active corrosion inhibition layer. This layer can release the inhibitors to prevent the corrosion at the metal/coating interface. The inhibitors are usually from the chromates enveloped in the resin matrix. In aqueous solution, hexavalent chromium existing in the resin matrix can transport and adsorb on the surface of substrate metals, their oxides or the intermetallics in the metal matrix where the reduction of hexavalent chromium to trivalent chromium takes place [13, 27]. The reduction reaction occurring on the active corrosion site is as follows:



The trivalent compound,  $Cr(OH)_3$ , is very stable and insoluble, allowing the anodes to be separated from the corrosive solution and inhibit the corrosion.

#### **2.2.4 Topcoat**

The topcoat acts as the first defence to the environment damage such as extreme weather and ultra-violet rays. The topcoat is often tailored to the application. For example, the topcoat designed for military applications has low glint and ground camouflage. To realize the above functions, the topcoat usually has a high pigment volume concentration (PVC), which will result in a porous structure of topcoat [28]. Therefore, the PVC in the topcoat must be controlled below the critical pigment volume concentration (CPVC) to balance the function realisation and structure. A pore-free multi-function topcoat will be a good barrier to the exterior exposure including water, acid rain, salts and UV, etc. [25].

### **2.3 Novel coating systems for corrosion protection of high strength aluminium alloys**

As previously mentioned, the application of chromates is very extensive in the conventional corrosion protection coating system. First, chromates are introduced in the form of chromic acid ( $H_2CrO_4$ ) to seal the porous layer of anodising coating. Second, chromate conversion coatings are used to replace the anodising coating due to the economic benefits and process stability. Third, chromates are commonly used as inhibiting pigments in the primer coatings. However, the importance of environmental protection has greatly increased the urgency to develop the

chromate replacements. To date, a variety of chromate replacements or technologies have been developed.

A variety of alternatives of chromate inhibitors have been developed, including inorganic inhibitors (molybdates [29, 30], phosphates [26]), organic inhibitors [31-33]) and rare earth metal inhibitors (cerium [34-39], lanthanum [40] and unrefined rare earth metal mixture i.e. misch metal (MM) [41, 42]). These alternative inhibitors are usually used as the active additives in the primer layer or conversion coating. They can form a dense, hydrophobic or insoluble layer at the metal surface through deposition, absorption or chelation to inhibit the dissolution of metals. However, the conventional corrosion protection system of aeronautic aluminium alloys more or less involves the release of volatile organic compounds (VOCs) or other hazardous air pollutants (HAPs). Therefore, enormous attention has been paid on the new and environmentally friendly corrosion protection systems.

### **2.3.1 Sol-gel coatings**

The sol-gel process usually involves the hydrolysis and condensation polymerisation process to form a functional film depending on the different applications. Sol-gel coating is a promising replacement for chromate conversion coatings due to the low synthesis temperature, chemical inertness, hydrophobic barrier protection and suitability for industrial production et al. [16]. Sol-gel technology was first introduced to be a pretreatment method for the corrosion protection of different metallic substrates. Khobaib et al. [43] found that an AA2024 substrate coated with a polyurethane layer can offer a comparable corrosion protection with the conventional chromate pretreated system.

However, results of artificial scribed corrosion tests showed that the performance of a sol-gel pretreated system was inferior to that of a chromate pretreated system. The poor corrosion resistance resulted from the formation of pores and cracks during the drying procedure, which provided the attack site for the corrosion media on the substrate surface of the aluminium alloy [44]. The introduction of organic components to the sol-gel systems at low temperature makes it possible to prepare a thicker, defect-free film with better bonding with organic top coatings and substrate metal, which can provide a more favourable barrier function to corrosion. Conde et al. [45] introduced three organic components to form polymeric sol-gel coatings and studied their properties, individually. They found that the hybrid films have an improved corrosion resistance. Parkhill et al. [46] prepared epoxy-silica sol-gel coatings on AA2024-T3. The results showed that the thin sol-gel coating with a thickness of 2.2  $\mu\text{m}$  provided an excellent barrier property in the accelerated corrosion tests compared to the standard Alodine-1200 type surface pre-treatment. Moreover, the hybrid films can be reinforced by adding nanoparticles, which can greatly improve corrosion protection properties. Most recently, Zheludkevich et al. [47] studied the corrosion protective properties of nanostructured sol-gel hybrid coatings to AA2024-T3. It was found that the presence of  $\text{ZrO}_2$  nanoparticles improved the corrosion protection of the sol-gel coatings. In addition, cerium-based compounds also have been introduced to the sol-gel coatings [48].

### **2.3.2 Plasma polymerised coatings**

In the process of low temperature plasma deposition, gaseous monomers are ionised by the plasma which is commonly generated through glow discharge,

radio-frequency discharge or microwave discharge. After the ionisation of monomers, they polymerise and deposit on the substrate surface at room temperature [49]. The plasma polymerised coating is usually very thin. However, the thin film with a thickness of several hundreds of nanometres has rather high adhesion to the metal substrate due to the covalent bonding. Furthermore, the highly cross-linked matrix of the film is a very good barrier to the corrosion media [16]. Due to these two most attractive advantages, low temperature plasma deposition has been introduced to prepare the corrosion protection coatings on many kinds of metal substrates such as carbon steel [50], aluminium [51] and aluminium alloy [52], etc. Recently, some researchers such as Yasuda et al. [53] have also proposed that low temperature plasma deposition is a feasible and economical process for industrial scale applications.

### **2.3.3 Multifunctional amorphous alloy coating**

Due to the excellent corrosion resistance of amorphous alloys, they have attracted increasing attention from corrosion engineers and scientists since their discovery. A great number of amorphous alloy systems have been studied in terms of corrosion protection applications such as Fe-, Zr- [54], Cu- [55] and Ni-based [56] amorphous alloys.

Most recently, Scully et al. have prepared an Al-Co-Ce coating, confirming the feasibility of preventing the corrosion of AA2024-T3 [57-59]. They also proposed a new corrosion protection coating system [18], shown in **Figure 2-3**. In this system, the Al-Co-Ce nanocrystalline/amorphous coatings regarded as the replacement of the roll-bonded cladding layer was found to be multifunctional, behaving as corrosion barrier and sacrificial anode, having active corrosion

inhibiting property. In addition, an Al-Co(Ni)-Y amorphous alloy coating has also been fabricated through plasma spraying and proven to have favourable corrosion resistance in salt fog tests [60, 61].

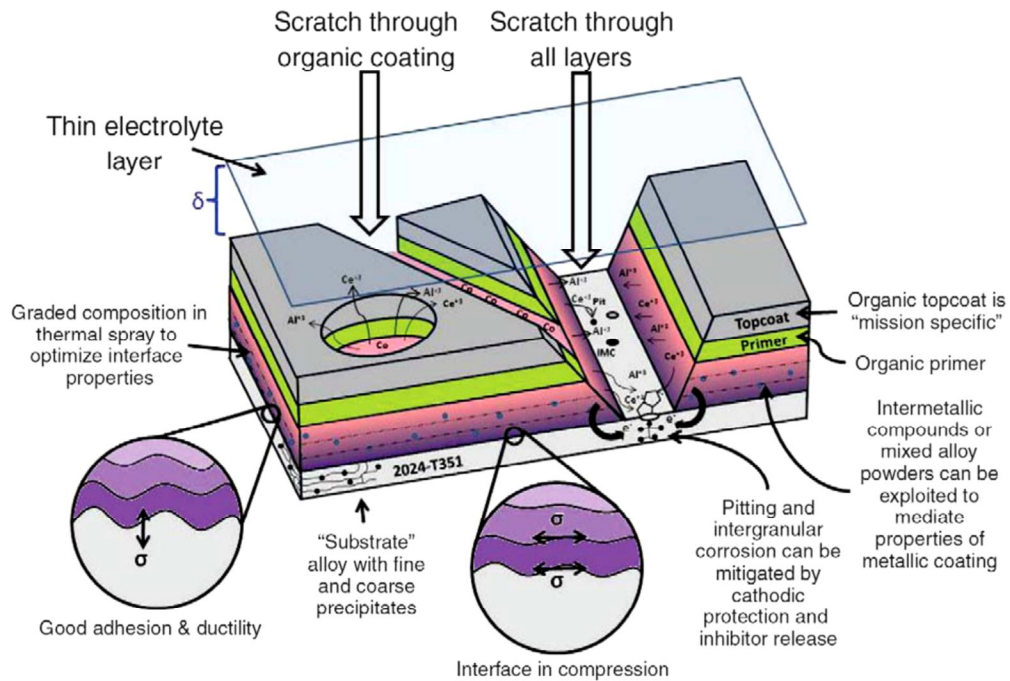


**Figure 2-3 Schematic of a new coating system for corrosion protection of AA 2024, comprised of a Al-Co-Ce nanocrystalline/amorphous coating, an organic primer, and an organic topcoat [18].**

## 2.4 Al-TM (transition metal)-RE (rare earth) amorphous alloys

### 2.4.1 Introduction

Binary alloys of Al-metalloid and Al-TM (TM=transition metal) systems were first tried to prepare Al-based amorphous alloys by the rapid solidification process, including Al-Si, Al-Ge and Al-TM (TM=Cu, Ni, Cr or Pd) alloys, etc. However, the single fully amorphous phase was not achieved until the discovery of Al-Fe-B

and Al-Co-B ternary amorphous alloys containing more than 50at.% Al in 1981. After that, the completely amorphous phase was also found in Al-Fe-Si, Al-Fe-Ge and Al-Mn-Si alloys prepared by roller melt-spinning techniques. Disappointingly, all the above amorphous alloys were brittle and therefore have not attracted much attention from researchers.

In 1987, Inoue et al. discovered an amorphous phase with good ductility in Al-Ni-Si and Al-Ni-Ge alloy systems [1, 2]. Since this discovery, a number of ternary ductile amorphous alloys consisting of Al-EM-LM (EM=early transition metal, LM=late transition metal) were found, such as Al-Zr-Cu, Al-Zr-Ni and Al-Nb-Ni [2] which contained above about 80 at% Al. Subsequently, some Al-LM-RE (RE=rare earth metal) ternary alloys were also discovered by He et al. and Inoue et al., which are exemplified by Al-TM-RE (RE=Ce, Gd or Y, LM=Fe, Co, Ni or Rh) [3] and Al-(Y, La, Ce)-(Fe, Co, Ni, Cu) [4, 5].

The mechanical properties of these Al-TM-RE alloys are especially outstanding. Both their tensile fracture strength (900~1100 MPa) and Vickers hardness (300~380 HV) greatly exceeded those of conventional crystalline aluminium alloys (up to 600 MPa and 150 HV, respectively) [6]. Due to the high content of aluminium, Al-TM-RE amorphous alloys also exhibited good bending ductility [7]. Moreover, the favourable corrosion resistance is another advantage of the Al-TM-RE amorphous alloys [8]. With a combination of good mechanical properties (ductility and strength) and chemical properties such as corrosion resistance, Al-TM-RE amorphous alloys have been extensively studied from various perspectives, especially the Al-(Fe, Co, Ni, Cu)-(Y, La, Ce) alloys systems.

### 2.4.2 Glass forming ability (GFA)

Generally, glass forming ability (GFA) is concerned with the constituent element species, atomic interactions and the movement of atoms in the amorphisation process. However, to date, there has not been a general model which can explain the mechanism of amorphous phase formation or crystallisation. Most conclusions about the GFA are drawn from experimental results and empirical rules. According to the experimental studies e.g. the small critical dimension of the Al-based amorphous alloys and high critical required cooling rate, the GFA of aluminium based amorphous alloy is generally weak compared with the conventional Cu-, Co-, RE- based and other alloy systems. This weak GFA has been explained in the aspects of undercooling behaviour and superheated melt viscosity, etc. Lu et al. [62] proposed a  $\gamma$  criterion to estimate the GFA of alloys.

$$\gamma = T_x / (T_g + T_l) \quad \text{Eq. 2-2}$$

where  $T_x$ ,  $T_g$  and  $T_l$  are the onset temperature of the crystallisation, the glass transition temperature and liquidus temperature, respectively. In this criterion, the GFA is not only concerned with the formation of amorphous structure in the solidification process, but also the suppression of crystallisation. Overall, the  $\gamma$  value of Al-based amorphous alloys is less than 0.35, which is lower than that of Zr or La-based amorphous.

In addition, the alloy viscosity in the liquid state also influences the GFA of the alloys. Generally, a high viscosity means a stronger GFA. In 1969, Turnbull et al. [63] proposed a formation mechanism of amorphous structure according to the classic nucleation theory of crystalline structure and built a relationship between the nucleation rate and the viscosity coefficient. Recently, Bian et al. [64]

proposed the concept of fragility of superheated melts. They found that the fragility of superheated melts (defined as  $M$ , given in the below formula) is closely related to the GFA in the Al-based amorphous alloys.

$$M = \left| \frac{\partial \eta(T) / \eta(T_L)}{\partial T / T_L} \right|_{T=T_L}, \eta = \eta_0 \exp\left(\frac{E}{RT}\right) \quad \text{Eq. 2-3}$$

where  $\eta$  is the liquid viscosity at an elevated temperature  $T$  above the melting point,  $E$  is active energy,  $R$  is the gas constant,  $T_L$  and  $\eta(T_L)$  are the liquidus temperature and viscosity at that temperature, respectively. Meng et al. [65] modified the  $M$  proposed by Bian et al. The modified fragility parameter  $M^*$  gives a much better explanation of the weak GFA of Al-based alloys by comparing with Pr-based alloys. In summary, the GFA of Al-based alloy is relatively weak compared with other glass forming alloy systems, which results in the difficulty in preparation of bulk amorphous alloy.

### 2.4.3 Glass formation range

Overall, Al-TM-RE amorphous alloys have a wide range of amorphous compositions. The compositional ranges for the formation of amorphous phase in Al-TM-Y [5], Al-TM-Ce [4] and Al-TM-La [5] (TM=Fe, Co, Cu and Ni) alloys were given by Inoue et al, as shown in **Figure 2-4**. The above amorphous phases were formed by melt spinning. It can be seen that in the Al-TM-Y and Al-TM-Ce systems, the formation range of the Al-Ni-(Y, Ce) alloy system is the largest, then Al-Cu-(Y, Ce), Al-Co-(Y, Ce) and Al-Fe-(Y, Ce). However, for the Al-TM-La systems, the Al-(Ni, Fe and Co)-La alloy systems have much wider formation ranges compared with Al-Cu-La system.

Particularly, the glass formation range of Al-Co-Ce alloy in the Al-rich corner was

studied by Gao et al. [66]. They investigated a good number of alloys compositions to identify the glass formation range of the Al-Co-Ce alloy, as shown in **Figure 2-5**. In their work, a single-wheel melt spinning technique was used to make amorphous alloys. From the figure, it can be seen that the glass formation range of Al-Co-Ce alloy system is relatively wide. The wide glass formation range means that the glass forming ability of this alloy system is not sensitive to the composition, which is beneficial for the preparation of coatings with these constituent elements.

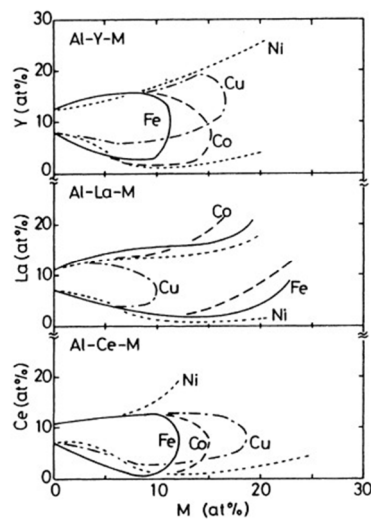


**Figure 2-4** Compositional ranges for formation of the amorphous phase in Al-TM-Y, Al-TM-Ce and Al-TM-La (TM=Fe, Co, Ni or Cu) systems [67]. The alloys were prepared by melt-spinning technique.

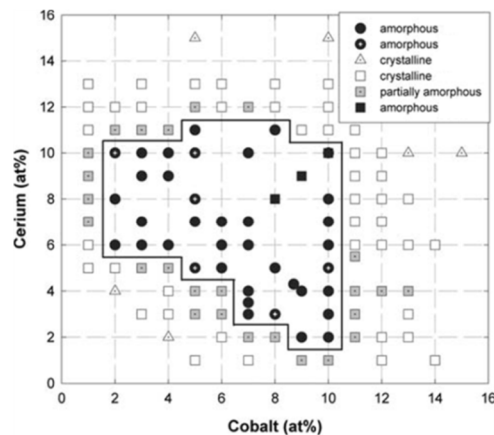


**Figure 2-5** Glass formation range of Al-Ce-Co alloy system in the Al-rich corner, whose border is marked by the solid lines [66]. The early reported work is also shown in references [4, 68].

## 2.4.4 Microstructure of Al-TM-RE nanocrystalline/amorphous alloy coatings

### 2.4.4.1 Al-Co-Ce based coatings

Scully et al. [14, 69] prepared nanocrystalline/amorphous Al-Co-Ce based coatings on AA2024 substrates by different spray techniques, including high velocity oxy-fuel spray (HVOF), pulsed thermal spray (PTS) and cold gas dynamic spray (CGDS). They found that the coatings prepared by either HVOF or PTS always have a typical splat microstructure and pores. The coatings are not as homogeneous as spun ribbon although many amorphous structures exist. However, the CGDS coatings are denser and more homogeneous than the HVOF or PTS ones. The microstructures of Al-8.3Co-7Ce (at.%) coatings prepared by HVOF, PTS and CDGS are shown in **Figure 2-6**, **Figure 2-7** and **Figure 2-8**, respectively.

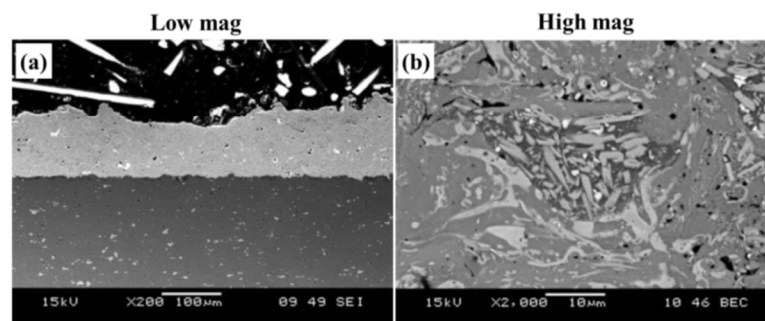


**Figure 2-6** Cross sectional SEM images of Al-8.3Co-7Ce (at.%) HVOF coating [14].

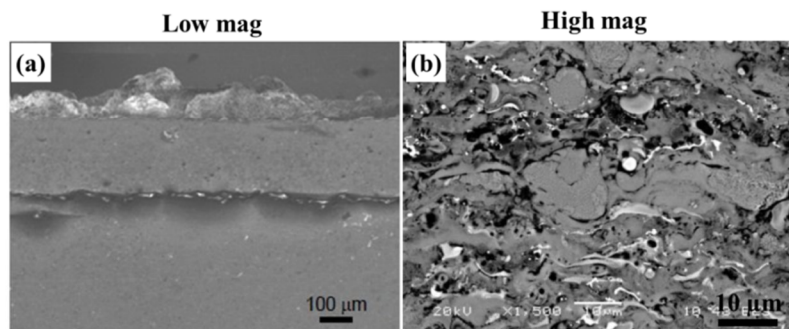


**Figure 2-7** Cross sectional SEM images of Al-8.3Co-7Ce (at.%) PTS coating [14].

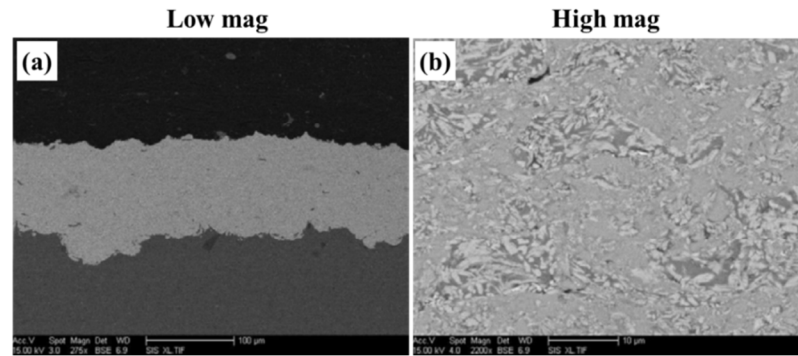


**Figure 2-8** Cross sectional SEM images of Al-8.3Co-7Ce (at.%) CGDS coating [69].

Their XRD result shows that the Al-Co-Ce coatings consisted of an amorphous matrix and small amounts of Al nanocrystals and  $\text{Al}_4\text{Ce}$  intermetallics. However, compared to the XRD pattern of feedstock powders, the amorphicity in the coating is increased. **Figure 2-9** shows the XRD patterns of Al-8.3Co-7Ce (at %) coatings.

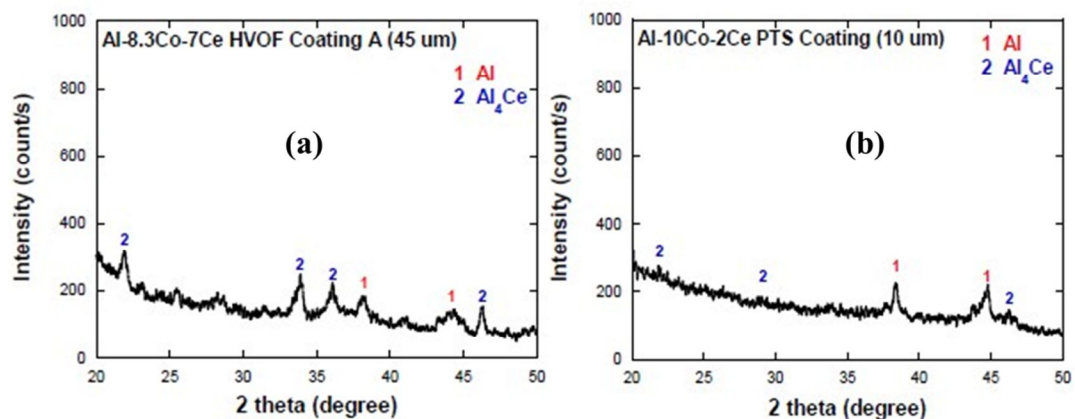


**Figure 2-9** XRD pattern of Al-8.3Co-7Ce (at %) alloy coatings[69]. (a) HVOF coating and (b) PTS coating.

#### 2.4.4.2 Al-Co-Y based coatings

Kato and van Aken et al. [60, 61] prepared Al-Co-Y based coatings on the AA7075 substrate through an air plasma spraying process. The coatings they produced also exhibited a typical lamella and porous structure. **Figure 2-10a** is a secondary electron SEM image of the  $\text{Al}_{85}\text{Ni}_5\text{Co}_2\text{Y}_8$  coating. There were still some crystalline phases in the amorphous matrix of the ternary Al-Co-Y alloy. However, when a small amount of nickel element was added into the alloy or some

aluminium elements were replaced by yttrium elements, the glass forming ability of Al-Co-Y based alloys greatly increased. In their studies, the  $\text{Al}_{81}\text{Ni}_5\text{Co}_2\text{Y}_{12}$  coating has the fewest nanocrystals and the best glass forming ability.

The XRD result of the  $\text{Al}_{85}\text{Y}_8\text{Ni}_5\text{Co}_2$  coating is shown in **Figure 2-10b**. As seen from Figure, there is an obvious hump in the pattern, which indicates that the coating has amorphous structure. However, the peaks of the Al phase also exist in the pattern. The existence of Al peaks shows that the coating is not fully amorphous but comprised of nanocrystals in the amorphous matrix.

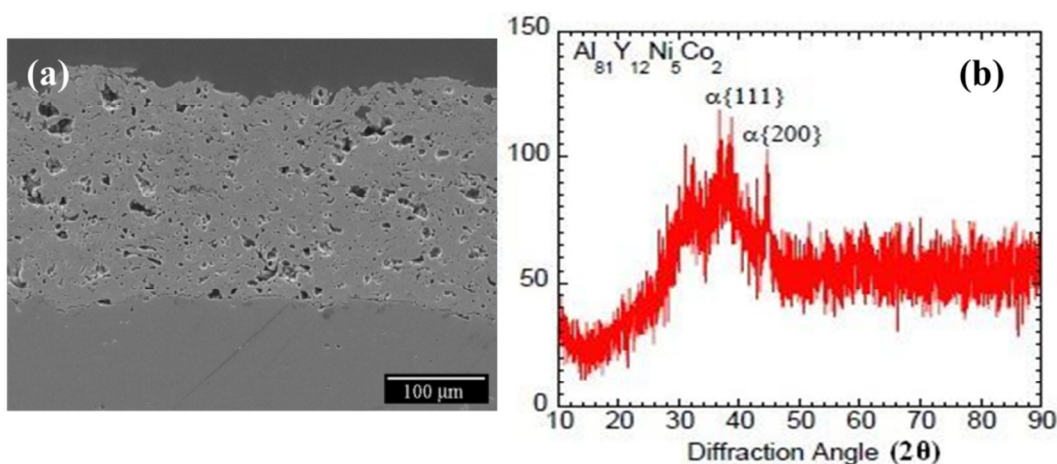


**Figure 2-10** Cross sectional SE image (a) and XRD pattern (b) of  $\text{Al}_{85}\text{Ni}_5\text{Co}_2\text{Y}_8$  coating prepared by plasma spraying [60].

#### **2.4.5 Corrosion behaviour of Al-TM-RE amorphous alloys and coatings**

Bulk metallic glasses have become a group of new materials with a large potential to be applied in a variety of engineering fields. Due to its high specific strength, aluminium-based bulk metallic glass is regarded as one of the most attractive bulk metallic glasses. During the past few decades, this new aluminium-based bulk metallic glass has been widely investigated for glass forming ability, thermal stability and mechanical properties, etc. It is necessary to understand the corrosion

behaviour of these materials when they are used in corrosive media, high-temperature or oxidising atmospheres. To date, a great number of studies have been conducted on the corrosion behaviour of Zr-, Fe-, Cu-, Ni-, Mg-, Ca- and Ti-based amorphous alloys. However, there are only limited published results regarding the Al-based amorphous alloys.

#### **2.4.5.1 General corrosion mechanism**

Overall, the mechanism of general corrosion for aluminium-based amorphous alloys is analogous to that for the conventional crystalline aluminium alloy. It is well known that aluminium alloys usually exhibit the active-passive behaviour which results in the formation of a passive film (mainly consisting of  $\gamma$ -Al<sub>2</sub>O<sub>3</sub> and other oxides) on the material surface. The dense, continuous, low-electrical conductivity and well-adherent film can hinder the corrosion process [70].

For the amorphous alloy, due to the rapid solidification process, it becomes possible to make more alloying elements dissolve in the alloy which can improve its passive ability. Therefore, the corrosion penetration rate (CPR) of the aluminium amorphous alloy is usually much lower than that of the conventional crystalline aluminium alloy [71]. Local corrosion commonly occurs on defects such as grain boundaries, precipitates and dislocations. Due to the chemical homogeneity and lack of defects, amorphous alloys generally possess better corrosion resistance than their crystalline counterparts.

As for Al-based amorphous alloys, Scully's group in U.S. conducted a series of studies about their corrosion behaviour. The alloys they investigated mainly included Al-Fe-Gd, Al-Ni-Y, Al-Ni-Gd and Al-Co-Ce alloys. In their work, they found that the general corrosion behaviour of a variety of Al-TM-RE alloys is

associated with the pH value of the corrosion solution [71]. For example, in aqueous solutions with an acidic pH, the passive dissolution rate of both Al-Fe-Gd and Al-Co-Ce fully amorphous alloys was slightly faster than that of pure polycrystalline aluminium. However, in the case of the solution with an alkaline pH, passive current densities were considerably decreased due to the presence of TM- or RE- enriched passive films on the alloy surface. The formation of a passive film was attributed to the relatively low solubility of Fe, Co, Gd and Ce oxides and hydroxides compared with Al oxide in alkaline solution. In a range of near-neutral solutions, no obvious differences in the passive current densities were observed between the amorphous alloys and the crystalline ones.

Compared to the crystalline aluminium alloys, the totally amorphous Al-TM-RE alloys containing more than 85at.% Al also exhibited excellent pitting corrosion resistance [71]. Both the pitting and repassivation potentials are several hundred millivolts higher than that of polycrystalline pure Al. Additionally, Jakab [72] investigated the active inhibition behaviour of Al-Co-Ce amorphous alloys. It was found that this amorphous alloy can inhibit corrosion by storing, releasing and delivering  $\text{Co}^{2+}$  and  $\text{Ce}^{3+}$  inhibitors. Overall, the Al-TM-RE amorphous alloys are thought to be a new promising corrosion resistant alloy family.

### **2.4.5.2 Effects of crystallisation**

A great amount of Al-rich, solute lean, face-centred cubic nanocrystals formed in the Al-based amorphous matrix by primary crystallisation in the heat treatment process. According to the studies of Scully's group, partial crystallisation of Al-TM-RE amorphous alloys has a slight influence on their corrosion resistance, and the excellent pitting corrosion resistance is not lost. Lucente [73] also found

that when the density of nanocrystals is less than  $10^{22}/\text{m}^3$  or the volume fraction is lower than 40%, the nanocrystalline/amorphous alloys still resist the corrosion compared to bulk Al [73]. However, complete crystallisation will result in the deterioration of corrosion resistance.

As well as the work of Scully's group, many attempts have been made by other researchers to investigate the effect of crystallisation on the corrosion resistance of the Al-based amorphous alloys. Wu et al. [74] investigated the effect of crystallisation on the corrosion performance of  $\text{Al}_{86}\text{Ni}_6\text{Cu}_2\text{La}_6$  amorphous alloy in 0.01 M NaCl solution through electrochemical measurement. The melt-spun  $\text{Al}_{86}\text{Ni}_6\text{Cu}_2\text{La}_6$  amorphous alloy was annealed to obtain the partially and fully crystallised forms. It was found that the corrosion resistance of the fully amorphous sample is much better than that of partially and fully crystallised samples. Furthermore, Lin et al. [75] investigated the crystallisation behaviour and corrosion resistance of as-spun  $(\text{Al}_{86}\text{Ni}_9\text{La}_5)_{98}\text{Zr}_2$  amorphous alloy. It was found that primary crystallisation of the amorphous phase enhanced the corrosion resistance of the amorphous alloy, while the secondary and complete crystallisation resulted in a decrease of corrosion resistance compared with the original amorphous alloy.

Green et al. [76] supposed that there should be a critical size of the crystals in determining their effect on the corrosion behaviour. Crystals with sizes above the critical value will become pitting attack sites and then influence the corrosion resistance of the whole amorphous alloy. However, if the crystals are very fine, the adverse effect of them will be very limited. Therefore, there is still some

controversy centred on whether the crystalline phase is detrimental to the corrosion resistance in the Al-based amorphous alloy system.

#### **2.4.5.3 Corrosion performance of Al-Co-Ce and Al-Co-Y coatings**

The corrosion behaviour and corrosion mechanism of coatings are different from those of the bulk materials because of their unique lamellar and porous microstructure. As for the Al-TM-RE amorphous alloy coatings, there is very limited literature about their corrosion behaviour or mechanism.

Scully et al. [18] studied the corrosion performances of Al-Co-Ce coatings by electrochemical experiments and salt fog tests. They found that Al-Co-Ce coatings usually have a higher pitting potential and repassivation potential than AA2024, which indicates that Al-Co-Ce coatings are good barriers for the corrosion of AA2024. Scully et al. also found that the open circuit potential (OCP) of Al-Co-Ce coatings can be several hundred millivolts lower than that of AA2024, which ensures a good sacrificial cathodic protection property. However, these electrochemical properties are greatly concerned with the alloy composition, shown in **Figure 2-11**.

Additionally, it was found that Al-Co-Ce alloy can release inhibiting ions, such as  $Ce^{3+}$  and  $Co^{3+}$ . When the scratches occur on the coating, inhibiting ions can retard the corrosion of the substrate aluminium alloy. Combining above characteristics of Al-Co-Ce coatings, they are expected to be used to replace or repair the cladding layer on the Al aluminium alloy. The researchers in Scully's group have conducted salt fog tests using artificially scratched samples [58]. In the salt fog tests, different samples were used including bare AA2024-T3, alclad samples and Al-Co-Ce coatings on the bare AA2024-T3. They found that the coating samples showed

slight corrosion outside the scratched region and no corrosion occurred within all the scratches with different sizes. However, for bare AA2024-T3 and Al-Clad samples, corrosion damage occurred not only outside scratches but also within the scratched regions, which is characterised by a reddish copper depleting appearance.

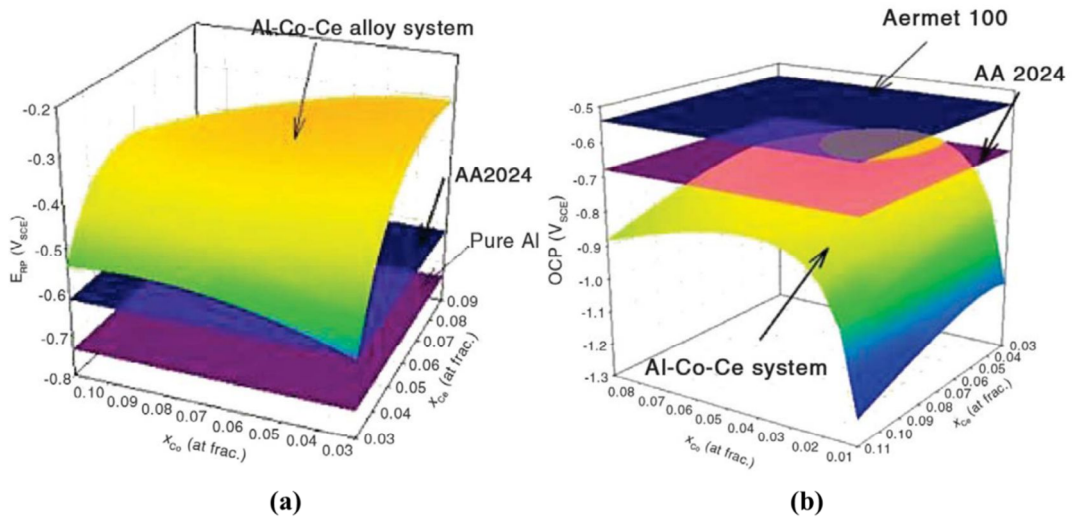


**Figure 2-11 The relationship between electrochemical property and Al-Co-Ce alloy composition. (a)  $E_{rp}$ , (b) OCP. The relationship shown is plotted from polynomial expressions developed from Scheffé polynomials based on tests conducted on amorphous MSR of various Al-Co-Ce alloys in 0.6 M NaCl solution at neutral pH [18].**

Kato and van Aken et al. [60, 61] prepared Al-Co-Y based coatings and studied corrosion behaviour through salt fog tests. They found that  $Al_{91}Y_4Co_5$  and  $Al_{89}Y_4Co_5Mo_2$  coatings have the best corrosion resistance. The application of silicon sealant can greatly improve the corrosion resistance of coatings. They also found that the coatings containing nickel elements showed poor corrosion resistance regardless of the yttrium content and the crystallinity of the coating. In addition, the coatings pretreated by laser melting did not show an improved corrosion resistance.

## 2.5 Preparation of bulk amorphous alloys, powders, coatings and surface layers

### 2.5.1 Bulk amorphous alloys

#### 2.5.1.1 Melting spinning

Melt spinning is a common technique to generate a bulk amorphous alloy, in which the arc or induction melted alloy is ejected and quenches on a rapidly rotating wheel, and finally transforms to amorphous state [77, 78], as shown in **Figure 2-12**. The molten alloy with a small volume can solidify within an extremely short time and eventually freeze the disordered atomic arrangement in the liquid state. However, due to the limited size of the products, this technique is always used as the tool to evaluate or compare the glass forming ability of the new alloys.

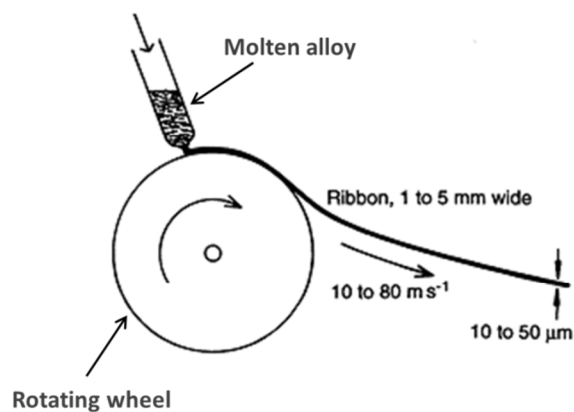


**Figure 2-12 Schematic diagram of melt spinning technique. The molten alloy generated by arc or induction heating is ejected onto the flat rim of a rapidly rotating wheel (typically made of copper) to produce a thin ribbon up to a few millimetres wide [77, 78].**

#### 2.5.1.2 Copper mould casting

To obtain 3-dimensional amorphous alloys, conventional rapid casting techniques are also applied. Copper mould casting is one of the most common and popular

methods. **Figure 2-13** shows the copper wedge mould casting equipment. In this process, the raw material (either pure metals or master alloys) in the crucible is heated and melted by the induction coil, and pushed into the wedge mould by the inert gas with a certain pressure. The melt solidifies quickly upon contacting with the cold copper mould which has good heat conduction capacity and can extract the heat from the melt rapidly. To improve the cooling effect, additional equipment such as a water cooling system can be used in the mould.

This method is widely used in the preparation of bulk amorphous alloys [79-81]. The application of wedge mould is to obtain different cooling conditions in the mould which is determined by the specific geometry of the mould. This technique has the advantage of investigating the amorphous-crystalline transition behaviour. Inoue et al. [79] placed a thermo-couple in the centre of the wedge mould in order to measure the cooling rate of the alloy at different positions.

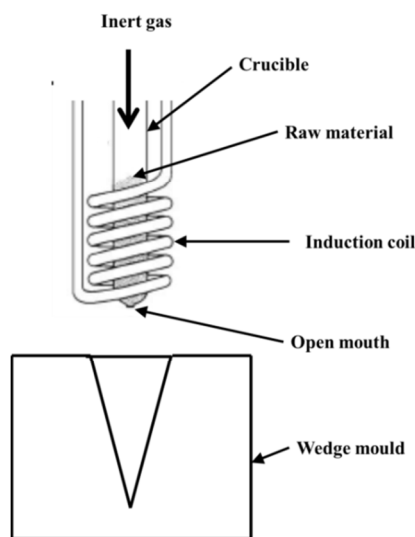


**Figure 2-13 Schematic diagram of wedge mould casting.**

### **2.5.2 Coatings**

Due to the low cost, simple equipment, flexible process and availability of field operation, thermal spraying is an important surface modification technique. It has

been widely used in many fields including repairing, remanufacturing and protection of the material surface. In the thermal spraying process, the spraying materials usually experience rapid solidification, which makes this technique promising to prepare amorphous alloy coatings. Thermal spraying is probably the most promising method to produce relatively thick amorphous surface layers to modify the wear or corrosion properties but not to influence the mechanical properties of substrate such as strength and ductility [82-84].

However, due to the unique lamellar and porous structure, thermal sprayed coatings do not display the excellent wear or corrosion resistance of the bulk consolidated amorphous alloys. Moreover, it is difficult to produce fully amorphous structures even in vacuum or low pressure environments, which results from the annealing effect of subsequent particles on the previously deposited layer. Because of these two mentioned disadvantage for utilising thermal spraying to produce amorphous alloy coatings, few amorphous alloy coatings prepared by thermal spraying have been successfully commercialised. However, many attempts have been made to prepare coatings with a higher content of the amorphous phase and more favourable microstructures through various thermal spraying technologies. Moreover, the cold spraying process has also been developed and used in preparing amorphous coatings.

#### **2.5.2.1 Plasma spraying**

In the plasma spraying process, a DC electric arc is used to ionise the plasma gas and generate the high temperature stream. The high temperature stream acts as the heat source to heat and melt the feedstock powders. Then, the fully or partially melted powders will deposit on the surface of the substrate by the carrying of the

inert gas. Plasma spraying is a relatively inert spraying process due to the use of inert or reducing gas as the plasma gas and carrier gas (e.g. N<sub>2</sub>, Ar, H<sub>2</sub> and He). The inert spraying process is beneficial to the formation of amorphous alloy coatings. However, oxidation of the feedstock powders is still inevitable because of the entrainment of air in the spray stream and high spraying temperature. Therefore, vacuum plasma (VPS) and low pressure plasma spraying (LPPS) have been developed to produce coatings with a higher content of amorphous phase.

Kishitake et al. [85, 86] prepared the amorphous Fe-based alloy coatings (Fe-10Cr-10Mo and Fe-17Cr-38Mo-4C) through three different plasma spray processes including conventional air plasma spray, low-pressure plasma spray and high-energy plasma spray. It was found that the coatings prepared by LPPS are almost amorphous, while the crystalline phase together with the amorphous phase was observed in the coatings obtained by APS (air plasma spraying) and HPS (high-energy plasma spraying). The corrosion resistance in H<sub>2</sub>SO<sub>4</sub> solution of these coatings was investigated. The amorphous coatings had comparable even better corrosion resistance when compared with the SUS316L stainless steel.

Recently, the air plasma spray process also has been used to produce the Al-TM-RE amorphous coatings. Van Aken and Kato prepared the Al-Co-Y based nanocrystalline-amorphous coatings using air plasma spray and studied their corrosion resistance through salt fog tests [60, 61]. They found that the coatings with the compositions of Al<sub>81</sub>Y<sub>12</sub>Ni<sub>5</sub>Co<sub>2</sub>, Al<sub>85</sub>Y<sub>8</sub>Ni<sub>5</sub>Co<sub>2</sub>, and Al<sub>89</sub>Y<sub>4</sub>Co<sub>5</sub>Mo<sub>2</sub> almost entirely consisted of the amorphous phase. Furthermore, the increase of the yttrium content was considered as the main factor in improving the glass forming ability of coatings.

### **2.5.2.2 High velocity oxygen/air fuel (HVOF) spraying**

High velocity oxygen fuel (HVOF) spraying is an important process to produce metal or cermet coatings. In the process of HVOF, the flame temperature of the HVOF process is lower than that in the process of plasma spraying, which can decrease the oxide content in the coatings. In addition, the particle velocity is higher in the HVOF process than that in the plasma spraying due to the special design of the nozzle. The high particle velocity will make the molten or half-molten particles impact onto the substrate surface with a relatively large kinetic energy, which results in good deformation to enhance the pore-filling and adhesion strength.

In view of the above advantages of HVOF process, many attempts have been made to produce amorphous alloy coatings. Kishitake et al. [83] prepared a Fe-10Cr-13P-7C amorphous coating through the HVOF technique and compared it with the coatings deposited by LPPS and HPS. Fe-10Cr-13P-7C coating prepared by the HVOF process showed the higher content of amorphous phase and better corrosion resistance in 1 N HCl solution and 1 N H<sub>2</sub>SO<sub>4</sub> solution than the coating prepared by HPS. However, both the content of the amorphous phase and the corrosion resistance were lower than that of the LPPS coating.

Otsubo et al. [84] studied the effects of alloy composition and HVOF process parameters on the quality of sprayed coatings. Several Fe-Cr-Mo-8P-2C coatings with different contents of Cr and Mo were produced using the HVOF technique under various process parameters. They found that during the preparation of coatings the flame temperature played an important role in determining the content of the amorphous phase. Lower flame temperatures meant a higher content of

amorphous phase in the coatings. While the coatings containing 10 wt.% Cr had a fully amorphous phase and the best corrosion resistance, which showed that the corrosion resistance greatly depended on the content of the amorphous phase.

In addition to the Fe-based coatings, Ni-based [87, 88] and Zr-based [82] coatings have been produced by the HVOF process. Recently, a multi-disciplinary research project was performed in the U.S. [69]. In this project, they prepared a multifunctional amorphous/nanocrystalline Al-Co-Ce coating using Al-13Co-26Ce feedstock powders with the size of 45  $\mu\text{m}$ . However, the fully amorphous Al-based coating has not been successfully prepared to date. It should be noted that all of the totally amorphous alloy coatings, such as previously mentioned Fe-based, Zr-based and Ni-based coatings, were prepared using fully amorphous feedstock powders. However, the feedstock powders used to prepare the above Al-based coatings were comprised of both amorphous and crystalline materials. Therefore, the state of feedstock powders may be a critical factor that resulted in a relatively low content of amorphous phase in the Al-based coatings.

Oxidation is a detrimental factor in the preparation of amorphous coatings. In order to reduce oxidation, a new high velocity air fuel (HVAF) process [89, 90] has been developed and introduced to prepare amorphous coatings. In the HVAF process, the air is used as the combustion-supporting gas instead of pure oxygen in the HVOF process, which makes it possible that a lower amount of oxygen will be involved in the HVAF spraying process. Recently, Ni-based and Fe-based amorphous coatings have been prepared using HVAF process. Compared with the coatings prepared by HVOF, the oxidation of the coatings prepared through the HVAF process is reduced, and the corrosion resistance of HVAF coatings is better.

Thus, the HVAF process is thought to be a more economical process and more promising to realise industrial production.

### **2.5.2.3 Detonation spraying**

In the detonation spraying, the coating materials (usually in the form of powder) are fed into a long, one-end closed and one-end open tubular barrel together with the carefully measured mixture of gases (usually oxygen and acetylene). A spark is used to ignite the gas mixture, which results in the detonation to heat and acceleration of the coating powder to impact onto a substrate material with a supersonic velocity. Between two detonations, nitrogen gas is used to purge the barrel. This detonation process is repeated many times a second. Due to the high velocity of the powders, the coatings prepared by the detonation spraying are denser and have stronger adhesion to the substrate.

Detonation spraying has been widely used to prepare various coatings, ranging from metallic alloys to hard ceramics [91]. Recently, Zhou et al. [92] has prepared a largely amorphised Fe-based alloy coating with the composition of  $\text{Fe}_{48}\text{Cr}_{15}\text{Mo}_{14}\text{C}_{15}\text{B}_6\text{Y}_2$  (at.%) by the detonation spraying process. The coating showed a typical lamellar structure with porosity below 2%. Electrochemical corrosion tests also indicated that the coating has excellent resistance to the local corrosion.

Two companies based in the U.S. named Enigmatics, Inc., and Science Applications International Corporation (SAIC) have developed a new coating technology, namely pulsed thermal spray (PTS), which is quite similar to detonation spraying in principle. Gauthier et al. [93] and Tailleart et al. [15] have prepared a great number of Al-Co-Ce (Mo) amorphous/nanocrystalline coatings on

AA2024-T351 through this technology. In this PTS process, rapid particle acceleration and heating results in a minimal residence time of the particles within a high enthalpy environment. In their work, the AA 2024-T351 substrates do not exceed 60 °C during the coating process. This also greatly limits the temperature increase of the substrate and suppresses the crystallisation of the coatings.

#### **2.5.2.4 Cold spraying**

Cold spraying, also called cold gas dynamic spraying (CGDS), is a newly developed spraying process. In the cold spraying process, the feedstock powders are accelerated by the inert propelling gas and finally impact on the surface of substrate metal at a rather high velocity. It has been confirmed that the speed of the feedstock powders must reach a critical value in order to get enough kinetic energy to form the coating. Due to the low temperature of the process, the cold spraying process has great advantages on depositing the fine powders [94] and the powders which are sensitive to high temperature. Therefore, the cold spray process is suitable for fabricating the amorphous coatings.

Recently, Cu-based [95, 96], Ni-based [97, 98], and Fe-based [99] amorphous alloy coatings have been prepared through the cold spray process. During the preparation of these coatings, the gas atomisation technique is used to produce feedstock powders of amorphous state. Because of the low process temperature which is below the crystallisation temperature of feedstock powders, the feedstock powders could almost totally keep the amorphous state.

**Figure 2-14** shows the SEM cross-sections of Ni-based and Fe-based coatings prepared by cold spray [98, 99]. From figure, it can be seen that the coating is dense, especially the Fe-based coatings. The XRD pattern corresponding to these

two coatings also showed that the coatings almost totally consist of the amorphous phase. Attributed to the fully amorphous and relatively dense structure, the coatings showed excellent corrosion and wear resistance.

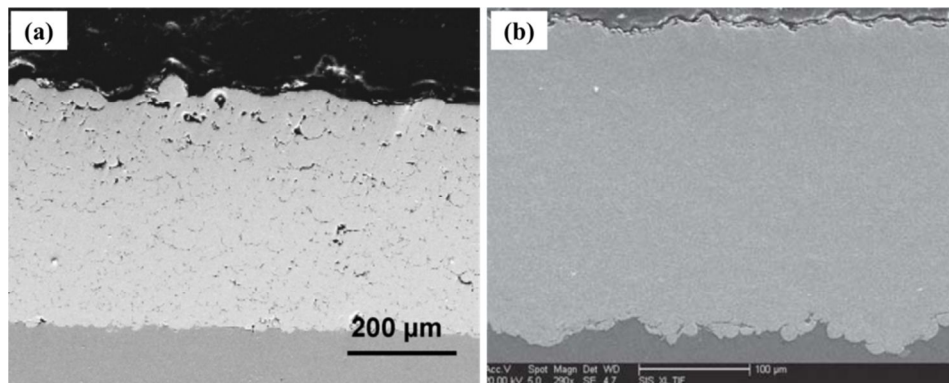


**Figure 2-14 Ni-based (a) and Fe-based (b) amorphous alloy coating prepared by the cold spray process [98, 99].**

An attempt has been made to prepare Al-based amorphous alloy coating using Kinetic Metallisation (KM) which is a particular variant of cold spray developed by a technology company named Inovati in the United States [100]. The feasibility of producing amorphous Al-based coating using cold spray process has been confirmed in Moran's work [101]. The nanocrystalline/amorphous feedstock powders with the size of 10 μm were used. The coatings they obtained were dense, although there were some nanocrystalline phases in the as-sprayed coatings.

In the cold spray process, particle diameter, working gas species, gas pressure, gas temperature, particle temperature and substrate temperature are important parameters to influence the coating quality and performance. Choi et al. [88] studied the effect of particle temperature on the deposition behaviour of Ni-based amorphous alloy coatings. It was found that the critical velocity of the feedstock powders decreased with increasing particle temperature. This might be due to the thermal softening of the bulk amorphous material when it was heated to the liquid

metal region between the glass transition temperature and the crystallization temperature.

### **2.5.3 Surface layers**

#### **2.5.3.1 Sputtering**

Sputtering is one of the physical vapour deposition (PVD) methods, which is widely used in many fields such as thin-film deposition, etching and analytical techniques. In the sputtering deposition process, atoms are ejected from a solid target material due to the bombardment of the target by energetic particles and then deposited onto a substrate material [102].

Sputtering is an important technique to prepare a variety of amorphous alloy coatings on the conventional crystalline materials. In the late 1980s, Yoshioka et al. deposited a series of Al-based amorphous coatings by the sputtering process. The alloy systems include both binary and ternary alloys, such as Al-Ti, Al-Zr, Al-Nb, Al-Mo, Al-W, Al-Mg-Ti and Al-Cr-Mo, etc. [103-107]. It was also found that these Al-based alloys especially ternary alloys exhibited excellent pitting corrosion resistance. In addition, Sanchette et al. [108] deposited Al-TM-(N) amorphous coatings by the process of reactive magnetron sputtering of composite Al-TM targets in the gas mixture of Ar and N<sub>2</sub>. However, to date, there has not been any attempt made to deposit Al-TM-RE alloys coatings by the sputtering process.

#### **2.5.3.2 Laser surface melting**

A variety of laser treatments have been widely used in the surface modification of materials for several decades, such as laser glazing, laser remelting and laser cladding, etc. In the laser surface melting process, a thin surface layer of the alloy

will be instantaneously melted by the irradiation of the high-energy density laser beam. In the case of the laser cladding process, powder feedstock with the high glass forming ability can be preplaced on the surface of the substrate metal or fed along with the laser treatment process. Immediately after the melting, the melted surface layer or the cladding layer will be rapidly quenched by the thermal conduction between the melted and the cold unmelted substrate metal, which results in a high cooling rate. The high cooling rate and appropriate metal composition, together with the favourable irradiation conditions, will finally promote the formation of amorphous alloy layers or coatings [109].

In 1976, a Pd-Cu-Si amorphous alloy coating was first achieved by Breinan et al. through continuous wave CO<sub>2</sub> laser glazing [110]. Since then, amorphous structures in various alloy systems have been obtained by laser treatment [111-113]. The amorphous alloy layers obtained through laser treatment exhibited excellent corrosion protection [114, 115].

However, the composition range which can form amorphous alloy coatings by laser treatment is quite narrow compared with that by conventional methods, such as melt spinning [114]. An annealing effect resulting from the overlapping of the subsequent track is also inevitable in the laser treating process, which may induce crystallisation and non-uniformity of amorphous alloy layer. In addition, due to the limited heating depth of the laser beam, it is difficult to obtain a thick amorphous alloy layer. Hirose et al. [116] reported that the thickness of the single amorphous phase Fe<sub>78</sub>B<sub>13</sub>Si<sub>9</sub> alloy layers quenched by CO<sub>2</sub> and YAG laser was 15 μm and ~3 - 7 μm, respectively. Recently, Wu et al. [117] prepared Fe<sub>57</sub>Co<sub>8</sub>Ni<sub>8</sub>Zr<sub>10</sub>Si<sub>4</sub>B<sub>13</sub>

amorphous coating with the thickness of 1.2 mm by using high-GFA alloy composition and suitable process parameters.

Recently, Hoekstra et al. [118] have successfully obtained an amorphous layer on the surface of a bulk crystalline alloy with the composition of  $\text{Al}_{84}\text{Co}_{7.5}\text{Ce}_{8.5}$  (at.%) by laser quenching. Due to the relatively homogeneous microstructure and lack of defects, this amorphous alloy layer also has enhanced corrosion resistance compared to its crystalline counterpart.

### 2.5.3.3 Electron beam surface melting

**Figure 2-15** shows the conventional electron beam components and operation of the electron beam materials processing. In conventional electron beam processing, the electrons released from the hot cathode are first accelerated to a high velocity, and then greatly focused to an electron beam with a high power density through focusing system. Upon bombarding on the target surface, the kinetic energy brought by the electrons can be converted to thermal energy. This thermal energy can cause a very high temperature which will melt or even vaporise the target material. Therefore, the generated electron beam can be used for welding, cutting, drilling, etc.

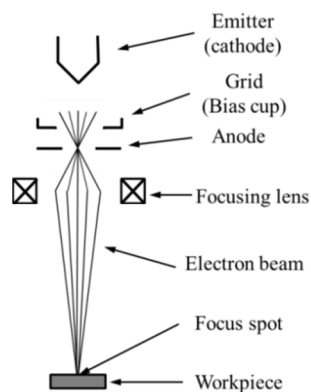


**Figure 2-15 Schematic diagram of conventional electron beam components and operation of electron beam materials processing.**

The power density distribution of the conventional electron beam is non-uniform, usually Gaussian distribution. Therefore, the centre of the beam spot can obtain more energy input compared with the edge. In the multi-track electron beam processing, the non-uniform power density distribution also results in the annealing of the overlapped irradiated area. In addition, in conventional continuous electron beam processing, the long irradiation time always results in the evaporation of the irradiated materials, which causes the scattering of the electron beam and energy loss. The application of the high-energy electron beam is well established as an effective method to prepare an amorphous coating or surface layer. A high-energy (0.5-1.5 MeV) scanning electron beam irradiation process has also been used to generate the amorphous phase in Zr and Cu based alloy [119].

### **2.5.4 Powders**

#### **2.5.4.1 Gas atomisation**

Gas atomisation is a very common technique to produce metal or alloy powders [120]. In this process, a molten metal flow is atomised into droplets by an inert gas with moderate pressure. The atomised droplets are rapidly solidified before they agglomerate or impact onto the atomising chamber. Although the products prepared by gas atomisation is powders with small size, the amorphous powder can be further processed into bulk metal glass through various powder metallurgical techniques such as sintering, hot extrusion and hot pressing and as a feedstock for thermal spraying. Therefore, gas atomisation has been an attractive approach and widely studied and applied.

Al-based amorphous powder had not been produced by gas atomisation until Inoue et al. reported that Al-Y-Ni amorphous powders was prepared by high-pressure gas atomisation in 1988 [121]. Since this successful case, a great variety of Al-based amorphous alloy powders have been produced by this method such as Al-Fe-Nd [122], Al-Ni-La [123], Al-Gd-Ni-Fe [124], Al-Ni-Ce-Fe-Cu [125] and Al-Ni-Y-Co-Fe [126]. The size of the atomised powder is a critical factor to determine the powder properties, such as the content of the amorphous phase and surface appearance. **Figure 2-16** shows the surface morphologies of atomised  $\text{Al}_{82}\text{Ni}_{10}\text{Y}_8$  powders with different diameters. It is seen that the smaller powder is smoother than the larger ones. In addition, there are no dendrites in the fine powders resulting from the non-equilibrium solidification. The XRD pattern of powders with different sizes also showed that fine powders had a higher content of the amorphous phase.

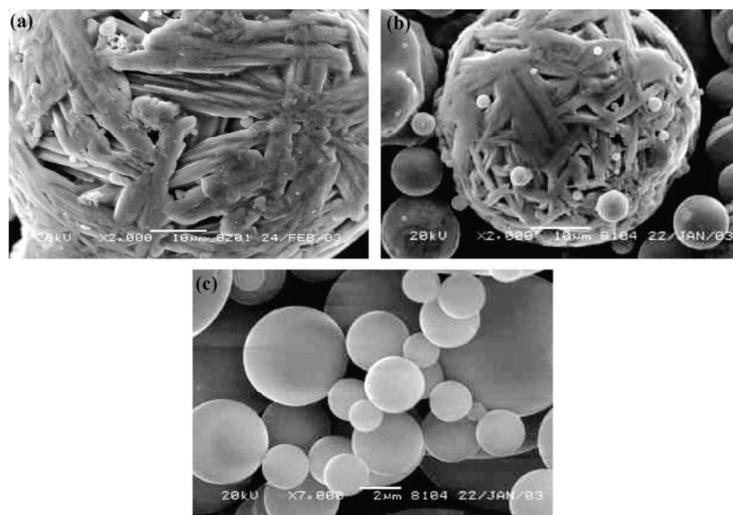


**Figure 2-16 Surface morphologies of atomised  $\text{Al}_{82}\text{Ni}_{10}\text{Y}_8$  powders with different diameters [127].**

Hong et al. [128] studied the microstructure and mechanical properties of atomised Al-14wt%Ni-14wt%Mm (Mm=misch metal) alloy powders and their extruded bar. It was found that the bar extruded by the fine powders had higher ultimate tensile

strength and elongation. In addition, the process parameters of gas atomisation such as the atomising gas composition, gas pressure and melt superheat temperature also influence the powder properties [124, 129].

#### **2.5.4.2 Mechanical alloying**

In 1970, Benjamin and his colleagues [130] developed a process named mechanical alloying (MA) to produce homogeneous composite particles. The particles achieved by this process with a dispersed and uniform internal structure, were successfully used to prepare oxide-dispersion strengthened Ni- and Fe-based superalloys by the hot consolidation process. Mechanical alloying (MA) is a solid-state powder processing technique. The process involves repeated cold welding, fracturing, and re-welding of constituent particles in a high-energy ball mill until all of the constituents are finely divided and uniformly distributed through the interior of each particle [130].

Due to the capability of the MA process to produce a variety of equilibrium and non-equilibrium alloy phases starting from mixed pure constitutive elements or pre-alloyed powders, there have been a great number of amorphous alloys prepared by MA in the past few decades. Koch et al. [131] prepared  $\text{Ni}_{60}\text{Nb}_{40}$  amorphous alloy by mechanically alloying of the pure Ni and Nb elements in a laboratory ball mill under a controlled environment in 1983. In addition, Al-based amorphous alloy powders have also been synthesised [132-135] by this process. The amorphous alloy powders prepared by the MA process can be used as the starting materials to produce bulk amorphous alloys through various consolidation techniques, such as sintering, hot or warm extrusion, etc.

In addition, much research work has been done to investigate the formation mechanism of the amorphous phase in a variety of alloy systems in the MA process [136]. To date, many mechanisms have been proposed for the amorphisation process induced by MA. However, there has not been a theory to clarify the amorphisation. It was generally accepted that the high concentration of defects increases the free energy system up to the level of an amorphous phase [137].

## **2.6 Large area electron beam surface melting**

### **2.6.1 Physical foundation**

The conventional electron beam process has been introduced in **Section 2.5.3.3**. To overcome its disadvantages, the low energy, high current, pulsed electron beam with larger beam spot size has been developed [138], as shown in **Figure 2-17**. In this electron beam source, before generation of electrons, argon with a pressure of 0.5 MPa is filled into the vacuum chamber. Once the argon pressure is reached, a magnetic field is triggered through the solenoid coil. When the magnetic field reaches a predetermined maximum intensity, a voltage is applied to the anode. The high anode voltage extracts the electrons from the cathode. Due to the presence of the above magnetic field, the electrons can move to the anode spirally around the flux lines of the magnetic field. During this spiral travelling of the electrons, electrons repeatedly collide with the pre-filled argon atoms. This penning effect results in the ionisation of the argon atoms and the formation of plasma around the anode.

When the concentration of the plasma reaches the pre-determined maximum (it usually takes 10-20  $\mu$ s), a voltage, i.e. the acceleration voltage (10-40 kV), which is much higher than the anode voltage will be triggered and applied to the cathode. Therefore, the electrons are greatly accelerated by this cathode voltage and move towards to the surface of the target, i.e. the workpiece. Simultaneously, when the electrons pass through the anode, the plasma generated around the anode greatly reduce the Coulomb force among the electrons, which improves the uniformity and increases the lifetime of the electron beam. In the formation and acceleration process of electrons, the plasma formation plays a role of buffer interface to build up the electron density around the cathode, and to maintain the uniformity of the electron density, as well as to extend the lifetime of the beam.

Based on the above description, this electron beam system has the advantages of radiation safety, simplicity of the high-voltage equipment and electron gun, long lifetime and large irradiation area, compared with the conventional electron beam system.

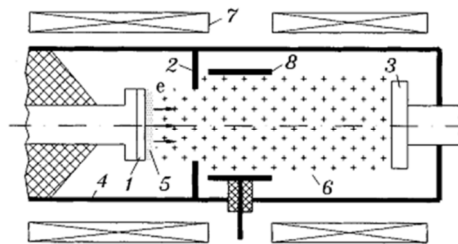


**Figure 2-17 Schematic diagram of low-energy, high-current electron beam sources using plasma-filled systems based on gas discharge plasma. 1-cathode, 2-anode, 3-workpiece, 4-vacuum chamber, 5-cathode plasma, 6-anode plasma, 7-solenoid, 8-Penning cell anode [138].**

## 2.6.2 Applications

As an emerging surface modification technique [138], low energy, high current, pulsed electron beam (LEHCPEB) has the same advantages as other high energy

beams, including a high cooling rate, short process time and limited effect on the substrate. In addition, LEHCPEB can process a large area (~60 mm diameter) with uniform intensity, thereby reducing the need for overlapping exposures and associated concerns relating to reheating and possible recrystallisation. Therefore, LEHCPEB has been extensively used in the surface engineering field.

Over the past decade, LEHCPEB has been applied to polish and improve the corrosion behaviour of mould surfaces, improve surface hardness, as well as the wear resistance of alloys. Uno et al. [139, 140] found that the metal mould surface was greatly smoothed by the electron beam irradiation. The corrosion resistance of an electron beam irradiated mould was also enhanced compared with the unirradiated surface. They also found that this electron beam process even improved the surface with a tilting angle of close to 90°, which indicates that the process can be used to treat intricate surfaces or structures. This is consistent with the work conducted by Murray et al. [141].

A great number of studies also found that the LEHCPEB has the ability to increase the surface hardness and thereby improve the wear resistance of the materials, such as carbon steels [142, 143], stainless steel [142], magnesium alloys [144], aluminium alloys [145, 146], titanium alloys [147, 148], etc. More relevant to the current work, Guan et al. [143] have observed localised amorphisation in a simple low-carbon steel by this process, giving evidence that the high-cooling rates associated with this technique can be applied for the preparation of the amorphous layer. However, the literature on amorphous surface layer preparation by this electron beam process is scarce.

### **2.6.3 Numerical simulation of temperature field and stress field**

The physical model for the temperature field in the LEHCPEB irradiated material surface was first built by Markov et al. [149] and Proskurovsky et al. [138]. Zou et al. [150] and Qin et al. [151, 152] also conducted the similar work. Based on their models, the dimensions of the beam-affect zone and heating/cooling rate were obtained by solving the heat equation numerically. The calculated results agree well with the experimental results. The related phenomena induced by LEHCPEB irradiation such as the formation of the craters and particles appeared on the irradiated surface were also explained. These physical models and related numerical simulation results are helpful to understand the thermal history of the material during such a short pulsed electron beam irradiation process.

In addition to the temperature field simulation, the thermal stress caused by the non-uniform dynamic temperature distribution in the irradiated materials was also simulated in above references [138, 149, 150, 152]. The calculated thermal stress was used to predict the dimension of hardening and tempering zones and explain the deformation mechanism of the irradiated materials.

The numerical simulation work mentioned above is mainly a single pulse process. However, in practice, multi-pulse irradiation is more common. Therefore, it is of interest to carry out the simulation to investigate the effect of number of pulses on the irradiated materials.

## **2.7 A summary of the literature review**

### **2.7.1 Research gap**

In reviewing the literature, the following areas where further work is needed to provide a deeper understanding of the behaviour of Al-TM-RE glass forming alloys, have been established.

#### **1. Microstructural characterisation of crystalline Al-TM-RE glass forming alloys**

Although there is a large body of work on the glass forming ability and preparation of Al-TM-RE amorphous alloys, the microstructure of crystalline Al-TM-RE alloys has been rarely reported [4, 5, 153-155]. Crystalline Al-TM-RE glass forming alloys often form the basis of subsequent treatments to induce amorphisation. However, in such processes the effect of prior crystalline microstructure needs to be further clarified.

#### **2. Large area electron beam irradiation of Al-Co-Ce glass forming alloys**

Some conventional surface engineering techniques such as thermal spray failed to prepare a fully Al-Co-Ce amorphous alloy coating, so there is a need for further development of processes that can form a largely amorphous surface layer. Large area electron beam irradiation has been widely applied in surface engineering for example for decreasing the surface roughness, enhancing the surface hardness and improving the wear and corrosion resistance. However, this technique has not been used to deliberately prepare an amorphous alloy layer. There also exists an interest in investigating the effect of process parameters and starting material

microstructures (such as phase type, size, distribution, etc.) on the formation of the amorphous layer.

### **3. Numerical simulation of the multi-pulse large area electron beam irradiation**

In some published work, a model was developed and used to simulate temperature field and thermal stress field in the LAEB process. However, most work is focussed on the single pulse process, and the energy accumulated from multi-pulse irradiation has not been considered. This energy accumulation can result in a temperature increase of the irradiated material and hence affect the temperature field of the materials in the subsequent irradiation pulse(s), so simulation of the multi-pulse LAEB process is required.

### **4. Corrosion behaviour of Al-Co-Ce alloy with different microstructures**

The corrosion behaviour of Al-Co-Ce nanocrystalline/amorphous coating prepared by thermal spray has been investigated by Scully et al. [8, 15, 156]. There is interest in exploring the corrosion behaviour of the amorphous surface layer generated by the LAEB process. In addition, although Scully et al. have studied the effect of crystallisation on the corrosion resistance of Al-Co-Ce alloys, the investigation was performed using the thermally annealed samples containing nano-sized Al crystals. However, in the thermal spray process, a large number of Al-Co-Ce, Al-Co and Al-Ce phases were also observed. Therefore, it is necessary to conduct a systematic investigation to figure out the effect of microstructural features on the corrosion behaviour of Al-Co-Ce amorphous alloys.

In addition, it is also worth examining the corrosion behaviour of the crystalline Al-Co-Ce alloy itself. The microstructure of alloys with different lengthscale

(crystalline phase size) and phase constitute (phase type) are also expected to show different corrosion performance.

### **2.7.2 Objectives of the research project**

1. To determine the relationship between solidification conditions and structures of Al-Co-Ce glass forming alloys with the compositions of  $\text{Al}_{88.0}\text{Co}_{6.0}\text{Ce}_{6.0}$ ,  $\text{Al}_{87.4}\text{Co}_{7.9}\text{Ce}_{4.7}$  and  $\text{Al}_{86.0}\text{Co}_{7.6}\text{Ce}_{6.4}$  (at.%) using three different solidification processes.
2. To investigate the formation of an amorphous layer in Al-Co-Ce alloys subjected to the LAEB surface treatment and understand the roles of LAEB processing parameters such as cathode voltage, number of pulses, starting material microstructure and laser pretreatment.
3. To develop a numerical finite difference model of the thermal history of samples subjected to LAEB treatment and to compare the results with Al-Co-Ce alloys and a model binary Al-Cu eutectic alloy
4. To investigate the corrosion behaviour of the Al-Co-Ce glass forming alloys with different microstructures, particularly, the amorphous alloy layer generated by the LAEB process.

## Chapter 3 Materials and experimental methods

### 3.1 Materials

In this work, one Al-Cu alloy and three Al-Co-Ce alloys were induction melted, cast and then treated by different surface engineering methods. The raw materials used in this work are pure metal ingots. The purity and supplier of metals are listed in **Table 3-1**. Pure Al, high strength aluminium alloy 2024 (AA2024) and alclad 2024 were used as reference materials to allow comparison of the corrosion behaviour difference of Al-Co-Ce alloy. The nominal chemical compositions of AA2024 and alclad 2024, as well as other details are shown in **Table 3-2**.

**Table 3-1 Purity and supplier of metals**

Metal	Purity	Supplier
Al	99.95%	-
Co	99.9%	Alfa Aesar
Ce	99%	Alfa Aesar
Cu	99.9%	Smiths Metal Centres Ltd
AA2024	-	Prime Metals

**Table 3-2 Nominal compositions of AA2024 and alclad 2024**

Nominal chemical composition (wt.%)				Sheet thickness	Temper condition
Core AA2024		Cladding layer			
Si	0.5	Si+Fe	0.7	3 mm	T3
Fe	0.5	Cu	0.1		
Cu	3.8-4.9	Mn	0.05		
Mn	0.3-0.9	Mg	0.05		
Mg	1.2-1.8	Zn	0.1		
Cr	0.1	V	0.05		
Zn	0.25	Ti	0.03		
Ti	0.15	Al	≥99.30		
Al	Balance				

*Notes: Value is the maximum if range is not shown.*

### 3.2 Wedge mould casting

In total, three Al-Co-Ce alloys and a binary Al-Cu alloy were cast. The chosen target compositions of the Al-Co-Ce alloys were in the glass forming range reported by Gao et al. [66], which are mapped in **Figure 3-1** and listed in **Table 3-3**. The target Al-Cu composition was that of the binary eutectic. Alloys were induction melted in a magnesia crucible and cast under an argon atmosphere. The melting and casting system are illustrated in **Figure 3-2**. The small Al, Co and Ce lumps with a size of approximately  $10 \times 10 \times 10$ ,  $5 \times 5 \times 2$  and  $3 \times 3 \times 3$  mm, respectively, were used to reduce the time of element diffusion and obtain a homogeneous composition. To get different cooling rates in the same casting, a wedge shaped mould with a wedge angle of  $\sim 17^\circ$  was used. The mould was made of carbon steel, which is shown in **Figure 3-3**. The maximum volume of the ingot that can be cast using this mould is  $\sim 183 \text{ cm}^3$ .

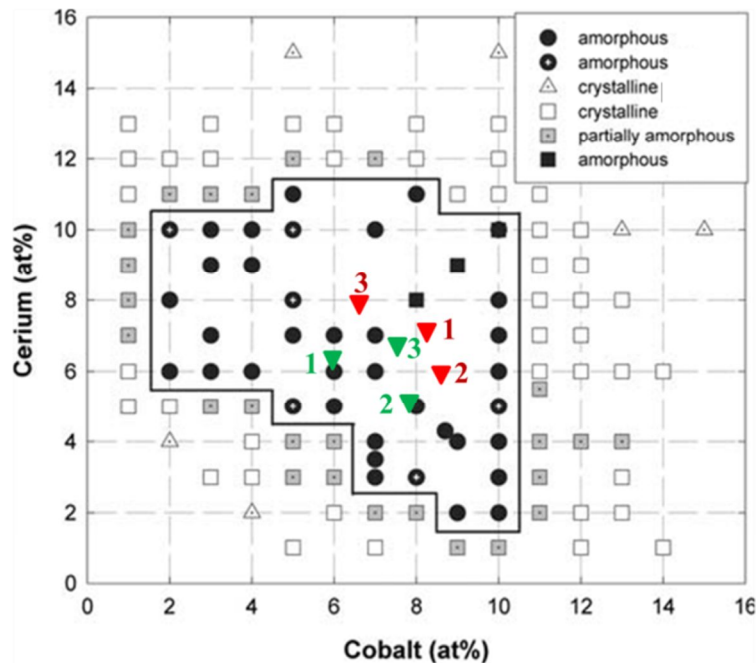


**Figure 3-1** Glass forming range of Al-Co-Ce alloy [66]. Red triangles are target compositions, while green ones are the measured compositions of the as-cast samples.

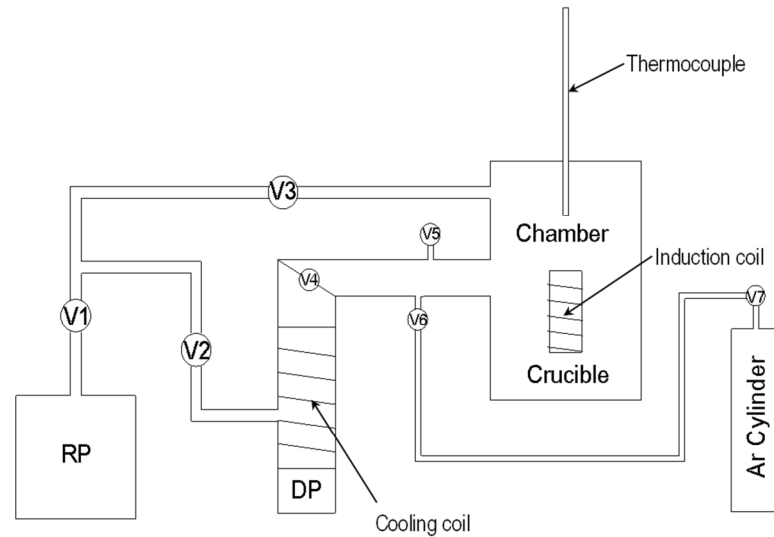


**Figure 3-2 Schematic of induction furnace (V1~V7-valves, RP-rotary pump, DP-diffusion pump.)**

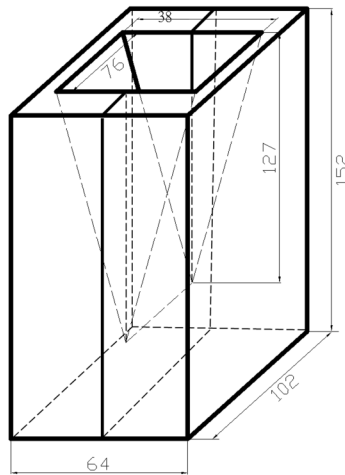


**Figure 3-3 Wedge mould and its dimensions**

Prior to casting, the mould was heated to 150 °C for 3 hours to remove any moisture and oil on the surface, and then cooled to room temperature in a drying furnace. A thin layer of carbon paste was spread on the inner surface to improve melt flow. Prior to the melting of the alloy, the chamber was evacuated by a two-level vacuum system. The pumping system consisted of a rotary pump and a diffusion pump, which can pump the chamber to a minimum pressure of less than  $10^{-3}$  mbar. Upon completing the pumping, argon was refilled into the chamber with a pressure of 500 mbar.

The heating was started after refilling argon into the vacuum chamber. The temperature of melt was monitored by a thin wire K-type thermocouple (RS Components Ltd.). The thermocouple was put in an alumina tube closed at one end to avoid damage and contamination resulting from the direct contact between the stainless steel sheath of thermocouple and the melt. When the metal began to melt, the thermocouple was lowered down into the melt to monitor the temperature. The power was gradually increased to make the melt reach the required pouring temperature (900 °C and 1100 °C for Al-Cu and Al-Co-Ce alloys, respectively). A holding time of 30 minutes at the pouring temperature was allowed to ensure complete melting and homogenisation of the melt. After casting, the ingots (shown in **Figure 3-4**) and mould were retained in the argon atmosphere to cool down for 30 minutes, in order to avoid oxidation.

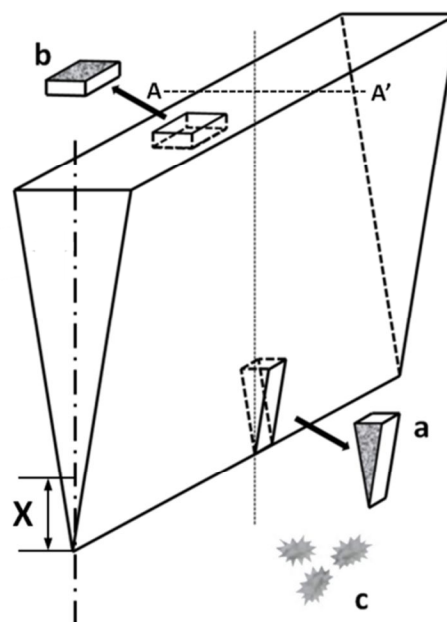


**Figure 3-4 Schematic diagram of the wedge cast: a) Sample for microstructure observation and composition analysis; b) Sample for laser surface melting and electron beam surface melting; c) Metal flakes in the split of wedge mould.**

The composition of the as-cast Al-Cu alloy was determined by energy dispersive X-ray spectroscopy (EDS) in the SEM. The compositions of the three Al-Co-Ce

alloys were determined by inductively coupled plasma optical emission spectrometry (ICP-OES), which was carried out by the Sheffield Assay Office, UK. ICP-OES results are presented in **Appendix 1**. The samples for EDS and ICP-OES analyses were taken from the tip of the wedge, as shown in **Figure 3-4**.

The measured compositions are plotted in **Figure 3-1** and listed in **Table 3-3**. It can be seen that the compositions of the three Al-Co-Ce alloys were  $\text{Al}_{88.0}\text{Co}_{6.0}\text{Ce}_{6.0}$ ,  $\text{Al}_{87.3}\text{Co}_{7.9}\text{Ce}_{4.7}$  and  $\text{Al}_{86.0}\text{Co}_{7.6}\text{Ce}_{6.4}$  (at%), which are still in the glass forming range for this alloy system [66]. Furthermore, the composition of alloy 3 is closer to the centre of the glass forming range. In addition, the microstructure of alloy 3 was found to be most sensitive to the solidification rate compared with the other three alloys (**This is presented in Chapter 5**). Alloy 3 was therefore chosen as the starting material for the subsequent laser surface melting and large area electron beam surface melting processes.

**Table 3-3 Compositions of three Al-Co-Ce alloys and Al-Cu alloy determined by ICP-OES and EDS, respectively.**

Composition		Al-Co-Ce			Al-Cu
		alloy 1	alloy 2	alloy 3	
Target composition	at. %	Al: 84.8 Co: 8.3 Ce: 6.9	Al: 85.8 Co: 8.6 Ce: 5.6	Al: 85.8 Co: 6.6 Ce: 7.6	Al: 82.6 Cu: 17.4
	wt.%	Al: 61.1 Co: 13.1 Ce: 25.8	Al: 64.2 Co: 14.0 Ce: 21.8	Al: 61.4 Co: 10.3 Ce: 28.3	Al: 66.8 Cu: 33.2
Measured composition	at. %	Al: 88.0 Co: 6.0 Ce: 6.0	Al: 87.4 Co: 7.9 Ce: 4.7	Al: 86.0 Co: 7.6 Ce: 6.4	Al: 82.7 Cu: 17.3
	wt.%	Al: 66.5 Co: 9.9 Ce: 23.6	Al: 67.7 Co: 13.4 Ce: 18.9	Al: 63.3 Co: 12.2 Ce: 24.5	Al: 67 Cu: 33

### 3.3 Laser surface melting (LSM) treatment

A YLR-2000SM ytterbium fibre laser (IPG laser, GmbH, Germany) with a wavelength of 1070 nm and a Gaussian (TEM<sub>00</sub>) beam profile was operated in the continuous wave mode at a power of 2 kW throughout this work. A 600  $\mu\text{m}$  diameter delivery fibre was used with a 192 mm focal length lens, producing a focused spot size with a measured diameter of 952  $\mu\text{m}$  using a Primes Focus Monitor. In order to produce a larger actual beam diameter, the samples were positioned 5 and 20 mm below the focus, which generated spot sizes of approximately 1.5 and 3.1 mm, respectively. The samples were clamped onto a table. The sample traverse speed also varied from 1000 to 6000 mm/min. The laser treatment was conducted in an argon atmosphere. **Figure 3-5** shows the laser surface melting operation.

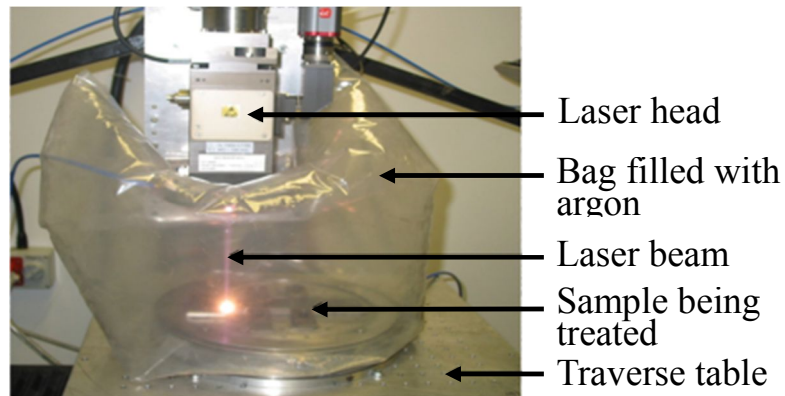


**Figure 3-5 Laser surface melting operation**

Laser treated Al-Cu alloy under different laser treatment parameters exhibited different microstructures (interlamellar spacings), which was used to evaluate the solidification velocity of the alloys in the various processes. LSM was also applied as a pre-treatment method of Al-Co-Ce alloy 3 to prepare a multi-track refined microstructure for the subsequent LAEB surface melting treatment.

The starting materials for the laser surface melting treatment were cut from the top of the wedge, as shown in **Figure 3-4b**. Before LSM treatment, the samples were polished using 6  $\mu\text{m}$  and 1  $\mu\text{m}$  diamond abrasive particles, in turn. The sizes of the samples used in laser surface melting (LSM) and LSM parameters on both Al-Cu and Al-Co-Ce alloy are summarised in **Table 3-4**.

**Table 3-4 Parameters for laser microstructural refinement of Al-Cu and Al-Co-Ce alloy 3.**

Alloy	Process	Sample code	Sample traverse speed (mm/min)	Distance away from the focus (mm)	Laser spot size (mm)	Sample size (mm)
Al-Cu	Single-track	AlCu1000-5	1000	5	1.5	15×15×3
		AlCu3500-5	3500	5	1.5	
		AlCu6000-5	6000	5	1.5	
Al-Co-Ce (alloy 3)	Multi-track	MT1000-20	1000	20	3.1	15×15×3
		MT6000-20	6000	20	3.1	
		MT6000-5	6000	5	1.5	

### 3.4 Large area electron beam (LAEB) surface melting treatment

#### 3.4.1 LAEB surface melting

A Sodick PF32A large area electron beam machine was used to irradiate samples. **Figure 3-6** and **Figure 3-7** show this machine and its components. The irradiation process is carried out under an inert nitrogen atmosphere at a pressure of 0.05 Pa. This inert gas is used as the medium for plasma build up required for the electron generation and beam propagation. The electron beam is approximately 60 mm in diameter with a pulse interval of 11 seconds, a pulse duration of 1  $\mu\text{s}$  and various energy density levels determined by the cathode voltage. Within the 60 mm beam

diameter and considering the small specimen size used in this study, the energy density is expected to be uniform [139], thereby ensuring the whole sample surface in this case is uniformly irradiated.



**Figure 3-6 Large area electron beam machine used in this work (Sodick PF 32A).**

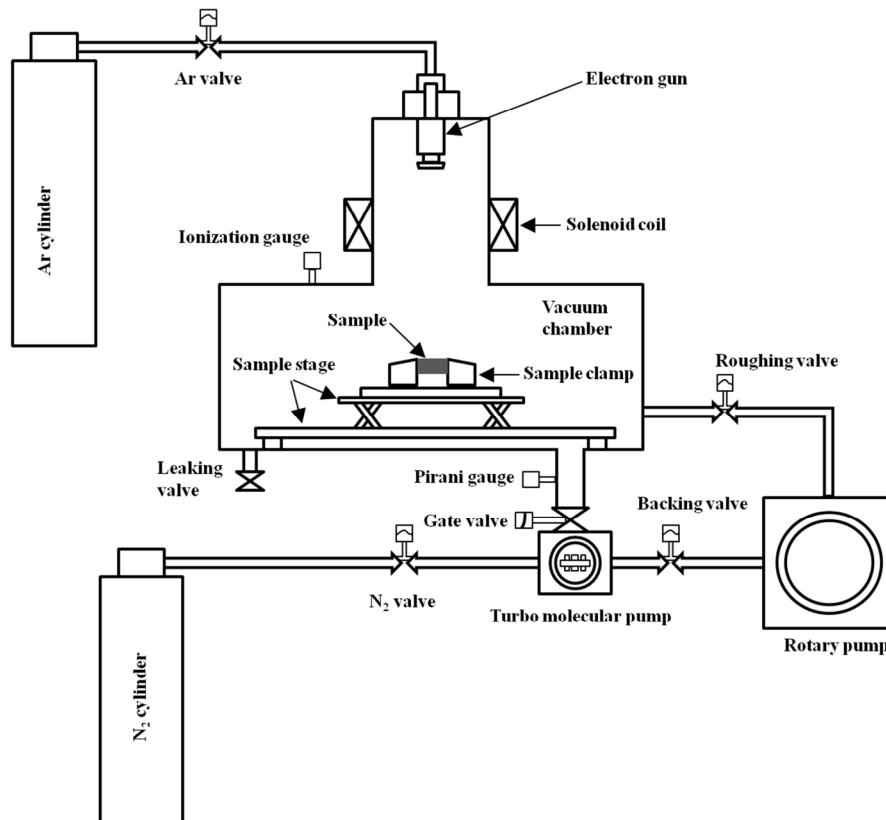


**Figure 3-7 Schematic diagram of Sodick PF 32A shown in Figure 3-6.**

Throughout the large area electron beam treatment, the samples were clamped onto a sample stage, as shown in **Figure 3-8**. There is a gap of  $\sim 10$  mm between the sample and sample stage. The distance between electron beam gun and sample, anode voltage and solenoid voltage were constants: 300 mm, 5 kV and 1.5 kV, respectively. The cathode voltage and number of pulses varied.

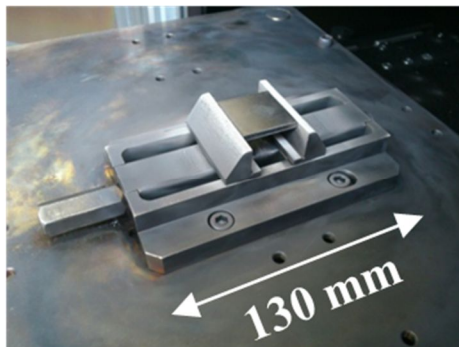


**Figure 3-8 Sample stage of Sodick PF 32A.**

The wedge mould cast materials were used as the starting materials for large area electron beam (LAEB) surface melting treatment. These starting materials were cut from the top of the wedge, as shown in **Figure 3-4b**. Before LAEB treatment, the samples were polished using, successively,  $6\ \mu\text{m}$  and  $1\ \mu\text{m}$  diamond abrasive. Multi-track LSM pre-treated Al-Co-Ce alloy 3 was also used as the starting material to investigate the effect of microstructural refinement on the development of amorphous surface layers. In this case, laser pretreatment before large area electron beam surface melting was performed on the as-cast material. Following the laser pre-treatment, a raised zone was produced in the centre of each laser track due to surface tension effects. Therefore, laser treated samples were lightly polished again so that flat samples were exposed to the LAEB irradiation. Laser treated material was then cut into  $\sim 5 \times 5 \times 3$  mm pieces for the following LAEB treatment. The sizes of the samples and process conditions used in the large area electron beam (LAEB) surface melting treatment are listed in **Table 3-5**.

**Table 3-5 Process conditions of the LAEB surface melting for Al-Cu and Al-Co-Ce alloys (LSM refers to prior laser surface melting).**

Alloy	Pre-treatment	Sample size (mm)	Large area electron beam conditions	
			Cathode voltage (kV)	Number of pulses
Al-Cu	-	15×15×3	35	1, 8, 25 and 150
Al-Co-Ce alloy 1	-	15×15×3	35	15
Al-Co-Ce alloy 2	-	15×15×3	25, 35, 40	15, 25
Al-Co-Ce alloy 3	-	15×15×3	15, 22, 29, 35, 40	1, 8, 15, 25, 50, 100 and 150
	LSM	5×5×3	35	8, 25 and 150

### 3.4.2 Sample temperature measurement

In the LAEB process, to estimate the maximum average temperature the samples reached during the irradiation, three 10×10×3 mm pure Al plates were irradiated with 50, 100 and 150 pulses of electron beam irradiation at 35 kV cathode voltage. Temperature labelling strips can permanently record the maximum temperature samples reached through the colour change of the temperature display area in the labelling strip. Prior to irradiation, temperature labelling strips (4 level, temperature ranges of 49-65 °C, 71-88 °C and 93-154 °C, RS Components Ltd.) were applied to the back of the samples. It was found that the samples reached 327 K, 355 K and 372 K when samples were irradiated with 50, 100 and 150 pulses, respectively.

## 3.5 Characterisation

### 3.5.1 Sample preparation

As-cast alloy ingots were cut along the middle plane A-A', as shown in **Figure 3-4**. The material near the tip of the wedge cast with a height of 20 mm was prepared

for microstructure observation and composition analysis. There are five observation positions which are located at 0 mm, 5 mm, 10 mm, 15 mm and 20 mm away from the tip of the wedge. In addition, the sample cut from the top of the wedge cast was also examined. The sample positions in the as-cast Al-Cu and Al-Co-Ce alloys are summarised in **Table 3-6**. The examined faces were on the middle line of the cross section which was cut along the plane of A-A', as shown in **Figure 3-4**. The examined faces were ground on 240, 400, 800 and 1200 grit SiC papers, in turn and successively polished on 6  $\mu\text{m}$  and 1  $\mu\text{m}$  diamond. The final polishing was performed with 0.05  $\mu\text{m}$  SiO<sub>2</sub> suspension. These prepared samples were used for scanning electron microscopy (SEM) and X-ray diffraction (XRD). Etching was not required for both SEM and XRD analyses.

In addition, in the wedge mould casting process, a small amount of melting metal was forced into the split between two halves of the wedge mould by the pressure of the melt in the casting process. Therefore, some metal flakes were found after casting, as shown in **Figure 3-4c**. These flakes were carefully collected and analysed using SEM.

**Table 3-6 Observation positions and sample codes in the wedge cast of Al-Cu and Al-Co-Ce alloys**

Alloy	Sample location (Distance away the wedge casting tip) /mm	Sample code
Al-Cu	X=0	AlCuW0
	X=5	AlCuW5
	X=10	AlCuW10
	X=15	AlCuW15
	X=20	AlCuW20
Al-Co-Ce (Alloy 1, 2 and 3)	X=0	AlCoCeW0
	X=5	AlCoCeW5
	X=10	AlCoCeW10
	X=15	AlCoCeW15
	X=20	AlCoCeW20
	X=50	AlCoCeW50

For the laser treated samples, the samples for SEM analysis were cut and mounted in a conductive resin, and then metallographically prepared as previously stated. The cross section of the laser tracks was observed. For XRD analysis, the top surface of the laser treated samples was examined. In this case, the samples were not mounted but underwent the same metallographical preparation procedure.

For the LAEB treated samples, the as-treated top surfaces were observed using SEM and analysed with glancing angle XRD without any grinding and polishing. However, for cross sectional examination, the samples were ground and polished with the same procedure used for laser pre-treated samples. For all the above analyses, no hot mounting was used in order to avoid the heat effect on the amorphous phase.

For pure Al, AA 2024 and alclad 2024 samples, optical microscopy and scanning electron microscopy were used for the examination before and after corrosion testing. The samples were ground and polished with the same procedure as described above. After polishing, Keller's reagent (a mixture of 95 mL distilled water, 2.5 mL HNO<sub>3</sub>, 1.5 mL HCl and 1.0 mL HF) was used to etch the samples. Etching was conducted for 2 minutes at room temperature. In particular, the above samples were not etched after corrosion testing.

### **3.5.2 Optical microscopy**

In this work, for the macroscopic examination of pure Al, AA2024 and alclad 2024 samples, a Nikon optical microscope together with ACT-1 software was used.

### **3.5.3 Scanning electron microscopy (SEM) and energy dispersive X-ray spectroscopy (EDS)**

The scanning electron microscope (SEM) produces an image using the signal resulting from the interaction of electron beam with the atoms in the surface and near surface of the sample. Secondary electron (SE) and backscattered electron (BSE) signals are most often used to image the sample. SE signal is usually generated from the top surface of the sample, so SE signal is used to image the surface topography. However, the BSE signal is very sensitive to the mean atomic number of the phases in the sample, and it is therefore used to analyse the compositional distribution.

In addition, the characteristic X-ray signal is also a useful signal to analyse the sample. The characteristic X-ray is generated by the quantized photon emitted when the electron at the outer-shell fills the vacancy in the inner-shell of the bombarded element. Due to the unique set of energy levels for each element, X-rays produced by energy level transition are characteristic to each element. Therefore, characteristic X-rays can be used to quantitatively analyse the chemical composition of the sample. This technique is called energy dispersive X-ray spectroscopy (EDS).

In this work, a FEI XL30 environmental scanning electron microscope with a field emission gun was used with 20 kV acceleration voltage and ~10 mm working distance. The magnification of images ranges from 300× to 160000×. Both SE and BSE imaging modes were used. The composition of different phases was determined by semi-quantitative, standardless EDS with the same SEM equipment and associated software (INCA).

### 3.5.4 X-ray diffraction analysis (XRD)

X-ray diffraction (XRD) is a method using the diffraction of X-rays by the irradiated material to determine the spatial arrangement of atoms. For crystalline materials the interplanar spacings can be determined by the position of X-ray diffracted peaks ( $2\theta$ ) according to Bragg's law. The intensity of specific peaks is determined by the arrangement and type of atoms in the unit cell. Comparison of the location and intensity of X-ray diffracted peaks with a database allows identification of the crystalline phases present. In addition, the phase fraction or grain orientation can be identified by the intensity difference of the diffracted peaks. For the amorphous material, there is no long range order; therefore, the diffraction of X-rays will be random. In the typical XRD pattern of the amorphous material, there is a hump at certain  $2\theta$  angle which corresponds to the short-range order of the atomic arrangement.

Due to this unique relationship between the atomic arrangement structure of the material and the diffracted pattern of X-ray, XRD is a powerful and widely used method for the phase analysis. In this work, XRD was used to investigate the phases present and qualitative phase fraction present in different samples. For bulk materials i.e. wedge cast materials, normal XRD analysis was used. X-ray diffraction (XRD) was conducted using a Siemens D500 X-ray diffractometer ( $\text{CuK}\alpha$ ) with a step size of  $0.02^\circ$  and a counting time per step of 2 s.

After laser surface melting and large area electron beam surface treatment, there is a microstructural transformed layer on the top surface of the treated material. To analyse the outer, treated layer in isolation, glancing angle XRD (GAXRD) using a Bruker D8 Advance diffractometer ( $\text{CuK}\alpha$ ) was carried out. In this work, GAXRD

patterns were collected with a step interval of  $0.02^\circ$ , a dwell time of 8 s and a  $2^\circ$  angle of incidence.

Due to the small incidence angle in glancing angle XRD, the penetration depth was greatly reduced. The AbsorbDX 1.1 software was used to calculate the X-ray penetration depth in both Al-Cu and Al-Co-Ce alloys for 90% contribution to the diffracted beam. Calculation showed the X-ray penetration depth varied with  $2\theta$ , ranging from  $3.5\ \mu\text{m}$  to  $4.0\ \mu\text{m}$  (Al-Cu alloy) and  $1.1\ \mu\text{m}$  to  $1.3\ \mu\text{m}$  (Al-Co-Ce alloy) for the  $2\theta$  range of  $15^\circ$  to  $80^\circ$ .

### **3.5.5 Micro-hardness testing**

For the as-cast Al-Co-Ce alloy, Vickers micro-hardness testing on different phases in the as-cast material was conducted using a LECO M400 micro-hardness tester. A load of 0.5 N (50 gf) and a dwell time of 15 seconds force was used. Nano-indentation testing was also performed using a Nanotest NTX (Micro. Materials Ltd.) to measure the hardness of the different phases in the as-cast material, with a Berkovich indenter with maximum loading of 50 mN. The loading and unloading rate was 10 mN/s, and the holding time at maximum loading was 60 seconds. The test was calibrated with a fused silica reference sample. In both types of hardness tests, between four and twelve indents with proper shape and spacing were made on each phase dependent on phase size, and then the average value and standard deviation were calculated.

### **3.5.6 Image analysis**

For the wedge mould casting Al-Co-Ce alloy, the phase fractions (in area, which is equivalent to volume fraction) of the three main phases in the cast ingots were

measured using “Image J” image analysis software based on the different phase contrasts. For LSM and LAEB treated samples, the dimensions of the laser melting pool, the length scale of the refined microstructure and the thickness of LAEB treated layer were also measured using “Image J”. In all above image analysis work, at least four measurements for every result were made, and then the average value and error were calculated.

In addition, the total length of cracks in the LAEB and LSM-LAEB treated layer was measured based on SEM images under the same magnification, and then the crack length per unit area of the examined sample surface (crack density) was calculated. For each crack density measurement, four SEM images with magnification of 300× were used. The SEM images used for crack density measurement have an area of 0.626 mm<sup>2</sup>, and the cracks with the minimum width of ~1.5 μm are visible.

In particular, interlamellar spacing  $\lambda$  of the Al-Cu eutectic alloy was measured. **Figure 3-9** shows the difference between the true interlamellar spacing  $\lambda_t$  and observed  $\lambda$  in the sample.  $\lambda \geq \lambda_t$  if the lamellae were not vertical to the observed surface. Therefore, to minimise the error, the minimum observed interlamellar spacing  $\lambda_{min}$  was taken as the best approximation to the true spacing in the measurement. Three measurements covering at least ten lamellae at different locations for each  $\lambda_{min}$  were made, the average value and standard deviation were then calculated. Detailed information for all the image analyses is listed in **Table 3-7**.

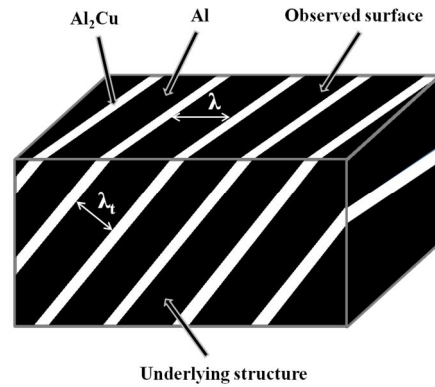


**Figure 3-9 Measurement of interlamellar spacing in Al-Cu eutectic alloy.**

**Table 3-7 Details of the image analysis**

Measurements	Analysed samples	Magnification of the images	Number of measurements
Phase fraction in area	Wedge cast Al-Co-Ce alloys	500×	4
Interlamellar spacing of Al/Al <sub>2</sub> Cu	Al-Cu eutectic alloy	80000× or higher	3
Dimension of the laser melting pool	LSM treated Al-Cu eutectic alloy	100×	4
Length scale of the refined microstructure by LSM	LSM Al-Co-Ce alloy 3	8000×	4
Thickness of LAEB treated layer	LAEB treated Al-Co-Ce alloys	2500×	4
Crack density of LAEB treated layer	LAEB treated Al-Co-Ce alloys	300×	4
Crack density of LSM-LAEB treated layer	LSM-LAEB treated Al-Co-Ce alloy 3	1000×	4
Exposed area of corrosion testing samples	Various alloys	400×	3

### 3.6 Corrosion testing

#### 3.6.1 Sample preparation

In this work, the corrosion behaviour of the as-cast, laser treated and large area electron beam treated Al-Co-Ce alloys was investigated through potentiodynamic polarisation testing and corrosion morphologies observation. In addition, corrosion tests of pure Al, AA 2024 and alclad 2024 were also performed to allow the

comparison of corrosion behaviour. **Table 3-8** gives detailed information of the samples used in the corrosion tests. These samples were prepared into working electrodes.

**Table 3-8 Detailed information of the samples used in potentiodynamic polarisation corrosion tests.**

Alloy	Process condition	Exposed area (cm <sup>2</sup> )
As-cast Al-Co-Ce (alloy 3)	Wedge mould casting	~1
LSM treated Al-Co-Ce (alloy 3)	6000 mm/min, 5cm	$\sim 5 \times 10^{-3}$
LAEB treated Al-Co-Ce (alloy 3)	35 kV, 8 pulses	$\sim 5 \times 10^{-3}$
LSM-LAEB treated Al-Co-Ce (alloy 3) layer 1	LSM: 4500 mm/min, 5 cm LAEB: 35 kV, 25 pulses	$\sim 5 \times 10^{-3}$
LSM-LAEB treated Al-Co-Ce (alloy 3) layer 2	LSM: 4500 mm/min, 5 cm LAEB: 35 kV, 8 pulses	$\sim 5 \times 10^{-3}$
AA2024	Bare plate	~1
	Alclad plate	~1
Pure Al	Al ingot	~1

For the as-cast Al-Co-Ce alloys, pure Al, AA2024 and alclad 2024, they were first mounted using nonconductive resin then wet polished with 6  $\mu\text{m}$  diamond paste, 1  $\mu\text{m}$  diamond paste and 0.05  $\mu\text{m}$  silica suspensions, in turn. After drying, the mounted samples were electrically connected with a threaded brass rod through the back of the resin. In order to eliminate the occurrence of crevice corrosion between samples and the resin, the edges of samples were lacquered. The schematic diagram of the electrode for the as-cast Al-Co-Ce alloys, pure Al, AA2024 and alclad 2024 is shown in **Figure 3-10**. The exposed area in this type of electrode was  $\sim 1 \text{ cm}^2$ .

For the laser or electron beam treated Al-Co-Ce alloy 3, it was not possible to prepare the working electrodes in the same way as the as-cast materials and AA2024 alloy due to the size limit imposed by cracking. An alternative method

was used. The samples were first clamped into a metallic crocodile clip which is connected with a conducting wire to the potentiostat. The crocodile clip has a plastic cover which can prevent its main body from the corrosion solution. At the mouth of the clip, apart from the required exposed area, the sample and clip were sealed with a water-proof glue (Araldite rapid adhesive). Normally, the test sample had an exposed area of  $\sim 5 \times 10^{-3} \text{ cm}^2$ . The schematic diagram of the working electrode with small exposed area is shown in **Figure 3-11**.

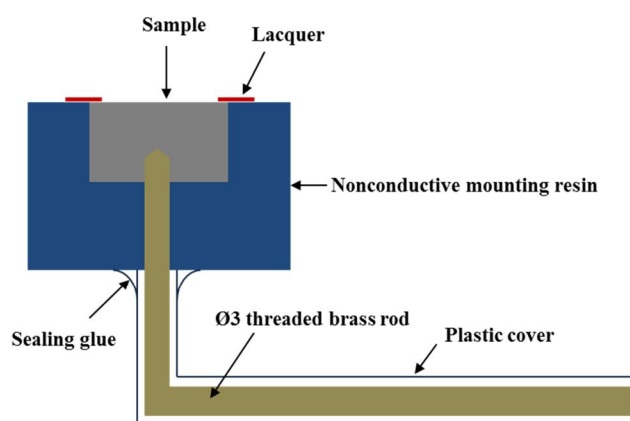


**Figure 3-10** Schematic of the working electrode with a large exposed area.

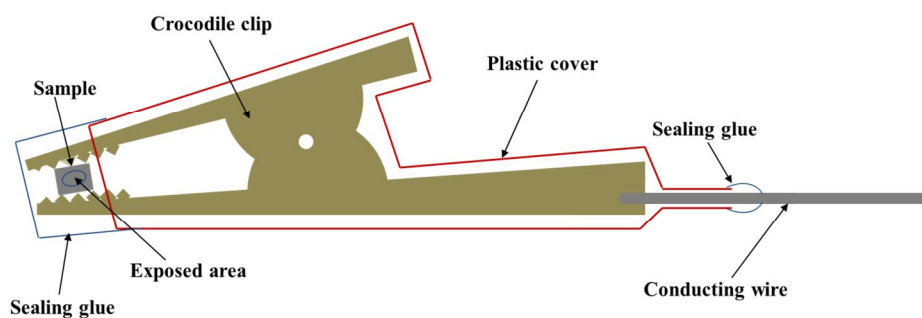


**Figure 3-11** Schematic of the working electrode with a small exposed area.

### 3.6.2 Potentiodynamic polarisation test

Before conducting the corrosion test, all samples were degreased with acetone, and then dried. Potentiodynamic polarisation tests were conducted by an ACM potentiostat (Gill 8) together with the accompanied software (Sequence). All

corrosion tests were performed in a standard three-electrode cell with 3.5 wt.% NaCl solution which was prepared by dissolving 36.3 g of NaCl in 1 L deionised water. The scanning rate of the potentiodynamic polarisation test was 10 mV/min. The saturated calomel electrode (SCE) and platinum plate electrode ( $\sim 1 \text{ cm}^2$ ) were used as reference and auxiliary electrode, respectively.

Before potentiodynamic polarisation scanning, a half-hour settle time was allowed to stabilise the test system. After stabilising, open circuit potential (OCP) was measured for an hour, and then the potentiodynamic polarisation test began. Nitrogen was used to deaerate the electrolyte throughout the corrosion testing. At least three scans were made on at least three different parallel samples for each type of materials. After the potentiodynamic polarisation scan, the samples were rinsed with flowing water and then dried. SEM and EDS were used to examine the changes of samples' microstructure, composition and corrosion morphology.

## Chapter 4 Characterisation of solidification conditions using an Al-Cu eutectic alloy

### 4.1 Introduction

The Al-Cu alloy system has been widely used to establish cooling rates during solidification in a wide variety of situations [157]. It is possible to use hypoeutectic alloys (e.g. Al-4.5wt%Cu) and measure secondary dendrite arm spacings (SDAS) which can then be related to cooling rate or to measure lamellar eutectic spacings in Al-33wt%Cu alloys which give a direct relationship with solidification velocity using the well-known Jackson-Hunt model of eutectic growth [158]. However, a limitation of the SDAS method is that under high temperature gradient conditions, secondary dendrite arms may not form in the 4.5wt%Cu alloy; cellular solidification could occur and so the correlation is not possible. Also, there is only very limited data on SDAS-cooling rate behaviour in more solute rich Al-Cu alloys.

In the present study, there are a number of reasons for choosing to use the Al-Cu eutectic approach. Firstly, the rapidly solidified layer does not have to nucleate, it is a competitive growth problem and so the key parameter is solidification front velocity. Secondly, the numerical model developed predicts, directly, solidification front velocity and so eutectic-based experiments will correlate more appropriately with the modelling results presented in **Chapter 7**. Thirdly, the microstructures of Al-33wt%Cu alloy prepared by various methods have been sufficiently

investigated to quantify the alloy's solidification velocity [158-164], so a large amount of data can be referenced.

In this work, Al-33wt%Cu eutectic alloy was first cast in a wedge metal mould, and then laser surface melting (LSM) and large area electron beam (LAEB) surface melting treatment were conducted on the as-cast sample surface. The microstructures derived from the above three processes were characterised through high-resolution SEM observation and XRD analysis. The solidification velocities were calculated based on the measurements of interlamellar spacing of the eutectic Al/Al<sub>2</sub>Cu structure and the well-known  $v\lambda^2 = K_0$  relationship [158] in an attempt to characterise the solidification conditions of different processes used in this work. In particular, the cooling rate of Al-Cu alloy treated in the LAEB process was estimated.

## 4.2 Experimental characterisation of Al-Cu eutectic solidification in different processes

### 4.2.1 Wedge mould casting

Figure 4-1 shows the XRD results of the wedge mould cast Al-Cu eutectic alloy. It can be seen that there was no apparent difference in phases among the samples at varying positions which were indicated as AlCuW0, AlCuW5, AlCuW10, AlCuW15 and AlCuW20. The phases in Al-Cu alloys were always Al and Al<sub>2</sub>Cu at all the five positions. However, the ratio of the Al peaks height at  $2\theta$  of  $\sim 38.5^\circ$  and  $\sim 45^\circ$  to the Al<sub>2</sub>Cu peak height at  $\sim 21^\circ$  decreased as the sample was closer to the tip. In addition, for the Al<sub>2</sub>Cu phase, the ratio of peaks height at  $\sim 43^\circ$  and  $48^\circ$  to the Al<sub>2</sub>Cu peak height at  $\sim 21^\circ$  decreased with decreasing distance between the sample and the tip of the wedge mould.

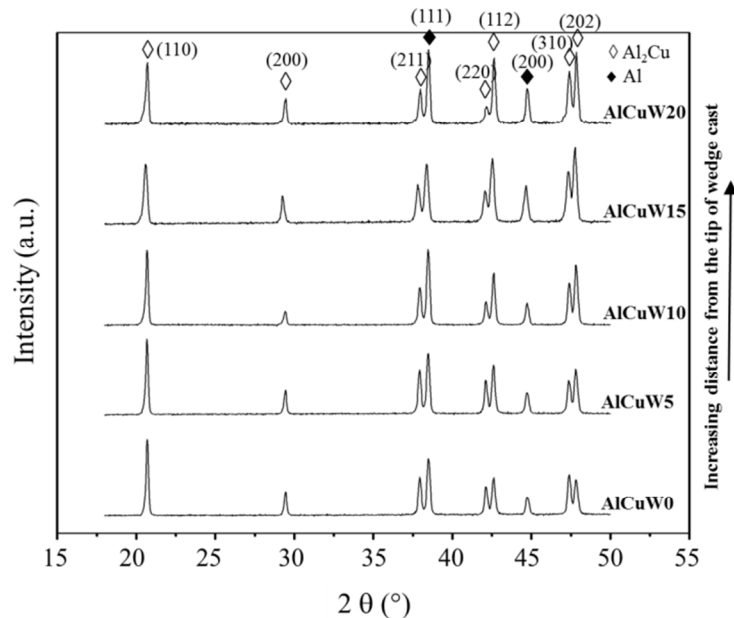
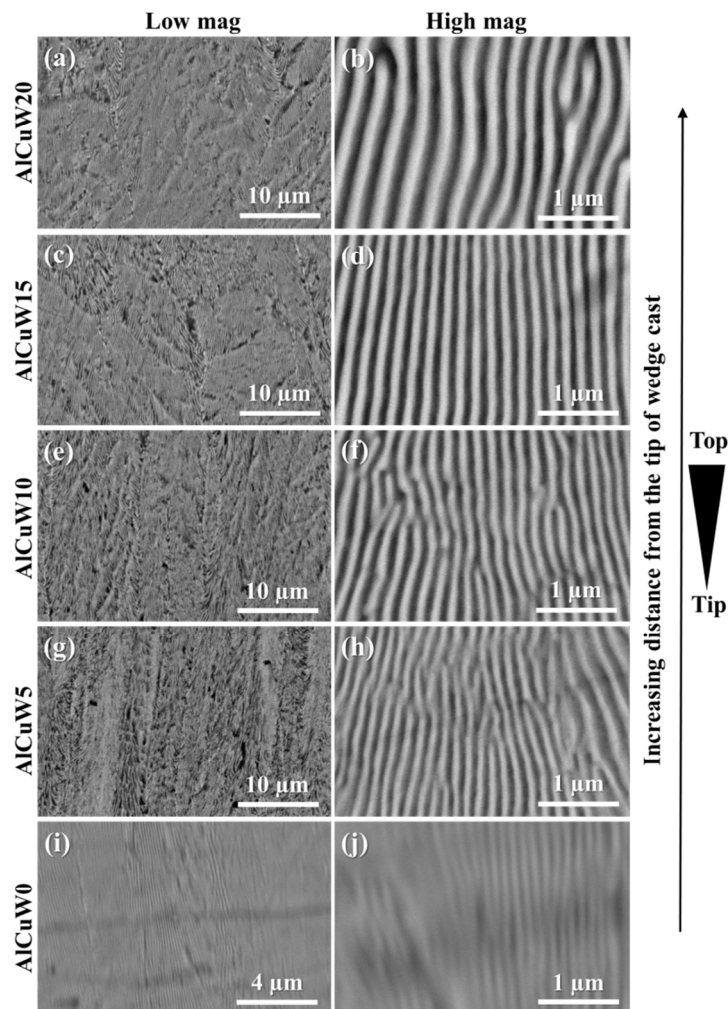


Figure 4-1 XRD results of the as-cast Al-Cu alloy at varying positions of the wedge mould where AlCuW0, AlCuW5, AlCuW10, AlCuW15 and AlCuW20 indicate the distance between the examined position and the tip of the wedge mould is 0, 5, 10, 15 and 20 mm, respectively.

**Figure 4-2** shows the microstructure of the as-cast Al-Cu alloy at different positions in the wedge mould. In the low magnification images, there were visible cellular boundaries between the eutectic grains. However, for the sample at the tip of the wedge (i.e. AlCuW0), bright lamellae were generally parallel to the middle line from the tip to the top of the wedge cast (**Figure 4-2i**). From the high magnification images, the interlamellar spacing of the Al/Al<sub>2</sub>Cu eutectic was seen to decrease as the sample was closer the tip of wedge cast. In addition, the width of the individual lamella also decreased.



**Figure 4-2** BSE images of the as-cast Al-Cu alloy at different positions of the wedge cast where AlCuW0, AlCuW5, AlCuW10, AlCuW15 and AlCuW20 indicate the distance from the tip of the wedge mould is 0, 5, 10, 15 and 20 mm, respectively. These examined regions were on the middle line of the cross section which was cut along the plane of A-A', as shown in Figure 3-4.

The interlamellar spacing values of the Al/Al<sub>2</sub>Cu eutectic at different positions are listed in **Table 4-1**. The measurement method has been described in **Section 3.5.6**. From **Table 4-1**, it is seen that the interlamellar spacing was strongly dependent on the position of the sample in the wedge mould. The interlamellar spacing in sample AlCuW20, i.e. the position of 20 mm away from the tip of wedge cast was 263 nm, which was twice that at the tip (130 nm).

**Table 4-1 Interlamellar spacing values of Al/Al<sub>2</sub>Cu eutectic at different positions in the wedge cast. Three measurements covering at least ten lamellae at different locations were made for each interlamellar spacing, the average value and standard deviation were then calculated.**

Sample code	Interlamellar spacing /nm
AlCuW20	263±8
AlCuW15	191±7
AlCuW10	161±9
AlCuW5	145±4
AlCuW0	130±3

#### 4.2.2 Laser surface melting (LSM)

**Figure 4-3** shows the glancing angle XRD results of laser surface melting (LSM) treated Al-Cu eutectic alloy. The samples treated with different treatment parameters are indicated as AlCu1000-5, AlCu3500-5 and AlCu6000-5 (Sample traverse speed was 1000, 3500 and 6000 mm/min, respectively, and all treated samples were positioned 5 mm away from the laser focus). It can be seen that there was no apparent change in the phase constituent for all three samples after LSM treatment. The materials still consisted of Al and Al<sub>2</sub>Cu phases as those present in the as-cast material. However, the ratio of the Al<sub>2</sub>Cu peak height at 2θ of ~21° to the Al peak height at ~38.5° decreased with increasing sample traverse speed. On the contrary, the relative peak height of the Al<sub>2</sub>Cu phase at 2θ of ~29° to that of the Al phase at ~38.5° increased with increasing sample traverse speed.

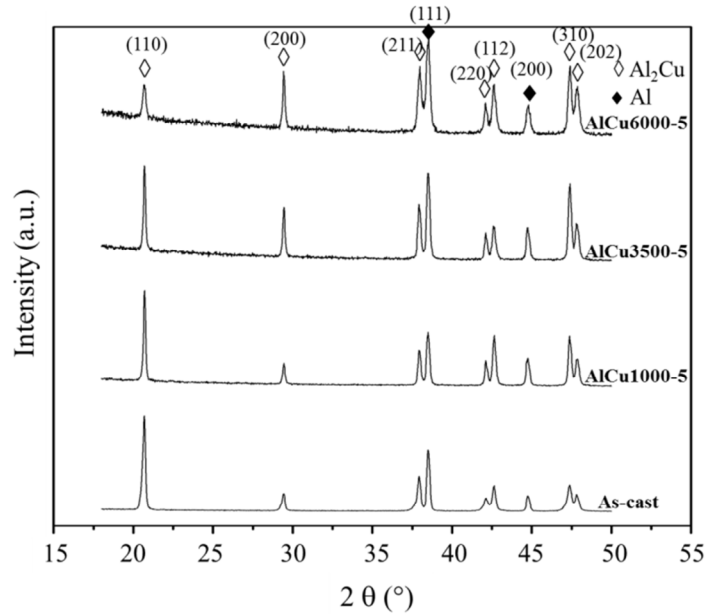


**Figure 4-3** Glancing angle XRD patterns of as-cast and LSM treated Al-Cu eutectic alloys. AlCu1000-5, AlCu3500-5 and AlCu6000-5 indicate the sample traverse speed was 1000, 3500 and 6000 mm/min, and the samples were positioned 5 mm away from the laser focus.

**Figure 4-4** shows the cross section and longitudinal section of the laser melted tracks under different treatment parameters. It can be seen that the shape and size of laser track are dependent on the sample traverse speed. The width ( $w$ ), maximum depth ( $D_{max}$ ) and cross sectional area ( $A$ ) of the laser track decreased with increasing the sample traverse speed. These dimensions of the laser tracks are listed in **Table 4-2**.

**Figure 4-5** presents the magnified images showing cross sections of the LSM treated Al-Cu eutectic alloy at different regions as labelled in **Figure 4-4** (**left column**). Generally, in all four regions, the Al/Al<sub>2</sub>Cu eutectic in the laser track was greatly refined compared with the unremelted substrate. In addition, the interlamellar spacing of the Al/Al<sub>2</sub>Cu eutectic structure decreased with increasing sample traverse speed. For region 1 and region 4 which are located at the edge and bottom of the laser melted track in the cross section, respectively, the lamellae in the laser tracks were found to be perpendicular to the interface of melted and

unmelted material. However, it can be seen that at the top surface i.e. region 2, lamellae were mostly perpendicular to the top surface. In region 3, the lamellae did not present preferential directions.

**Figure 4-6** presents the magnified images showing longitudinal sections of LSM treated Al-Cu eutectic alloy at different regions as labelled in **Figure 4-4 (right column)**. The lamellae in region 1 were found to be perpendicular to the bottom of the laser tracks. For region 2, the direction of lamellae was apparently changed, which indicates the direction of eutectic growth changes as the sample moves.

Considering the relatively uniform and regular eutectic lamellar structure, the interlamellar spacing values of the Al/Al<sub>2</sub>Cu eutectic present in region 2 of the longitudinal sections of three laser tracks (**Figure 4-6b,d and f**) were measured and listed in **Table 4-2**. The measurement method has been described in **Section 3.5.6**. It can be seen that the interlamellar spacing of the eutectic structure in the laser tracks decreased to less than 100 nm, which was smaller than that seen in the wedge mould cast alloy. Particularly, the interlamellar spacing in the sample AlCu6000-5 decreased to 39 nm.

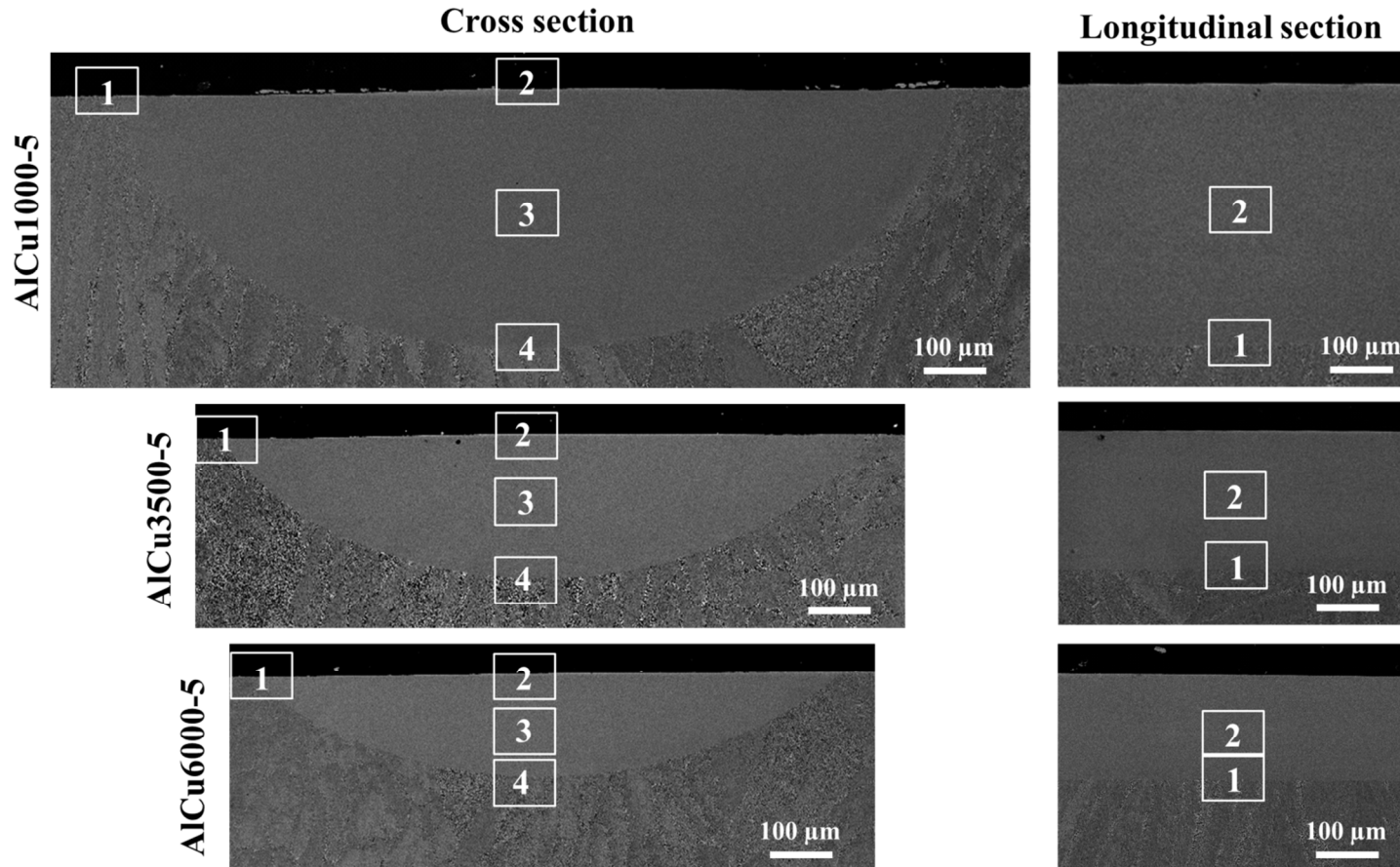


Figure 4-4 Cross section and longitudinal section of laser tracks in the Al-Cu eutectic alloy. AlCu1000-5, AlCu3500-5 and Al-Cu6000-5 indicate the samples treated with sample traverse speeds of 1000, 3500 and 6000 mm/min, respectively, and the samples were positioned 5 mm away from the laser focus. The longitudinal section was cut along the middle line of the laser track in the direction of sample moving.

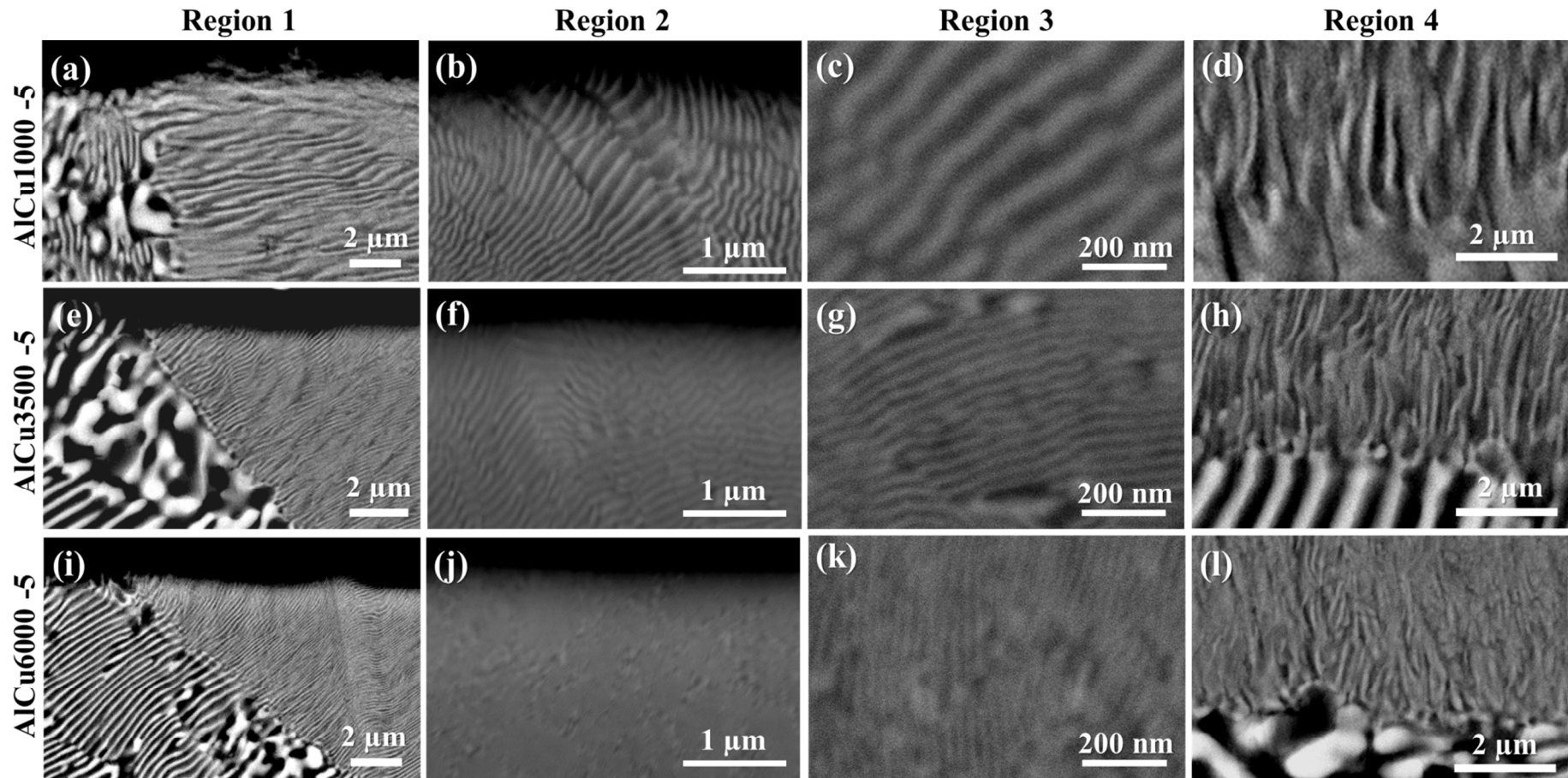


Figure 4-5 BSE images showing cross sectional microstructures of LSM treated Al-Cu eutectic alloy at different regions as shown in Figure 4-4.

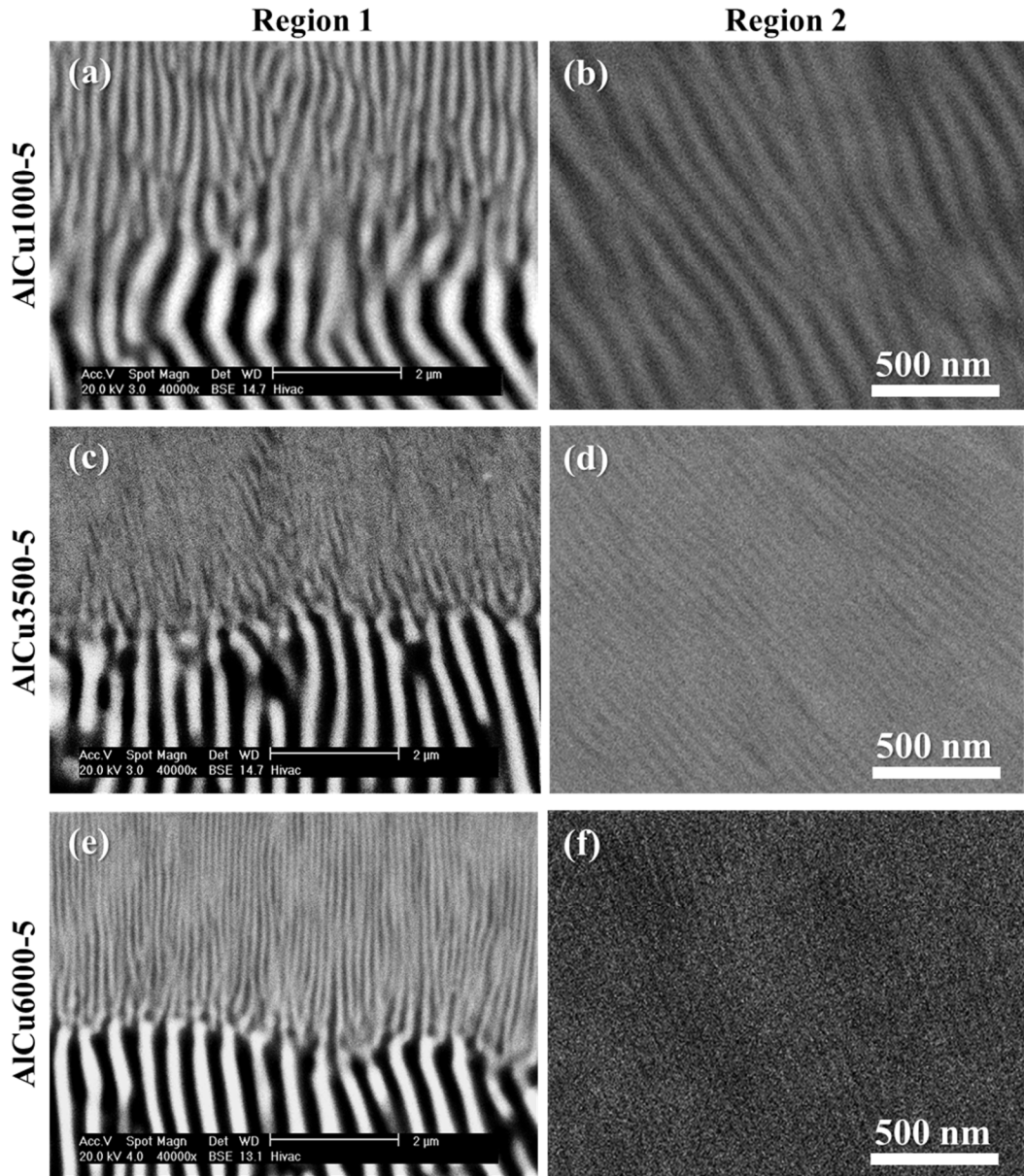


Figure 4-6 BSE images showing longitudinal section of the LSM treated Al-Cu eutectic alloy at different regions.

Table 4-2 Dimensions and interlamellar spacing of laser tracks. All values shown are the averages based on at least three measurements. The errors are standard deviations. Interlamellar spacing values were measured based on the images at region 2 in the longitudinal sections (Figure 4-6b,d and f).

Sample code	Cross section			Longitudinal section
	Maximum width, $w / \mu\text{m}$	Maximum depth, $D_{max} / \mu\text{m}$	Cross-section area, $A / \mu\text{m}^2$	Interlamellar spacing, $\lambda / \text{nm}$
AlCu1000-5	$1380 \pm 7$	$423 \pm 5$	$445227 \pm 7502$	$98 \pm 7$
AlCu3500-5	$1056 \pm 1$	$236 \pm 2$	$175590 \pm 4813$	$52 \pm 5$
AlCu6000-5	$963 \pm 1$	$172 \pm 2$	$110839 \pm 1350$	$39 \pm 5$

### 4.2.3 Large area electron beam (LAEB) treatment

**Figure 4-7** shows the GAXRD results of Al-Cu alloys after LAEB treatment. When the sample was subjected to 1 pulse of LAEB irradiation at 35 kV cathode voltage, the peaks of both Al and Al<sub>2</sub>Cu phases were found to become broader compared with the as-cast material, there was also an additional small peak appearing at ~40°. With an increase of the number of LAEB pulses to 8, there were three additional peaks seen in the XRD pattern at 2θ of 39.5, 44.4 and 46.0° (**Figure 4-8**), while the peak intensity of Al and Al<sub>2</sub>Cu phases greatly decreased. The peaks at 2θ of 39.5 and 46.0° are consistent with the formation of cubic close packed (c.c.p.) supersaturated solid solution reported by Scott and Leake [161]. In their work, supersaturated Al-Cu solid solution with the eutectic composition was prepared by the splat quenching technique. The peak at 2θ of 44.4° is thought to be from the Al<sub>4</sub>Cu<sub>9</sub> phase considering that this is the strongest peak position of the Al<sub>4</sub>Cu<sub>9</sub> phase. The appearance of the peak at 2θ of 44.4° also might be due to the formation of any metastable phase such as the θ'' or θ' phase.

For the sample which was subjected to 25 pulses of LAEB irradiation, the three additional peaks seen in the 8 pulses treated sample disappeared, but the peaks of Al and Al<sub>2</sub>Cu phase were apparently broadened. The peaks of Al also exhibited an apparent shift to the high angle (**Figure 4-9**). This suggests the decrease of the lattice parameter of Al due to a supersaturation of Cu atoms. GAXRD pattern of 150 pulses sample was similar to that of the as-cast material. However, compared with that in the as-cast material the peak relative intensity of the Al<sub>2</sub>Cu phase in the 150 pulses sample showed an apparent decrease except for the (112) peak.

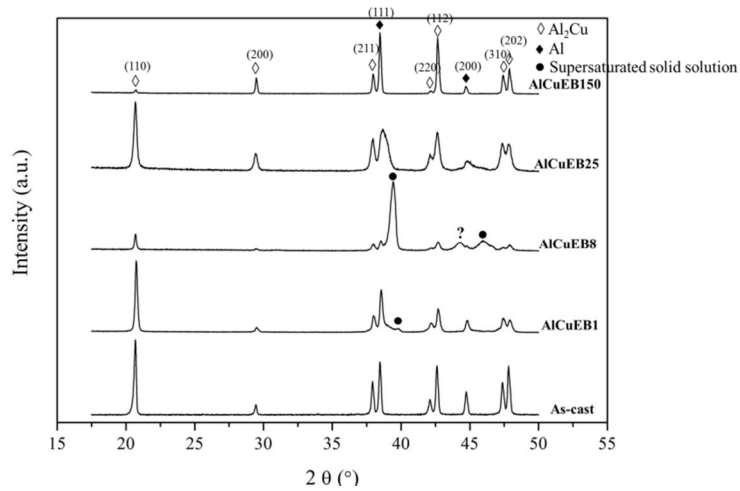


**Figure 4-7 GAXRD results of Al-Cu alloy before and after LAEB treatment. EB1, EB8, EB25 and EB150 indicate that the samples were treated with 1, 8, 25 and 150 pulses of LAEB irradiation, respectively.**

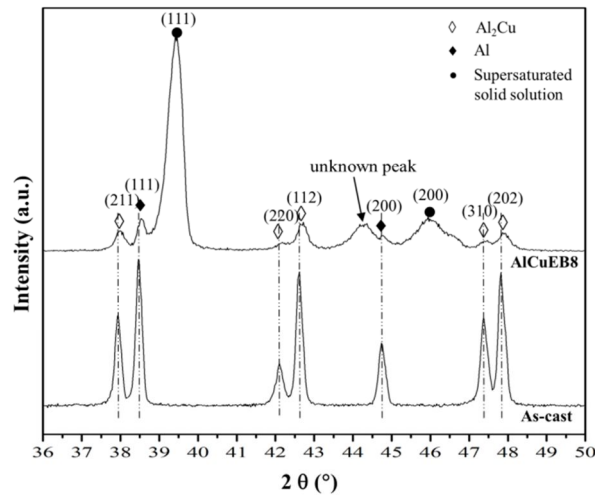


**Figure 4-8 GAXRD spectra of AlCuEB8 and as-cast material with the range of  $2\theta$  between  $36^\circ$  and  $50^\circ$ .**

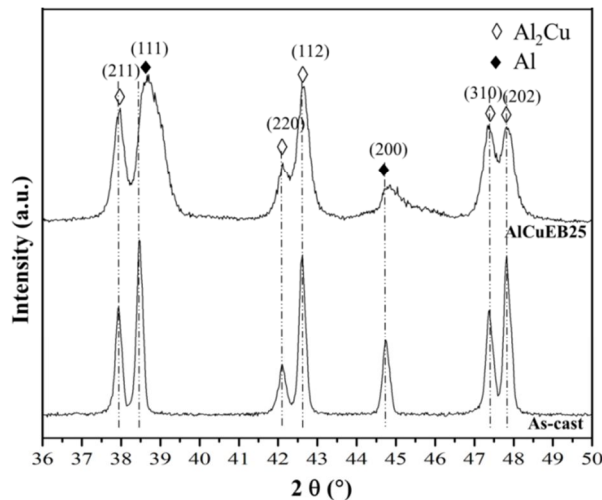


**Figure 4-9 GAXRD spectra of AlCuEB25 and as-cast material with the range of  $2\theta$  between  $36^\circ$  and  $50^\circ$ .**

**Figure 4-10** shows the surface morphologies of the as-cast and LAEB treated Al-Cu alloys. Grinding and polishing were applied on the as-cast material, but not on LAEB treated materials. No etching was conducted for any samples. It can be seen that there was not an obvious change when the sample was treated with 1 pulse of LAEB irradiation compared with the as-cast material. Although there was a slight remelting appearance in some localised regions, the sample still retained the original lamellar eutectic structure consisting of dark Al and bright  $Al_2Cu$  phases (**Figure 4-10c and d**).

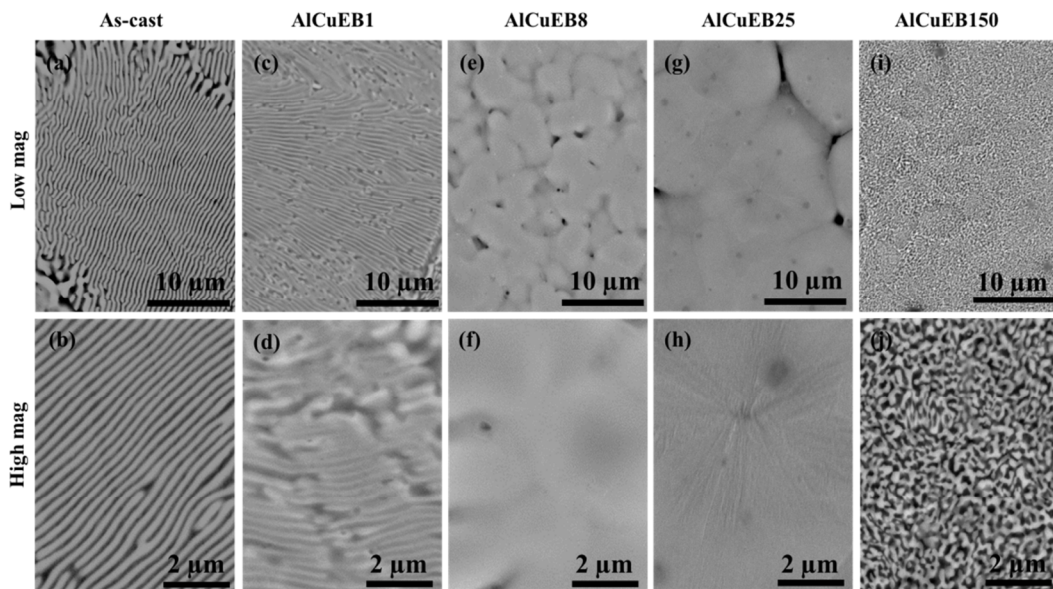


**Figure 4-10** Surface morphology (BSE images) of as-cast and LAEB treated Al-Cu alloy under 35 kV with different numbers of pulses, as indicated by EB1, EB8, EB25 and EB 150.

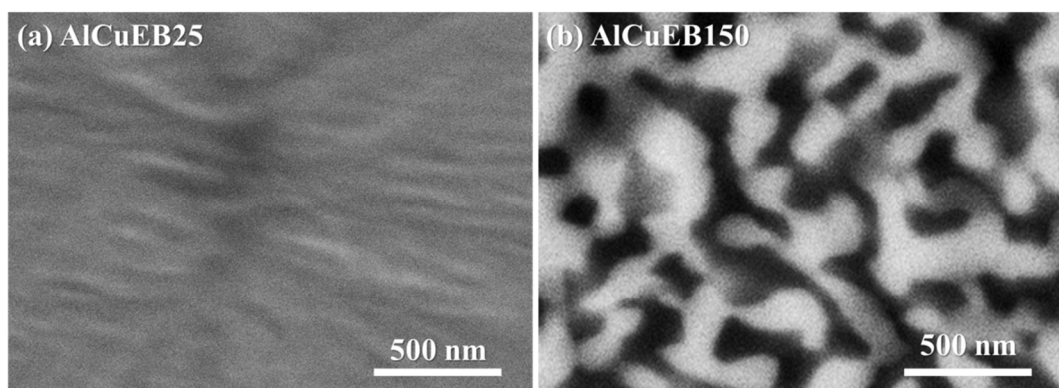


**Figure 4-11** Local magnified SEM images (BSE) of 25 (a) and 150 (b) pulses of LAEB treated Al-Cu alloy shown in Figure 4-10.

**Figure 4-12** shows the cross sectional morphology of the LAEB treated Al-Cu alloy with different numbers of pulses. **Table 4-3** lists the remelted layer thickness for different samples. It can be seen that the thickness of the remelted layer increased with increasing number of LAEB pulses. The remelted layer thickness in 1 pulse treated sample was very thin, which was less than 1  $\mu\text{m}$  from the high magnification image (**Figure 4-12b**). However, when 8, 25 and 150 pulses of LAEB irradiation were applied to the samples, the remelted layer thickness increased greatly, which reaches to approximately 6.0, 14.9 and 16.7  $\mu\text{m}$ , respectively.

From the high resolution images, 1 pulse LAEB treated sample was found to retain the Al/Al<sub>2</sub>Cu eutectic lamellar structure as that shown in the as-cast material. 150 pulses sample also showed the same irregular eutectic structure as that observed in the surface morphology (**Figure 4-10j** and **Figure 4-11b**). For 8 and 25 pulses treated samples, very uniform composition was found in the cross sections of both samples under the magnitude of  $\times 10000$  (**Figure 4-12d** and **f**). The cell boundaries shown in **Figure 4-10e** and **g** also disappeared. However, the top surface is seen to exhibit some fluctuations, which is more apparent in the sample treated with 25 pulses of LAEB irradiation (**Figure 4-12f**).

In a combination of top view and cross sectional view images of the LAEB treated Al-Cu eutectic alloy, there is no stable lamellar eutectic structure in 8, 25 and 150 pulses of LAEB treated samples. In addition, the 1 pulse treated sample did not exhibit sufficient remelting. Therefore, for LAEB treated samples, no valid interlamellar spacing was used to calculate the solidification velocity.

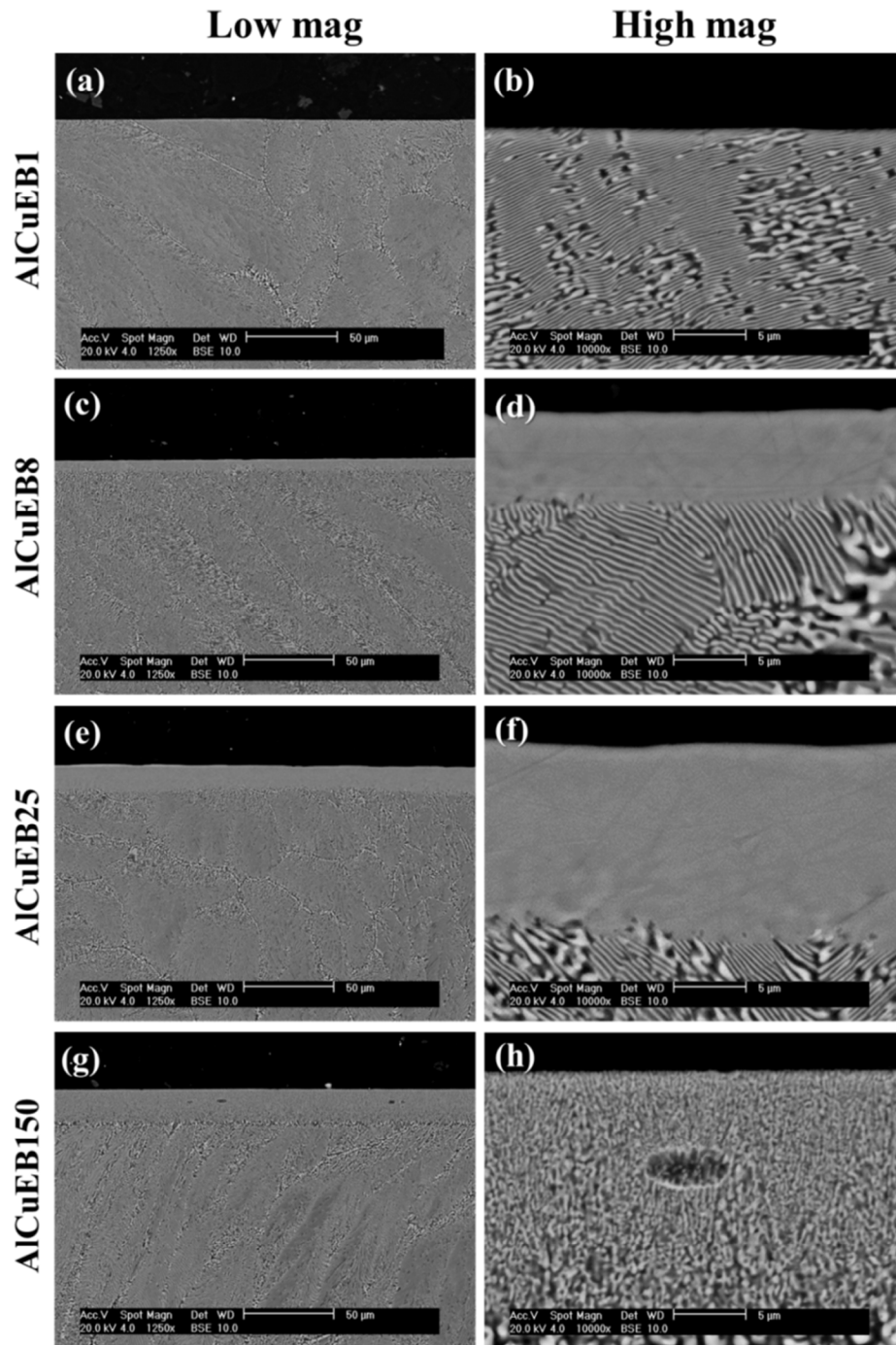


Figure 4-12 Cross sectional morphologies of Al-Cu alloy after electron beam treatment with different numbers of pulses at 35 kV cathode voltage.

Table 4-3 Thickness of the LAEB remelted layers in Al-Cu eutectic alloy. All values shown are the average based on at least three measurements. The errors are standard deviations.

Sample code	AlCuEB1	AlCuEB8	AlCuEB25	AlCuEB150
Remelted layer thickness ( $\mu\text{m}$ )	$0.7 \pm 0.1$	$6.0 \pm 0.1$	$14.9 \pm 0.8$	$16.7 \pm 0.6$

### 4.3 Solidification velocity calculation

#### 4.3.1 Wedge mould casting and laser surface melting

According to Jackson-Hunt's theory [158], the relationship between the interlamellar spacing ( $\lambda$ ) and the solidification velocity ( $v$ ) of the eutectic alloy can be written as follows:

$$\lambda^2 v = K_0 \quad \text{Eq. 4-1}$$

where  $K_0$  is a constant. Although different researchers reported slightly different values for  $K_0$  [162, 165], this constant is always close to  $1 \times 10^{-10} \text{ cm}^3/\text{s}$ . Therefore,  $K_0$  used in this work is equal to  $1 \times 10^{-10} \text{ cm}^3/\text{s}$ . Based on **Eq. 4-1**, the solidification velocity values of as-cast and laser treated Al-Cu eutectic alloys are presented in **Table 4-4**.

**Table 4-4 Solidification velocity of as-cast and laser treated Al-Cu eutectic alloys.**

Process	Sample code	Average interlamellar spacing $\lambda$ (nm)	Solidification velocity (m/s)
Wedge mould casting	AlCuW20	263±8	0.0014
	AlCuW15	191±7	0.0027
	AlCuW10	161±9	0.0039
	AlCuW5	145±4	0.0048
	AlCuW0	130±3	0.0059
Laser surface melting	AlCu1000-5	98±7	0.0104
	AlCu3500-5	52±5	0.0370
	AlCu6000-5	39±5	0.0657

#### 4.3.2 LAEB treatment

Based on GAXRD results and microstructure observation shown in **Section 4.2.3**, LAEB treated layer did not exhibit a model lamellar structure. The microstructural

characterisation results indicated that the condition of the steady eutectic growth has been disturbed in LAEB process. It is well documented that the Jackson-Hunt model is valid for low to medium growth rates, predicting that the interlamellar spacing ( $\lambda$ ) is related to the solidification rate ( $v$ ) [163, 166]. Based on TMK theory [166], the spacing begins to decrease rapidly with velocity and the  $\lambda$ - $v$  curve bends back when a limiting velocity is reached. Under a high solidification rate, steady-state lamellar eutectic growth cannot occur.

Looking back to microstructures of LAEB treated samples AlCuEB8, AlCuEB25 and AlCuEB150 (**Figure 4-10** and **Figure 4-11**), they were apparently different from the regular, coupled, lamellar structure. Therefore, it is thought that the solidification rate of the above samples has surpassed the limit shown in TMK theory. Wang and Trevedi have calculated the limit value of interlamellar spacing and corresponding solidification rate for the steady eutectic growth in Al-32.7Cu (wt.%) alloy, which are 3.8 nm and 1.539 m/s, respectively [164].

In addition, based on XRD results and microstructural features of LAEB treated Al-Cu eutectic alloys, the alloy structure experienced apparent change. When the number of LAEB pulses was 8, the alloy exhibited a single phase Al supersaturated solid solution. With an increase of the LAEB pulses number to 25, the single phase decomposed into the refined Al/Al<sub>2</sub>Cu lamellar structure, which indicates the decrease of the solidification velocity. Furthermore, when the alloy was subjected to 150 pulses of LAEB irradiation, the eutectic structure became coarse in addition to the disappearance of the broaden phases peaks in the GAXRD pattern.

It should be noted that the GAXRD pattern of the alloy irradiated with 1 pulse of LAEB also showed evidence of the formation of the single phase Al supersaturated solid solution, considering the small peak located at  $39.5^\circ$  which is the strongest peak of the single phase. However, due to the small thickness of the remelted layer, the strong background of the unremelted eutectic Al and  $\text{Al}_2\text{Cu}$  phases might affect the identification of the single phase. Therefore, considering the phase transition (single phase→refined eutectic→coarse eutectic) in LAEB treated samples, it can be proposed that the solidification rate of LAEB treated samples decreased with increasing number of pulses. Therefore, the limit value of the solidification rate of 1.539 m/s mentioned above is thought to be the minimum solidification rate of LAEB treated samples in this work.

## **4.4 Discussion**

### **4.4.1 Effect of the process parameters on the solidification velocity**

#### **4.4.1.1 Wedge mould casting**

The solidification velocities of Al-Cu eutectic alloy at different positions of the wedge cast have been calculated based on the interlamellar spacing of the Al/ $\text{Al}_2\text{Cu}$  eutectic structure. The solidification velocity of the wedge cast alloy was found to decrease with increasing distance from the tip of the wedge cast. This is thought to be due to the special geometry of the wedge mould. At the tip of the wedge cast, a small amount of melt can be cooled down by the surrounding cold mould with a much bigger thickness. With increasing distance from the tip of the wedge cast, the volume ratio of the melt to the surrounding cold mould decreased, which decreased the cooling rate of the melt.

Based on the microstructure observation (**Figure 4-2**), it can be seen that the lamellae in the sample at the very tip of wedge (i.e. AlCuW0) were parallel to the middle line on the cross section which was cut along the plane of A-A'. This indicates that the heat of the melt located at this investigated position transferred downwards. This is attributed to the extremely small thickness of the melt and the direct contact with the mould at the tip of the wedge. However, the melt elsewhere was in contact with the side walls of the mould.

#### 4.4.1.2 Laser surface melting

For the LSM treatment, the shape of the laser track varied with laser treatment parameters (sample traverse speed in this work). With increasing sample traverse speed, the energy input per unit length decreases, considering shorter irradiation time but same laser power. To describe the laser energy input on the unit length of the laser track, the linear energy density  $E_l$  was calculated as follows:

$$E_l = \frac{(l_t / v_b)P}{l_t} = \frac{P}{v_b} \quad \text{Eq. 4-2}$$

where  $v_b$  is the sample traverse speed,  $l_t$  is the length of the laser track and  $P$  is the laser power. In this work,  $l_t$  and  $P$  are 15 mm and 2000 W, respectively.

Based on **Eq. 4-2**, the linear energy densities for the sample treated with different sample traverse speeds of 1000, 3500 and 6000 mm/min are 120, 34.3 and 20 J/mm. These different linear energy densities resulted in the different levels of energy input in the laser treated sample and thereby caused different volumes of remelted alloy. It has been seen that the cross sectional dimension of the laser track decreased with increasing sample traverse speed in terms of the width, maximum depth and cross section area of the laser track (**Figure 4-4 and Table 4-2**).

In addition, different sample traverse speeds also resulted in a variation in solidification velocity. It has been calculated that the solidification velocity increases with increasing sample traverse speed. Under the same cooling condition, the high sample traverse speed brought less energy input which can be conducted away more quickly by the cold substrate. Therefore, the remelted material can have a faster solidification, i.e. higher solidification velocity.

#### **4.4.1.3 LAEB treatment**

According to the GAXRD results and microstructure observation of the samples treated with different number of LAEB pulses (**Section 4.2.3**), overall, the solidification velocity of the LAEB treated Al-Cu eutectic alloy decreased with increasing number of pulses. This is thought to be due to the energy accumulation from multi-pulse treatment. Considering the pulsed characteristic of the LAEB process, the previous pulses of irradiation can increase the substrate temperature, and hence decrease the temperature gradient between the treated layer and substrate in the last pulse treatment. The solidification rate was hence decreased.

In addition, the LAEB treated Al-Cu alloy with the eutectic composition did not exhibit steady-state lamellar eutectic growth. Therefore, the samples had the highest solidification velocity in the LAEB process compared with those in wedge mould casting and laser surface melting processes. The high solidification velocity of the LAEB treated alloy is due to the features of the LAEB process including extremely short pulse duration and thin remelted layer, and the self-quenching effect of the treated layer.

#### 4.4.2 Cooling rate of LAEB treated alloy

In this work, the LAEB process exhibits the highest solidification velocity compared with other processes, which suggests the potential in the generation of amorphous phase. Cooling rate is known as a critical factor to evaluate the possibility of the formation of amorphous phase. Therefore, the cooling rate of the LAEB treated Al-Cu alloy was calculated based on the estimated solidification velocity given in **Section 4.3.2**. This calculation is based on the splat cooling process [160, 165] considering the magnitude of the solidification velocity and the analogous thickness of the irradiated layer to the splat thickness. The parameters and constants used in the calculation of cooling rate are listed in **Table 4-5**. **Figure 4-13** is the schematic of the solidification of the LAEB treated Al-Cu alloy. There are two calculation methods as follows:

**Table 4-5 Parameters and constants used in the calculation of cooling rate for the LAEB treated Al-Cu alloy.**

Parameters	Symbol	Unit	Value
Area of the LAEB sample	$A$	$\text{cm}^2$	2.25
Total thickness of LAEB remelted layer	$R_0$	cm	Varied with LAEB condition
Volume of the solidified material	$V$	$\text{cm}^3$	Varied with time
Solidified layer thickness of the LAEB layer	$R_s$	cm	Varied with time
Heat flux density	$q_e$	$\text{W}/\text{m}^2$	
Heat loss rate	$q_r$	W	
Heat transfer coefficient	$h$	$\text{W}/\text{m}^2\cdot\text{K}$	Constant
Volumetric specific heat	$c_v$	$\text{J}/\text{cm}^3\cdot\text{K}$	2.7264
Solidification temperature	$T_s$	K	821
Ambient temperature	$T_a$	K	293
Volumetric latent heat of fusion	$\Delta H_f$	$\text{J}/\text{cm}^3$	1313.28
Solidification rate	$v$	m/s	1.539
Cooling rate	$\upsilon$	K/s	$4.44 \times 10^7$

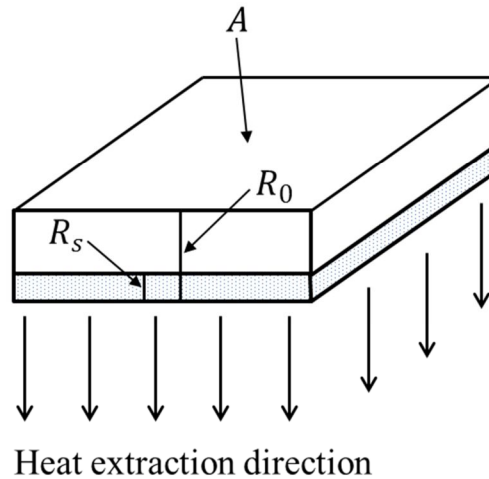


**Figure 4-13 Schematic of solidification of the LAEB treated Al-Cu alloy. The shadow area represents the solidified region.**

**Method 1:**

Due to the perfect contact between the molten surface layer, which grows directly from the solid, and the solid alloy which acts as substrate, the heat transfer coefficient at the interface is essentially infinitely high. Therefore, the Biot number will also be effectively infinite leading to the requirements for Newtonian cooling being satisfied. On this basis the following model can be applied i.e. heat extraction  $q_e(A/V)$  by the substrate can lead to a temperature decrease of the melt with cooling rate of  $\nu=dT/dt$ , or alternatively, an increase of solidified fraction  $f_s$ .

Thus,

$$q_e(A/V) = c_v \frac{dT}{dt} \quad \text{Eq. 4-3}$$

$$q_e(A/V) = \Delta H_f \frac{df_s}{dt} \quad \text{Eq. 4-4}$$

where  $q_e$  is the heat flux density,  $A/V$  is the ratio of area ( $A$ ) to volume ( $V$ ) of the solidified material,  $c_v$  and  $\Delta H_f$  are specific heat and latent heat of solidification per unit volume, respectively. In the process of LAEB treatment, the direction of heat extraction is perpendicular to the interface between the treated layer and the

substrate (**Figure 4-13**). Therefore, in this case, the solidified fraction in volume can be written as

$$f_s = \frac{AR_s}{AR_0} = \frac{R_s}{R_0} \quad \text{Eq. 4-5}$$

The differential of  $f_s$  can be written as

$$\frac{df_s}{dt} = \frac{1}{R_0} \frac{dR_s}{dt} \quad \text{Eq. 4-6}$$

where  $\frac{dR_s}{dt} = v$ . Therefore, the cooling rate can be obtained in

$$v = \frac{\Delta H_f}{c_v} \frac{1}{R_0} v \quad \text{Eq. 4-7}$$

### Method 2:

When Newtonian cooling conditions apply in the situation of this work, the latent heat of solidification involved per unit volume of the metal with the thickness of  $dx$  solidifying on a substrate in a time of  $dt$  is equal to the heat loss through the substrate in a time of  $dt$ .

Thus:

$$\Delta H_f A dx = hA(T_s - T_a) dt \quad \text{Eq. 4-8}$$

where  $h$  is the heat transfer coefficient,  $T_s$  and  $T_a$  are the solidification temperature and ambient temperature, respectively. The solidification velocity  $v$  can also be written as:

$$v = \frac{dx}{dt} = \frac{h(T_s - T_a)}{\Delta H_f} \quad \text{Eq. 4-9}$$

Alternatively, considering the rate of heat loss ( $q_r$ ) from the remelted layer at any time,

$$q_r = Vc_v \frac{dT}{dt} = hA(T_s - T_a) \quad \text{Eq. 4-10}$$

Replacing  $\frac{dT}{dt} = v$  and  $A/V = 1/R_0$ , where  $R_0$  is the thickness of the remelted layer,

$$h = \frac{R_0 c_v v}{T_s - T_a} \quad \text{Eq. 4-11}$$

Equating **Eq. 4-9** and **Eq. 4-11**,

$$v = \frac{\Delta H_f}{c_v} \frac{1}{R_0} v \quad \text{Eq. 4-12}$$

Comparing **Eq. 4-7** and **Eq. 4-12**, it can be seen they are exactly same as each other.

The parameters and constants used in above calculations have been listed in **Table 4-5**. In the present work, the thickness of the LAEB treated layer  $R_0$  was measured from the sample AlCuEB150, which is 16.7  $\mu\text{m}$ . The limit value for the steady-state eutectic growth in Al-32.7Cu (wt.%) alloy according to TMK model [164] is taken as the corresponding solidification rate (1.539 m/s). Based on **Eq. 4-7** or **Eq. 4-12**, the cooling rate is  $4.44 \times 10^7$  K/s. This value is based on the steady-state eutectic growth limit of reference [164] along with the assumption of Newtonian cooling in the molten layer. Given that the molten layer is epitaxially solidified in the solid and that the thickness of the molten layer is  $< 50 \mu\text{m}$ , Newtonian cooling should be a valid approximation. The value of cooling rate calculated here is in reasonable agreement with that which was estimated by Scott and Leake in 1975 [161]. In their work, Al-Cu splat with an eutectic composition was estimated to

cool at  $\sim 10^8$  K/s. In the present work, this calculated cooling rate of  $4.44 \times 10^7$  K/s is expected to be capable of generating the Al-based amorphous alloy.

## 4.5 Summary

- Al-Cu alloy in the wedge mould casting exhibited a regular lamellar Al/Al<sub>2</sub>Cu eutectic structure. The interlamellar spacing decreased as the sample was closer to the tip of the wedge cast.
- LSM process greatly refined the lamellar structure of Al-Cu eutectic alloy. The interlamellar spacing decreased with increasing sample moving speed.
- The solidification velocity of wedge cast and LSM treated Al-Cu eutectic alloys was calculated according to the  $v\lambda^2 = K_0$  relationship. Generally, the Al-Cu eutectic alloy in the LSM process had a higher solidification velocity than in wedge mould casting.
- The LAEB process largely changed the eutectic lamellar structure due to the high solidification rate. Based on XRD and microstructure observation results of the remelted layer, the solidification rate decreased with increasing number of pulses. The estimated minimum cooling rate of the LAEB treated sample reached the magnitude of  $10^7$  K/s based on the limit of the steady eutectic growth.

## Chapter 5 Wedge mould casting and laser surface melting of Al-Co-Ce alloys

### 5.1 Introduction

In **Chapter 4**, it was determined that wedge mould casting, laser surface melting and large area electron beam surface melting processes can provide different solidification rates for the Al-Cu eutectic alloy depending on the processing conditions. Overall, large area electron beam surface melting can generate the highest solidification rate, then laser surface melting and wedge mould casting. In this chapter, bulk Al-Co-Ce alloys were first cast by mixing pure metal elements through wedge mould casting. As-cast alloys were then treated by the overlapped multi-track laser surface melting process in order to refine the alloy microstructure. Both wedge cast and laser pre-treated samples will be used as the starting materials for the following large area electron beam surface melting treatment.

For wedge mould casting, three alloys with different compositions (**Appendix 1**) were cast. However, in the case of laser surface melting, only alloy 3 with the composition of  $\text{Al}_{86}\text{Co}_{7.6}\text{Ce}_{6.4}$  was treated. The composition of alloy 3 was found to be located in the centre of the glass forming range of the Al-Co-Ce alloys, which can minimise the risk of the composition getting out of the glass forming composition range should there be any composition change during the laser or subsequent large area electron beam treatment. In addition, the microstructure of alloy 3 was found to be more sensitive to solidification velocity than that of alloys 1 and 2 based on the microstructural observation of wedge mould cast materials.

## 5.2 Wedge mould casting of Al-Co-Ce alloys

### 5.2.1 SEM results

#### 5.2.2.1 At the top of the wedge

**Figure 5-1** shows the microstructures of the three as-cast materials with a distance of 50 mm from the tip of the wedge cast. It can be seen that the three as-cast alloys with different compositions (**Table 3-3**) exhibited different microstructures.

Alloy 1 had three main phases including bright phase 1, dark region 2 and grey phase 3. For alloy 2, there were similar dark eutectic region 2 and the same grey phase 3 as those seen in alloy 1. However, no large bright phase 1 was found in alloy 2. In the case of alloy 3, there were two more phases present in addition to those three phases present in alloys 1 and 2. Phase 4 surrounding the phase 3 particles had a clearly distinct contrast level, and hence different average atomic number compared to the phase 3. Phase 5 with a small size was found to be located in the dark eutectic region 2. Phase 5 also exhibited a different contrast level compared with other phases.

In addition to the difference in phase type, the microstructure of the three alloys differed in lengthscale. Alloy 1 exhibited the smallest microstructural lengthscale compared to the other two alloys. This shows the sensitivity of microstructural lengthscale to the precise alloy composition.

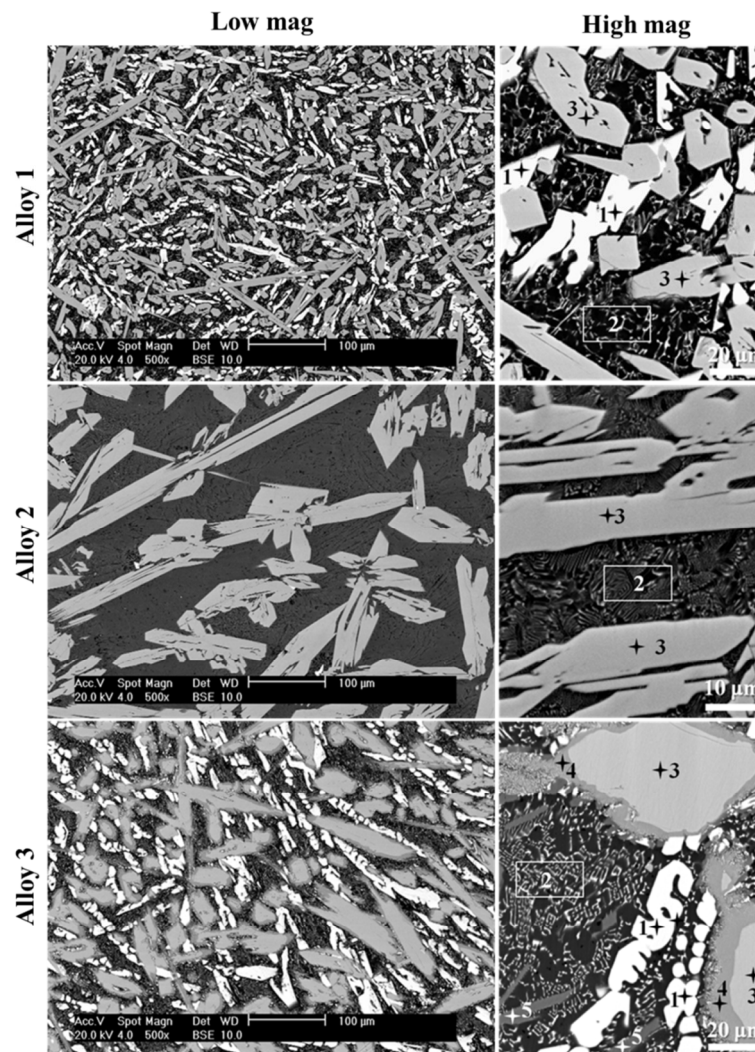


**Figure 5-1** BSE images of as-cast materials with different compositions. The samples were cut from the top of the wedge with a distance of 50 mm from the tip of the wedge cast, as shown in Figure 3-4b.

### 5.2.2.2 At the middle of the wedge

**Figure 5-2** shows the microstructures of the three wedge alloys at different positions. In each case, there is some indication of microstructural refinement closer to the tips of the wedge casts due to the higher solidification rates. The change of alloy microstructure with solidification rate is most apparent in alloy 3.

For alloy 1 (**first column of Figure 5-2**), it is shown that there were three different phases evenly distributed in the cast alloy, including bright phase 1, dark region 2 and grey phase 3 which are similar to those seen in **Figure 5-1**. The size of phases

1 and 3 was very small; grey phase 3 was mostly less than 20  $\mu\text{m}$  long, and the bright phase 2 was even smaller (less than 10  $\mu\text{m}$  long).

For alloy 2 (**second column of Figure 5-2**), overall, the phase size was much bigger than that at corresponding locations in alloy 1. There were few small bright phases surrounding the grey phase in the cases of  $x=20$  and 15 mm. With decreasing  $x$ , these bright phases almost disappeared. In addition, the grey phase existing in alloy 2 was found to be much larger than that in alloy 1.

For alloy 3 (**third column of Figure 5-2**), the alloy was found to consist of three phases which were very similar to those seen in alloy 1. However, it is seen that the size of bright and grey phases in alloy 3 was bigger than that seen in alloy 1. In addition, these two phases also decreased in size with decreasing  $x$  value, which is most apparent here compared to the other two alloys.

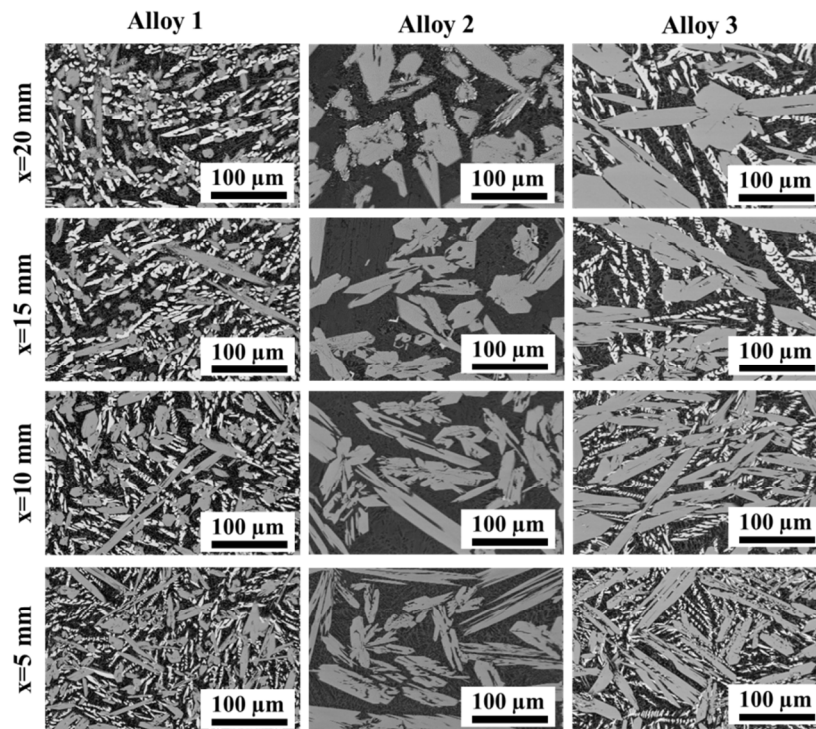


**Figure 5-2** BSE images of the three as-cast alloys at different positions.  $x$  presents the distance from the tip of the wedge cast. The samples were cut from the wedge casts as shown in Figure 3-4a.

### 5.2.2.3 At the tip of the wedge

**Figure 5-3** shows the microstructures of the whole tips with the length of  $\sim 1000$   $\mu\text{m}$  in the three wedge cast alloys, as well as the corresponding magnified selected regions. For alloy 1, in this length range, the microstructure of the as-cast alloy did not have apparent change with increasing distance from the tip. From the magnified image, it can be seen that the alloy was comprised of bright phase 1, dark region 2 and grey phase 3, which was consistent with that shown in the top (**first row of Figure 5-1**) and middle (**first column of Figure 5-2**) of the wedge cast. The bright phases and grey phases were in the form of dendrites and scattered in the dark matrix. The dark region was also found to be not uniform, but consisted of sub-micron lamellar structures. The size of the bright phase was  $\sim 10$   $\mu\text{m} \times 1$   $\mu\text{m}$ , which was smaller than that of grey phases ( $\sim 20$   $\mu\text{m} \times 1$   $\mu\text{m}$ ).

In alloy 2, there were two main phases, but no bright phase found. The grey phases were distributed in the dark matrix. From the magnified image, it is seen that the size of the grey phase in alloy 2 was much bigger than that seen in alloy 1. With increasing distance from the tip, the size of grey phases showed a slight increase. Compared with alloy 1, dark regions consisting of small lamellar eutectic structures were seen to have more area fraction in alloy 2.

In alloy 3, the phases present were similar to that seen in alloy 1. However, both bright and grey phase in alloy 3 exhibited bigger sizes compared with that in alloy 1. From the magnified image, it is seen that there were extremely few bright phases in the very tip. With increasing distance from the tip, more and more bright phases were observed. Furthermore, the grey phase dendrites obviously had a larger size compared with the bright phases.

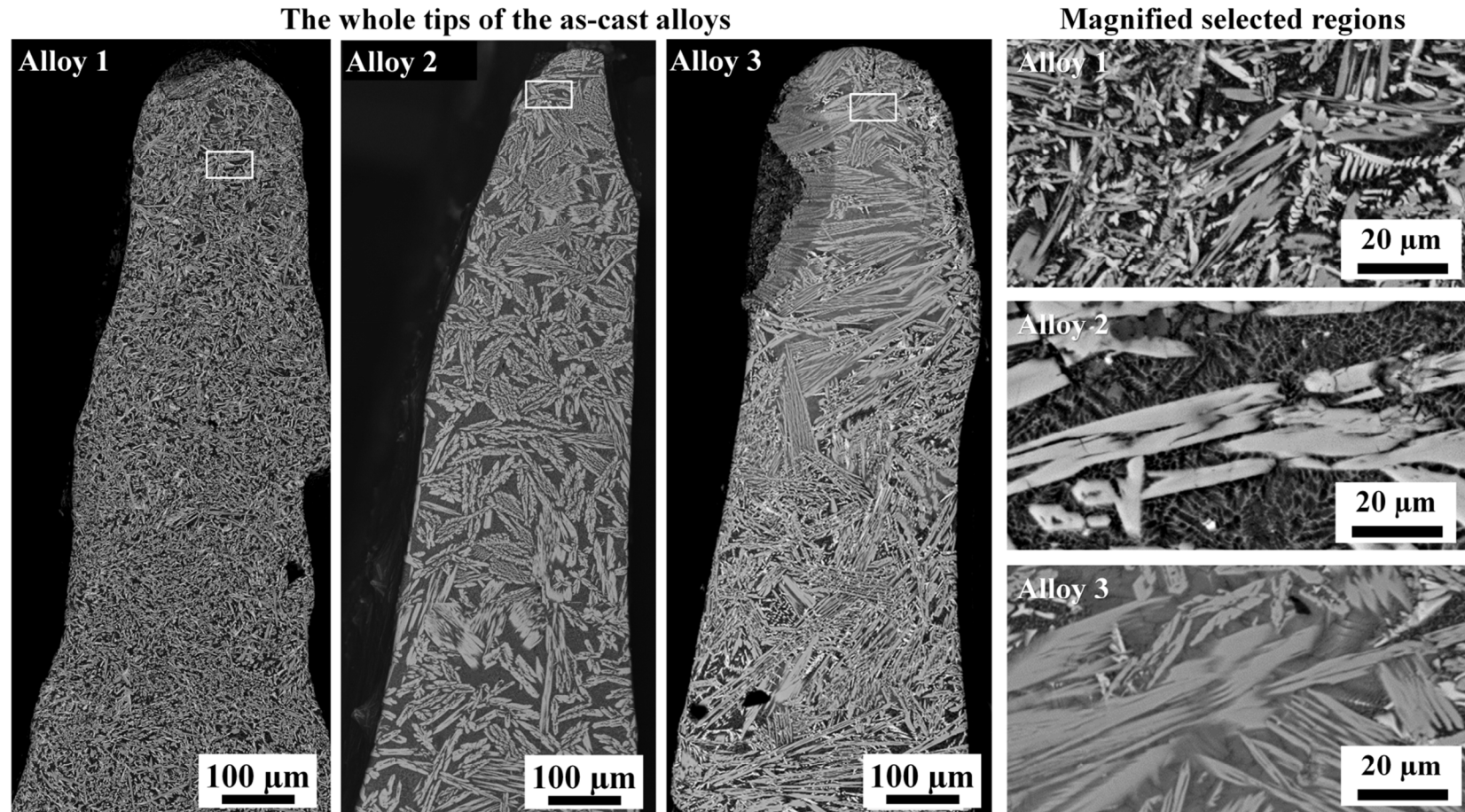


Figure 5-3 BSE images of the whole tips and corresponding magnified selected region in the three as-cast alloys. The samples were cut from the tip of the wedge cast as shown in Figure 3-4a. A large pore that formed during casting is seen in alloy 3.

### 5.2.2 EDS results

**Figure 5-4** and **Table 5-1** summarise the phases present and their chemical compositions in the three as-cast alloys. For the grey phase, in all the three alloys the content of Al in the grey phase increased with decreasing  $x$  i.e. the distance from the tip of the wedge cast. On the contrary, the content of Co and Ce in all the three alloys decreased with decreasing  $x$ . For all the three alloys, when  $x=5, 10, 15, 20$  and  $50$  mm the compositions of grey phase were very similar. The atomic ratio of elements was nearly 8:2:1 (Al:Co:Ce). However, when  $x=0$ , the grey phase was found to contain less cerium compared with other locations.

For the bright phase, there was no Co element found in this phase despite that there was  $\sim 0.5$  at.% Co when  $x=0$ . The content of Al and Ce generally kept at the stable level when  $x=5, 10, 15, 20$  and  $50$  mm with the atomic ratio of 11:3. However, when  $x=0$ , Al exhibited an apparent increase, while the content of Ce apparently decreased. It should be noted that in alloy 2 there was no bright phase found at  $x=0, 5$  and  $10$  mm.

For the dark region, there were always more than 96% Al and a small amount of Co and Ce elements although the content of Ce in alloy 3 (5.5%) was much higher than that in other alloys when  $x=0$ . Overall, the content of Al, Co and Ce in this region exhibited the opposite change with decreasing  $x$  compared with that in the grey phase.

In particular, two extra phases seen in alloy 3 (**Figure 5-1**) were also analysed. Phase 4 surrounding the grey phase was found to contain Al, Co and Ce as that in grey phase. However, the content of Al in phase 4 was higher than that in the grey phase. In addition, phase 5 was found to consist of Al and Co with the atomic ratio of 9:2.

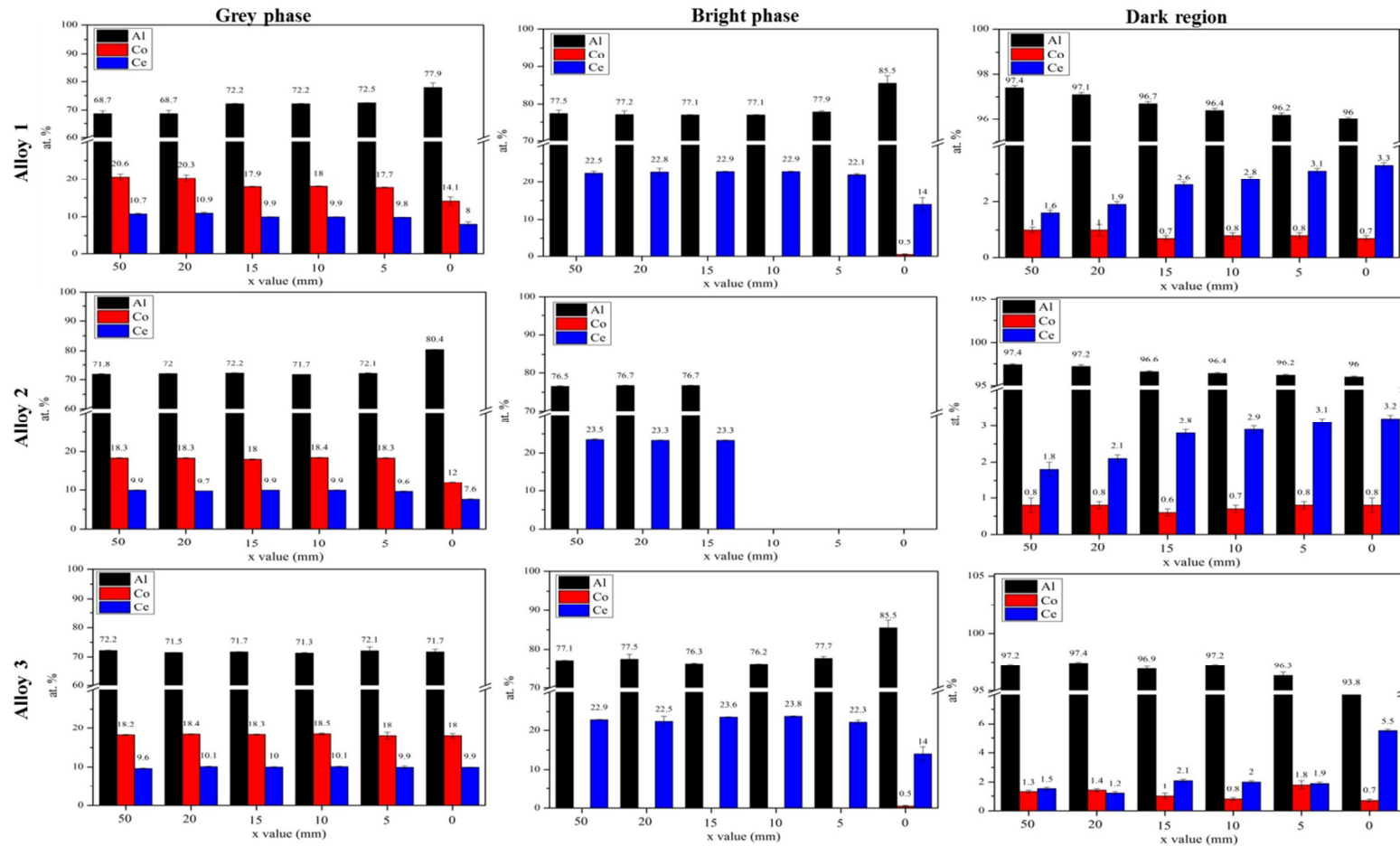


Figure 5-4 Composition of three phases in the three wedge cast alloys, shown as a function of distance, x, from the wedge tip.

**Table 5-1 EDS results of the three as-cast alloys at different positions of the wedge cast.**

Location (x/ mm)	region	Alloy 1			Alloy 2			Alloy 3		
		Al (at%)	Co (at%)	Ce (at%)	Al (at%)	Co (at%)	Ce (at%)	Al (at%)	Co (at%)	Ce (at%)
50	<i>grey phase</i>	68.7±1.0	20.6±0.8	10.7±0.2	71.8±0.2	18.3±0.1	9.9±0.1	72.2±0.5	18.2±0.1	9.6±0.5
	<i>bright phase</i>	77.5±0.9	0	22.5±0.5	76.5±0.2	0	23.5±0.2	77.1±1.0	0	22.9±1.0
	<i>dark region</i>	97.4±0.1	1.0±0.1	1.6±0.1	97.4±0.1	0.8±0.2	1.8±0.2	97.2±0.2	1.3±0.2	1.5±0.2
20	<i>grey phase</i>	68.7±1.2	20.3±0.9	10.9±0.3	72.0±0.1	18.3±0.1	9.7±0	71.5±0.1	18.4±0	10.1±0.1
	<i>bright phase</i>	77.2±1.0	0	22.8±1.0	76.7±0.1	0	23.3±0.1	77.5±1.3	0	22.5±1.3
	<i>dark region</i>	97.1±0.1	1.0±0.2	1.9±0	97.2±0.2	0.8±0.1	2.1±0.1	97.4±0	1.4±0	1.2±0
15	<i>grey phase</i>	72.2±0	17.9±0	9.9±0	72.2±0.1	18.0±0.1	9.9±0	71.7±0.1	18.3±0.1	10.0±0
	<i>bright phase</i>	77.1±0.1	0	22.9±0.1	76.7±0.1	0	23.3±0.1	76.3±0.2	0	23.6±0.1
	<i>dark region</i>	96.7±0	0.7±0	2.6±0	96.6±0	0.6±0	2.8±0	96.9±0.2	1.0±0.2	2.1±0
10	<i>grey phase</i>	72.2±0	18.0±0	9.9±0	71.7±0	18.4±0.1	9.9±0.2	71.3±0.2	18.5±0.2	10.1±0.1
	<i>bright phase</i>	77.1±0.1	0	22.9±0.1	–	–	–	76.2±0.1	0	23.8±0.1
	<i>dark region</i>	96.4±0	0.8±0	2.8±0	96.4±0	0.7±0	2.9±0	97.2±0	0.8±0	2.0±0
5	<i>grey phase</i>	72.5±0.1	17.7±0	9.8±0.07	72.1±0.2	18.3±.1	9.6±0.4	72.1±1.3	18.0±0.9	9.9±0.4
	<i>bright phase</i>	77.9±0.3	0	22.1±0.3	–	–	–	77.7±0.5	0	22.3±0.5
	<i>dark region</i>	96.2±0	0.8±0.1	3.1±0	96.2±0	0.8±0.1	3.1±0	96.3±0.3	1.8±0.3	1.9±0
0	<i>grey phase</i>	77.9±1.7	14.1±1.1	8.0±0.6	80.4±0.1	12.0±0.2	7.6±0.1	71.7±1.0	18.0±0.6	9.9±0.1
	<i>bright phase</i>	85.5±2.0	0.5±0.2	14.0±1.8	–	–	–	85.5±2.0	0.5±0.2	14.0±1.8
	<i>dark region</i>	96.0±0	0.7±0.1	3.3±0	96.0±0.1	0.8±0.2	3.2±0.1	93.8±0.1	0.7±0.1	5.5±0

- Notes: 1. x presents the distance between the examined location and the tip of the wedge cast.  
 2. Errors included represent the standard deviation of repeated measurements.  
 3. In alloy 2, bright phase presented only in the locations where x=15, 20 and 50 mm.

### 5.2.3 XRD results

**Figure 5-5** shows the XRD spectra of Al-Co-Ce alloys at the three different positions of the wedge cast. The analyses were conducted on the samples which are shown in **Section 5.2.1** and **Section 5.2.2**. Generally, they are clearly the spectra of multi-phase crystalline materials. Due to the similar XRD peaks, there might be some possible crystalline phases including  $\text{Al}_8\text{Co}_2\text{Ce}$ ,  $\text{Al}_4\text{CoCe}$ ,  $\text{Al}_{11}\text{Ce}_3$ ,  $\text{Al}_4\text{Ce}$  and Al in the cast alloys. However, according to the EDS results shown in **Section 5.2.2**, the composition of the Al-Co-Ce and Al-Ce phase was closer to  $\text{Al}_8\text{Co}_2\text{Ce}$  and  $\text{Al}_{11}\text{Ce}_3$ , respectively. Therefore, Al,  $\text{Al}_8\text{Co}_2\text{Ce}$  and  $\text{Al}_{11}\text{Ce}_3$  phases were identified in this work.

Combining with EDS analyses shown in **Section 5.2.2**, the phase 1 (bright phase) and phase 3 (grey phase) can be identified as  $\text{Al}_{11}\text{Ce}_3$  and  $\text{Al}_8\text{Co}_2\text{Ce}$ , respectively. The dark region (region 2) was comprised of pure Al and  $\text{Al}_{11}\text{Ce}_3$ . However, phases 4 and 5 shown in **Figure 5-1** cannot be unambiguously identified. A few unidentified peaks presented in the XRD pattern, as well as the possibility of additional peaks being hidden by overlapping might be consistent with the presence of these two unidentified phases.

From figures, in alloys 1 and 3, the ratio of the intensity of the  $\text{Al}_{11}\text{Ce}_3$  peak ( $2\theta = \sim 34^\circ$  and  $\sim 35.5^\circ$ ) to that of the  $\text{Al}_8\text{Co}_2\text{Ce}$  phase ( $2\theta = \sim 34.5^\circ$  and  $\sim 36.5^\circ$ ) decreased with decreasing distance from the tip of the wedge cast. This suggests that there were fewer  $\text{Al}_{11}\text{Ce}_3$  phases in the tip. However, in alloy 2, this decrease was not as apparent as that seen in other two alloys. This is consistent with the microstructure observation (**Figure 5-1**, **Figure 5-2** and **Figure 5-3**). It should be clarified that the presence of  $\text{Al}_{11}\text{Ce}_3$  phase peaks in the XRD pattern of alloy 2 is mostly attributed to the sub-micron lamellar  $\text{Al}_{11}\text{Ce}_3$  existing in the Al/ $\text{Al}_{11}\text{Ce}_3$  eutectic region i.e. dark region 2 shown in **Figure 5-1**.

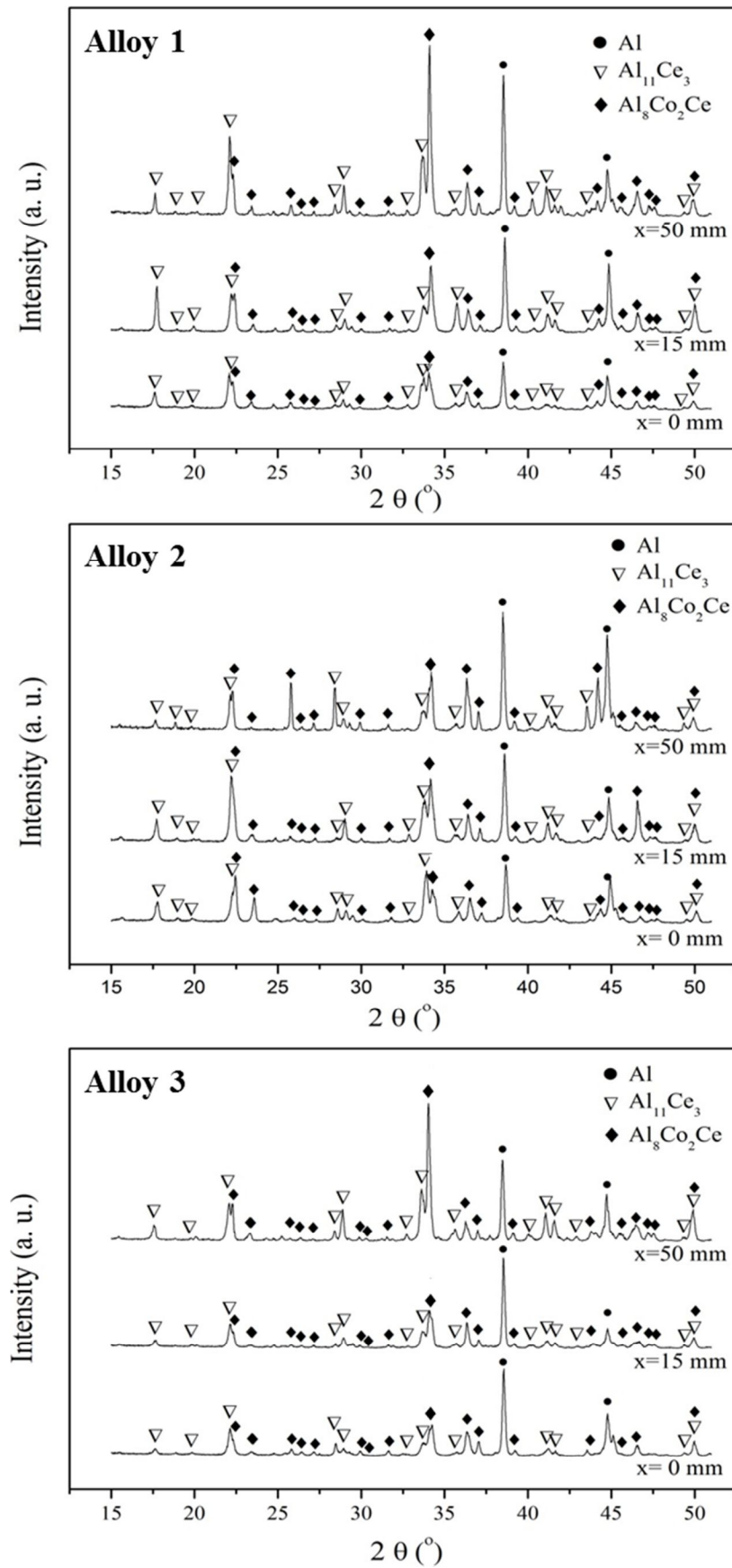


Figure 5-5 XRD spectra of wedge cast Al-Co-Ce alloys at different positions.

#### 5.2.4 Phase fraction

Phase fractions (in area) of the Al-rich eutectic, the  $\text{Al}_8\text{Co}_2\text{Ce}$  and the primary  $\text{Al}_{11}\text{Ce}_3$  present in the cast alloys were examined through image analysis of SEM images taken at different locations of the wedge cast (**Figure 5-1**, **Figure 5-2** and **Figure 5-3**). The relationship between phase fraction and location in the wedge cast is shown in **Figure 5-6**.

For alloy 1 (**Figure 5-6a**), the phase fraction of the Al-rich eutectic was higher than those of the  $\text{Al}_8\text{Co}_2\text{Ce}$  and the primary  $\text{Al}_{11}\text{Ce}_3$ . With increasing  $x$  value, the fraction of the primary  $\text{Al}_{11}\text{Ce}_3$  increased from 5.5% to 20.5%. However, the phase fraction of the  $\text{Al}_8\text{Co}_2\text{Ce}$  decreased from 47.3% to 28.6%. For the Al-rich eutectic (Al/ $\text{Al}_{11}\text{Ce}_3$ ), there was limited increase in area fraction when  $x$  value increased.

For alloy 2 (**Figure 5-6b**), the primary  $\text{Al}_{11}\text{Ce}_3$  fraction was extremely low. The phase fraction only increased to 0.2% and 0.8%, even when  $x$  value increased to 15 and 20 mm. The Al-rich eutectic in alloy 2 had a bigger phase fraction than the  $\text{Al}_8\text{Co}_2\text{Ce}$ . In addition, the Al-rich eutectic and the  $\text{Al}_8\text{Co}_2\text{Ce}$  showed the opposite change with  $x$ , which was consistent with that seen in alloy 1.

For alloy 3 (**Figure 5-6c**), the  $\text{Al}_8\text{Co}_2\text{Ce}$  had the highest phase fraction excluding the case of  $x=50$  mm. However, the phase fraction of the  $\text{Al}_8\text{Co}_2\text{Ce}$  decreased from 60.6% to 23.5% when  $x$  value increased from 0 to 50 mm. On the contrary, the Al/ $\text{Al}_{11}\text{Ce}_3$  eutectic showed an obvious increase from 38.6% to 54.7%. The primary  $\text{Al}_{11}\text{Ce}_3$  also exhibited an increase with increasing  $x$  value from 0.8% ( $x=0$ ) to 13.8% ( $x=50$  mm).

It should be noted that in some cases of image analysis for phase area measurements, there were also some  $\text{Al}_9\text{Co}_2$  phases present in the alloys. However, due to similar contrast level to the dark eutectic region, they were included into the measurement of the  $\text{Al}/\text{Al}_{11}\text{Ce}_3$  eutectic. Therefore, the fraction of the  $\text{Al}/\text{Al}_{11}\text{Ce}_3$  eutectic region may be slightly overestimated.

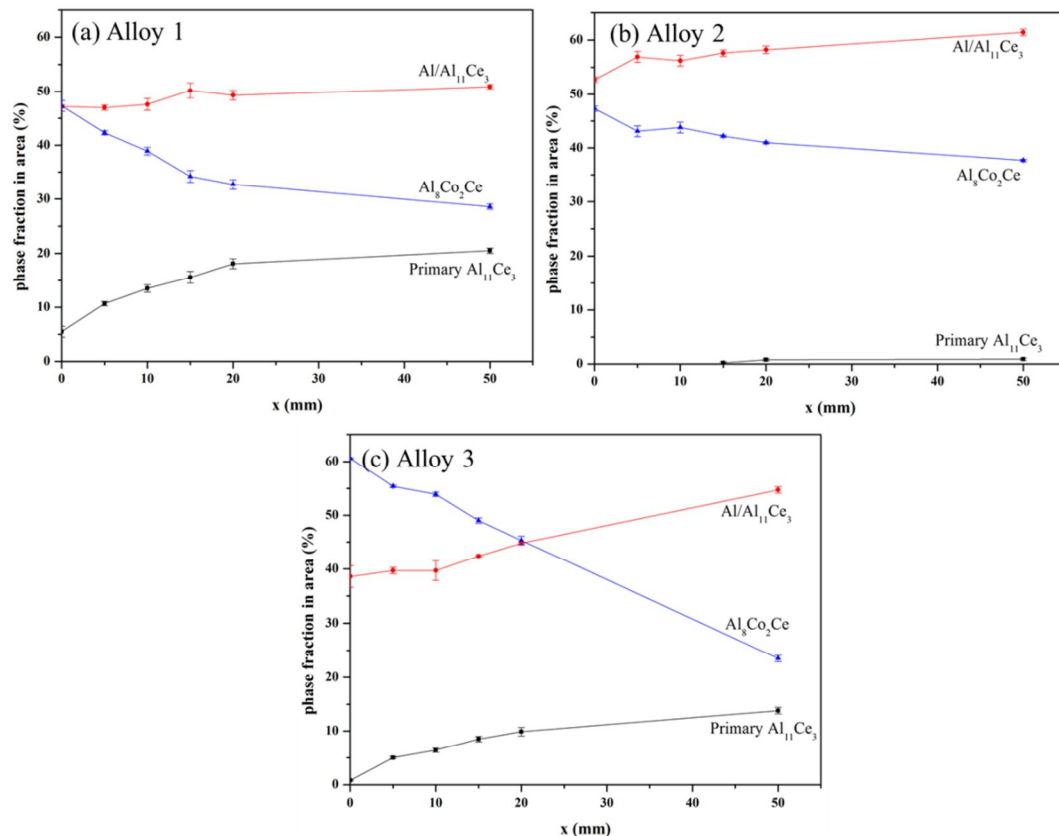


**Figure 5-6** Phase fractions of three main phases in the three cast alloys (in area).  $x$  represents the distance of the examined location from the tip of wedge cast. Error bars are standard deviations of 3~4 measurements.

### 5.2.5 Micro-hardness of different regions in the as-cast alloy 3

The micro-hardness of different regions in the as-cast alloy 3 was measured through Vickers micro-hardness tests and nanoindentation. The measurement details have been given in **Section 3.5.5**. The results of Vickers micro-hardness testing and nanoindentation are listed in **Table 5-2**. It can be seen that the

$\text{Al}_8\text{Co}_2\text{Ce}$  phase had the highest micro-hardness among the three main phases ( $7.29\pm 0.76$  and  $9.9\pm 0.4$  GPa in Vickers micro-hardness and nanoindentation hardness, respectively), while the micro-hardness of the eutectic region was the lowest ( $0.87\pm 0.25$  and  $1.0\pm 0.1$  GPa in Vickers micro-hardness and nanoindentation micro-hardness, respectively). For the  $\text{Al}_{11}\text{Ce}_3$  phase, Vickers micro-hardness testing did not obtain valid results due to the small phase size. However, in the nanoindentation test  $\text{Al}_{11}\text{Ce}_3$  phase had an intermediate micro-hardness ( $3.2\pm 0.3$  GPa) compared with other regions.

**Figure 5-7** shows a Vickers indentation in the  $\text{Al}_8\text{Co}_2\text{Ce}$  phase. This indentation was not regarded as a valid one in the measurement of hardness. It can be observed that the loading has induced cracking within the  $\text{Al}_8\text{Co}_2\text{Ce}$  phase, initiating from a corner of the indentation. This indicates the brittleness characteristic of the  $\text{Al}_8\text{Co}_2\text{Ce}$  phase.

**Table 5-2 Micro-hardness test results on different regions in the as-cast alloy 3.**

Region	Eutectic region	$\text{Al}_8\text{Co}_2\text{Ce}$	$\text{Al}_{11}\text{Ce}_3$
Vickers micro-hardness (GPa)	$0.87\pm 0.25$	$7.29\pm 0.76$	-
Nanoindentation micro-hardness (GPa)	$1.0\pm 0.1$	$9.9\pm 0.4$	$3.2\pm 0.3$

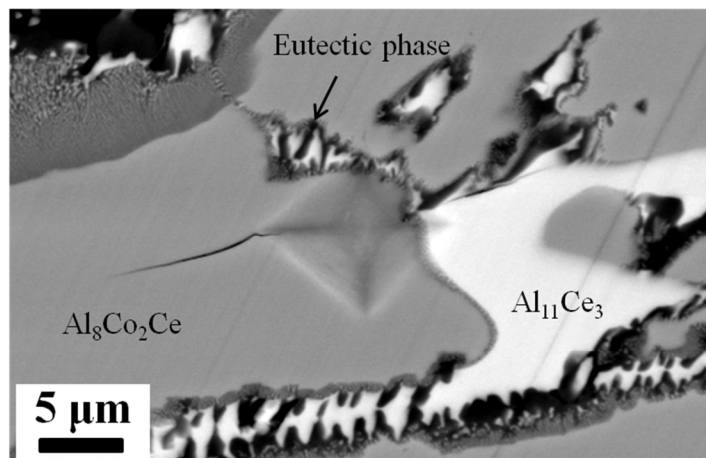


**Figure 5-7 Crack induced by loaded force in Vickers micro-hardness testing of alloy 3. This indentation was not regarded as a valid one in the measurement of hardness.**

### 5.2.6 Metal flakes in the split of wedge mould

After wedge mould casting, there were a few metal flakes found in the split of the wedge mould. The microstructure of these metal flakes in alloy 1 was analysed, and localised homogeneous microstructure found. **Figure 5-8** shows two exemplified regions. It can be seen that both regions were located at the thinner part of the flakes compared to the neighbouring dendrite microstructure regions. The sizes of these two homogeneous regions were similar,  $\sim 200 \mu\text{m}$  in diameter. Magnified SEM images in the back scattered mode show that there were a few bright crystals unevenly distributed in the homogeneous matrix. A transition region between the homogeneous region and dendritical region in the metal flake is shown in **Figure 5-9**. Along the direction of the arrow in figure, there were more and bigger crystals found in the homogeneous matrix. The shape of those crystals was also changed from spherical to dendritical.

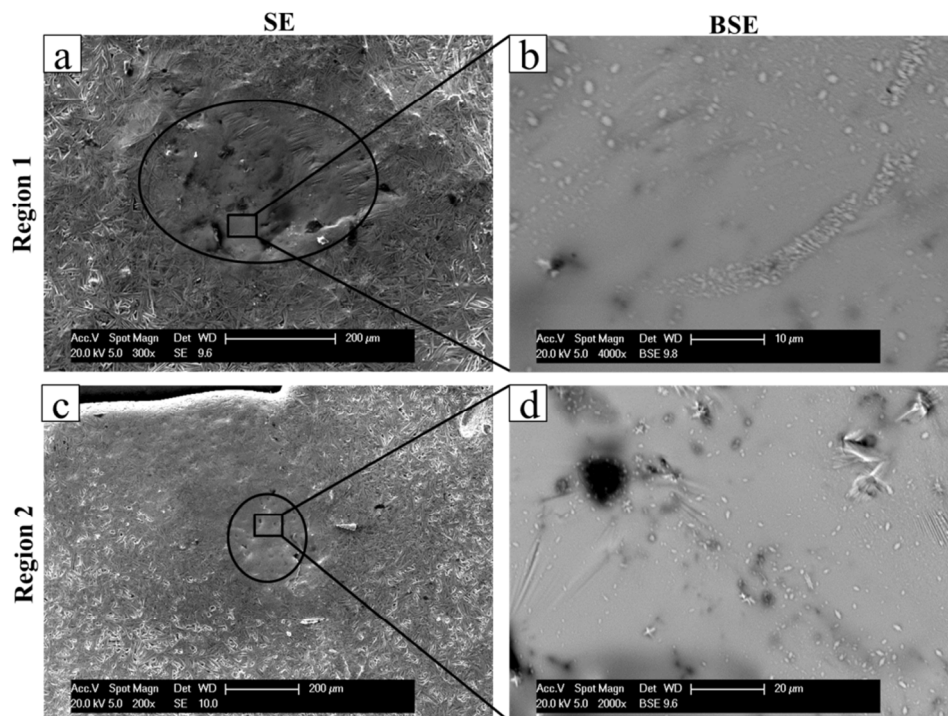


**Figure 5-8** Homogeneous microstructure in the flakes of alloy 1.

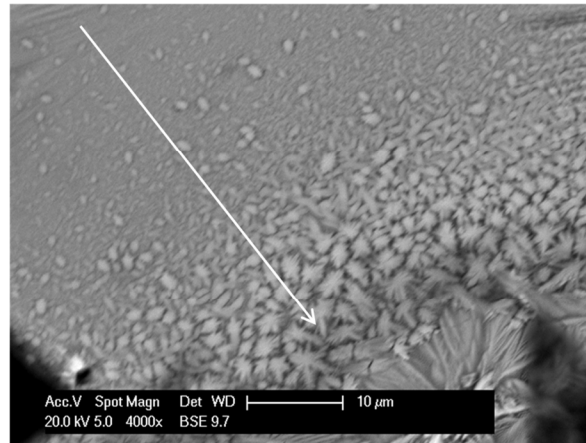


**Figure 5-9** BSE image showing the transition between the homogeneous region and the dendritical region.

## **5.3 Overlapped multi-track laser surface melting of Al-Co-Ce alloy 3**

### **5.3.1 SEM results**

**Figure 5-10** and **Table 5-3** show the cross sectional microstructure and characteristic parameters of the laser treated samples. It can be seen that the laser tracks produced by different parameters had different dimensions. For MT1000-20 sample, with a distance of 20 mm from the focus and a sample traverse speed of 1000 mm/min, both the width (3.2 mm) and maximum depth (690  $\mu\text{m}$ ) of the laser track were the largest among the three laser treated samples. For MT6000-20 sample, the increased sample traverse speed made the laser track have an obvious decrease in both width and depth, which were 1.7 mm and 255  $\mu\text{m}$ , respectively. In particular, MT6000-5 sample with a distance of 5 mm from the focus and a sample traverse speed of 6000 mm/min, the width of the laser track had a slight decrease. However, the maximum depth of the laser track increased compared with that in MT6000-20 sample.

In addition, the overlapped region between two neighbouring tracks had apparently smaller depth compared to the centre of the track. After surface polishing of laser treated samples to remove the raised zone in the laser tracks, it can be seen that the samples still had at least 50  $\mu\text{m}$  refined microstructure, which is far thicker than the possible thickness of the LAEB treated layer (always less than 10  $\mu\text{m}$ ).

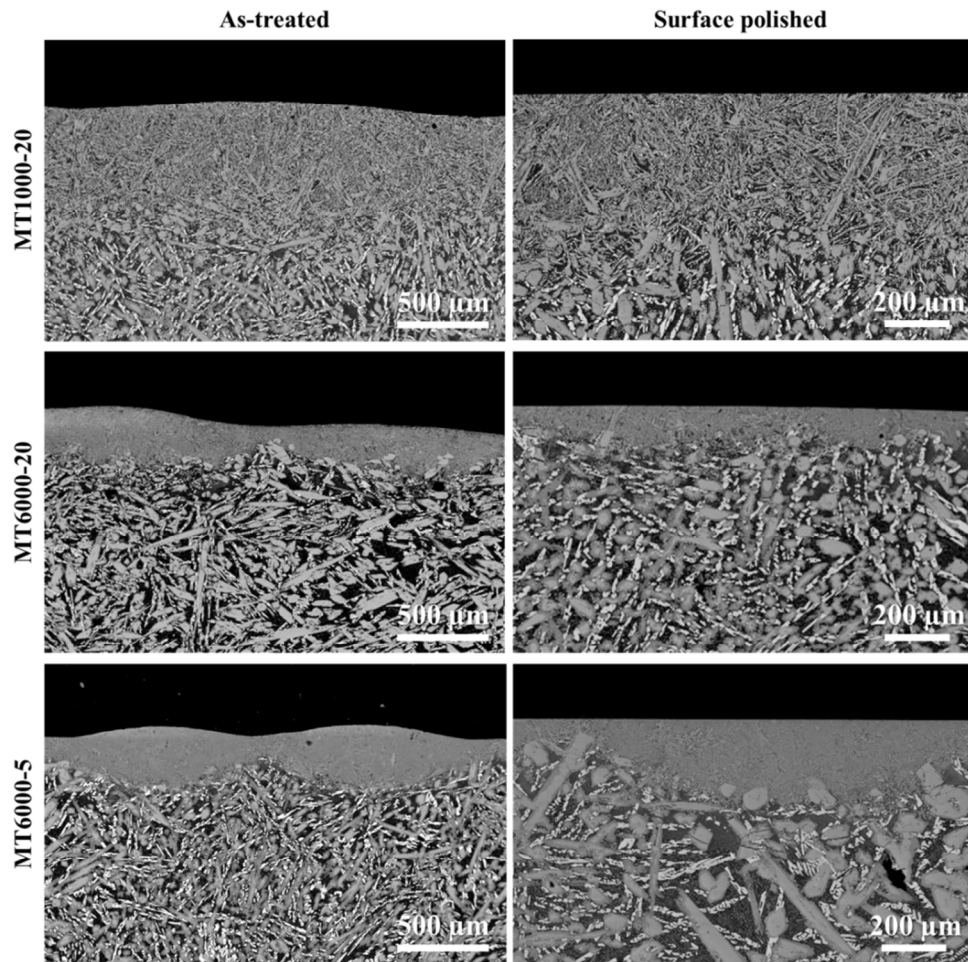


**Figure 5-10 BSE images showing the cross section of the multi-track laser treated sample with different laser parameters.**

**Table 5-3 Characterisation of laser tracks under different conditions.**

Sample code	Width of single track (mm)	Maximum depth ( $\mu\text{m}$ )	Particle size of $\text{Al}_8\text{Co}_2\text{Ce}$ phase ( $\mu\text{m}$ )	Particle spacing of neighbouring $\text{Al}_8\text{Co}_2\text{Ce}$ phase ( $\mu\text{m}$ )
MT1000-20	$3.2 \pm 0.1$	$690 \pm 30$	$\sim 20 \times 5$	$\sim 5$
MT6000-20	$1.7 \pm 0.1$	$255 \pm 20$	$\sim 20 \times 2$	$\sim 0.5$
MT6000-5	$1.4 \pm 0.1$	$333 \pm 27$	$\sim 20 \times 0.5$	$\sim 0.2$

**Figure 5-11** and **Figure 5-12** show the magnified microstructure of laser treated alloys. Laser treatment greatly refined the microstructure of the Al-Co-Ce alloy. The as-cast material had large  $\text{Al}_8\text{Co}_2\text{Ce}$  particles,  $\sim 100 \times 20 \mu\text{m}$  in size (**Figure 5-11a**). The grey phase in sample MT1000-20 was  $\sim 20 \times 5 \mu\text{m}$ . The MT6000-20 and MT6000-5 samples were seen to consist of further refined grey phases with characteristic feature sizes of  $\sim 20 \times 2 \mu\text{m}$  and  $\sim 20 \times 0.5 \mu\text{m}$ , respectively.

With decreasing particle size of  $\text{Al}_8\text{Co}_2\text{Ce}$  phase, the particle spacing between two neighbouring particles also decreased. For the as-cast material, the particle spacing was  $\sim 30 \mu\text{m}$ . In samples MT1000-20, MT6000-20 and MT6000-5, the particle spacing was  $\sim 5$ ,  $\sim 0.5$  and  $\sim 0.2 \mu\text{m}$ , respectively.

In addition, for samples MT6000-20 and MT6000-5, very few, small primary  $\text{Al}_{11}\text{Ce}_3$  phase particles were observed in the treated samples (**Figure 5-11c** and **d**). The magnified eutectic region in the laser treated sample (**Figure 5-12**) shows that the bright sub-micron lamellar phase ( $\text{Al}_{11}\text{Ce}_3$ ) evenly distributed in the darker matrix (pure Al), which is similar to that seen in the as-cast material.

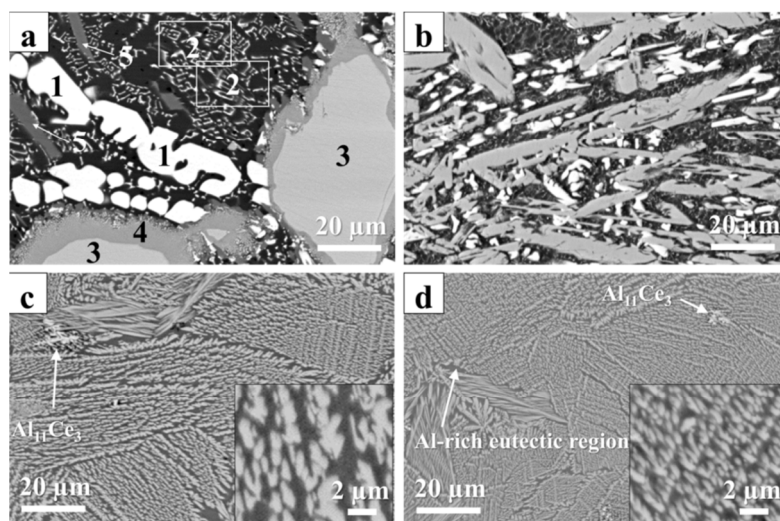


**Figure 5-11** BSE images of as-cast and laser pre-treated Al-Co-Ce alloys: (a) as-cast material; (b) MT1000-20; (c) MT6000-20; (d) MT6000-5. Insets in (c) and (d) present the magnified local region in the corresponding image.

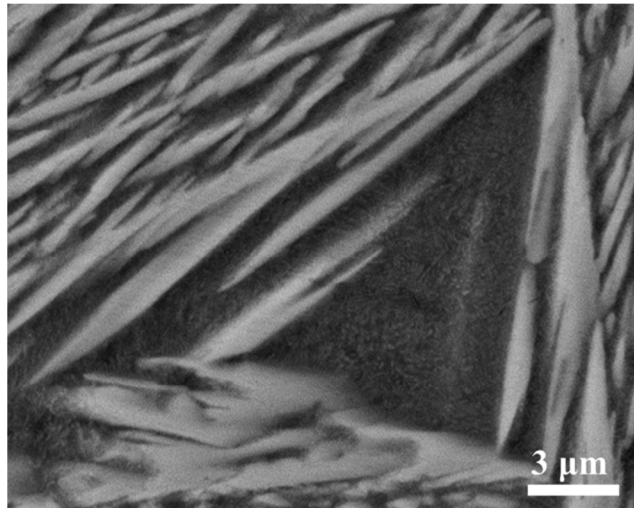


**Figure 5-12 Magnified Al-rich eutectic region in sample MT6000-5 (BSE).**

### 5.3.2 EDS results

The overall composition of the above darker eutectic region in both as-cast and laser treated samples was analysed by EDS, as shown in **Table 5-4**. Results show that MT1000-20 sample and as-cast material had a similar composition in the darker region. However, samples MT6000-20 and MT6000-5 exhibited a higher content of Ce (5.1%) compared with the as-cast material and sample MT1000-20 (2.6%). This variation in composition was also confirmed by the contrast level difference between the dark region and the grey  $\text{Al}_8\text{Co}_2\text{Ce}$  phase in the back scattered mode SEM images (**Figure 5-11**). The above contrast level difference in the as-cast material was more apparent than that in laser treated materials.

**Table 5-4 Overall composition of the eutectic region under different laser treatment parameters.**

Sample code	Overall composition of Al/ $\text{Al}_{11}\text{Ce}_3$ eutectic region (at.%)		
	Al	Co	Ce
MT1000-20	97.0	0.4	2.6
MT6000-20	94.5	0.4	5.1
MT6000-5	94.4	0.5	5.1

### 5.3.3 XRD results

**Figure 5-13** shows XRD patterns of the as-cast material and multi-track laser treated materials. It can be seen that the laser treated samples were still consisted of three main phases, including Al,  $\text{Al}_{11}\text{Ce}_3$  and  $\text{Al}_8\text{Co}_2\text{Ce}$ . The presence of  $\text{Al}_{11}\text{Ce}_3$  peaks in XRD patterns of laser treated samples is thought to be from the Al/ $\text{Al}_{11}\text{Ce}_3$  eutectic region, which has been seen in **Figure 5-12**. However, compared with the as-cast material, the  $\text{Al}_{11}\text{Ce}_3$  phase was reduced by the laser pre-treatment considering the decreased ratio of the intensity of  $\text{Al}_{11}\text{Ce}_3$  peaks ( $2\theta = \sim 34^\circ$  and  $\sim 35.5^\circ$ ) to that of the  $\text{Al}_8\text{Co}_2\text{Ce}$  phase ( $2\theta = \sim 34.5^\circ$  and  $\sim 36.5^\circ$ ).

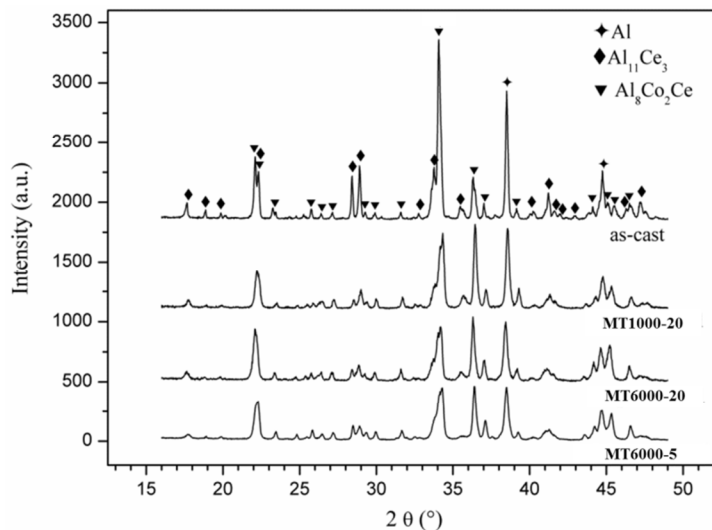


**Figure 5-13** XRD patterns of as-cast and laser pre-treated samples.

## 5.4 Discussion

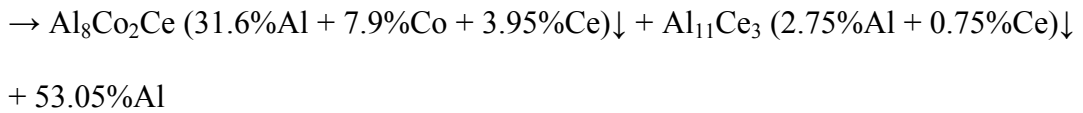
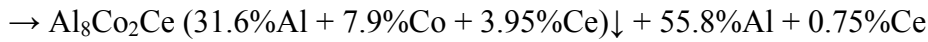
### 5.4.1 Wedge mould casting

#### 5.4.1.1 Determination of solidification process

**Figure 5-14** shows the phase diagram of Al-Co-Ce alloys reported by Gao et al. [66]. In the solidification process,  $\text{Al}_8\text{Co}_2\text{Ce}$  (i.e.  $\tau_1$ ) first forms due to its highest



Based on the phase diagram above, the final phase fraction after the solidification can be roughly calculated. Considering the existence of very few  $Al_9Co_2$  phases, it is assumed that there is no  $Al_9Co_2$  phase formed in the solidification process of Al-Co-Ce alloys. Therefore, all Co in the liquid phase first forms into the  $Al_8Co_2Ce$  phase, then all Ce forms into the  $Al_{11}Ce_3$  phase and finally the pure Al phase solidifies after the depletion of Co and Ce. Taking alloy 2 ( $Al_{87.4}Co_{7.9}Ce_{4.7}$ ) for example, the solidification process is described as follows:



Based on the calculations above, the atomic percentage of Al in the three solidified phases is 53.05%, 31.6% and 2.75% for Al,  $Al_8Co_2Ce$  and  $Al_{11}Ce_3$ , respectively. The crystal structures (Al atom number in each cell and cell volume) of the three phases can be obtained from ICSD, shown in **Table 5-5**. Phase volume ratio of the three phases in the entire solidified alloy can be obtained as follows:

$$\frac{P_{at}(Al)}{N_{at}(Al)} V_{ce}(Al) : \frac{P_{at}(Al_8Co_2Ce)}{N_{at}(Al_8Co_2Ce)} V_{ce}(Al_8Co_2Ce) : \frac{P_{at}(Al_{11}Ce_3)}{N_{at}(Al_{11}Ce_3)} V_{ce}(Al_{11}Ce_3)$$

where  $P_{at}$ ,  $N_{at}$  and  $V_{ce}$  are atomic percentage of Al element in different phases, the number of Al atoms in each crystal cell and the volume of the crystal cell, respectively. Therefore, the phase volume percentage ratio is 52.6%(Al):43.1%( $Al_8Co_2Ce$ ):4.3%( $Al_{11}Ce_3$ ).

Similarly, the phase volume percentage in alloys 1 and 3 were also calculated and shown in **Table 5-6**. It should be noted that in this estimation Co in the alloys was totally considered to form  $Al_8Co_2Ce$  phase rather than both  $Al_8Co_2Ce$  and  $Al_9Co_2$  phase. Therefore, the phase fraction of  $Al_8Co_2Ce$  will be overestimated.

**Table 5-5 Crystal structure parameters of the three phases.**

phase	Crystal structure parameters	
	Number of Al Atoms in each cell, $N_{at}$	Cell volume, $V_{ce}$ ( $\text{\AA}^3$ )
Al	4	66.407
$Al_8Co_2Ce$	32	730.558
Primary $Al_{11}Ce_3$	22	577.715

**Table 5-6** summarises the microstructure present in the three cast alloys and the phase fractions from both image analysis ( $x=50$  mm) and calculations above. Generally, the calculated phase fractions of the three different phases are close to the experimental results, which exhibited the similar relation to the corresponding alloy composition. It can be seen that alloy 1 with the lowest Co content had the lowest phase fraction of  $Al_8Co_2Ce$  phase. For alloy 2 which has the lowest Ce content among the three alloys, it exhibited the lowest  $Al_{11}Ce_3$  phase fraction. In the case of alloy 3 which had the lowest Al content, it exhibited the lowest phase fraction of the Al phase.

Based on the comparison of the phase fraction from both image analysis (**Figure 5-6**) and calculations (**Table 5-6**), it can be proposed that the solidification ( $x=50$  mm) in the wedge mould casting present in this work was very close to the equilibrium solidification process. Therefore, the whole solidification paths can be defined as  $L_0 \rightarrow Al_8Co_2Ce + L_1 \rightarrow Al_8Co_2Ce + \text{primary } Al_{11}Ce_3 + L_2 \rightarrow Al_8Co_2Ce + \text{primary } Al_{11}Ce_3 + \text{eutectic } Al_{11}Ce_3/Al + Al_9Co_2$ , which is consistent with the equilibrium solidification reported by Gao et al. [66], as shown in **Figure 5-14**.

However, for alloys in other positions of the wedge cast, the phase fractions of different phases were far from the calculated one (**Figure 5-6**), which suggests a non-equilibrium solidification at these positions.

**Table 5-6 Summary of the phases present and phase fractions in the three alloys.**

Alloy		Alloy 1	Alloy 2	Alloy 3		
Composition (at.%)		Al <sub>88.0</sub> Co <sub>6.0</sub> Ce <sub>6.0</sub>	Al <sub>87.4</sub> Co <sub>7.9</sub> Ce <sub>4.7</sub>	Al <sub>86.0</sub> Co <sub>7.6</sub> Ce <sub>6.4</sub>		
Phases present at different locations	tip	<ul style="list-style-type: none"> <li>• Eutectic</li> <li>• Al<sub>8</sub>Co<sub>2</sub>Ce</li> <li>• Primary Al<sub>11</sub>Ce<sub>3</sub></li> </ul>	<ul style="list-style-type: none"> <li>• Eutectic</li> <li>• Al<sub>8</sub>Co<sub>2</sub>Ce</li> </ul>	<ul style="list-style-type: none"> <li>• Eutectic</li> <li>• Al<sub>8</sub>Co<sub>2</sub>Ce</li> <li>• Primary Al<sub>11</sub>Ce<sub>3</sub></li> </ul>		
	x=5 mm				<ul style="list-style-type: none"> <li>• Eutectic</li> <li>• Al<sub>8</sub>Co<sub>2</sub>Ce</li> <li>• Primary Al<sub>11</sub>Ce<sub>3</sub></li> </ul>	<ul style="list-style-type: none"> <li>• Eutectic</li> <li>• Al<sub>8</sub>Co<sub>2</sub>Ce</li> <li>• Primary Al<sub>11</sub>Ce<sub>3</sub></li> </ul>
	x=10 mm					
	x=15 mm		<ul style="list-style-type: none"> <li>• Eutectic</li> <li>• Al<sub>8</sub>Co<sub>2</sub>Ce</li> <li>• Primary Al<sub>11</sub>Ce<sub>3</sub></li> </ul>	<ul style="list-style-type: none"> <li>• Eutectic</li> <li>• Al<sub>8</sub>Co<sub>2</sub>Ce</li> <li>• Primary Al<sub>11</sub>Ce<sub>3</sub></li> </ul>	<ul style="list-style-type: none"> <li>• Eutectic</li> <li>• Al<sub>8</sub>Co<sub>2</sub>Ce</li> <li>• Primary Al<sub>11</sub>Ce<sub>3</sub></li> <li>• Al<sub>9</sub>Co<sub>2</sub></li> <li>• Al-rich AlCoCe</li> </ul>	
	x=20 mm					
	x=50 mm					
Image analysed phase fraction x=50 mm (%)	Al-rich	48.9	59.7	53.7		
	Al <sub>8</sub> Co <sub>2</sub> Ce	30.6	39.5	23.5		
	Al <sub>11</sub> Ce <sub>3</sub>	20.5	0.8	13.8		
Calculated phase fraction in volume (%)	Al	51.3	52.6	44.8		
	Al <sub>8</sub> Co <sub>2</sub> Ce	31.9	43.1	40.6		
	Al <sub>11</sub> Ce <sub>3</sub>	16.8	4.3	14.6		

#### 5.4.1.2 Effect of the solidification rate on the alloy microstructure

Due to the special geometry of the wedge mould, the microstructure of the alloy varied with location, i.e. solidification rate. The solidification rate of Al-Cu eutectic alloy in the same wedge mould has been calculated in **Chapter 4** based on the well know  $v\lambda^2 = K_0$  equation. The influence of solidification rate on the microstructure of Al-Co-Ce alloy can be described as below.

Firstly, the primary  $\text{Al}_{11}\text{Ce}_3$  phase rarely or did not appear when the solidification rate was very high, i.e. when  $x$  was small. This phenomenon was clearly seen in alloys 2 and 3 (**Figure 5-3**). According to the phase diagram of Al-5Co-Ce shown in **Figure 5-14a**, the disappearance of the primary  $\text{Al}_{11}\text{Ce}_3$  phase indicates that the phase transition that occurred in the alloy was only  $L_0 \rightarrow \text{Al}_8\text{Co}_2\text{Ce} + L_1$ . There was not any low-temperature phase transition generated. With decreasing solidification rate, i.e. increasing distance from the tip of the wedge cast, there was a greater and greater extent of  $\text{Al}_{11}\text{Ce}_3$  phases in the alloy. The appearance of the  $\text{Al}_{11}\text{Ce}_3$  phase suggests the occurrence of low-temperature phase transition reaction.

Secondly, the solidification rate also influenced the size of both the  $\text{Al}_8\text{Co}_2\text{Ce}$  phase and the primary  $\text{Al}_{11}\text{Ce}_3$  phase. **Figure 5-1**, **Figure 5-2** and **Figure 5-3** show that the size of the above phases increased with the decrease of solidification rate. This is attributed to the well-known effect that the lower solidification rate is beneficial to the grains growth of crystalline phases, while high solidification rates can restrain the growth of grains.

Thirdly, the overall composition of the dark region i.e. the Al/ $\text{Al}_{11}\text{Ce}_3$  eutectic also varied with location in the wedge mould (**Figure 5-4** and **Table 5-1**). At the tip of the wedge cast, the dark region usually had a higher concentration of alloying elements. However, with increasing distance from the tip, the dark region showed a decreased alloying element concentration. This decrease in the concentration of Ce and Co is also due to the enhanced nucleation and growth of the primary  $\text{Al}_{11}\text{Ce}_3$  phase in the solidification with a low solidification rate.

Finally, based on the characterisation of metal flakes found in the split of the wedge mould, the Al-Co-Ce alloys in this work exhibited greatly enhanced compositional homogeneity (**Figure 5-8**). This indicates the possible formation of the single-phase solid solution or amorphous phase due to the suppression of crystallisation by the high solidification rate. The melt in the split of the wedge mould had an extremely small thickness. In addition, the heat extraction in the split conducted in two directions. Therefore, the cooling condition of these thin flakes in the split is beneficial to obtain a high solidification rate, which consequently generated the single phase or amorphous phase.

#### **5.4.1.3 Effect of the alloy composition on the alloy microstructure**

The composition of the alloy is an important factor to determine the microstructure of the cast alloys. The experimental and calculation investigation on the phase fraction has shown that the fraction of different phases at the corresponding same position of the wedge cast was strongly dependent on the overall composition of the cast alloy. In particular, alloy 3 showed the strongest microstructural sensitivity to the solidification rate (**Figure 5-1**, **Figure 5-2**, **Figure 5-3** and **Figure 5-6**).

The observed microstructures were consistent with the phase diagram. Based on the phase diagram of the Al-Co-Ce alloy (**Figure 5-14b**) and lever rules, with increasing cobalt content in the alloy, the fraction of the  $\text{Al}_8\text{Co}_2\text{Ce}$  phase (i.e.  $\tau_1$  phase in the phase diagram) will be increased. Therefore, alloy 2 which has the lowest content of Co showed the largest phase fraction of the  $\text{Al}_8\text{Co}_2\text{Ce}$  compared to the other two alloys (**Figure 5-6**), especially at the position of  $x=50$  mm in the wedge mould. In addition, based on **Figure 5-14a**, the low content of Ce also results in a small fraction of phase primary  $\text{Al}_{11}\text{Ce}_3$ . Therefore, alloy 2 showed

very few primary  $\text{Al}_{11}\text{Ce}_3$  regions even when the solidification rate has been decreased when  $x=50$  mm (**Figure 5-1** and **Figure 5-6**).

### 5.4.2 Laser surface melting

In this work, laser surface melting treatment greatly refined the microstructure of the as-cast Al-Co-Ce alloy due to the rapid solidification rate. Laser treatment melts a thin layer of material; this then rapidly cools and solidifies as heat is conducted away by the unremelted underlying material, generating a refined microstructure. The microstructural refinement of the as-cast material was mainly shown by the decrease of particle size and particle spacing of the  $\text{Al}_8\text{Co}_2\text{Ce}$  phase. The fractions of phases present have also been altered by the laser treatment due to the high solidification rate which led to the non-equilibrium microstructures. The rapid solidification also changed the overall composition of the Al-rich eutectic region by increasing the concentration of Ce in the Al-rich region (**Table 5-4**), and eliminated the  $\text{Al}_9\text{Co}_2$  phase (**Figure 5-11**).

The effect of treatment parameters on the microstructure of Al-Co-Ce alloy was also investigated. Results show that the higher sample traverse speed increased the solidification rate of the treated alloy, which is consistent with that seen in the solidification of the laser treated Al-Cu eutectic alloy (**Chapter 4**). The effect of sample traverse speed on the solidification rate has been discussed in **Section 4.4.1.2**. In addition, the microstructure of the Al-Co-Ce alloy was further refined when the sample was closer to the laser focus (MT6000-5) compared with that of sample MT6000-20. This is due to the decrease of laser spot size. When the distance between the sample and the laser focus decreased from 20 to 5 mm, the

laser spot size decreased from 3.1 to 1.5 mm (**Table 3-4**). The small spot size resulted in an increase of power density and thermal gradient in the laser treated sample, which thereby increased the cooling rate of the remelted surface.

## 5.5 Summary

- Three crystalline Al-Co-Ce alloys with different compositions were prepared by wedge mould casting. The microstructures under different solidification rates were characterised through SEM, XRD, EDS and image analysis.
- As-cast alloys were consisted of the Al/Al<sub>11</sub>Ce<sub>3</sub> eutectic, the Al<sub>8</sub>Co<sub>2</sub>Ce phase and the primary Al<sub>11</sub>Ce<sub>3</sub> phase. The phase constituent and phase size were dependent on the solidification rate and alloy composition.
- The characterisation of metal flakes found in the split of the wedge mould suggests the possible formation of homogeneous solid solution or amorphous phase in the Al-Co-Ce alloy used in this work.
- Laser treatment parameters such as sample traverse speed and focus distance influenced laser track dimensions and microstructure.
- Laser surface melting greatly refined the microstructure of the as-cast Al-Co-Ce alloy. Al<sub>9</sub>Co<sub>2</sub> and primary Al<sub>11</sub>Ce<sub>3</sub> phases were almost eliminated, and the size of Al<sub>8</sub>Co<sub>2</sub>Ce phase was greatly reduced.
- Laser surface melting also slightly changed the overall composition of the Al/Al<sub>11</sub>Ce<sub>3</sub> eutectic region by increasing the concentration of Ce.

## Chapter 6 LAEB treatment of Al-Co-Ce alloys

### 6.1 Introduction

In **Chapter 5**, the microstructure of the Al-Co-Ce alloy produced by wedge mould casting and laser surface melting has been investigated. Results showed that the above two processes are not capable of providing a high enough cooling rate to transform crystalline Al-Co-Ce alloy to the amorphous state. However, under these processes, the microstructure of Al-Co-Ce alloy varied with cooling rate. In particular, the metal flakes in the split of wedge mould were found to be comprised of crystals in the uniform matrix which is expected to be in the amorphous state.

In addition, in **Chapter 4**, the cooling rate calculation of Al-Cu alloy in large area electron beam irradiation treatment showed that the cooling rate of Al-Cu can reach up to  $10^7$  K/s. Therefore, large area electron beam (LAEB) surface melting is expected to be capable of generating the amorphous layer in this Al-based glass forming ability.

In this chapter, the fabrication of amorphous layer in Al-Co-Ce alloy through LAEB will be investigated, as well as the effects of treatment parameters (cathode voltage, number of LAEB pulses) and initial microstructure. Microstructural characterisation of all treated alloys is included. Laser pretreatment mentioned in this chapter is referred to the overlapped multi-track laser surface melting treated on Al-Co-Ce alloy 3. L1, L2 and L3 pretreatment indicates the laser treatment of MT1000-20, MT6000-20 and MT6000-5, respectively, as presented in **Section 5.3**.

## **6.2 Effect of LAEB treatment parameters**

### **6.2.1 Effect of number of pulses**

#### **6.2.1.1 Surface morphology**

**Figure 6-1** shows the surface changes of one of Al-Co-Ce alloys, alloy 3, as a function of the number of LAEB pulses using 35 kV cathode voltage. Overall, with increasing number of pulses, the heterogeneity of as-cast materials was greatly reduced. For the sample treated with 1 pulse of LAEB irradiation, the as-cast material showed almost no change, with the three main crystalline phases retaining their original shapes, and phase boundaries remained defined. However, with increasing numbers of pulses, the crystalline phases experienced obvious melting and inter-phase diffusion.

After 8 pulses of irradiation, it was difficult to distinguish different phases, as mixing due to diffusion had occurred. In addition, there was an obvious decrease of the area of the dark eutectic region in the treated sample. When the material was treated with 25 pulses of LAEB irradiation, a relatively homogenous compositional distribution can be observed on the sample surface, as indicated by the uniformity of contrast in back-scattered imaging. Distinct phase boundaries were not observed in the treated layer.

For the sample subjected to further LAEB irradiation (100 or 150 pulses), a highly homogenised surface was seen. Also, the phase distinction in the original as-cast material was almost completely eliminated.

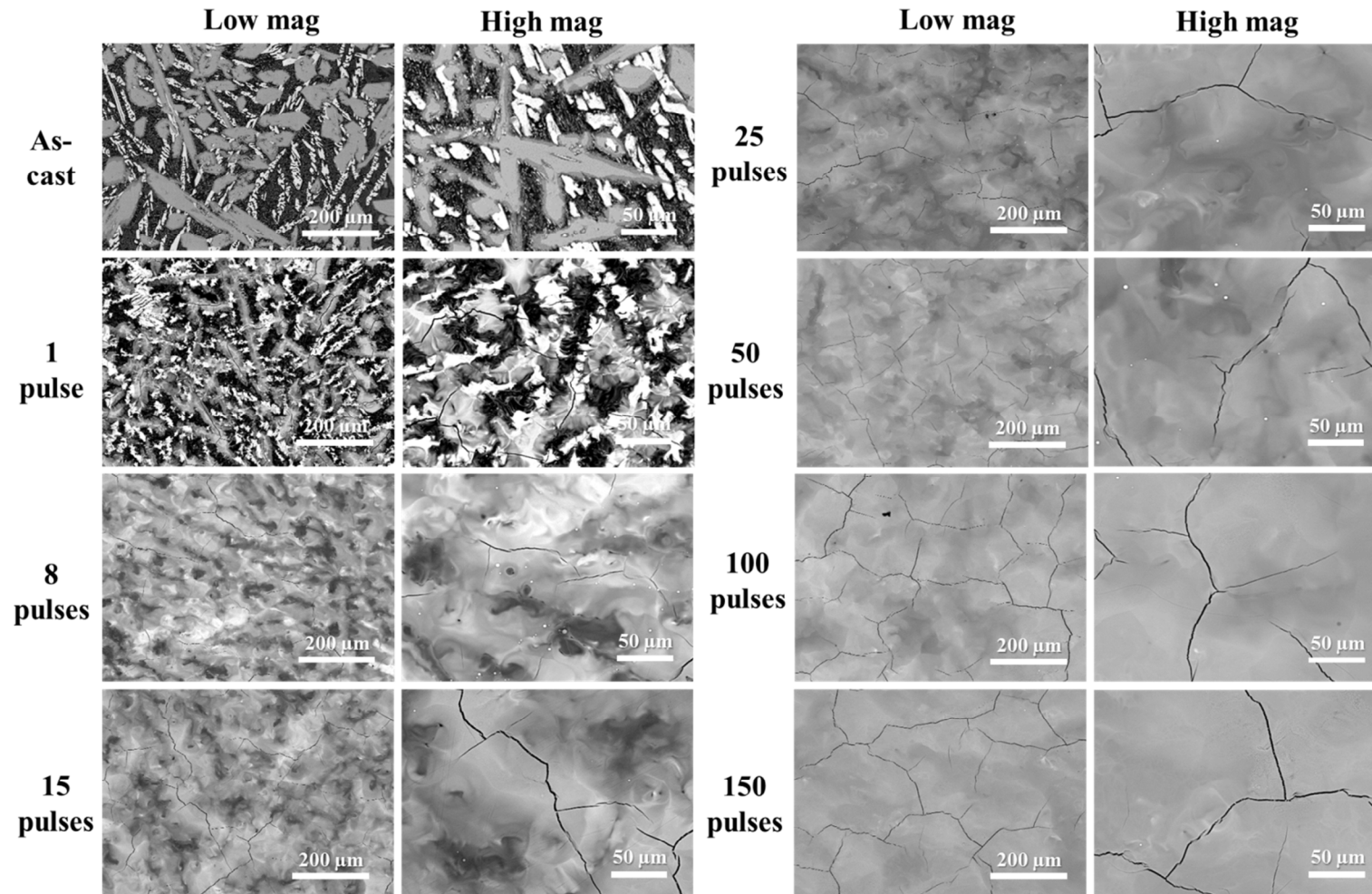
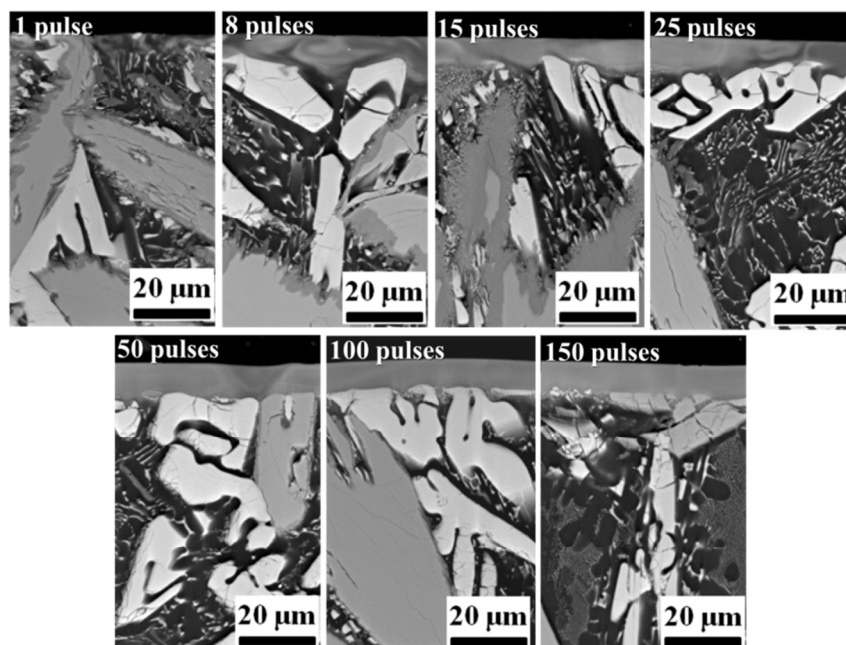


Figure 6-1 BSE images showing the surface morphology of the LAEB treated Al-Co-Ce alloy 3 (35 kV, different number of pulses).

### 6.2.1.2 Cross sectional morphology

Cross-sections of samples irradiated at 35 kV and varying numbers of pulses are shown in **Figure 6-2**. The corresponding thicknesses of treated layers are also plotted (**Figure 6-3**). When the sample surface was subjected to 1 pulse of irradiation, some remelting but little diffusion occurred. Also, the remelted layer was relatively thin (2.8  $\mu\text{m}$ ). However, with an increase of numbers of pulses to 8, the treated layer thickness had a notable increase. An increase of  $\sim 3 \mu\text{m}$  can be seen from the plot of thicknesses. In addition, the remelting and homogenisation of the treated layer due to diffusion were more noticeable. When the sample was subjected to 100 pulses of irradiation, the treated layer exhibited a straight interface with the underlying substrate. The treated layer itself also became more homogeneous in composition. Compared to the rapid increase of the treated layer thickness for the 8 pulses treated sample, further pulses had a reduced effect in increasing the thickness of the remelted layer.



**Figure 6-2** BSE images showing cross sectional morphologies of the LAEB treated Al-Co-Ce alloy 3 (35 kV and increasing number of pulses).

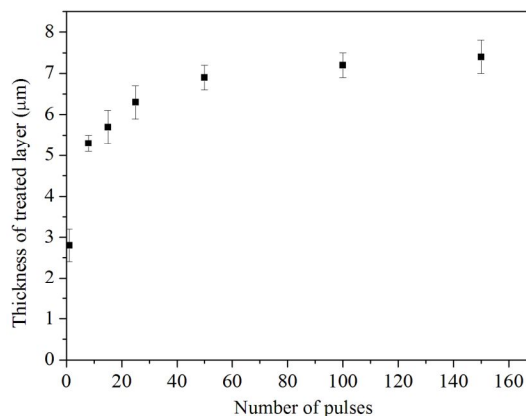


**Figure 6-3 Thickness of the LAEB remelted layer in the Al-Co-Ce alloy 3 versus number of pulses (35 kV cathode voltage)**

### 6.2.1.3 Cracking

It should be noted that cracking of varying severity was observed on all treated samples. It was also observed that the cracks preferentially formed at the locations of the grey  $\text{Al}_8\text{Co}_2\text{Ce}$  phase in the sub-surface. This was seen on the surfaces of samples which are not completely homogenised i.e. 1, 8 and 15 pulse treated sample (**Figure 6-1**). For homogenous, transformed surfaces, cross-sectional examination again shows that the cracking was correlated with the location of large underlying  $\text{Al}_8\text{Co}_2\text{Ce}$  precipitates (**Figure 6-4**). It is seen that the crack propagated in the large  $\text{Al}_8\text{Co}_2\text{Ce}$  phase under the treated layer. The crack depth was approximately 90  $\mu\text{m}$ .

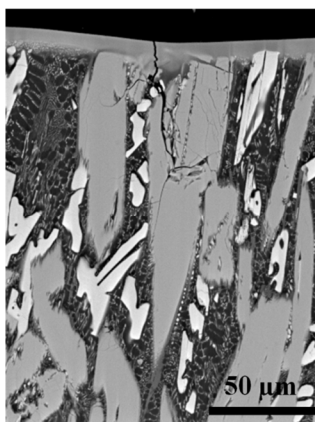


**Figure 6-4 Cracking correlated with the location of underlying  $\text{Al}_8\text{Co}_2\text{Ce}$  precipitates in the LAEB treated Al-Co-Ce alloy 3 (35 kV, 150 pulses).**

Observation of cracks formed on samples treated with 35 kV cathode voltage and increasing numbers of pulses was used to characterise the extent of surface cracking by the measurement and calculation of crack length per unit area (crack density). **Figure 6-5** shows the relationship between crack density and number of pulses. Overall, crack density shows no apparent change with increasing number of pulses. Despite this, from the surface morphologies shown in **Figure 6-1**, it can be seen that the length of individual cracks increased, and after treatment with 35 kV and 150 pulses, cracks were observed to have joined together and formed a continuous network.

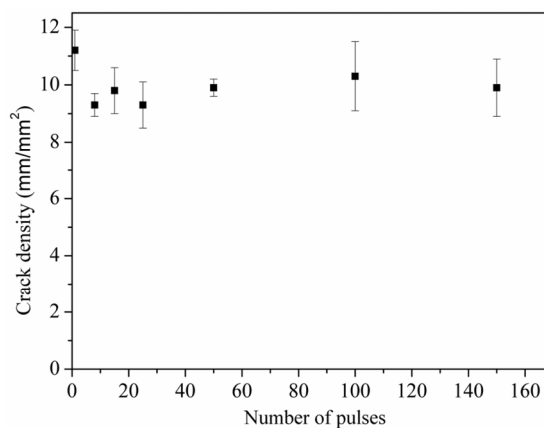


**Figure 6-5 Crack density of the LAEB treated Al-Co-Ce alloy 3 with different number of pulses under 35 kV cathode voltage.**

#### 6.2.1.4 Phase transformation

**Figure 6-6** shows GAXRD patterns of LAEB treated samples which were irradiated with 35 kV and increasing numbers of pulses. Compared with the XRD result of the as-cast material, the crystalline peak intensity in the electron beam treated samples was significantly decreased, particularly in samples treated with 35 kV and 8 or more pulses of LAEB irradiation. With increasing number of pulses, an obvious amorphous hump began to appear located at  $38^\circ$  ( $2\theta$ ) in the spectra of all treated samples. The disappearance of most of the crystalline peaks

was also observed, which indicates significant amorphous phase formation in the treated layer. However, several crystalline peaks with low intensities were still present in the spectra of the treated samples. It is also seen that there was an obvious increase in the intensity of crystalline peaks when the material was treated with 100 pulses of LAEB irradiation compared to 50, 25 and 15 pulses. Particularly when the material was treated with 35 kV and 150 pulses, crystalline phase peak intensity exceeded that of the samples treated with 35 kV, 8 and 15 pulses.

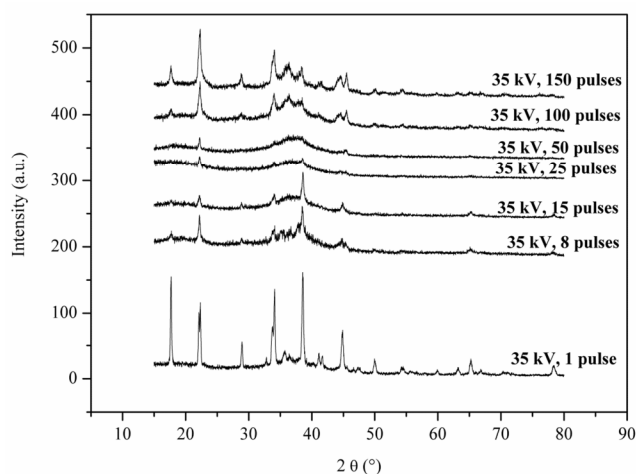


**Figure 6-6 GAXRD patterns of the LAEB treated Al-Co-Ce alloy 3 (35 kV and increasing number of pulses).**

In addition to the reappearance of crystalline peaks in GAXRD spectra, the crystallisation was also seen in some local regions of the treated layer when the sample was treated with 100 or more pulses of LAEB irradiation. **Figure 6-7** shows the crystallisation in a local area of the treated layer for the sample treated with 35 kV and 150 pulses. It is seen that in some regions the treated layer did not exhibit a uniform composition (**Figure 6-7a**). There were a few columnar crystals with the length of 1~2  $\mu\text{m}$  in region 1 (**Figure 6-7b**). In addition, a large number of nearly spherical crystallised particles were also found in region 2 (**Figure 6-7c**), the diameter of these crystals is approximately 500 nm. In this figure, both region

1 and region 2 were seen to be close to the crack. However, no correlation can be confirmed between crack and crystallisation since the crystallisation also occurred in region 3 which was far away from the crack.

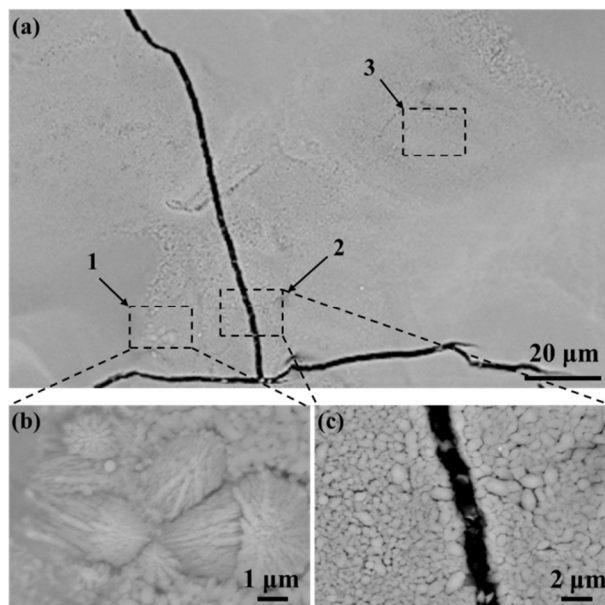


**Figure 6-7 BSE images showing localised crystallisation in the LAEB treated layer for Al-Co-Ce alloy 3 (35 kV and 150 pulses). Regions 1, 2 and 3 highlight three regions in which crystallisation occurred.**

## 6.2.2 Effect of cathode voltage

### 6.2.2.1 Surface morphology

**Figure 6-8** shows the surface morphology of the 100 pulses of LAEB treated Al-Co-Ce alloy 3 under different cathode voltages (15, 22, 29, 35 and 40 kV). It can be seen that the heterogeneity of the sample surface had an apparent decrease with increasing cathode voltage. In the back scattered SEM images, phase boundaries became gradually less distinct and finally disappeared. In other words, diffusion has occurred among different crystalline phases shown in the as-cast material. Especially, when the sample was irradiated under 40 kV cathode voltage, the sample surface exhibited a greatly improved compositional distribution with the greatest uniformity of phase contrast.

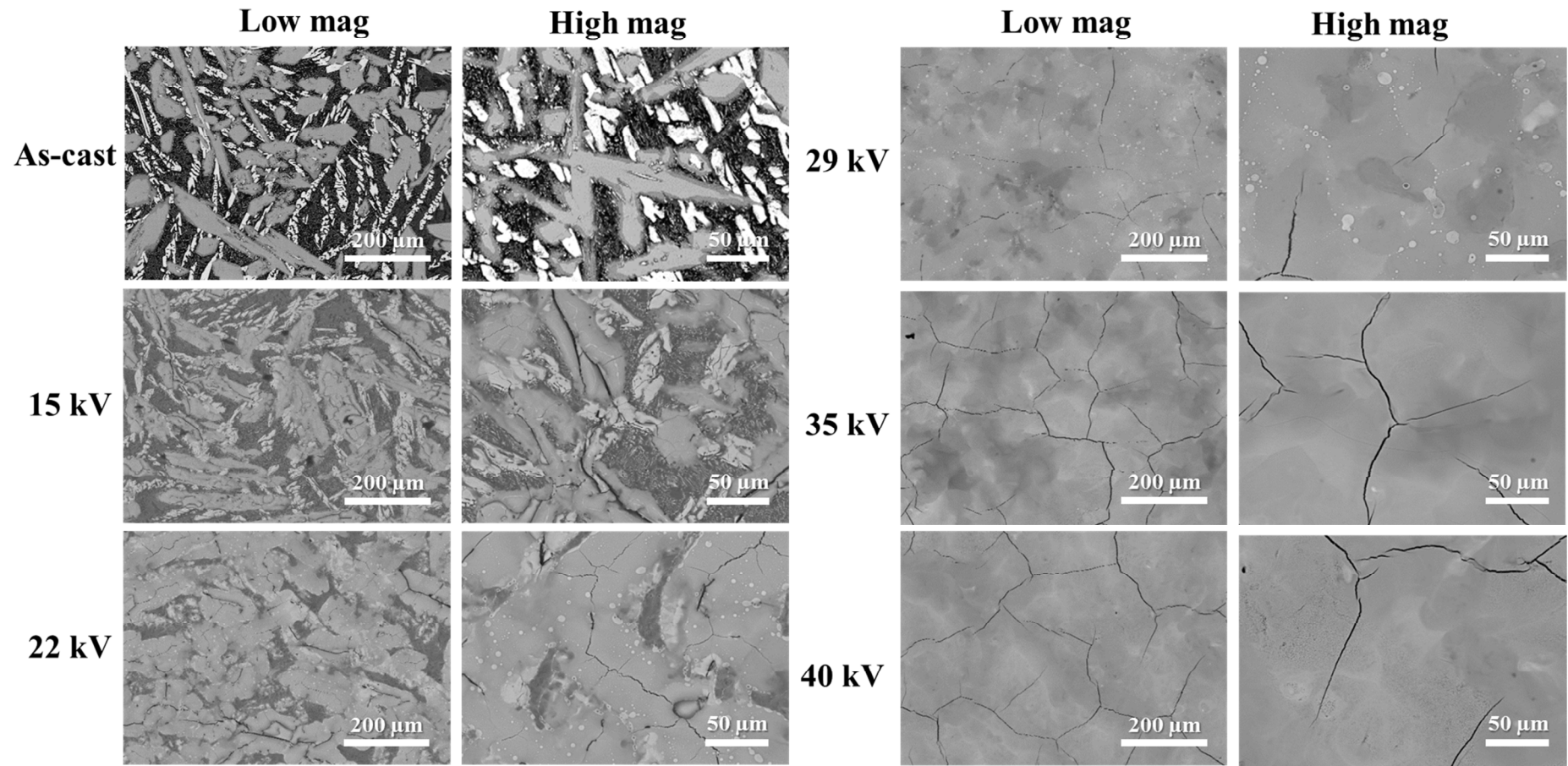


**Figure 6-8 BSE images showing the surface morphology of the LAEB treated Al-Co-Ce alloy 3 (100 pulses at different cathode voltages).**

### 6.2.2.2 Cross sectional morphology

**Figure 6-9** shows the cross sectional morphologies and the remelted layer thickness of LAEB treated samples (100 pulses and varying cathode voltages). Overall, the extent of homogenisation and the remelted layer thickness increased with increasing cathode voltage. For the 15 kV treated sample, a discontinuous remelted layer with a thickness of  $\sim 1.2 \mu\text{m}$  formed on the sample surface. When the sample was treated at 22 kV, obvious remelting and diffusion was found on all three main phases, a relatively uniform remelted layer was also seen. For the 29 kV treated sample, a  $\sim 3.5 \mu\text{m}$  treated layer with a uniform composition was found. With a further increase of cathode voltage to 40 kV, the homogenisation of the remelted layer was enhanced, and the thickness increased up to  $\sim 9 \mu\text{m}$ .

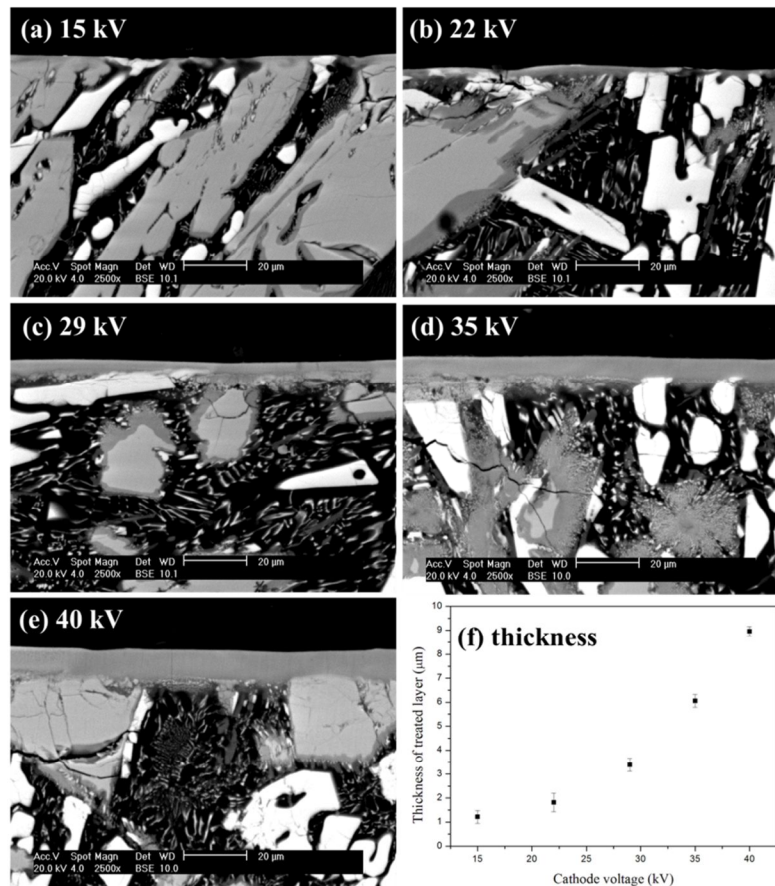


**Figure 6-9** BSE images of cross sections of the LAEB treated Al-Co-Ce alloy 3 and remelted layer thickness (100 pulses and varying cathode voltages).

### 6.2.2.3 Cracking

Cracking was found to occur on all treated samples. When the sample was treated under 15 and 22 kV cathode voltage, cracks were found to be located at large grey  $\text{Al}_8\text{Co}_2\text{Ce}$  phases (**Figure 6-8**). With increasing cathode voltage, this relation became not as clear as that seen in 15 and 22 kV treated samples. For 29 and 35 kV samples, the cracks were found to form a network and evenly distribute on the whole surface. However, the 29 kV treated sample showed the smallest extent of cracking.

**Figure 6-10** shows the crack density of 100 pulses treated samples under different cathode voltages. 15 kV and 22 kV treated samples had a higher crack density (above  $10 \text{ mm/mm}^2$ ). It should be noted that the treated layer in 15 and 22 kV samples were incomplete; cracks mostly occurred in slightly remelted  $\text{Al}_8\text{Co}_2\text{Ce}$  phase particles (**Figure 6-8**). The crack density of the 29 kV treated sample had an apparent decrease and reached the minimum ( $\sim 4.5 \text{ mm/mm}^2$ ). However, for the 35 and 40 kV treated samples, crack density increased again, although the compositional homogeneity had an apparent improvement.

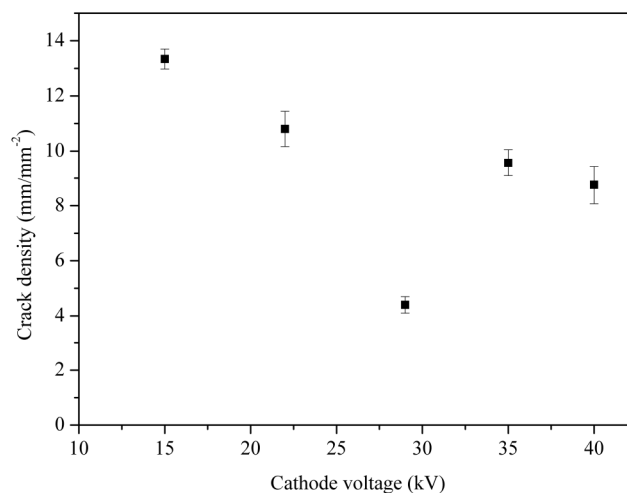


**Figure 6-10 Crack density of the LAEB treated Al-Co-Ce alloy 3 with different cathode voltages (100 pulses).**

#### 6.2.2.4 Phase transformation

**Figure 6-11** shows the glancing angle XRD results of 150 pulses treated samples under different cathode voltages. It can be seen that the number of the crystalline phase peaks in the LAEB treated samples decreased compared to that seen in the as-cast material. In particular, for the 29 kV treated sample, there was an apparent hump located at  $38^\circ$  ( $2\theta$ ). Crystalline phase peaks were also greatly reduced both in number and intensity. However, when samples were treated under 35 kV and 40 kV, the crystalline phase peaks reappeared and increased again.

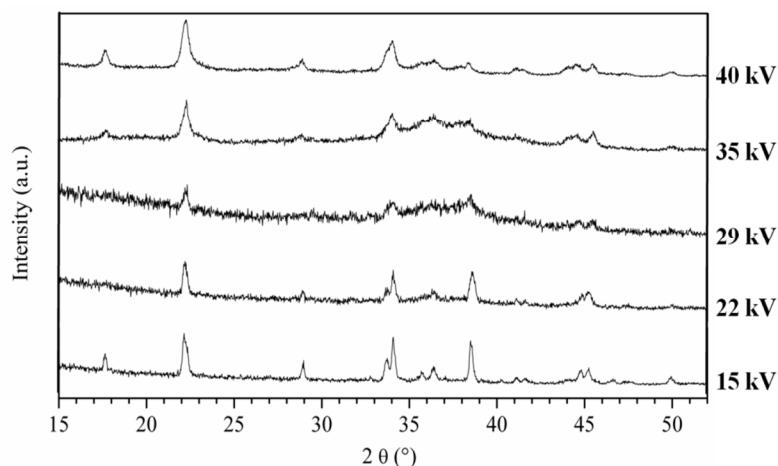


**Figure 6-11** Glancing angle XRD of the LAEB treated Al-Co-Ce alloy 3 (100 pulses and different cathode voltages).

Localised crystallisation was also found in the treated layers for the 100 pulses of LAEB treated sample under 35 kV and 40 kV cathode voltage. Taking the 40 kV treated sample for example, the localised crystallisation in the treated layer is shown in **Figure 6-12**. From **Figure 6-12a**, it can be seen that the crystals had a diameter of less than  $1\ \mu\text{m}$ . It is also seen that the crystal size had an obvious decrease at the location close to transition region between the crystalline region and the amorphous region (**Figure 6-12b**). This is consistent with the observation shown in **Figure 6-7**.

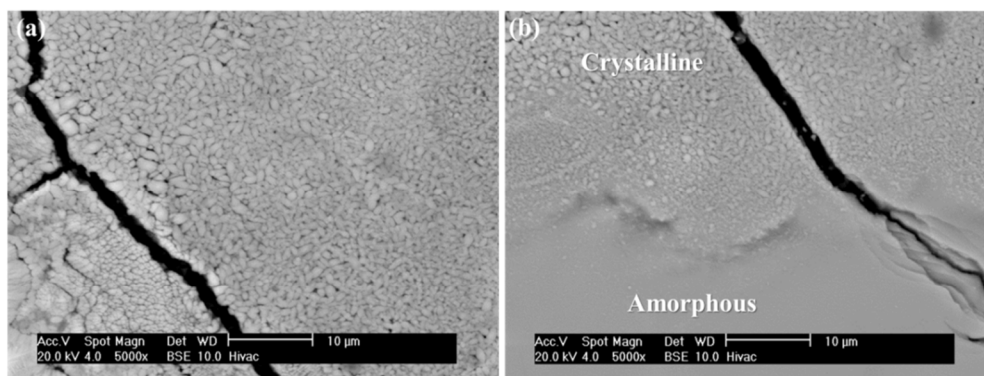


**Figure 6-12 Localised crystallisation in the LAEB treated layer in Al-Co-Ce alloy 3 (40 kV cathode voltage and 100 pulses).**

### 6.3 Effect of as-cast alloy original microstructures

#### 6.3.1 Microstructure characterisation

**Figure 6-13** shows the microstructures of the three as-cast Al-Co-Ce alloys before and after LAEB treatment under the same treatment parameters (35 kV cathode voltage and 8 pulses). Detailed characterisation of as-cast materials has been presented in **Chapter 5**. It can be seen that the three alloys subjected to the same LAEB treatment exhibited different morphologies. Alloy 1 with the smallest size of crystalline phases showed the highly improved homogeneity after LAEB treatment compared to the as-cast sample. In addition, the bright  $\text{Al}_{11}\text{Ce}_3$  phase has also shown a decrease in both quantity and size. For alloy 2, the contrast between grey phase and dark phase was still clear although obvious remelting could be seen. The grey phase still exhibited the original shape. For alloy 3, the sample surface showed an intermediate extent of remelting and homogenisation due to the intermediate size of crystalline phases ( $\text{Al}_{11}\text{Ce}_3$  and  $\text{Al}_8\text{Co}_2\text{Ce}$ ). However, compared to the alloy 1, there were more bright phases, i.e.  $\text{Al}_{11}\text{Ce}_3$  left in LAEB treated alloy 3. Cracking was also found. Alloy 1 exhibited the slightest extent of cracking than alloys 2 and 3.

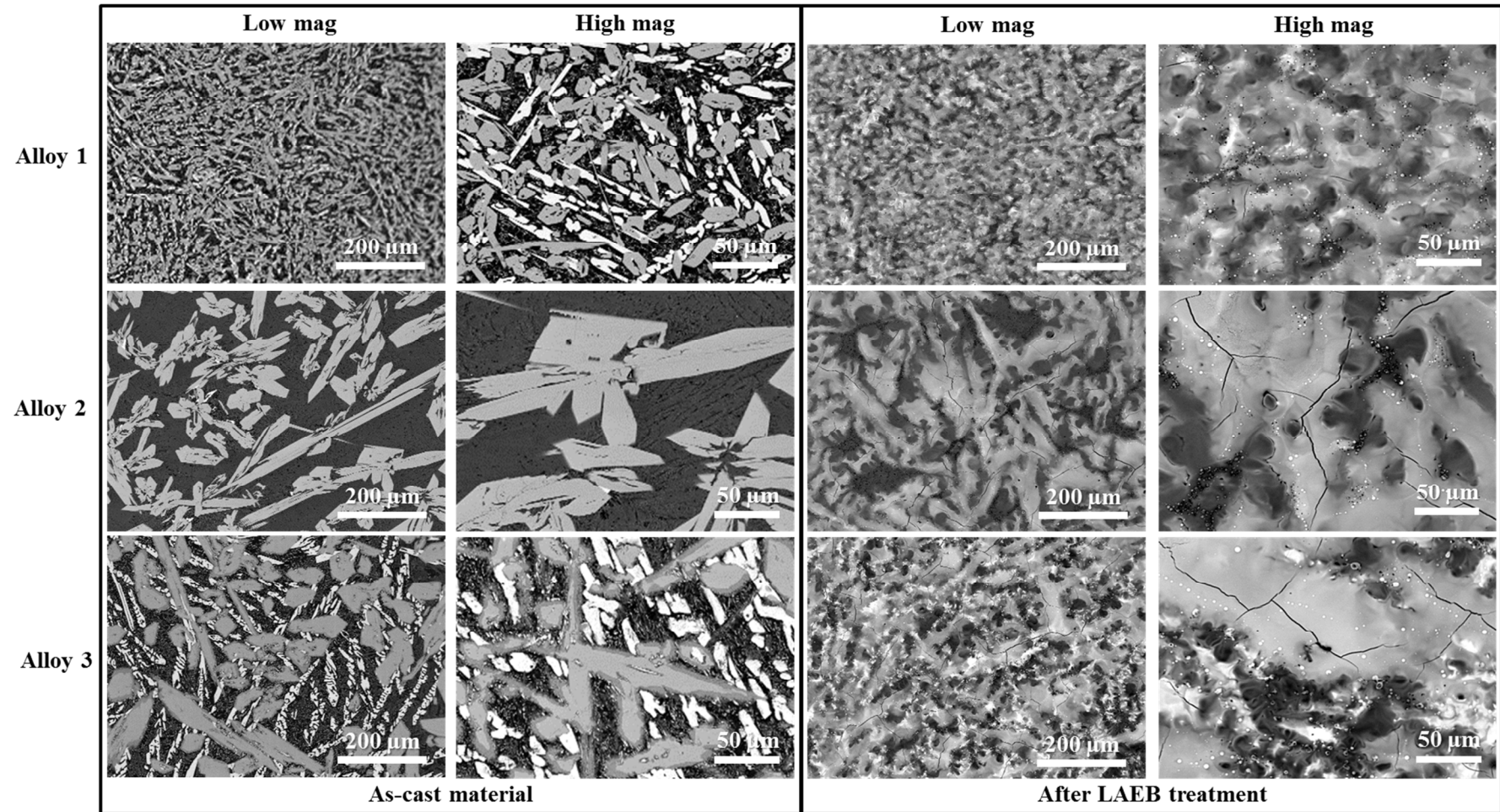
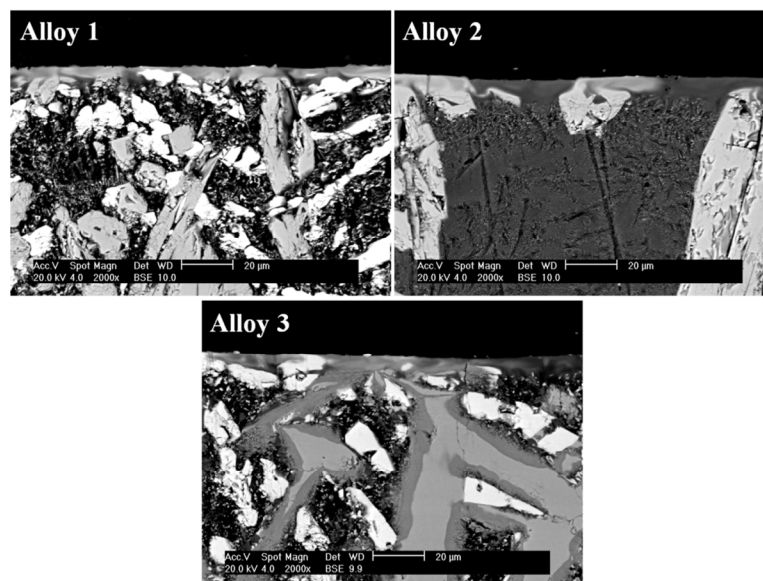


Figure 6-13 BSE surface images of as-cast and LAEB treated Al-Co-Ce alloys with different initial microstructures (35 kV, 8 pulses).

**Figure 6-14** shows the cross sectional morphologies of LAEB treated samples with different initial microstructures (35 kV, 8 pulses). It can be seen that the compositional homogeneity of the treated layer was dependent on the microstructure of the as-cast material. In alloy 1, the treated layer showed a relatively uniform contrast compared with the other two alloys. However, there were still  $\text{Al}_{11}\text{Ce}_3$  and  $\text{Al}_8\text{Co}_2\text{Ce}$  phase particles in the treated layer. These phase particles were not fully melted and diffused into the treated layer. In the case of alloy 2, the treated layer showed an apparent contrast at different phases; the region near the large  $\text{Al}_8\text{Co}_2\text{Ce}$  phase was still bright, while the regions near the eutectic were still dark. For alloy 3, the treated layer exhibited an intermediate extent of remelting and diffusion. Local regions near the eutectic were still very dark although these regions experienced apparent remelting.



**Figure 6-14** BSE images showing cross sections of LAEB treated Al-Co-Ce alloys with different initial microstructures (35 kV, 8 pulses).

### 6.3.2 Glancing angle XRD results

**Figure 6-15** shows the XRD patterns of the three as-cast alloys after the same LAEB irradiation (35 kV, 8 pulses). Generally, there were much fewer crystalline

peaks in all three XRD patterns of LAEB treated samples, compared to that of the as-cast materials. Alloy1 exhibited a more apparent hump located at  $38^\circ$  ( $2\theta$ ) in the XRD pattern than alloy 2 and alloy 3. However, there were still a few peaks of crystalline phases in the XRD pattern.

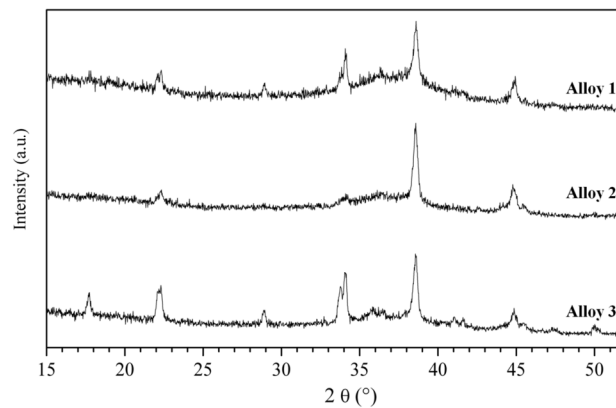


**Figure 6-15** Glancing angle XRD results of three Al-Co-Ce alloys after the same LAEB treatment (35 kV, 8 pulses).

#### **6.4 Effect of laser microstructural refinement**

LAEB treatment has successfully generated the largely amorphous layer on the Al-Co-Ce glass forming alloy under suitable treatment parameters, such as 100 pulses at cathode voltage of 29 kV and 25~50 pulse at 35 kV. However, cracking of the amorphous layers was found to occur at large, pre-existing particles of the  $\text{Al}_8\text{Co}_2\text{Ce}$  phase.

In **Section 6.3**, as-cast alloy 1 with the smallest size of the crystalline phase especially the  $\text{Al}_8\text{Co}_2\text{Ce}$  phase, was found to have the lowest crack density after LAEB treatment, compared with the other two as-cast alloys which have larger phase size. This suggests that the small original phase size has a beneficial effect on the cracking control of the treated layer.

Laser processing is a well-known method of microstructural refinement, which has been applied on many alloys. In **Chapter 5**, the laser surface melting process has been proven an effective method to refine the microstructure of the Al-Co-Ce alloy. Therefore, in this section a prior laser surface treatment was used to investigate whether a refined microstructure could reduce or eliminate the occurrence of cracking in the LAEB treated layers. Detailed characterisation of laser refined microstructures has been included in **Chapter 5**.

In this section, the comparison of the only LAEB treated sample and the LSM-LAEB treated sample will be made in terms of amorphisation extent and crack density. In this section, considering the sensitivity of microstructure to the solidification rate shown in **Figure 5-2**, alloy 3 was chosen as the starting material.

#### **6.4.1 Surface morphology**

**Figure 6-16** shows the surface morphology of LAEB treated samples with different initial microstructures. For the samples without any laser pre-treatment, the LAEB remelted surface layer was still markedly heterogeneous after 8 pulses. With increasing numbers of pulses, this layer gradually became homogeneous.

For the laser pre-treated samples, the remelted layer generally became more uniform in composition with decreasing grain size of the microstructural features of the initial material and increasing number of pulses. The lengthscale over which heterogeneities exist was decreased for the refined microstructures compared to the initial material.

It should be also noted that a large number of round white particles were observed on the surface of all samples after LAEB treatment. Fewer, larger particles were

seen on the LAEB treated as-cast material, whereas a higher number of smaller particles were seen for laser pre-treated materials. Detailed investigation of these particles will be presented in **Section 6.5**.

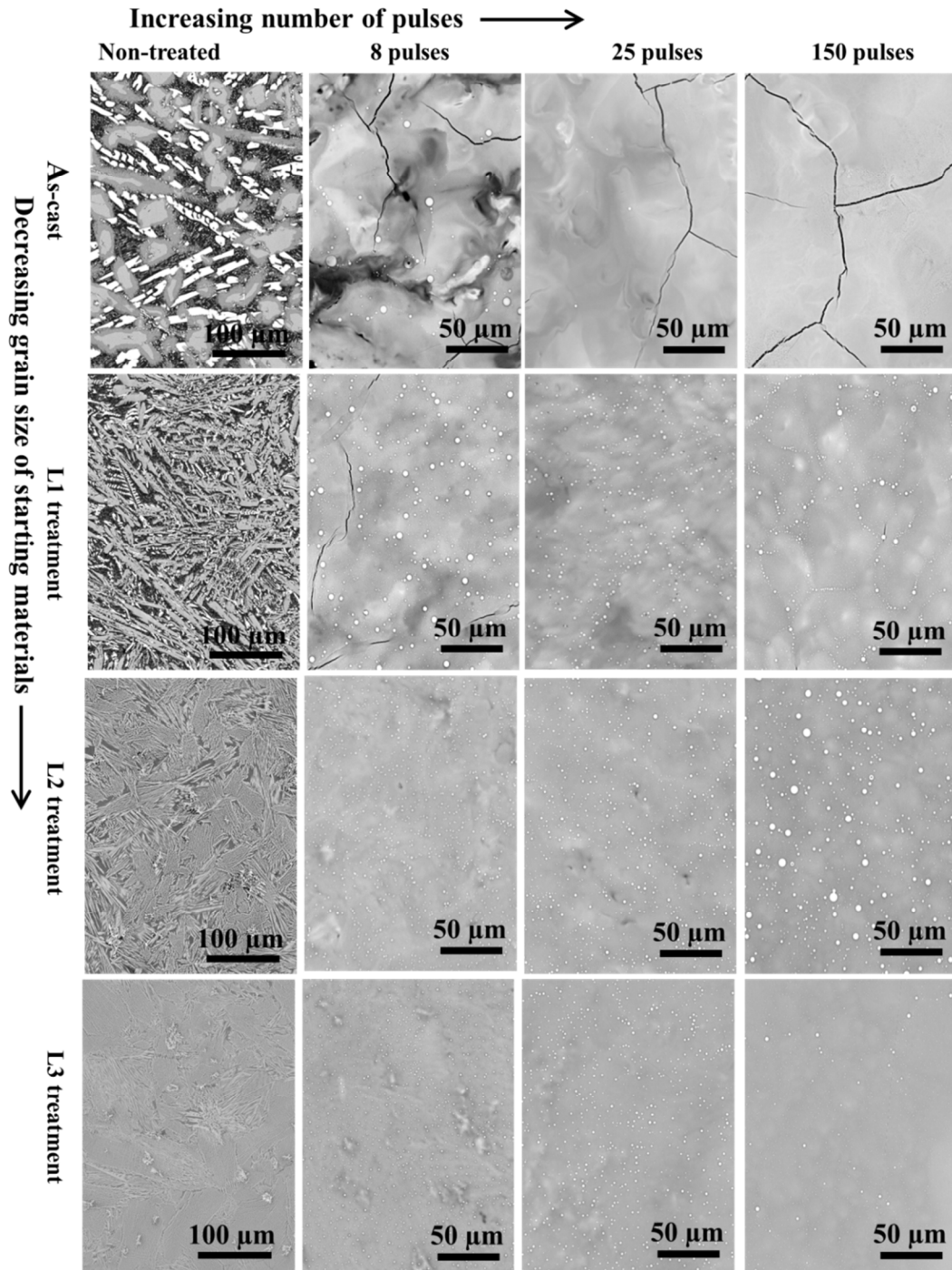


**Figure 6-16** BSE images showing plan views of the LAEB treated Al-Co-Ce alloy 3 with different initial microstructures and numbers of LAEB pulses.

L1, L2 and L3 pretreatment indicates the laser treatment of MT1000-20, MT6000-20 and MT6000-5, respectively, as presented in Section 5.3.

### 6.4.2 Cross sectional morphology

**Figure 6-17** shows the cross sections of LAEB treated samples with the as-cast and laser pre-treated initial microstructure. For any given sample there was some variation in the thickness of the treated layer, this was most apparent for the as-cast samples where the thickness of the treated layer varied with the underlying crystalline phase type.

In the LAEB treated as-cast samples, the treated layer was thinner in regions above  $\text{Al}_{11}\text{Ce}_3$  and  $\text{Al}_8\text{Co}_2\text{Ce}$  phases compared to regions above the eutectic, particularly for the 8 pulse sample. The fluctuation of the thickness of the treated layer had a similar lengthscale to the microstructure of the starting material. There was less variation in the laser refined structures, resulting in a more regular, straighter interface between the treated layer and bulk substrate. The homogeneity of the treated layer was increased by both laser microstructural refinement and increasing the number of LAEB pulses.

This LAEB treated layer varied in thickness between 4 and 7.5  $\mu\text{m}$  as a function of sample type and number of LAEB pulses (**Figure 6-18**). For each sample type, the thickness of the treated layer increased with the number of LAEB pulses. However, it can be seen that the rate of increase in thickness of the treated layer decreased with the number of pulses, increasing the number of pulses from 25 to 150 only increased the thickness of the remelted layer by about 10%. The thickness of the treated layer was greatest for the as-cast material, then L3, L2 and L1 samples.

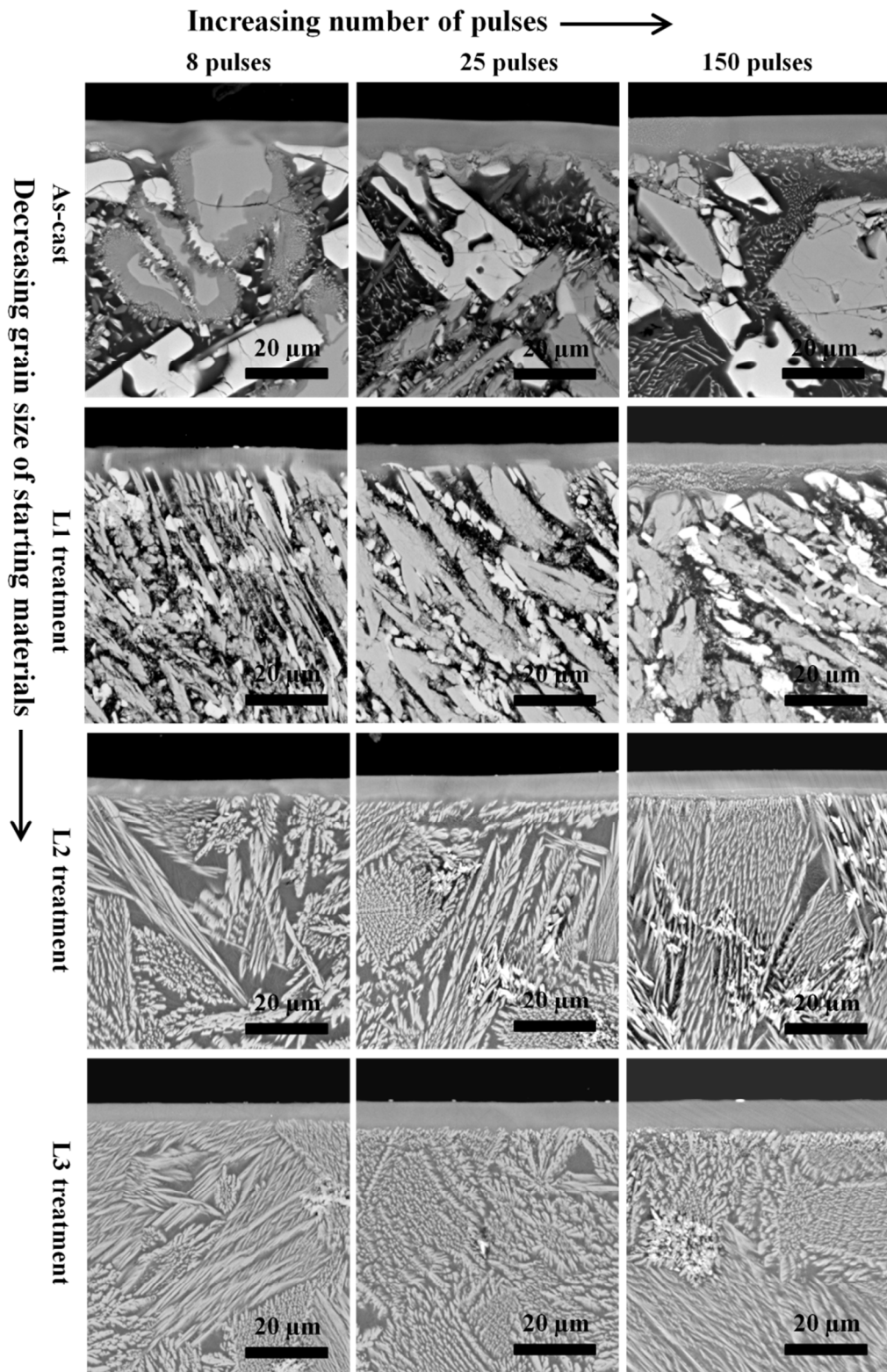


**Figure 6-17** Cross section morphology (back scattered electron SEM images) of the LAEB treated Al-Co-Ce alloy 3 with different initial microstructures and numbers of LAEB pulses. L1, L2 and L3 pretreatment indicates the laser treatment of MT1000-20, MT6000-20 and MT6000-5, respectively, as presented in Section 5.3.

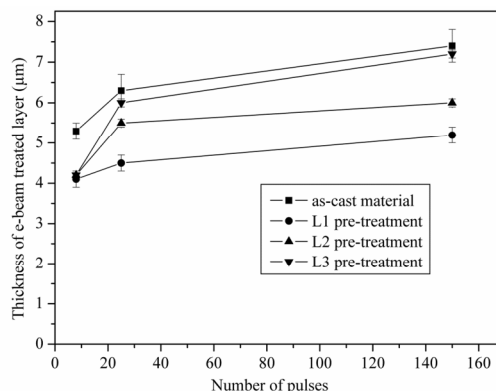


**Figure 6-18 Remelted layers thickness as a function of the number of pulses in the LAEB treated Al-Co-Ce alloy 3 with different initial microstructures. L1, L2 and L3 pretreatment indicates the laser treatment of MT1000-20, MT6000-20 and MT6000-5, respectively, as presented in Section 5.3.**

### 6.4.3 Cracking

Generally, for laser pre-treated samples, the extent of LAEB induced cracking was notably less compared to the as-cast material (**Figure 6-16** and **Figure 6-19**). The cracks in the LAEB treated as-cast material preferentially formed within the lighter contrast regions of the large  $\text{Al}_8\text{Co}_2\text{Ce}$  phase. Similar correlation between the crack location and the  $\text{Al}_8\text{Co}_2\text{Ce}$  phase was also seen for the laser pre-treated samples. For all samples, the extent of cracking increased with the number of pulses. However, the majority of cracking was generated within the first 25 pulses, accompanied by a small increase in the crack density with increasing number of pulses from 25 to 150. However, in the case of the as-cast material, the majority of cracking formed within the first 8 pulses.

**Figure 6-20** shows the localised cross sectional morphologies of the LAEB treated samples (35 kV, 150 pulses) with different initial microstructures (as-cast and L3 pre-treated samples). Cracks can be seen in both types of sample. When the LAEB irradiation was applied to the as-cast material, the crack propagated in the large  $\text{Al}_8\text{Co}_2\text{Ce}$  phases over the distance of up to  $\sim 70 \mu\text{m}$ . However, in the case of L3

laser pre-treated sample, the cracking stopped in the depth of  $\sim 20\ \mu\text{m}$ , which was much shorter than that in the LAEB treated as-cast sample. In addition, the crack in the laser pre-treated sample after LAEB treatment was narrower compared with that in the as-cast material.

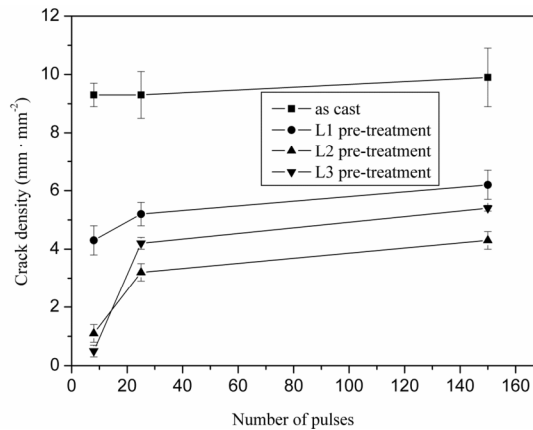


**Figure 6-19 Crack density of LAEB treated layers in Al-Co-Ce alloy 3 as a function of the number of LAEB pulses. L1, L2 and L3 pretreatment indicates the laser treatment of MT1000-20, MT6000-20 and MT6000-5, respectively, as presented in Section 5.3.**

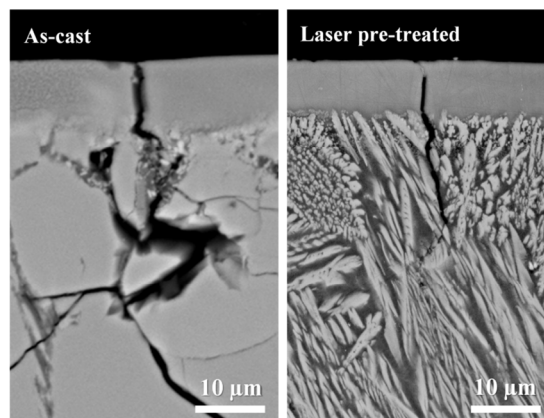


**Figure 6-20 Localised cross sectional morphologies showing the cracks in the LAEB treated Al-Co-Ce alloy 3 with different initial microstructures (35 kV, 150 pulses).**

#### 6.4.4 Phase transformation

**Figure 6-21** shows the glancing angle XRD results of LAEB treated layer with different initial microstructures. Obvious crystalline peaks were seen in the GAXRD spectra of all samples that were LAEB treated without any prior laser

treatment. After 25 pulses the crystalline peaks decreased in intensity and an amorphous hump was present at  $2\theta \approx 37^\circ$ . After 150 pulses the crystalline peaks reappeared and the amorphous hump was no longer discernable. There were markedly fewer crystalline peaks in the GAXRD spectra of treated samples with laser pre-treatment. Those peaks were significantly smaller than those in **Figure 6-21** and an amorphous hump was seen at  $2\theta \approx 37^\circ$ . Several small crystalline peaks can be seen in the GAXRD spectrum of the sample which underwent L3 laser pre-treatment and 150 LAEB pulses.

Small crystallites were found in localised regions of the as-cast sample treated with 150 pulses (**Figure 6-22**), this is consistent with the XRD results in **Figure 6-21**. Such crystallites were not visible in the laser pre-treated sample after the same number of LAEB pulses.

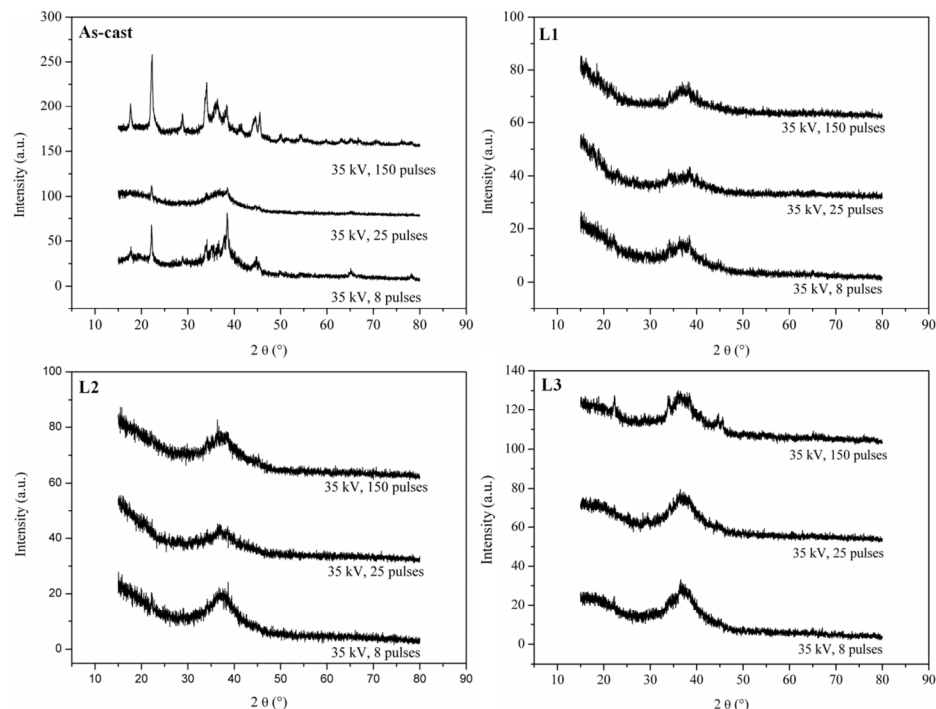


**Figure 6-21** GAXRD spectra of LAEB treated layers with different initial microstructures. L1, L2 and L3 pretreatment indicates the laser treatment of MT1000-20, MT6000-20 and MT6000-5, respectively, as presented in Section 5.3.

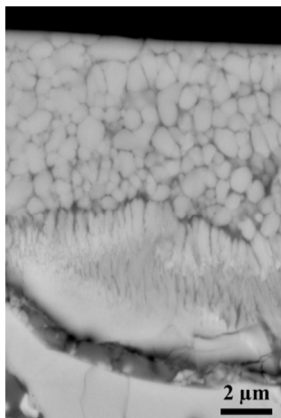


**Figure 6-22** BSE images showing the cross section of the LAEB treated as-cast alloy 3 (35 kV, 150 pulses).

### 6.5 Formation of craters and particles

It has been noticed that bright particles and craters appeared on the irradiated sample surface, especially on the samples irradiated by fewer pulses of LAEB and lower cathode voltage (**Figure 6-1**, **Figure 6-8**, **Figure 6-13** and **Figure 6-16**). To obtain further understanding of the formation of these particles and craters, high resolution SEM images of 15 pulses of LAEB irradiated Al-Co-Ce alloy 2 at 25 kV and 40 kV were taken.

**Figure 6-23** shows the microstructure of LAEB treated samples in plan view. Overall, the 40 kV treated sample exhibited a higher extent of homogenisation. In addition, there were also many spherical particles and craters scattered on the LAEB treated surface (especially 25 kV treated sample). However, for 40 kV treated cathode voltage, these craters and particles were greatly eliminated (**Figure 6-23b** and **d**). Furthermore, these craters were found to be mostly located in the darker contrast regions i.e. the Al/Al<sub>11</sub>Ce<sub>3</sub> eutectic regions in the as-cast material.

This preferential location of the craters and particles was clearly seen in a magnified image of the 25 kV treated sample, as shown in **Figure 6-24**. The

particles were found to have a similar size to the adjacent craters. EDS spot analysis (**Table 6-1**) was performed for the particles A and B shown in **Figure 6-24**. These particles had the composition close to the  $Al_{11}Ce_3$  phase. However, it should be noted that there will be some inaccuracy in composition analysis due to the small size of the particles.

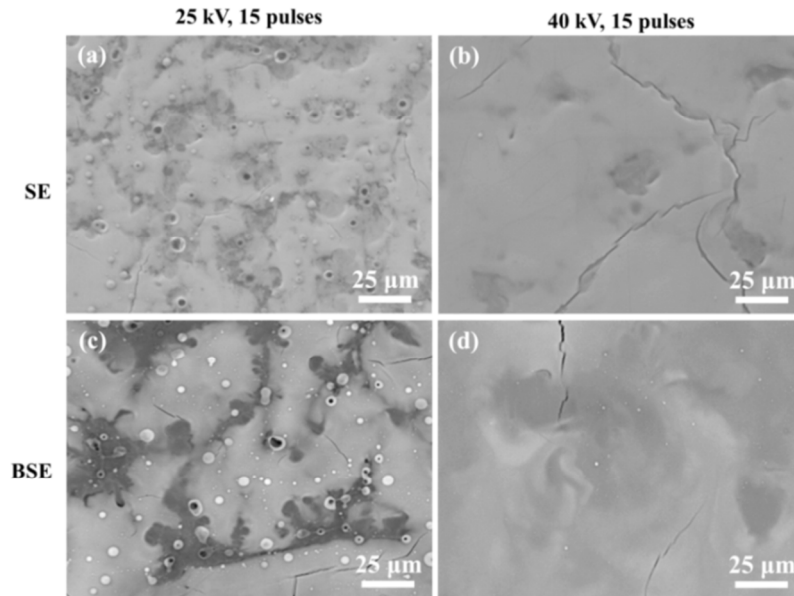


**Figure 6-23** SE and BSE images of LAEB treated materials in plan view using 25 kV and 40 kV cathode voltage.

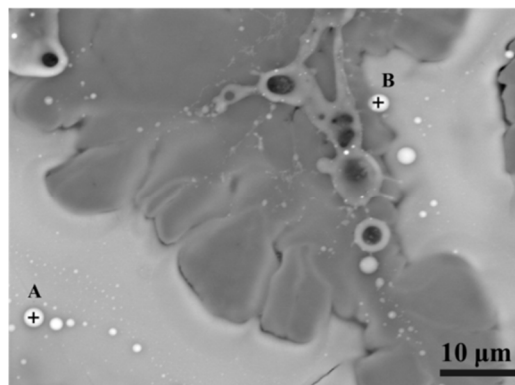


**Figure 6-24** BSE image of 25 kV treated materials showing the craters and particles on the treated layer.

**Table 6-1** EDS results of the particles on the remelted layer surface of 8 pulses of LAEB irradiated Al-Co-Ce alloy 2, as shown in **Figure 6-24**.

Particle	Element composition (at.%)		
	Al	Co	Ce
A	76.0	4.8	19.2
B	82.1	3.5	14.4

## **6.6 Discussion**

### **6.6.1 General formation mechanism of the amorphous layer**

In the LAEB process LAEB, electrons are first accelerated by a high cathode voltage. Once these electrons impact on the surface of the original bulk material, the kinetic energy of high velocity electrons is transformed into thermal energy which quickly increases the temperature of a near surface volume. Due to the temperature increase, melting and diffusion will occur in the treated layer.

Generally, there are two necessary conditions for the amorphisation of Al-Co-Ce alloy in LAEB treatment. First, the crystalline phases melt and diffuse to achieve a homogeneous composition i.e. the glass forming composition. This needs a sufficiently high temperature and enough time for the melting and diffusion. Second, upon obtaining a homogeneous composition, a fast enough cooling rate is a required for the alloy to form the amorphous phase. Insufficient cooling rate cannot suppress the formation of the crystalline phase.

In this work, LAEB has an extremely short pulse duration of 1  $\mu$ s, which results in a rapid heating and cooling rate of materials in the LAEB treatment. Under this high cooling rate, the molten alloy can retain the disordered atomic arrangement i.e. the amorphous state, which is line with previous observation of glass formation in this alloy system using a pulsed laser surface melting technique [118].

### **6.6.2 Homogenisation**

The new elemental distribution in the treated sample is determined by the extent of diffusion in the liquid phase. In this work, the as-cast Al-Co-Ce samples treated

with lower cathode voltage and fewer numbers of pulses showed slightly improved homogeneity in elemental distribution compared to the as-cast material. When the as-cast Al-Co-Ce sample was treated with a more intense electron beam (higher cathode voltage) or higher number of pulses, the sample surface exhibited a more uniform elemental distribution due to the sufficient diffusion time for different phases, as shown in **Figure 6-1** and **Figure 6-8**. This adequate elemental diffusion made the sample surface acquire a uniform composition i.e. the glass forming composition in this case. In this work, the chemical composition of the as-cast Al-Co-Ce alloy 3 was greatly homogenised when it was subjected to 100 pulses of LAEB irradiation (**Figure 6-1**).

In **Section 6.3**, it has been seen that Al-Co-Ce alloy 1 with the smallest crystalline phase exhibited the highest extent of homogenisation after the same LAEB treatment compared to the other two alloys, which indicated the effect of initial microstructure on the homogenisation of LAEB treated sample. In **Chapter 5**, laser surface melting as a pre-treatment can greatly refine the microstructure of the as-cast Al-Co-Ce alloy and eliminate the large  $\text{Al}_8\text{Co}_2\text{Ce}$  phase particles. Therefore, the time required by the alloy to obtain a uniform composition can be reduced. In **Section 6.4**, it has been seen that the laser pre-treated alloy was greatly homogenised even after only 8 pulses due to the refinement of the alloy microstructure, i.e. the decreased particle size, particle spacing of the  $\text{Al}_8\text{Co}_2\text{Ce}$  phase and the composition difference between different phases in the irradiated microstructure (**Figure 6-16**).

The number of LAEB pulses required for the homogenisation of the irradiated alloys has been found to be dependent on the initial microstructure. For the as-cast

alloy 3, 150 pulses of LAEB irradiation were required to homogenise the chemical composition of the irradiated alloy. However, for the alloy which was subjected to the laser pretreatment, the required number of pulses for alloy homogenisation was greatly reduced to 8 pulses. In this work, due to the existence of Ce in  $\text{Al}_8\text{Co}_2\text{Ce}$  phase,  $\text{Al}_{11}\text{Ce}_3$  phase and Al/ $\text{Al}_{11}\text{Ce}_3$  eutectic, the diffusion of Ce in molten Al could be assumed to be the determining factor for melt homogenisation. This diffusion time of Ce in molten Al can be estimated as follows. First, the diffusion coefficient of Ce in Al was calculated according to Arrhenius equation

$$D = D_0 \exp(-Q / RT) \quad \text{Eq. 6-1}$$

where  $D_0$  and  $Q$  are the diffusion constant and the diffusion activation energy of Ce in pure Al, which are  $1.0 \times 10^{-4} \text{ m}^2/\text{s}$  and 91 kJ/mol, respectively [167].  $R$  is the universal gas constant (8.314 J/mol).  $T$  was assumed to be equal to the melting point of Al-Co-Ce alloy 3, which is 1308 K. Based on **Eq. 6-1**, the diffusion coefficient,  $D$ , of Ce in pure Al can be calculated, to be  $2.32 \times 10^{-8} \text{ m}^2/\text{s}$ .

In addition, the relationship between the diffusion distance ( $L_0$ ) and diffusion time ( $t_d$ ) is assumed to follow the equation below

$$L_0 = K_D \sqrt{Dt} \quad \text{Eq. 6-2}$$

where  $K_D$  is a constant, which was assumed to be 2. In this work, the particle spacing presented by the  $\text{Al}_8\text{Co}_2\text{Ce}$  phases was used as the diffusion distance. The particle spacing values of different structures have been obtained in **Chapter 5**. Therefore, the diffusion time of Ce in pure Al for different microstructure can be obtained, as shown in **Table 6-2**. From table, it can be seen that the estimated diffusion time for the as-cast alloy to achieve uniform composition is longer than

that of the LSM treated alloy. This therefore is in agreement with the larger number of pulses needed to achieve homogenisation experimentally.

**Table 6-2 Comparison of the estimated diffusion time for the as-cast and LSM treated (MT1000-20) Al-Co-Ce alloy 3 to homogenise along with the number of pulses used experimentally.**

Initial structure	Intermetallic particle spacing, $L_0$ ( $\mu\text{m}$ )	Estimated diffusion time, $t_d$ (s)	LAEB pulses used in experiments, $N_p$
As-cast alloy 3	$\sim 30$	$9.7 \times 10^{-3}$	150
LSM treated alloy 3 (MT1000-20)	$\sim 5$	$2.7 \times 10^{-4}$	8

### 6.6.3 Amorphisation

Due to the short pulse duration (a few  $\mu\text{s}$  [139]) and small volume of the LAEB affected material, the treated surface will rapidly cool and solidify through heat transfer to the underlying bulk. It has been estimated that pulsed electron beam irradiation can obtain a cooling rate of  $10^8 \sim 10^9$  K/s [142, 150, 151]. Under the action of this high cooling rate, the molten alloy with a glass forming composition can retain the disordered atomic arrangement i.e. the amorphous state. The results presented in this work show that homogenous amorphous layers were achieved using some suitable treatment parameters, such as 100 pulses at cathode voltage of 29 kV and 25~50 pulse at 35 kV.

In the case of the laser pretreated sample, the refined microstructure not only decreased the time required for microstructural homogenisation, but also the time required for amorphisation. Therefore, more extensive homogenisation, and amorphisation, is seen for fewer pulses in the laser refined material. In this present work, the alloy was greatly homogenised and amorphised after only 8 pulses (**Figure 6-16**). The decreased required time for homogenisation also reduced the

danger of significant bulk sample pre-heating which could affect cooling rate and potentially make amorphisation less likely.

#### 6.6.4 Crystallisation

When 100 and 150 pulses of LAEB at 35 kV cathode voltage were applied to the sample surface (Al-Co-Ce alloy 3), crystalline peaks indicate that the material examined by GAXRD is not fully amorphous, but consists of some crystallisation within an amorphous matrix. The existence of spherical and columnar crystals in the treated layer (**Figure 6-7**) confirmed the GAXRD results. In addition, the crystallisation also occurred on the 100 pulses of electron beam treated Al-Co-Ce alloy 3 at 40 kV cathode voltage (**Figure 6-12**).

The occurrence of the crystallisation mentioned above may be explained by a decrease in thermal gradient between the treated layer and the substrate, thereby reducing the cooling rate and permitting crystallisation as opposed to amorphous phase formation. The decrease of thermal gradient is caused from the temperature increase of the substrate material, i.e. the heat accumulation which has been confirmed by our temperature measurement work. It was found that the samples reached 327 K, 355 K and 372 K when samples were irradiated with 50, 100 and 150 pulses, respectively (**This is presented in Section 3.4.2.**). This indicates that the large area electron beam process generated a progressive increase in the temperature of the substrate when excessive pulses of irradiation were applied.

The reappearance of crystalline peaks in the 35 kV, 150 pulses of LAEB irradiated laser pretreated material was also seen in the glancing angle XRD results. However, crystalline phases were not seen in the SEM image of the sample as that observed in the SEM image of 150 pulses irradiated as-cast material. The absence

of visible crystalline phases in the SEM image of the latter material may simply be due to a very small, sub-micron, crystal size. The crystallisation may result from reduced cooling rates due to progressive temperature increase of the substrate with additional pulses as that in the LAEB treated as-cast samples.

In addition, crystallisation did not occur all over the sample surface, but in some localised regions. It is thought that the appearance of localised regions of crystalline phases in the amorphous matrix may result from any remaining slight compositional heterogeneity of the treated layer. It is also possible that local variations in thermal gradients and cooling rates may arise due to the phases present in the underlying microstructure, i.e. any variation in thermal conductivity of the different phases would generate small differences in thermal history.

### **6.6.5 Cracking**

In addition to the phase transformation of the treated layer, cracks were also observed as a result of electron beam irradiation. Cracks were observed on all electron beam treated samples. **Figure 6-25a** shows a schematic diagram of the cracking in the LAEB treated as-cast material. The LAEB surface treatment generates a thermal gradient in the material. After solidification, the hot treated layer contracts more than the cold underlying substrate. A tensile stress is generated in the surface, and near surface material, due to this differential contraction. If this tensile stress exceeds the fracture strength of any material in the near surface area then that material will crack.

LAEB treatment of the as-cast Al-Co-Ce alloy showed that cracking was correlated with the existence of large  $\text{Al}_8\text{Co}_2\text{Ce}$  phase particles. This is due to the brittleness characteristic of this phase (**Section 5.2.5**). These large and brittle

$\text{Al}_8\text{Co}_2\text{Ce}$  phase particles act as easy cracking initiation sites in the as-cast material, these particles also provide easy growth paths for crack propagation, as shown in **Figure 6-20a**.

**Figure 6-25b** shows the cracking in the laser pre-treated sample after LAEB irradiation. Laser pre-treatment has eliminated the easy crack initiation sites and crack growth paths i.e. microstructural refinement has prevented the formation of large  $\text{Al}_8\text{Co}_2\text{Ce}$  phase particles. Hence cracking becomes less likely and the few cracks that do form are shorter and terminate rapidly in the relatively ductile refined microstructure (**Figure 6-20b**).

It should also be noted that the as-cast material contains a number of different phases which will have different coefficients of thermal expansion. Stresses arising from differential thermal expansion will contribute to crack generation.

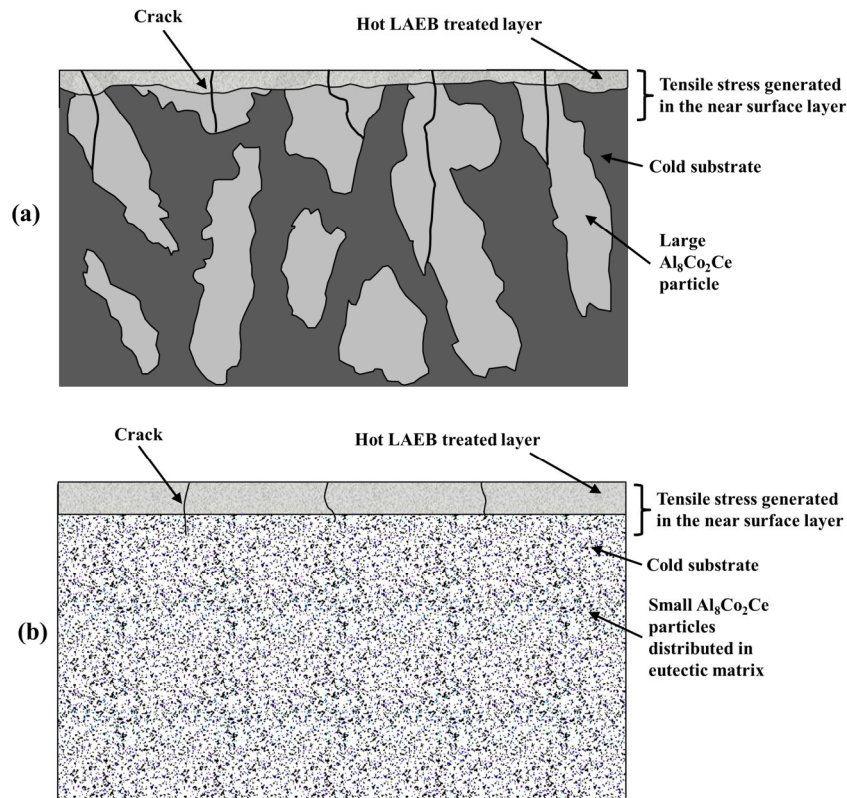


**Figure 6-25 Schematics of cracking in different LAEB treated samples: (a) as-cast sample and (b) laser microstructural refined sample.**

### 6.6.6 Formation of craters and particles

The LAEB treatment under 25 kV cathode voltage notably caused the formation of some craters and spherical particles on the treated sample surface (**Figure 6-23a and c**). Based on the energy distribution function [138], it is known that the energy distribution and power density of the heat source under each cathode voltage reaches a maximum below the surface where the depth is 1/3 of the electron range, i.e. the electron penetration depth. This is consistent with the results reported by Qin et al. [168]. The resultant subsurface melting and volume expansion of melt will exert stresses on the surrounding material. When this thin overlying layer cannot afford the exerted stresses, it can rupture, resulting in the observed eruption of craters and ejected particles as has been previously reported [146, 168, 169].

In this work, the craters were mostly seen in the remelted Al/Al<sub>11</sub>Ce<sub>3</sub> eutectic regions. This is thought to be due to the heterogeneous microstructure of the as-cast Al-Co-Ce alloy. The different phases existing in the as-cast material have different melting points. The eutectic region with low melting point will melt first, providing an easy path for the eruption mentioned above. This is consistent with the results reported by Qin et al. [152, 168]. In their work, it was suggested that the formation of the craters preferably occurred at the defects zones such as grain boundaries and vacancies. In this work, the size and composition of the particles formed on the treated sample were also found to be very close to the Al<sub>11</sub>Ce<sub>3</sub> phase in the original as-cast material. Therefore, the formation of craters and particles on the LAEB treated surface can be further attributed to the eruption of Al<sub>11</sub>Ce<sub>3</sub> phase in the subsurface of the eutectic regions. Walker et al. also reported that the crater formation was related to the existence of precipitates [146]. In summary, the

highly inhomogeneous as-cast material used in this work is particularly susceptible to the formation of craters and particles.

Fewer craters and particles were observed for the higher cathode voltage samples. This is attributed to the larger cathode voltage resulting in the increased electron penetration range, and associated deeper region of subsurface melting. The increased depth will make eruption more difficult. The effect of the cathode voltage on the electron range will be presented in **Chapter 7**. Therefore, in this work, the craters and particles in the 40 kV treated sample were greatly reduced (**Figure 6-23b and d**).

## 6.7 Summary

- 25 - 50 pulses of 35 kV and 100 pulses of 29 kV electron beam irradiation successfully transformed a 6 - 7  $\mu\text{m}$  surface layer of  $\text{Al}_{86.0}\text{Co}_{7.6}\text{Ce}_{6.4}$  to the amorphous state. Amorphisation requires surface melting, sufficient time for melt homogenisation and rapid cooling.
- Localised crystallisation of the amorphous state occurred under treatment with excessive numbers of pulses (100 and 150) at 35 kV, or higher cathode voltages (40 kV) with 100 pulses, due to the decrease of cooling rate by progressive heat accumulation in the bulk sample.
- Cracks were observed to form on almost all LAEB treated samples. These were correlated with the presence of the large and brittle  $\text{Al}_8\text{Co}_2\text{Ce}$  phase.
- Initial microstructure of the Al-Co-Ce alloy affects the extent of homogenisation of the LAEB treated layer. Alloy 1 with smallest size of

phases exhibited the best and most rapid homogenisation under the same LAEB treatment parameters compared to alloy 2 and alloy 3.

- Laser microstructural refinement decreased the number of LAEB pulses required for the homogenisation and amorphisation of Al-Co-Ce alloy.
- Prior laser microstructural refinement successfully decreased the extent of cracking of the amorphous surface layer following LAEB. The suppressed cracking of laser pre-treated LAEB treated Al-Co-Ce amorphous layer was due to the removal of large, brittle,  $\text{Al}_8\text{Co}_2\text{Ce}$  phase particles.
- The formation of craters and particles on the LAEB treated samples surface was thought to be due to the prior melting and eruption of the sub-surface of the irradiated sample.

## **Chapter 7 Numerical simulation of multi-pulse LAEB**

### **irradiation process**

#### **7.1 Introduction**

When a material is irradiated by a high current pulsed electron beam, the sample will experience the heating and cooling process under the action of energy deposition of electrons. This thermal process including the heat propagation and redistribution within the irradiated sample will result in physical and chemical changes of the irradiated sample. The temperature field is very useful to understand the surface modification process of pulsed electron beam melting. However, due to the short irradiation time (1~2  $\mu\text{s}$ ), a small irradiated volume (treated layer thickness is normally just a few microns) and high heating/cooling rate (usually  $\sim 10^8$ - $10^9$  K/s [150, 152]), it is extremely difficult to measure the temperature distribution and cooling rate which directly influence the surface modification. Since the entire heating and cooling process takes place in such a short space of time, it is impossible to observe the microstructural changes while they are taking place. Thus, it is necessary to build a proper physical model and develop a mathematical method to simulate this process.

In this chapter, a nonstationary heat transfer model with an external pulsed heat source (electron beam) is built, and a finite difference method is used to solve the heat transfer equation. Al-Cu eutectic alloy and Al-Co-Ce alloy, which have been investigated in the experimental work, as well as pure Al with well documented thermal properties, are modelled in the work and reported in this Chapter.

**Table 7-1 Symbols used in this modelling work (1/2)**

Symbol	Parameter	Unit	Value
$A$	sample area	$m^2$	$2.25 \times 10^{-4}$
$B_i$	local Biot number		
$c$	specific heat	J/kg·K	
$C_0$	constant in electron range equation	$kg/m^2V^{3/2}$	$1 \times 10^{-4}$
$C_a$	cathode voltage of LAEB	V	
$D$	sample thickness	m	$3 \times 10^{-3}$
$d_m$	thickness of the remelted layer	m	
$\Delta\tau$	time step	s	$1 \times 10^{-9}$
$\Delta T_0$	theoretical temperature increase from 1 pulse LAEB treatment	K	
$\Delta T_{cm}$	temperature compensation for latent heat	K	
$\Delta T_{N_p}$	theoretical temperature increase from $N_p$ pulse LAEB treatment	K	
$\Delta T_{N_p}^{exp}$	experimental temperature increase from $N_p$ pulse LAEB treatment	K	
$\Delta T_{N_p}^{est}$	estimated temperature increase from $N_p$ pulse LAEB treatment	K	
$\Delta T_i^j$	the temperature increase of the single node $j$ at the time of $i$	K	
$\Delta x$	spatial increment	m	$5 \times 10^{-7}$
$\varepsilon$	emissivity coefficient		0.06
$e$	electron charge of LAEB	coulomb	$1.6 \times 10^{-19}$
$E$	energy density of LAEB	J/m <sup>2</sup>	
$E_0$	electron energy of LAEB	keV	
$f(x)$	energy distribution function		
$f(Q_{N_p})$	fraction of energy loss in the total energy input by $N_p$ pulse LAEB treatment		
$F_0$	local Fourier number		
$h$	heat transfer coefficient	W/m <sup>2</sup> K	$1.3 \times 10^4$
$H_m$	latent heat of fusion and solidification	J/kg	
$i$ or $j$	superscript of $t$ or $T$ in time		
$J$	current density of LAEB	A/m <sup>2</sup>	$2 \times 10^6$
$\lambda$	thermal conductivity	W/m·K	
$L_v$	volume power density of LAEB	W/m <sup>3</sup>	
$v$	solidification velocity	m/s	
$N$ or $n$	subscript of $t$ or $T$ in spatial location		
$N_m$	number of the remelted nodes		
$N_p$	number of LAEB pulses		
$N_p^{th}$	pulse sequence number		
$q$	general heat flux	W/m <sup>2</sup>	
$q_1$	heat flux from the left node	W/m <sup>2</sup>	
$q_2$	heat flux to the right node	W/m <sup>2</sup>	

**Table 7-1 Symbols used in this modelling work (2/2)**

Symbol	Parameter	Unit	Value
$q_3$	heat flux produced by heat source	W/m <sup>2</sup>	
$q_f$	heat flux of heat transfer at the bottom surface	W/m <sup>2</sup>	
$q_r$	heat flux of radiation at the top surface	W/m <sup>2</sup>	
$Q$	general heat or energy	J	
$Q_f$	heat loss of the node at the bottom surface	J	
$Q_0$	energy input from 1 pulse LAEB treatment	J	
$Q_{bd}$	total energy loss from the boundaries	J	
$Q_L$	latent heat absorbed or released during melting or solidification	J	
$Q_r$	heat loss of the node at the top surface	J	
$Q_{N_p}$	theoretical energy input from $N_p$ pulse LAEB treatment	J	
$Q_{N_p}^{\text{exp}}$	experimental energy increase from $N_p$ pulse LAEB treatment	J	
$Q_{N_p}^{\text{est}}$	estimated energy input from $N_p$ pulse LAEB treatment	J	
$Q_{total}^i$	total energy at the moment of $i$	J	
$\rho$	density	kg/m <sup>3</sup>	
$r_0$	electron range of LAEB	m	
$\sigma$	Stefan-Boltzmann constant	W/m <sup>2</sup> ·K <sup>4</sup>	$5.67 \times 10^{-8}$
$\tau$	pulse duration of LAEB	second	$1 \times 10^{-6}$
$t_0^j$	melting time for node $j$ after 1 pulse irradiation	s	
$t_{\text{max}}^j$	the time that node $j$ reached maximum temperature	s	
$t_{\text{melt}}^j$	the time that node $j$ started the melting	s	
$t_{\text{onset-solid}}^j$	the time that node $j$ started the solidification	s	
$t_{\text{solid}}^j$	the time that node $j$ finished the solidification	s	
$T$	general temperature	K	
$T_0$	initial temperature	K	293
$T_m$	melting point	K	
$T_{\text{surr}}$	surrounding temperature	K	293
$T_1^i$	the temperature of the node 1 at the top surface at the moment of $i$	K	
$T_{\text{max}}^j$	the maximum temperature for node $j$	K	
$T_{N+1}^i$	the temperature of the node at the bottom surface at the time of $i$	K	
$T_x^i$	temperature of node $x$ at the time of $i$	K	
$v$	cooling rate	K/s	
$V$	volume	m <sup>3</sup>	

## 7.2 Mathematical model

### 7.2.1 Heat transfer equation

**Figure 7-1** is the schematic diagram of the one dimensional heat transfer model. In this model, the heat transfer is unidirectional, i.e. along the axis of a slender rod. We define the heat involved in the heat transfer as  $Q$ , the cross sectional area of the slender rod as  $A$ , the density as  $\rho$ . The heat capacity and thermal conductivity of the material are  $c$  and  $\lambda$ .  $T(t,x)$  is the temperature of the material with the length of  $\Delta x$  at time of  $t$ .

Based on the Fourier law, heat flux in the rod can be written as follows:

$$q = \frac{Q}{tA} = -\lambda \frac{\partial T}{\partial x} \quad \text{Eq. 7-1}$$

where  $q_1$  and  $q_2$  represent the heat flux flowing into and out of the material with a length of  $\Delta x$ , respectively.  $q_3$  is the heat flux produced by the heat source. Under the action of the above three heat fluxes, the net heat flux change of the material is defined as  $q_c$ . According to the heat conservation law, one can obtain:

$$q_c = q_1 + q_2 + q_3 \quad \text{Eq. 7-2}$$

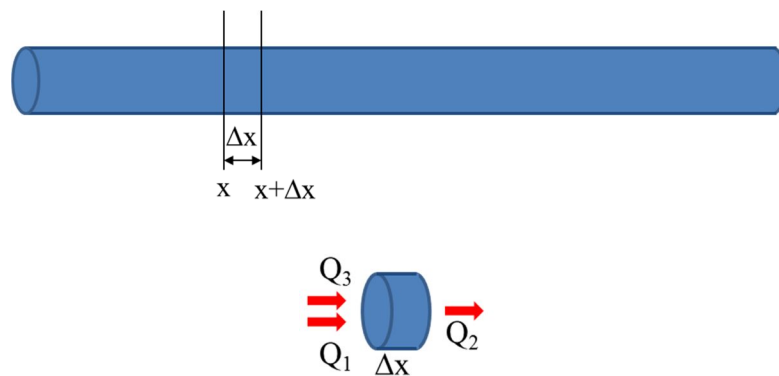


**Figure 7-1 One-dimension heat transfer model**

**Figure 7-2** shows the diagrams of the numbering system for the nodal points. Based on the finite volume method, the heat transfer equation can be written in the form of a finite difference equation as follows:

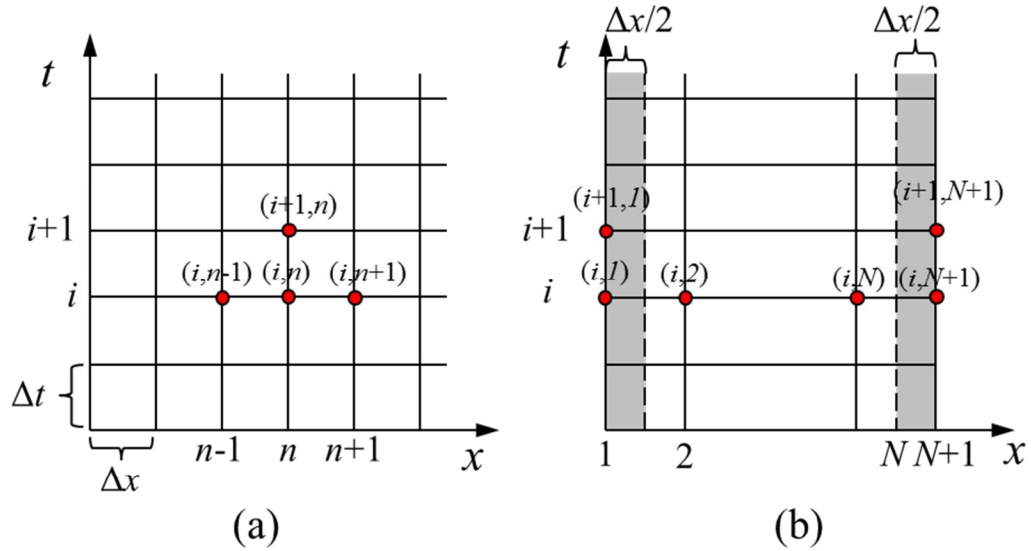


**Figure 7-2** Diagram for the numbering system of nodal points. (a) Interior Nodes; (b) Nodes at boundaries.

**Interior Nodes (Figure 7-2a):**

$$q_1 = \lambda \frac{T_{n-1}^i - T_n^i}{\Delta x} \quad \text{Eq. 7-3}$$

$$q_2 = \lambda \frac{T_{n+1}^i - T_n^i}{\Delta x} \quad \text{Eq. 7-4}$$

$$q_3 = Lv\Delta x \quad \text{Eq. 7-5}$$

As for the net change of the heat flux, it can result in a temperature change ( $\Delta T$ ) at time of  $t + \Delta t$ , which can be expressed as follows:

$$q_c = \rho c \Delta x \Delta T / \Delta t \quad \text{Eq. 7-6}$$

Therefore, **Eq. 7-2** can be rewritten as:

$$\lambda \frac{T_{n-1}^i - T_n^i}{\Delta x} + \lambda \frac{T_{n+1}^i - T_n^i}{\Delta x} + Lv\Delta x = \rho c \Delta x \frac{T_n^{i+1} - T_n^i}{\Delta t} \quad \text{Eq. 7-7}$$

Rearranging **Eq. 7-7**, one can obtain:

$$T_n^{i+1} = F_0(T_{n-1}^i + T_{n+1}^i) + (1 - 2F_0)T_n^i + \frac{\Delta t}{\rho c} Lv \quad \text{Eq. 7-8}$$

where  $F_0 = \frac{\lambda \Delta t}{\rho c (\Delta x)^2}$ .

**Nodes at the boundaries (Figure 7-2b):**

**(1) Top surface**

Considering the position of the node at the top surface, the length of the cell is half of that of the interior cells. There is also no conduction heat flux flowing into the top surface from the left neighbouring cell,  $q_l$  is therefore equal to zero. In this work, LAEB treatment was conducted in an argon atmosphere with a pressure of 0.5 Pa. The heat convection with the environment was hence ignored. The main heat transfer mechanism of the top surface was assumed to be radiation. Therefore, the heat flux flowing out resulting from radiation can be written as:

$$q_r = \sigma \varepsilon \left[ (T_{sur})^4 - (T_1^i)^4 \right] \quad \text{Eq. 7-9}$$

where  $\sigma$  and  $\varepsilon$  are the Stefan-Boltzmann constant ( $5.67 \times 10^{-8} \text{ W/m}^2 \cdot \text{K}^4$ ) and emissivity coefficient, respectively.  $T_{sur}$  is the temperature of the surrounding environment. In this work,  $\varepsilon$  of Al and Al alloy was taken from the highly polished aluminium, which is 0.06.  $T_{sur}$  is assumed to be a constant of 293 K.

The finite difference equation for the nodes at the top surface can be written as:

$$\lambda \frac{T_2^i - T_1^i}{\Delta x} + \sigma \varepsilon \left[ (T_{sur})^4 - (T_1^i)^4 \right] + Lv \frac{\Delta x}{2} = \rho c \frac{\Delta x}{2} \frac{T_1^{i+1} - T_1^i}{\Delta t} \quad \text{Eq. 7-10}$$

Rearranging **Eq. 7-10**, one can obtain:

$$T_1^{i+1} = 2F_0 T_2^i + (1 - 2F_0)T_1^i + 2 \frac{\sigma \varepsilon \Delta t}{\rho c \Delta x} \left[ (T_{sur})^4 - (T_1^i)^4 \right] + \frac{\Delta t}{\rho c} Lv \quad \text{Eq. 7-11}$$

However, if the adiabatic condition applies on the top surface, i.e. there is no heat flux flowing out of the top surface, the difference equation can be simplified as:

$$\lambda \frac{T_2^i - T_1^i}{\Delta x} + Lv \frac{\Delta x}{2} = \rho c \frac{\Delta x}{2} \frac{T_1^{i+1} - T_1^i}{\Delta t} \quad \text{Eq. 7-12}$$

Rearranging **Eq. 7-12**, one can obtain:

$$T_1^{i+1} = 2F_0 T_2^i + (1 - 2F_0) T_1^i + \frac{\Delta t}{\rho c} Lv \quad \text{Eq. 7-13}$$

## (2) Bottom surface

Similarly, a half-length cell was used in this case as that at the top surface. Also, considering the position of the node, there is no conduction heat transfer to the right cell. However, in this work, the LAEB treated samples were fixed to a metal clamp (**Figure 3-8**). Therefore, there will be a heat transfer from the treated samples to the clamp. The heat flux flowing out resulting from the heat transfer to the clamp can be written as:

$$q_f = h(T_{surr} - T_{N+1}^i) \quad \text{Eq. 7-14}$$

where  $h$  is the heat transfer coefficient for this sample-clamp system. In this work,  $h = 13000 \text{ W/m}^2 \cdot \text{K}$ , which is estimated based on the temperature labelling measurement and preliminary calculation results. Detailed procedure of estimation will be presented in **section 7.3.2**.

The finite difference equation for the nodes at the bottom surface can be written as:

$$\lambda \frac{T_N^i - T_{N+1}^i}{\Delta x} + h(T_{surr} - T_{N+1}^i) + Lv \frac{\Delta x}{2} = \rho c \frac{\Delta x}{2} \frac{T_{N+1}^{i+1} - T_{N+1}^i}{\Delta t} \quad \text{Eq. 7-15}$$

Rearranging **Eq. 7-15**, one can obtain:

$$T_{N+1}^{i+1} = 2F_0 T_N^i + (1 - 2F_0) T_{N+1}^i + 2F_0 B_i (T_{surr} - T_{N+1}^i) + \frac{\Delta t}{\rho c} Lv \quad \text{Eq. 7-16}$$

where  $B_i = \frac{h\Delta x}{\lambda}$ .

Similarly as the top surface, if the adiabatic condition applies on the bottom surface, i.e. there is no heat flux flowing out of the top surface, the difference equation can be simplified as:

$$\lambda \frac{T_N^i - T_{N+1}^i}{\Delta x} + Lv \frac{\Delta x}{2} = \rho c \frac{\Delta x}{2} \frac{T_{N+1}^{i+1} - T_{N+1}^i}{\Delta t} \quad \text{Eq. 7-17}$$

Rearranging **Eq. 7-17**, one can obtain:

$$T_{N+1}^{i+1} = 2F_0 T_N^i + (1 - 2F_0) T_{N+1}^i + \frac{\Delta t}{\rho c} Lv \quad \text{Eq. 7-18}$$

As for the initial condition, the temperature at time of  $t=0$  was set as a constant of 293 K, i.e.  $T_i=293$  K.

In the finite difference method, to ensure the calculation stability and minimise the

error, the term of  $1 - 2F_0$  (where  $F_0 = \frac{\lambda \Delta t}{\rho c (\Delta x)^2}$ ) in the finite difference equation

must be larger than zero. Therefore, the stability condition of the finite difference equation can be written as follows:

$$\frac{\lambda \Delta t}{\rho c (\Delta x)^2} < \frac{1}{2} \quad \text{Eq. 7-19}$$

Rearranging **Eq. 7-19**, one can obtain:

$$\Delta t < \frac{\rho c}{2\lambda} (\Delta x)^2 \quad \text{Eq. 7-20}$$

In this work, based on the above equation and the calculation efficiency, the experimental results were taking into account the determination of the grid dividing, as well as the calculation accuracy. A uniform grid spacing ( $\Delta x$ ) of  $5 \times 10^{-7}$  m was used throughout this modelling. For the time spacing ( $\Delta t$ ), a constant of  $1 \times 10^{-9}$  s was used for the entire programme.

## 7.2.2 Heat source

In this work, the thermal behaviour is triggered by an external heat source i.e. a pulsed electron beam. The heat source is described by the following equation [138].

$$L_v(x,t) = \frac{J(t)E_0(t)}{r(t)e} f(x) = \frac{J(t)C_a(t)}{r(t)} f(x) \quad \text{Eq. 7-21}$$

where  $L_v(x,t)$  is the volume power density of the heat source ( $\text{W}/\text{m}^3$ ),  $J(t)$  is the current density ( $\text{A}/\text{m}^2$ ),  $E_0(t)$  is the electron energy (keV),  $e$  is electron charge (Coulomb),  $C_a(t)$  is the cathode voltage of electron beam (V),  $r(t)$  is electron range (m) i.e. the maximum penetration depth of electrons in the target, and  $f(x)$  is the distribution function of electron energy losses in depth  $x$ .  $f(x)$  can be expressed by a third-degree polynomial [138] as follows:

$$f(x) = 1 - \frac{9}{4} \left( \frac{x}{r(t)} - \frac{1}{3} \right)^2, x \in [0; r] \quad \text{Eq. 7-22}$$

while  $r(t)$  was found from the formula [138] as follows:

$$r(t) = C_0 \left[ \frac{E_0(t)}{e} \right]^{\frac{3}{2}} / \rho = C_0 [C_a(t)]^{\frac{3}{2}} / \rho \quad \text{Eq. 7-23}$$

where  $C_0$  is a constant equal to  $10^{-4} \text{ kg}/\text{m}^2 \cdot \text{V}^{3/2}$  and  $\rho$  is the density of material.

To quantify the energy input in the LAEB treatment, the energy input  $Q_0$  can be calculated based on  $L_v(x,t)$  and the pulse duration of electron beam ( $\tau$ ).

$$Q_0 = L_v(x,t)\tau V = \int_0^r \frac{J(t)C_a(t)\tau}{r(t)} Af(x)dx \quad \text{Eq. 7-24}$$

To simplify the calculation,  $J(t)$  and  $C_a(t)$  were assumed to be independent from the time, i.e.  $J$  and  $C_a$ , respectively. For our electron beam equipment, the

maximum energy density ( $E$ ) and cathode voltage ( $C_a$ ) is  $1 \times 10^5 \text{ J/m}^2$  and 40 kV respectively. The pulse duration ( $\tau$ ) used in the model is  $1 \times 10^{-6} \text{ s}$ . The energy density ( $E$ ) can be written as:

$$E = C_a J \tau \quad \text{Eq. 7-25}$$

Rearranging **Eq. 7-25**, the current density ( $J$ ) can be calculated as follows:

$$J = E / C_a \tau = \frac{1 \times 10^5 \text{ J/m}^2}{4 \times 10^4 \text{ V} \times 1 \times 10^{-6} \text{ s}} = 2.5 \times 10^6 \text{ A/m}^2 \quad \text{Eq. 7-26}$$

Considering the practical fluctuation of the energy density of the electron beam, 80% of the maximum current density was used, i.e.  $2 \times 10^6 \text{ A/m}^2$ . **Table 7-2** lists the parameters of the LAEB heat source and other constants.

**Table 7-2 Parameters of LAEB heat source and the details of sample.**

Symbols	Parameter	Unit	Value
$E$	Energy density	$\text{J/m}^2$	$1 \times 10^5$
$J(t), J$	Current density	$\text{A/m}^2$	$2 \times 10^6$
$C_a(t), C_a$	Cathode voltage	V	varied
$\tau$	Pulse duration	s	$1 \times 10^{-6}$
$A$	Sample area	$\text{m}^2$	$2.25 \times 10^{-4}$
$D$	Sample thickness	m	$3 \times 10^{-3}$

In this work, the energy input varied because different cathode voltages were used, which can be calculated according to **Eq. 7-24**. Based on the energy input, the overall temperature increase was also estimated as follows:

$$\Delta T_0 = \frac{Q_0}{\rho c A D} \quad \text{Eq. 7-27}$$

where  $\Delta T_0$  is the overall temperature increase of irradiated material by the single pulse LAEB treatment,  $A$  and  $D$  are the sample area ( $2.25 \times 10^{-4} \text{ m}^2$ ) and thickness ( $3 \times 10^{-3} \text{ m}$ ), respectively. The overall temperature increase of the single pulse LAEB irradiation for different cathode voltages is listed in **Table 7-3**.

**Table 7-3 Energy input and theoretical overall temperature increase (1 pulse) under different cathode voltages for pure Al, Al-Cu and Al-Co-Ce alloys.**

Material	Cathode voltage $C_a$ (kV)	Total energy input of 1-pulse irradiation $Q_0$ (J)	Theoretical temperature increase of 1-pulse irradiation $\Delta T_0$ (K)
Al	35	12.19	7.53
Al-Cu	35	12.34	6.71
Al-Co-Ce alloy 3	15	5.72	2.58
	22	8.1	3.66
	29	10.37	4.68
	35	12.28	5.54
	40	14	6.32

### 7.2.3 Latent heat

In the heating and cooling of the materials, when the temperature of materials reaches some specific levels, such as melting point or phase transition temperature, latent heat will be absorbed or released accompanied by the phase transition. Therefore, latent heat is a very important factor to influence the thermal behaviour of the materials, which needs special consideration in the simulation.

To simplify the simulation, only latent heat of melting (solidification) was considered in this work, and an equivalent heat method was used. In this equivalent heat method, the latent heat will be equivalently converted to the temperature change. This equivalent temperature change or temperature compensation will be added or subtracted to the corresponding nodal temperature.

For example, in the melting of the material, the absorbed heat  $Q_L$  of the material with a volume element of  $\Delta V$  is

$$Q_L = H_m \rho \Delta V \quad \text{Eq. 7-28}$$

The temperature decrease ( $\Delta T_{cm}$ ) of the volume of material resulting from this heat absorption is

$$\Delta T_{cm} = \frac{Q_L}{\rho c \Delta V} \quad \text{Eq. 7-29}$$

Therefore,  $\Delta T_{cm} = \frac{H_m}{c}$ , where  $H_m$  is the latent heat of fusion (J/kg),  $c$  is the specific heat at the melting point of the material and  $\rho$  is the density of the material (kg/m<sup>3</sup>).

In this work, for the simulation of this absorption of latent heat, the temperature of a volume element remains at the melting point by compensating a negative temperature over a number of time steps until the accumulated temperature compensation reaches  $\Delta T_{cm}$ , i.e. the latent heat is accounted for. Similarly, for the solidification process, the same temperature compensation of  $\Delta T_{cm}$  during the release of latent heat is used. It should be noted that this is based on an assumption that the material has the same latent heat before and after experiencing remelting. The consideration of the latent heat in calculation is shown in **Figure 7-3**.

#### 7.2.4 Physical and thermal properties of alloys

In this numerical calculation, three materials including pure aluminium, Al-Cu eutectic alloy and Al-Co-Ce alloy 3 were modelled. The sample thickness and area for all three materials were  $3 \times 10^{-3}$  m and  $2.25 \times 10^{-4}$  m<sup>2</sup>, respectively. **Table 7-4** lists the physical and thermal properties of the three materials. The properties of pure Al and Al-Cu alloy are from references [165, 170].

As for the as-cast Al-Co-Ce alloy, the density was obtained through measuring the volume and mass of the samples using a pycnometer (AccuPyc 1330) and an analytical balance with the accuracy of 0.1 mg (OHAUS). The melting point and the latent heat of the as-cast Al-Co-Ce alloy were achieved through DSC analysis,

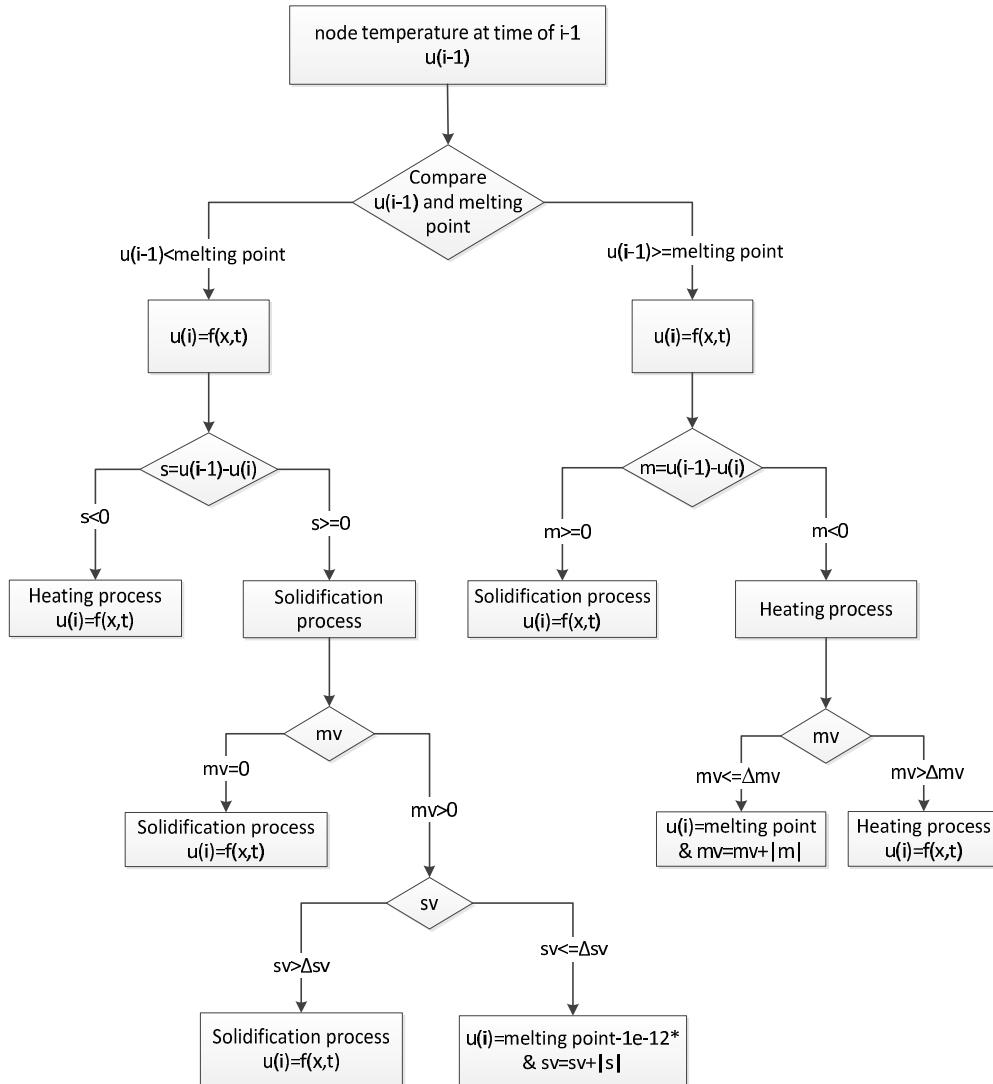
as presented in **Appendix 2**. Specific heat and thermal conductivity of as-cast Al-Co-Ce alloy 3 at room temperature were measured using a laser flash apparatus (LFA 472, NETZSCH), and all measurements were carried out by the Advanced Materials Research Laboratory at the University of Strathclyde, UK (see **Appendix 3**).

**Table 7-4 Physical and thermal properties of the three materials.**

Property	symbol	Unit	Value		
			Pure Al	Al-Cu	Al-Co-Ce
Density	$\rho$	kg/m <sup>3</sup>	2710	3840	3740
Melting point	$T_m$	K	933	821	1308
Latent heat of fusion and solidification	$H_m$	10 <sup>5</sup> J/kg	3.87	3.42	1.60
Heat capacity	$c$	J/kg·K	885	710	877
Thermal conductivity	$\lambda$	W/m·K	239.9	125.0	60.5
Temperature compensation for the latent heat of fusion and solidification	$\Delta T_{cm}$	K	362.0	481.7	182.8

### 7.2.5 Programme flow chart

Figure 7-3 is the programme flow chart of the simulation. The programme code was written using Matlab 7.12.0 compiler language (see Appendix 4).



**Notes:**

- (1) This flow chart gives the programme for the calculation of the temperature at time step  $i$ .
- (2)  $f(x,t)$  represents the finite difference equation. The interior nodes and the nodes at the boundaries have different equations.
- (3)  $s$  and  $m$  represent the temperature difference between time  $i$  and  $i-1$ ,  $mv$  and  $sv$  represent the accumulated temperature compensation for the melting and solidification process, respectively.
- (4)  $\Delta mv$  and  $\Delta sv$  represent the total temperature compensation for the melting and solidification process, respectively.

**Figure 7-3 Flow chart of the programme.**

## 7.3 Results

### 7.3.1 Validation of code

To validate the code, the energy in the entire sample at different time was calculated based on the calculation results assuming the adiabatic boundary conditions for both ends of the sample. Adiabatic boundary conditions indicate that there was not heat flux flowing out of the sample. Therefore, the temperature change of the sample should obey the energy conservation law.

The total energy at time of  $i$  was added up for the whole thickness of the sample i.e. all the nodes ( $j=1\sim N+1$ ). The total energy  $Q_{total}^i$  was calculated according to the equation below:

$$Q_{total}^i = \sum_{j=1}^{j=N+1} c \rho A \Delta x \Delta T_i^j \quad \text{Eq. 7-30}$$

where  $c$  is the heat capacity,  $A$  and  $\rho$  is the area and density of the sample, respectively,  $\Delta x$  is the spatial spacing, and  $\Delta T_i^j$  is the temperature increase of node  $j$  at time of  $i$ .

**Figure 7-4** shows the temperature distribution of pure Al at different time steps of 1 pulse LAEB treatment (The pulse duration is  $1 \times 10^{-6}$  s.). When the time is  $10^{-5}$  s and  $10^{-4}$  s, the surface temperature of the irradiated sample was found to be apparently higher than the below substrate where the temperature was still at the initial temperature. However, the temperature redistribution occurred with increasing time. When the time is 0.1 s, the temperature of the entire sample was almost the same. In other words, the sample began to have a uniform temperature.

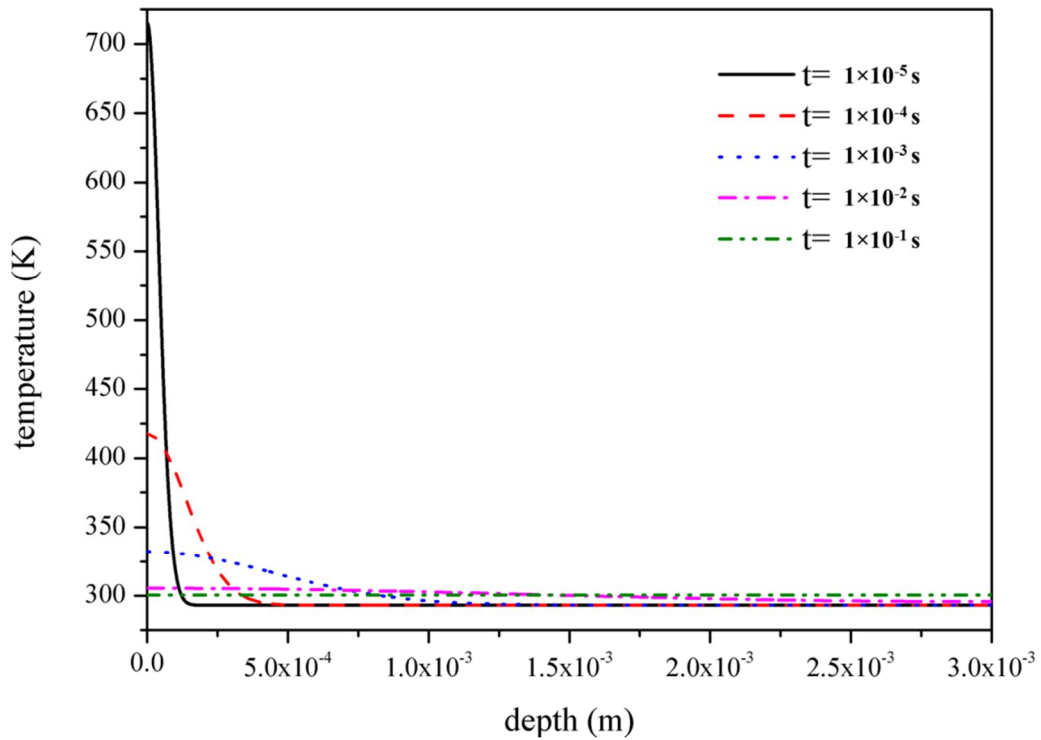


**Figure 7-4 Temperature versus depth in pure Al at different time steps of the 1 pulse LAEB treatment.**

**Table 7-5** lists the variation of total energy in the irradiated pure Al sample (35kV, 1 pulse) after switching off the heating from the external heat source i.e. electron beam. The original energy input is 12.19 J based on the calculation shown in **section 7.2.2 (Table 7-3)**. It can be seen that the total energy slightly decreased with time. However, the difference from the original energy input started to become stable when the time increased to  $1 \times 10^{-2}$  s. The absolute error and relative error were 0.34393 J and 2.82%, respectively. Such small errors indicate that the code used in this work is valid.

**Table 7-5 Variation of total energy in the irradiated pure Al sample with time under 35 kV cathode voltage (1 pulse).**

Time (s)	Energy (J)	Absolute error (J)	Relative error (%)
$1 \times 10^{-5}$	11.90528	0.28903	2.37
$1 \times 10^{-4}$	11.86516	0.32915	2.70
$1 \times 10^{-3}$	11.85365	0.34066	2.79
$1 \times 10^{-2}$	11.85038	0.34393	2.82
$1 \times 10^{-1}$	11.85033	0.34398	2.82

## 7.3.2 Estimation of heat transfer coefficient

### 7.3.2.1 Experimental and theoretical overall temperature increase

Based on the temperature labelling measurement conducted on the pure Al sample, it was found the temperature at the bottom of the samples reached 327 K, 355 K and 372 K when samples were irradiated with 50, 100 and 150 pulses of LAEB treatment, respectively (This is presented in **Section 3.4.2**). The initial temperature of the sample for these measurements was 293 K, therefore, the experimental temperature increase ( $\Delta T_{N_p}^{\text{exp}}$ ) relative to initial temperature (293 K) was 34, 62 and 79 K for the above corresponding number of pulses of LAEB treatment, respectively. Based on these temperature increases, the experimental energy increase by the above pulses of LAEB treatment ( $Q_{N_p}^{\text{exp}}$ ) can be calculated as below:

$$Q_{N_p}^{\text{exp}} = c\rho AD\Delta T_{N_p}^{\text{exp}} \quad \text{Eq. 7-31}$$

It has been calculated that the energy input ( $Q_0$ ) and theoretical temperature increase per pulse LAEB treatment ( $\Delta T_0$ ) for pure Al under 35 kV cathode voltage are 12.19 J and 7.53 K (**Table 7-3**). Therefore, the total energy input ( $Q_{N_p}$ ) and total theoretical temperature increase caused by  $N_p$  pulses of LAEB treatment ( $\Delta T_{N_p}$ ) can be calculated by

$$Q_{N_p} = Q_0 N_p \quad \text{Eq. 7-32}$$

$$\Delta T_{N_p} = N_p \Delta T_0 \quad \text{Eq. 7-33}$$

In this work, the difference in both temperature increase ( $\Delta T_{N_p} - \Delta T_{N_p}^{\text{exp}}$ ) and energy increase ( $Q_{N_p} - Q_{N_p}^{\text{exp}}$ ) between the experimental and the theoretical value

was calculated. **Table 7-6** shows the comparison of theoretical and experimental results in the temperature increase and energy increase, as well as the fraction of the experimental energy loss in the total theoretical energy input. It can be seen that more than 90% of the input energy was lost during the LAEB treatment. These losses are primarily attributed to the heat conduction to the sample clamp. In addition, the fraction energy loss also increased with increasing number of pulses. **Figure 7-5** shows the plot of the fraction of energy loss against the number of pulses, as well as the fitted function. **Table 7-6** also lists the average experimental temperature increase by 1-pulse LAEB treatment ( $\Delta T_0^{exp}$ ) as 0.68, 0.62 and 0.53 K, respectively.

**Table 7-6 Theoretical and experimental temperature increase and energy increase for different number of pulses LAEB treated pure Al under 35 kV cathode voltage.**

Parameters	Number of pulses, $N_p$		
	50	100	150
Total experimental temperature increase, $\Delta T_{N_p}^{exp}$ (K)	34	62	79
Total theoretical temperature increase, $\Delta T_{N_p}$ (K)	376.71	753.42	1130.14
Difference in total temperature increase between experimental and theoretical value, $\Delta T_{N_p} - \Delta T_{N_p}^{exp}$ (K)	342.71	691.42	1051.14
Experimental temperature increase from 1 pulse LAEB treatment, $\Delta T_0^{exp}$ (K)	0.68	0.62	0.53
Experimental energy increase, $Q_{N_p}^{exp}$ (J)	50.03	100.35	127.86
Total theoretical energy input, $Q_{N_p}$ (J)	609.72	1219.43	1829.15
Total energy loss, $Q_{N_p} - Q_{N_p}^{exp}$ (J)	554.69	1119.08	1701.28
$f(Q_{N_p}) = \frac{Q_{N_p} - Q_{N_p}^{exp}}{Q_{N_p}}, \%$	90.97	91.77	93.01

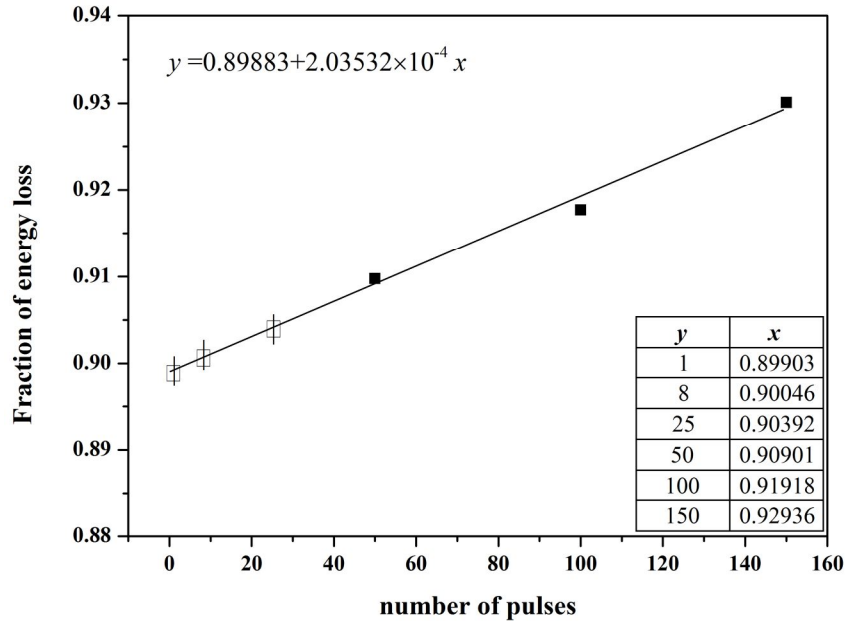


**Figure 7-5 Fraction of energy loss versus number of pulses for pure Al. Solid dots are experimental results. Hollow dots are the results from the fitted function. The function and values are shown in the figure.**

### 7.3.2.2 Estimation of heat transfer coefficient

According to the boundary conditions, the total heat loss  $Q_{bd}$  can be written as:

$$Q_{bd} = Q_r + Q_f \quad \text{Eq. 7-34}$$

where  $Q_r$  and  $Q_f$  represent the heat fluxes flowing out of the irradiated sample from the top surface and bottom surface, respectively.  $Q_r$  and  $Q_f$  can be expressed with  $\varepsilon$  and  $h$ , as well as the temperature of the nodes at the boundaries.

**For the top surface:**

$$Q_r = \sum_{i=0}^{i=11s} \sigma \varepsilon [(T_1^i)^4 - (T_{surr})^4] A \Delta t \quad \text{Eq. 7-35}$$

where  $T_1^i$  is the temperature of the node at the top surface of the sample,  $\varepsilon$  is equal to 0.06 which is the value for the highly polished aluminium plate at 577°C. Based on the preliminary calculation performed with the adiabatic boundary conditions,  $T_1^i$  between 0 and 0.1 s were obtained. According to **Eq. 7-35**, the

energy of radiation is very weak when the boundary temperature is close to the surrounding temperature. **Figure 7-4** shows that when the time was 0.1 s, the temperature of the treated sample at the top surface has been stable at 300.32 K. Therefore, considering the consumption of the calculation time, energy loss between 0 and 0.1 s was thought to be equal to the  $Q_r$ , which is 0.00127 J.

**For the bottom surface:**

$$Q_f = \sum_{i=0}^{i=11s} h(T_{N+1}^i - T_{surr})A\Delta t \quad \text{Eq. 7-36}$$

The heat loss is still significant even the temperature has been close to the surrounding temperature. Therefore, it is necessary to know the temperature of the node at the bottom surface of the sample during the whole 11 seconds. Here, assumptions below were made to estimate  $T_{N+1}^i$  and the total heat loss:

- (a) The maximum temperature obtained from the temperature labelling measurement is the temperature of the node at the bottom surface at the time of 11 seconds;
- (b) The temperature increase in each pulse of LAEB treatment is constant (0.68 K);
- (c) The temperature of the sample at the bottom surface increased linearly;
- (d) For 1-pulse treatment, the sample temperature at the bottom surface increased to 293.68 K at the time of 11 s;
- (e) The temperature of surroundings ( $T_{surr}$ ) is a constant during the individual irradiation process.

Based on the temperature labelling measurement, the heat loss ( $Q_{bd}$ ) also can be expressed by:

$$Q_0 = Q_{bd} + c\rho AD\Delta T_0 \quad \text{Eq. 7-37}$$

where  $Q_0$  is the total energy input of the heat source (12.19 J according to **Table 7-3**),  $\Delta T_0$  is the experimental temperature increase of 1-pulse treatment (0.68 K according to assumption (b)),  $A$  and  $D$  are the sample area and thickness, respectively.

Based on the above assumption (c), the function of temperature at the bottom surface of the sample ( $T_{N+1}^i$ ) and time is expressed by:

$$T_{N+1}^i(t) = 293 + 0.06182t \quad \text{Eq. 7-38}$$

Substituting **Eq. 7-38** into **Eq. 7-36**, **Eq. 7-36** can be rewritten as follow:

$$Q_{bd} = \left[ \sum_{t=0}^{t=11s} h(293 + 0.06182t - T_{surr})A\Delta t \right] + Q_r \quad \text{Eq. 7-39}$$

where  $Q_{bd}$  can be obtained from **Eq. 7-37**,  $h$  in **Eq. 7-39** is thereby solved.  $h=13000 \text{ W/m}^2\text{K}$ , if  $Q_r \approx 0$ .

### 7.3.3 Number of LAEB pulses and equivalent initial temperature

Before LAEB treatment, the sample is at room temperature (293 K), and the temperature of the sample surface will increase immediately when the first LAEB pulse irradiates the sample, and finally gets redistributed and uniform within the entire sample. This new balanced temperature will be kept until the next pulse of irradiation is applied. When the next pulse irradiates the sample, the temperature increases again and then gains the new stable temperature and the sample will wait for the next pulse. This repetitive procedure will continue until the desired number of pulses is applied to the sample. From **Figure 7-4**, it is clearly seen that the

sample reaches the stable temperature within a short time ( $\sim 0.1$  s), which is far shorter than the pulse interval time of 11 s.

The effect of the number of pulses on the irradiated samples is significant in understanding the LAEB process. However, based on the above repetitive procedure of LAEB treatment, if one aims to simulate the LAEB process with a few pulses, the single pulse programme needs to be repeated a specific number of times. In practice, for the sample in the above repetitive procedure, initial temperature of the sample is the only different parameter between two neighbouring pulses of irradiation. In this work, in order to avoid the long calculation time, the equivalent initial temperature of the sample was used to simplify the simulation of the multi-pulse LAEB process.

In this work, the energy input from each pulse of LAEB treatment was assumed to be constant, which theoretically results in a constant temperature increase. **Table 7-2** has presented the theoretical value of temperature increase within the entire sample after a single pulse of LAEB irradiation. The initial temperature for the specific individual pulse of LAEB irradiation (with the pulse sequence number of  $N_p^{th}$ ) can hence be calculated by adding up the temperature increases from the previous LAEB pulse(s). This means increasing the number of pulses is equivalent to accumulating the temperature increase from the previous LAEB pulse(s).

However, from the temperature labelling measurement it has been seen that the experimental temperature increase is much lower than the theoretical one. **Table 7-6** and **Figure 7-5** have shown the energy loss fraction as a function of the number of pulses for pure Al. Considering the similar cooling conditions, it is assumed that the LAEB treated Al-Cu eutectic and Al-Co-Ce alloy have the same

energy loss fraction as pure Al. Therefore, the estimated energy increase  $Q_{N_p-1}^{est}$  for LAEB treated Al-Cu and Al-Co-Ce alloys when  $N_p-1$  pulses of LAEB treatment are performed can be calculated as follows:

$$Q_{N_p-1}^{est} = [1 - f(Q_{N_p-1})](N_p - 1)Q_0 \quad \text{Eq. 7-40}$$

where  $Q_0$  is the energy increase from the single pulse treatment (**Eq. 7-24** and **Table 7-3**),  $f(Q_{N_p-1})$  is the fraction of energy loss for  $N_p-1$  pulses of LAEB irradiation (**Table 7-6** and **Figure 7-5**). The temperature increase  $\Delta T_{N_p-1}^{est}$  caused by this energy increase can be calculated according to the equation below:

$$\Delta T_{N_p-1}^{est} = \frac{Q_{N_p-1}^{est}}{\rho c A D} \quad \text{Eq. 7-41}$$

Thus, the initial temperature for the next pulse LAEB treatment (with the pulse sequence number of  $N_p^{th}$ ) is  $T_i + \Delta T_{N_p-1}^{est}$ . In other words, after  $N_p-1$  pulses of LAEB treatment, the initial temperature of the next LAEB pulse (i.e. the  $N_p^{th}$  pulse) is  $T_i + \Delta T_{N_p-1}^{est}$ . **Table 7-7** lists the estimated initial temperature for the individual  $N_p^{th}$  pulse LAEB irradiation after  $N_p-1$  pulses of treatment under 35 kV cathode voltage for both Al-Cu alloy and Al-Co-Ce alloy. **Table 7-8** lists the estimated initial temperature of Al-Co-Ce alloy for the 100<sup>th</sup> pulse LAEB irradiation under different cathode voltages.

**Table 7-7 Estimated initial temperature for the  $N_p^{th}$  pulse LAEB irradiation after  $N_p-1$  pulses of treatment under 35 kV cathode voltage.**

Alloy	$N_p-1$	Theoretical energy input from $N_p-1$ of pulses treatment, $Q_{N_p-1}$ (J)	Fraction of energy loss for $N_p-1$ pulses of treatment, $f(Q_{N_p-1})$	Estimated energy increase from $N_p-1$ pulses of treatment, $Q_{N_p-1}^{est}$ (J)	Estimated temperature increase caused by $N_p-1$ pulses of treatment, $\Delta T_{N_p-1}^{est}$ (K)	Estimated initial temperature $T_i$ for the $N_p^{th}$ pulse treatment, $T_i + \Delta T_{N_p-1}^{est}$ (K)
Al-Cu	7	86.38	0.90025	8.61	4.68	297.68
	24	296.16	0.90371	28.52	15.50	308.5
	49	604.66	0.90880	55.14	29.96	322.96
	99	1221.66	0.91898	98.98	53.78	346.78
	149	1838.66	0.92916	130.26	70.78	363.78
Al-Co-Ce	7	85.96	0.90025	8.57	3.87	296.87
	14	171.92	0.90168	16.9	7.63	300.63
	24	294.72	0.90371	28.38	12.82	305.82
	49	601.72	0.9088	54.88	24.79	317.79
	99	1215.72	0.91898	98.5	44.49	337.49
	149	1829.72	0.92916	129.62	58.55	351.55

**Table 7-8 Estimated initial temperature of Al-Co-Ce alloy for the 100<sup>th</sup> pulse irradiation under different cathode voltages.**

Cathode voltage, $C_a$ (kV)	Total energy input of 1-pulse treatment $Q_0$ (J)	Theoretical energy input from 99 pulses of treatment, $Q_{99}$ (J)	Fraction of energy loss for 99 pulses of treatment, $f(Q_{99})$	Estimated energy increase from 99 pulses of treatment, $Q_{99}^{est}$ (J)	Estimated temperature increase caused by 99 pulses of treatment, $\Delta T_{99}^{est}$ (K)	Estimated initial temperature $T_i$ for the 100 <sup>th</sup> pulse treatment, $T_i + \Delta T_{99}^{est}$ (K)
15	5.72	566.28	0.91898	45.88	20.72	313.72
22	8.1	801.9	0.91898	64.97	29.35	322.35
29	10.37	1026.63	0.91898	83.18	37.57	330.57
35	12.28	1215.72	0.91898	98.50	44.49	337.49
40	14	1386	0.91898	112.29	50.72	343.72

### 7.3.4 Modelling results of Al-Cu alloy

**Figure 7-6** shows the near-surface temperature of the 1 pulse of LAEB treated Al-Cu alloy with time under 35 kV cathode voltage. Overall, the remelting and solidification of the LAEB treated sample mainly occurred in a very short time and small depth. The thickness of the remelted layer was less than approximately 15  $\mu\text{m}$ . This remelted layer completed remelting and solidification within approximately 6  $\mu\text{s}$ . In addition, it can be seen that the remelting process was faster than the solidification process at the same depth. In this section, the number of pulses is changed to investigate the effect on the thermal behaviour of LAEB treated Al-Cu alloy. Parallel with the experimental work shown in **Chapter 4**, the number of pulses was 1, 8, 25, 50, 100 and 150.

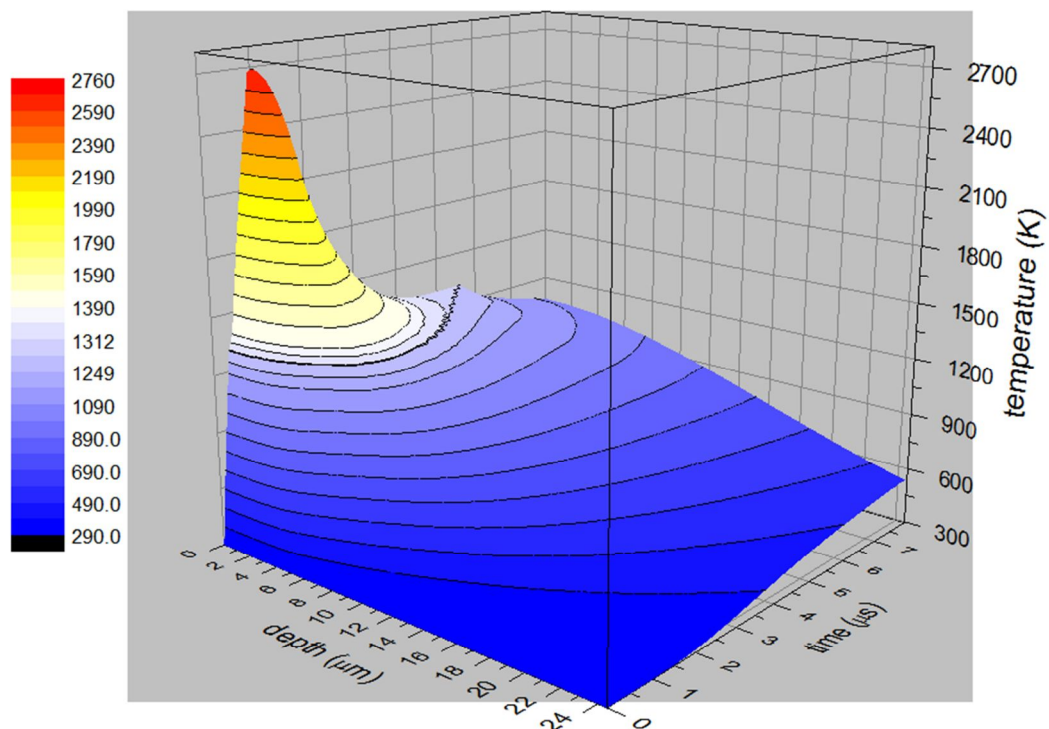


**Figure 7-6** Near-surface temperature field of 1 pulse of LAEB treated Al-Cu alloy at the under 35 kV cathode voltage.

### 7.3.4.1 Thickness of the LAEB remelted layer

The thickness of the LAEB remelted layer can be determined by the maximum temperature of the irradiated sample at different depths. Once the maximum temperature is higher than the melting point, the material will undergo remelting. Therefore, this thickness ( $d_m$ ) describes the maximum depth of the irradiated layer where it has reached the melting point. However, it should be noted that the thickness of the LAEB remelted layer is not equal to the compositionally homogenised thickness of the irradiated layer if the melting time is insufficient.

**Figure 7-7** plots the remelted layer thickness of the LAEB treated Al-Cu alloy against the initial temperature under 35 kV cathode voltage. It can be seen that the thickness of the remelted layer was between 12 and 14  $\mu\text{m}$ , which did not increase very much with increasing initial temperature. The comparison of this calculated thickness and experimental homogenised layer thickness shown in **Chapter 4** will be presented in **Section 7.4.2**.

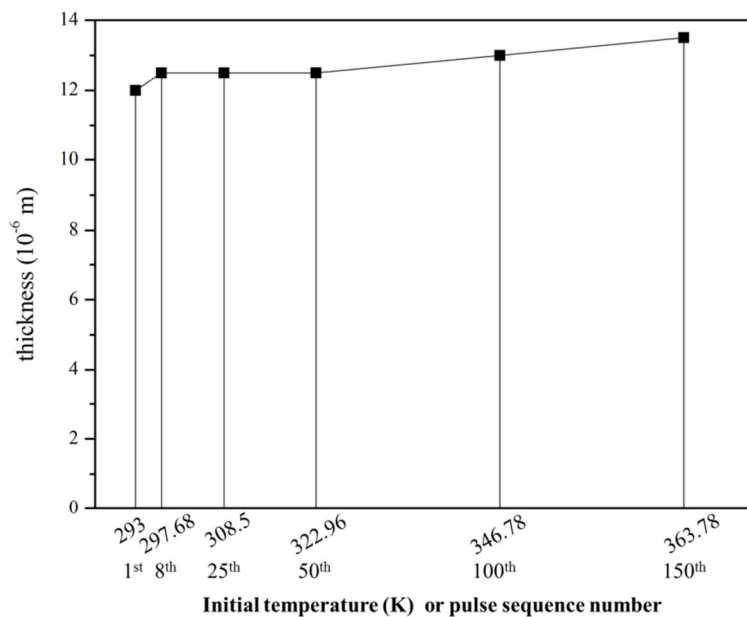


**Figure 7-7 Remelted layer thickness of the LAEB treated Al-Cu alloy versus initial temperature (pulse sequence number) at 35 kV cathode voltage.**

### 7.3.4.2 Melting time

Due to the pulsed nature of the LAEB process, the remelting and even homogenisation of the treated layer is attributed to the accumulated effect of the multi-pulse irradiation. In addition to the temperature, the melting time is also significant for the irradiated material to determine the extent of remelting, diffusion and homogenisation. Based on the modelling results, the melting time of the single-pulse LAEB irradiated layer was thus calculated in this work. The melting time of the treated layer at different depths was calculated as follows:

$$t_0^j = t_{melt}^j - t_{solid}^j \quad \text{Eq. 7-42}$$

where  $t_0^j$  is the time difference between the node  $j$  starting melting at time  $t_{melt}^j$  and completing solidification at time  $t_{solid}^j$ . This melting time can describe the time duration of the sample being at and above the melting point, i.e. the time of the sample in the liquid form. Therefore, a longer melting time means a higher extent of diffusion and homogenisation of the remelted layer.

**Figure 7-8** shows the melting time of the single-pulse LAEB treated layer with different initial temperatures (i.e. pulse sequence numbers) at different depths under 35 kV cathode voltage. It can be seen that the higher initial temperature resulted in a longer melting time at all depths. With decreasing initial temperature, the melting time decreased. However, it should be noted that the melting time difference between different initial temperatures was small. In addition, for all cases (different initial temperatures), the melting time of the treated layer also decreased with increasing depth.

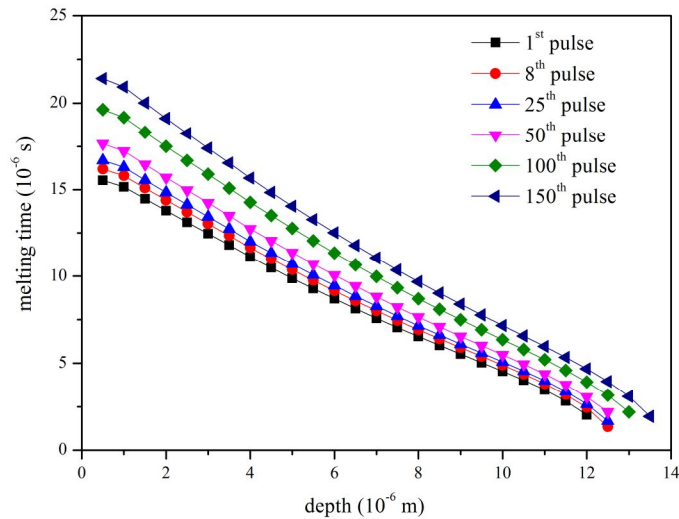


**Figure 7-8 Melting time of the LAEB treated layer versus depths in Al-Cu alloy with different initial temperatures (pulse sequence numbers) at 35 kV cathode voltage.**

In particular, the melting time at the top surface of the treated layer with different initial temperatures (pulse sequence numbers) is shown in **Figure 7-9**. It can be seen that the melting time linearly increased with the initial temperature, i.e. pulse sequence number. The fitting function of their relationship is also shown in **Figure 7-9**. The relationship between the melting time and experimental homogenised layer thickness will be presented in **Section 7.4.3**.

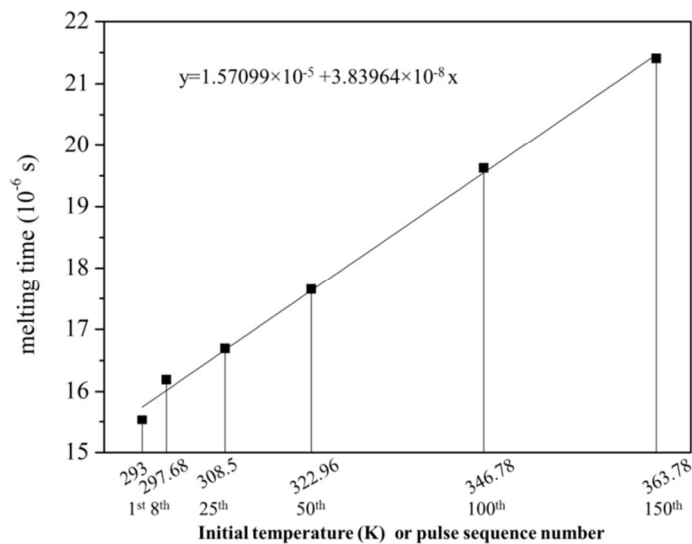


**Figure 7-9 Melting time of the top surface versus initial temperature (pulse sequence number) in the LAEB treated Al-Cu alloy. The fitting function of melting time versus initial temperature (pulse sequence number) is also shown.**

### 7.3.4.3 Solidification velocity $v$ and cooling rate $\nu$

**Figure 7-10** plots the top surface temperature against time of the LAEB treated Al-Cu alloy with different initial temperatures (pulse sequence numbers) under 35 kV cathode voltage. It can be seen that the sample was rapidly heated to the maximum temperature within  $\sim 1 \mu\text{s}$ . However, the solidification process took a much longer time compared with the heating process. In addition, the samples treated with different initial temperatures completed the solidification within different lengths of time. The completion time for the solidification increased with increasing initial temperature.

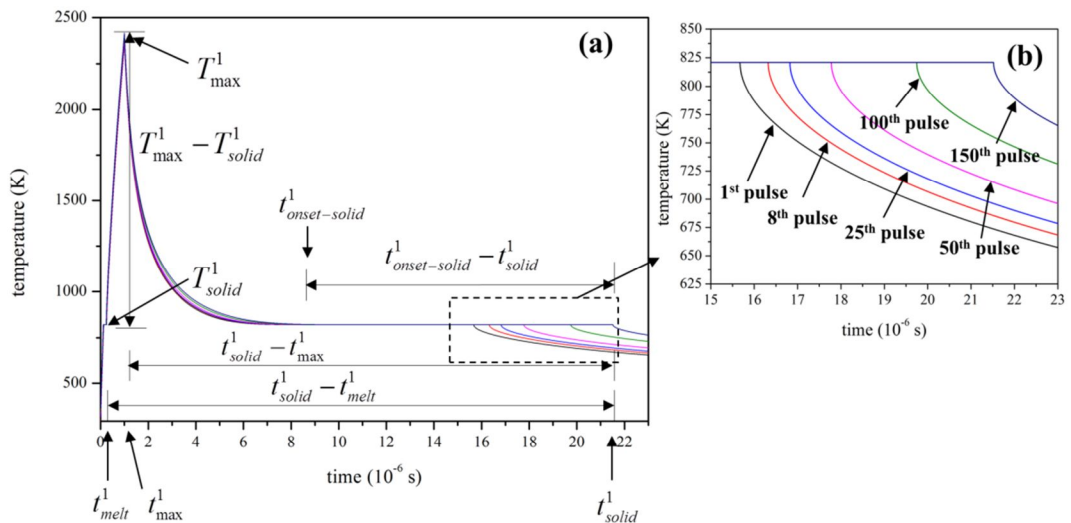


**Figure 7-10** Top surface temperature versus time of the LAEB treated Al-Cu alloy with different initial temperatures (pulse sequence numbers) under 35 kV cathode voltage.

To quantify the solidification process, the solidification velocity and cooling rate were calculated as follows:

**For the solidification velocity,**

$$v = \frac{\sum_{j=1}^{j=N_m} \Delta x / (t_{solid}^j - t_{onset-solid}^j)}{N_m} \quad \text{Eq. 7-43}$$

where  $\Delta x$  is the grid spacing. Node  $j$  starts the solidification at time of  $t_{onset-solid}^j$ , and completes at time of  $t_{solid}^j$ . Over this time period, the temperature of this node is kept at the solidification temperature until the solidification completion.  $N_m$  is the number of the nodes which underwent remelting and solidification. Solidification velocity describes the average moving speed of the solidification front in different depths.

**For the cooling rate,**

$$v = \frac{\sum_{j=1}^{j=N_m} [(T_{max}^j - T_{solid}^j) / (t_{solid}^j - t_{max}^j)]}{N_m} \quad \text{Eq. 7-44}$$

where node  $j$  reaches the maximum temperature of  $T_{max}^j$  at time of  $t_{max}^j$ , and completes the solidification at the temperature of  $T_{solid}^j$  and time of  $t_{solid}^j$  (solidification completion time). Cooling rate  $v$  describes the average rate of the nodes cooling from the maximum temperature to the solidification temperature.

**Figure 7-11** and **Figure 7-12** show the solidification velocity and cooling rate of the LAEB treated layer in Al-Cu alloy with different initial temperatures, respectively. The solidification velocity decreased with increasing initial temperature, which was  $\sim 0.75$  m/s when the initial temperature was 293 K, and decreased to  $\sim 0.57$  m/s when the initial temperature increased to 363.78 K. In addition, overall, the cooling rate of the LAEB treated layer was at the magnitude of  $10^7$  K/s. The resolidified layer of the sample treated with a lower initial temperature was found to have a higher cooling rate compared with that with a higher initial temperature. This is similar to that seen in the solidification velocity.

The comparison of the solidification velocity/cooling rate and experimental results shown in **Chapter 4** will be presented in **Section 7.4.4**.

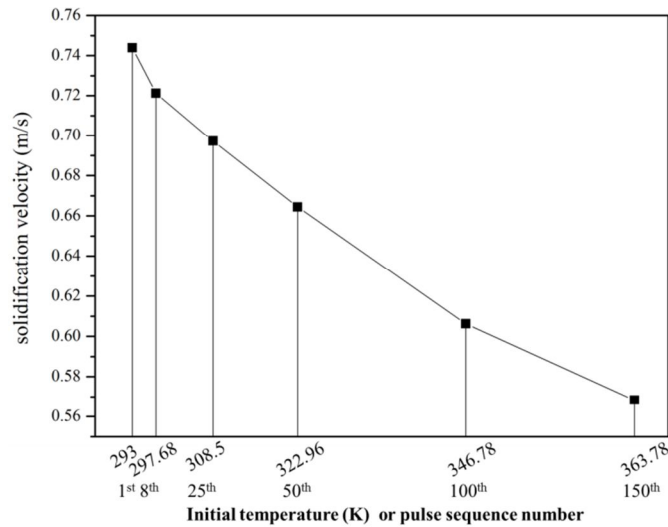


**Figure 7-11 Solidification velocity of the LAEB treated layer in Al-Cu alloy versus initial temperature (pulse sequence number) at 35 kV cathode voltage.**

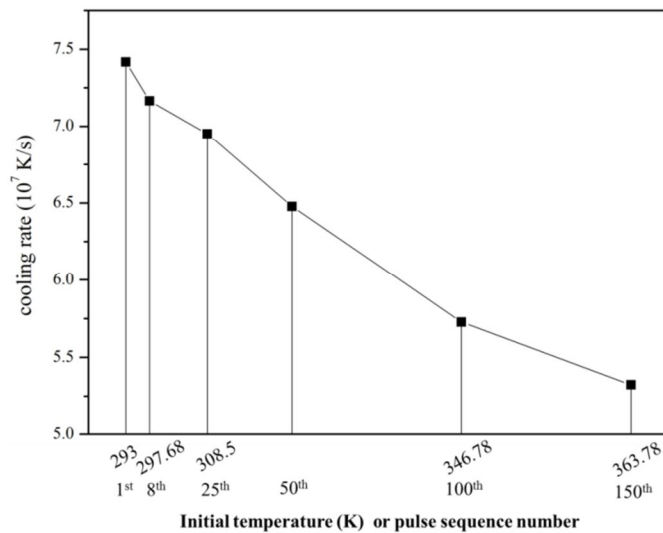


**Figure 7-12 Cooling rate of the LAEB treated layer in Al-Cu alloy versus initial temperature (pulse sequence number) at 35 kV cathode voltage.**

### 7.3.5 Modelling results of Al-Co-Ce alloy 3

**Figure 7-13** shows the near-surface temperature with time in the LAEB treated Al-Co-Ce alloy 3 (35 kV, 1 pulse, initial temperature of 293 K). It can be seen that the sample surface reached the melting point and completed the melting process within a very short time. When the electron beam was turned off at 1  $\mu$ s, the

sample within the electron penetration range ( $5.5 \mu\text{m}$ ) reached the maximum temperature. Overall, the solidification process (the time used for the sample solidifying from the maximum temperature to solidification temperature) was much longer than the heating time (the time used for the sample melting from the melting point to the maximum temperature).

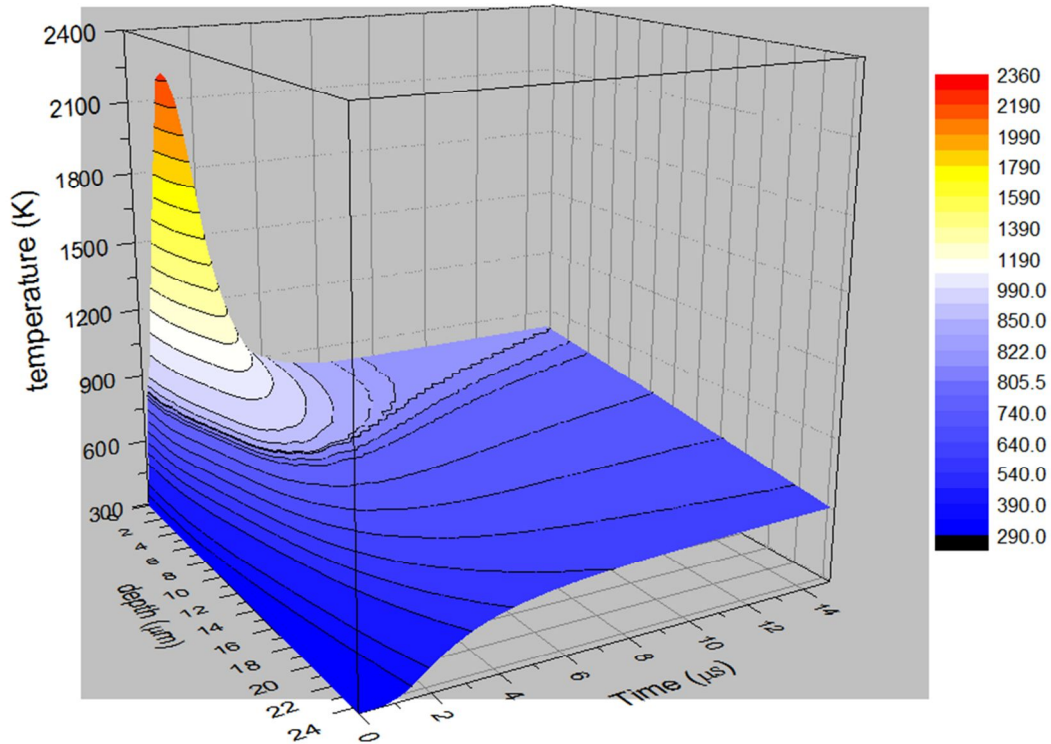


**Figure 7-13 Near-surface temperature field of 1 pulse of LAEB treated Al-Co-Ce alloy under 35 kV cathode voltage.**

In this section, both initial temperature and cathode voltage are changed to investigate their effects on the thermal history of the LAEB treated Al-Co-Ce alloy. The definitions of the thickness of LAEB treated layer, melting time, solidification velocity and cooling rate shown in this section are exactly same as those presented in **Section 7.3.4**. The comparisons of these data and experimental ones shown in **Chapter 6** will be also presented in the **Section 7.4.2, 7.4.3 and 7.4.4**.

### 7.3.5.1 Effect of initial temperature

#### (1) Thickness of LAEB remelted layer

**Figure 7-14** plots the remelted layer thickness against the initial temperature/pulse number. From figure, it can be seen that the thickness of the LAEB remelted layer did not show an apparently change with the increase of the initial temperature/pulse number, which was kept in the range of 7 to 7.5  $\mu\text{m}$ .

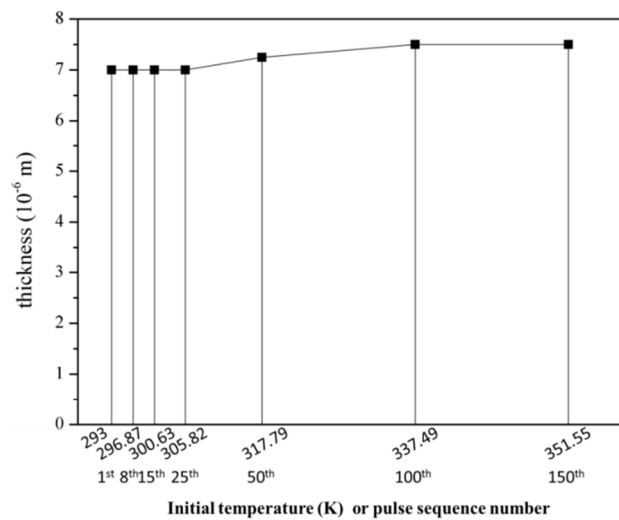


**Figure 7-14** Remelted layer thickness of the LAEB treated Al-Co-Ce alloy versus initial temperature (pulse sequence number) at 35 kV cathode voltage.

#### (2) Melting time

**Figure 7-15** plots the melting time against the depths of single pulse LAEB treated Al-Co-Ce alloy with different initial temperatures (pulse sequence numbers) under 35 kV cathode voltage. It can be seen that when the initial temperature was 351.55 K the sample surface had the longest melting time at all the depth. With decreasing initial temperature, the melting time decreased. However, it should be noted that the melting time difference between different initial temperatures was not large. In addition, for all cases (different initial temperatures), the melting time decreased with increasing depth.

The melting time of the irradiated layer at the top surface of LAEB irradiated Al-Co-Ce alloy is also plotted against the initial temperature i.e. the pulse sequence number (**Figure 7-16**). It can be seen that the melting time also linearly increased with the pulse sequence number as that seen in the modelling of the LAEB treated Al-Cu alloy.

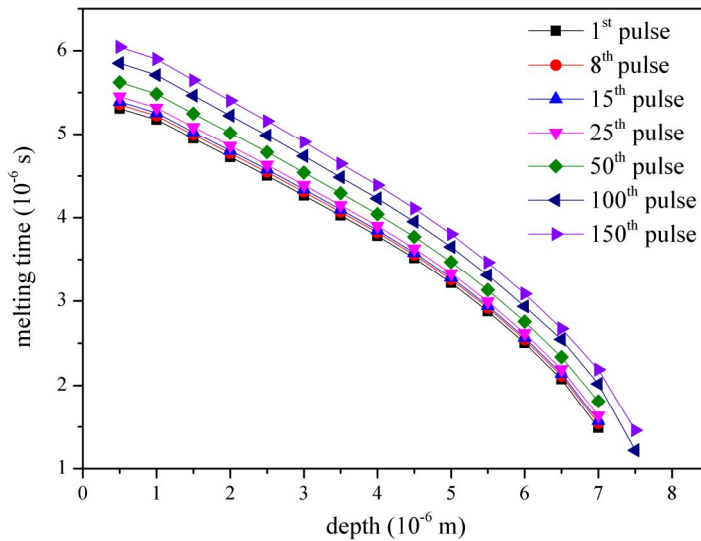


**Figure 7-15 Melting time versus depths of the LAEB treated layer in Al-Cu alloy with different initial temperatures (pulse sequence numbers) at 35 kV cathode voltage.**

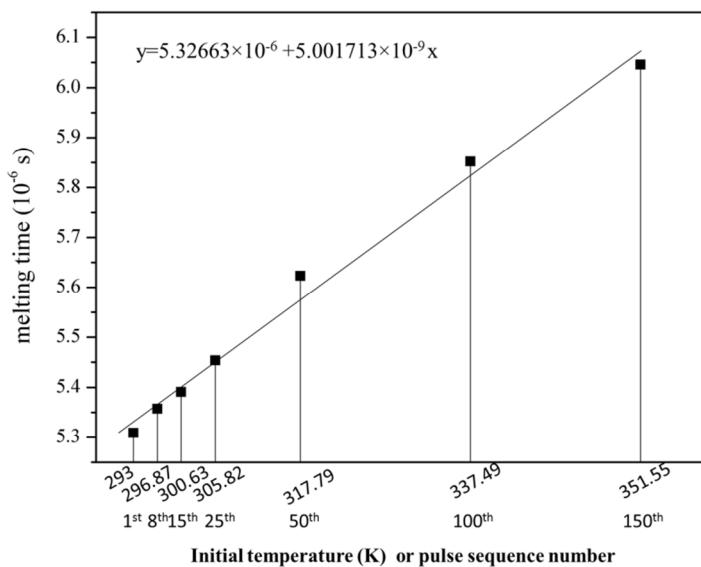


**Figure 7-16 Melting time of the top surface versus initial temperature (pulse sequence number) of the LAEB treated layer in Al-Cu alloy at 35 kV cathode voltage. The fitting function of melting time versus initial temperature (pulse sequence number) is also present.**

### (3) Solidification velocity and cooling rate

**Figure 7-17** plots the top surface temperature against time of the LAEB treated Al-Co-Ce alloy with different initial temperatures (pulse sequence numbers) under 35 kV cathode voltage. Overall, the initial temperature did not affect the top surface temperature very much. The top surface reached the maximum temperature at  $\sim 1 \mu\text{s}$ . During this heating process, there was a very narrow melting plateau. However, during the cooling process, the solidification plateau was much wider. In addition, from the magnified image, the completion time of the solidification increased with increasing initial temperature.

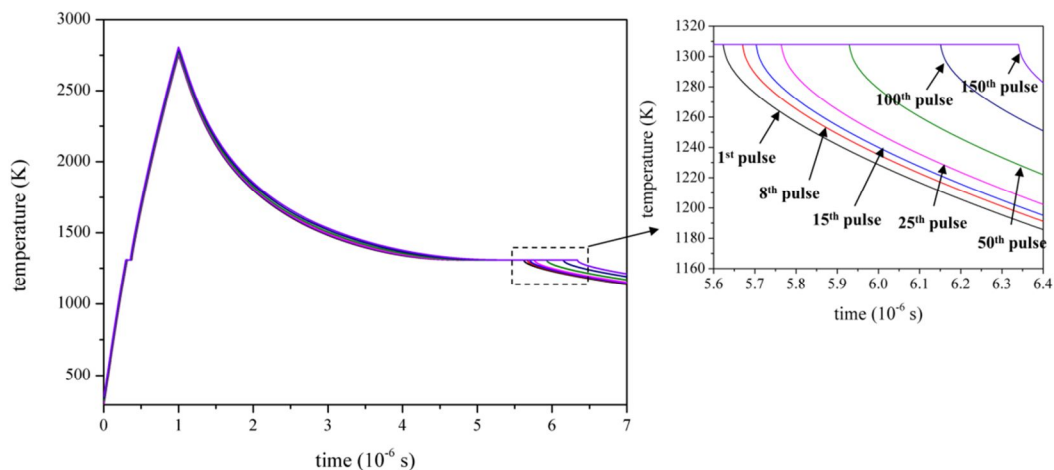


**Figure 7-17 Top surface temperature versus time of the LAEB treated Al-Co-Ce alloy with different initial temperatures (pulse sequence numbers) at 35 kV cathode voltage.**

**Figure 7-18** and **Figure 7-19** show the solidification velocity and cooling rate of the LAEB treated layer in Al-Co-Ce alloy with different initial temperatures (pulse sequence numbers) under 35 kV cathode voltage, respectively. Overall, the solidification velocity decreased with increasing initial temperature. When the initial temperature was 293 K, the velocity was  $\sim 2.30$  m/s. However, when the initial temperature increased to 351.55 K, the velocity decreased to  $\sim 2.08$  m/s.

Overall, the cooling rate of the LAEB treated layer was at the magnitude of  $10^8$  K/s. In addition, the cooling rate of the treated Al-Co-Ce alloy also decreased with increasing initial temperature, which is similar to that seen in the modelling of the LAEB treated Al-Cu alloy. In other words, the treated layer with the lower initial temperature exhibited the larger cooling rate.

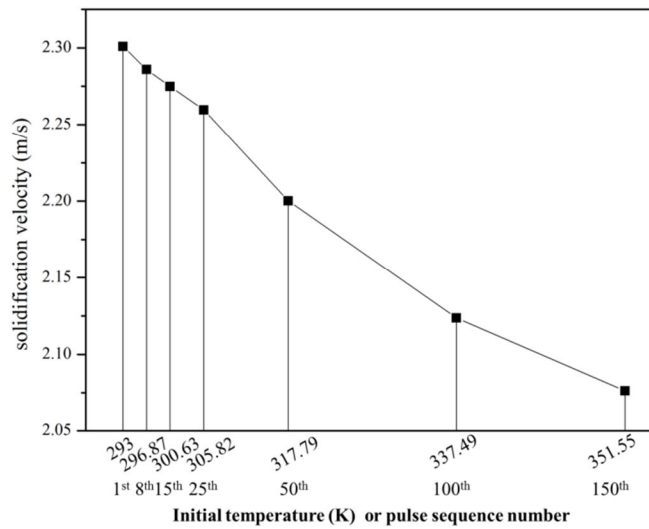


**Figure 7-18 Solidification velocity of the LAEB treated layer versus initial temperature (pulse sequence number) at 35 kV cathode voltage.**

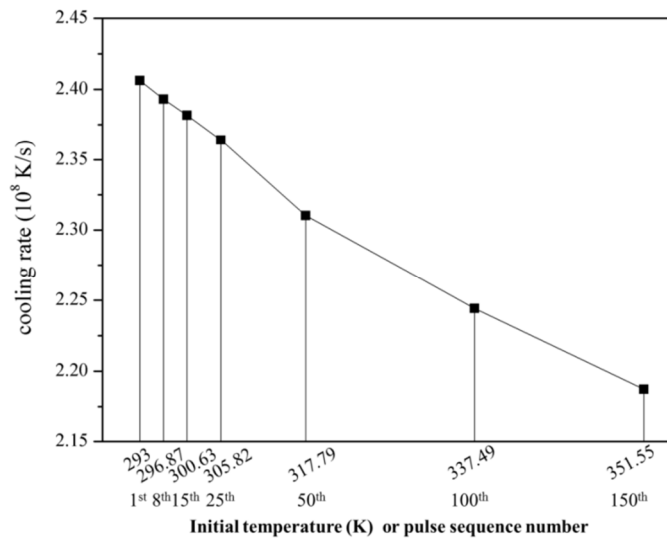


**Figure 7-19 Cooling rate of the LAEB treated layer in Al-Co-Ce alloy versus initial temperature (pulse sequence number) at 35 kV cathode voltage.**

### 7.3.5.2 Effect of cathode voltage

#### (1) Thickness of LAEB remelted layer

**Figure 7-20** plots the remelted layer thickness of the 100<sup>th</sup> pulse LAEB treated Al-Co-Ce alloy under different cathode voltages. It can be seen that the remelted layer thickness linearly increased with increasing cathode voltage. When the cathode voltage was 15 kV, the remelted layer thickness was only 2.5  $\mu\text{m}$ , while it reached 8.5  $\mu\text{m}$  when the cathode voltage increased to 40 kV.

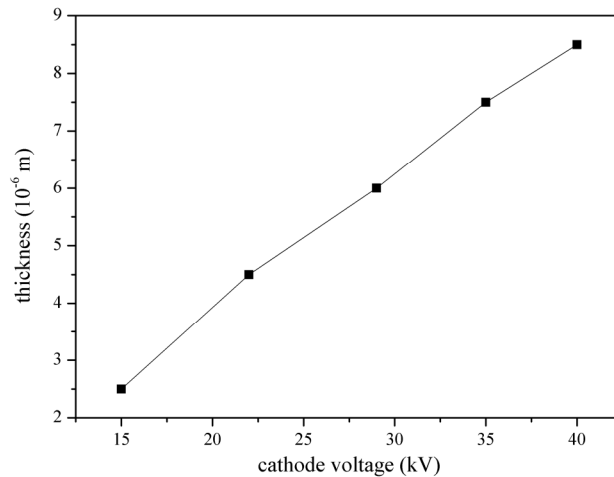


**Figure 7-20 Remelted layer thickness of the 100<sup>th</sup> pulse LAEB treated Al-Co-Ce alloy versus cathode voltage.**

## (2) Melting time

**Figure 7-21** plots the melting time of the 100<sup>th</sup> pulse LAEB irradiated Al-Co-Ce alloy against depth under different cathode voltages. Overall, the melting time increased with increasing cathode voltage at the same depth of the LAEB remelted layer. For the top surface, the longest melting time in the case of 40 kV was  $\sim 7.5$   $\mu\text{s}$ , which was much bigger than that ( $\sim 1$   $\mu\text{s}$ ) in the case of 15 kV. In addition, the melting time decreased with increasing depth of the LAEB irradiated layer under all different cathode voltages.

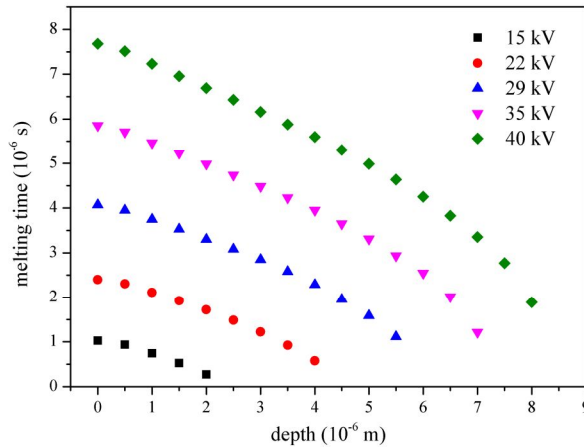


**Figure 7-21 Melting time of the 100<sup>th</sup> pulse LAEB treated Al-Co-Ce alloy at different depths versus cathode voltage.**

**(3) Solidification velocity and cooling rate**

**Figure 7-22** plots the top surface temperature against time of the 100<sup>th</sup> LAEB irradiated Al-Co-Ce alloy under different cathode voltage. Overall, the sample irradiated with a high cathode voltage required a much longer time to solidify from the maximum temperature to the solidification temperature compared with the sample treated with high cathode voltage, which results in the smaller slope of the cooling curve. On the contrary, during the heating process, the curve of the sample treated with a low cathode voltage was steeper than that of the sample treated with a high cathode voltage.

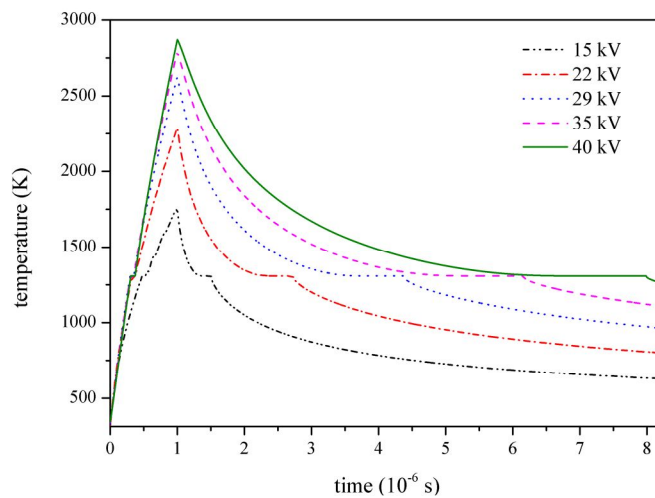


**Figure 7-22 Top surface temperature versus time of the 100<sup>th</sup> LAEB treated Al-Co-Ce alloy at different cathode voltages.**

**Figure 7-23** and **Figure 7-24** show the solidification velocity and cooling rate of the 100<sup>th</sup> pulse LAEB treated layer under different cathode voltages, respectively. The solidification velocity was found to decrease with increasing cathode voltage. Under 15 kV cathode voltage, the solidification velocity of the LAEB treated layer was ~6.5 m/s, while it decreased to ~1.8 m/s under 40 kV cathode voltage. Generally, the cooling rate of the sample was at a magnitude of 10<sup>8</sup> K/s for all of the cases. In addition, the cooling rate of the treated layer decreased with increasing cathode voltage.

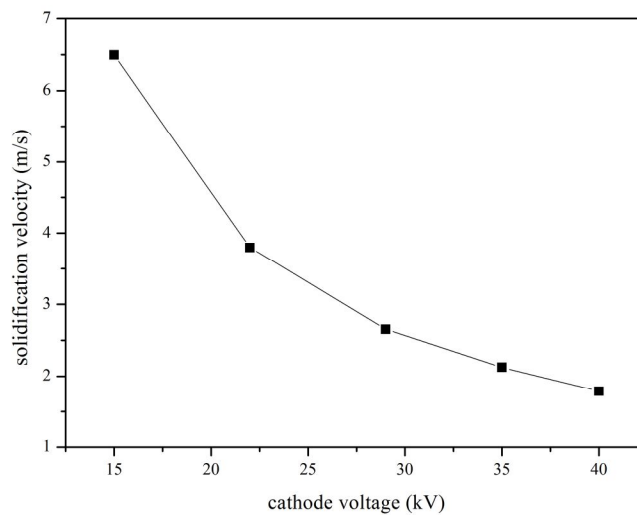


**Figure 7-23 Solidification velocity versus cathode voltage of the 100<sup>th</sup> pulse LAEB treated layer in Al-Co-Ce alloy.**

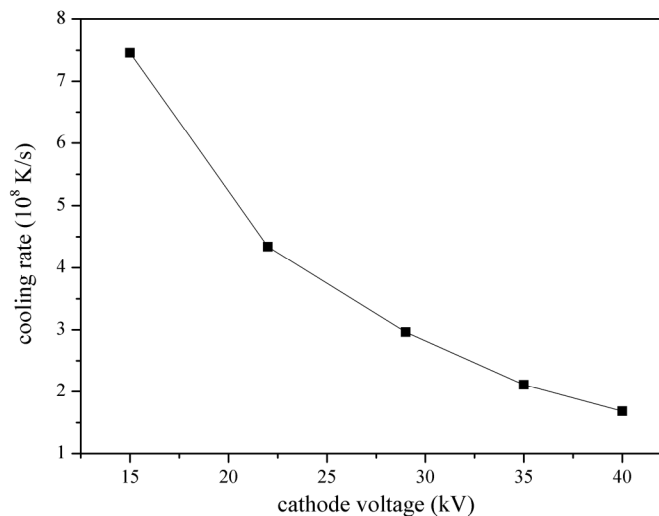


**Figure 7-24 Cooling rate versus cathode voltage of the 100<sup>th</sup> pulse LAEB treated layer in Al-Co-Ce alloy.**

## 7.4 Discussion

### 7.4.1 Features of the heat source

From **Eq. 7-21**, **Eq. 7-22** and **Eq. 7-23**, the heat source was described in terms of the electron range, energy distribution and volume power density in the target (i.e. the irradiated alloy material). **Figure 7-25**, **Figure 7-26** and **Figure 7-27** show their corresponding results for Al-Co-Ce alloy under different cathode voltages, respectively. It is seen that the electron range increased with increasing cathode voltage (**Figure 7-25**). In combination of the above equations and figures, the energy distribution and power density of the heat source under each cathode voltage reached their maximum when the depth was 1/3 of the electron penetration range. This is consistent with the results reported by Qin et al. [151]. This suggests that the treated layer at the subsurface of the sample will melt earlier than the top surface.

In the experimental results presented in **Chapter 6**, a large number of particles and craters were found on the surface of LAEB irradiated samples. The formation of these particles and craters is thought to be resulted from the melting of the subsurface prior to that of the top surface. This is consistent with the features of the heat source. The melting of the subsurface can cause the rapid volume expansion which will thereby cause the eruption of melting material. Eruption leaves the vacancy i.e. the craters. The expelled material will subsequently fall on the sample surface and cause the formation of the particles. Many publications also observed this kind of eruption phenomenon [146, 151, 169].

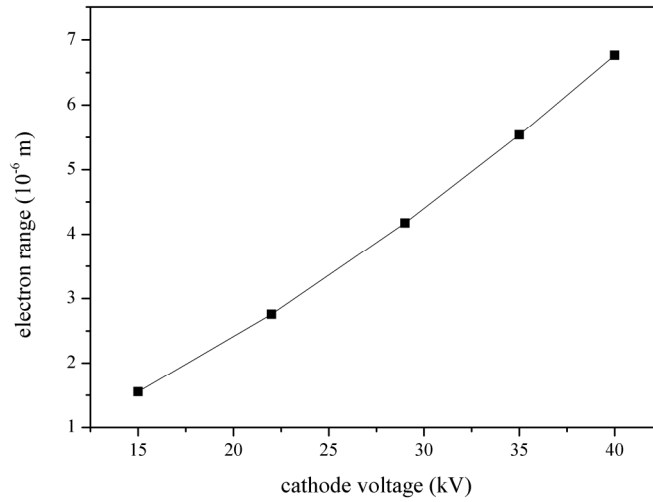


**Figure 7-25 Electron penetration range in the irradiated alloy versus cathode voltage.**

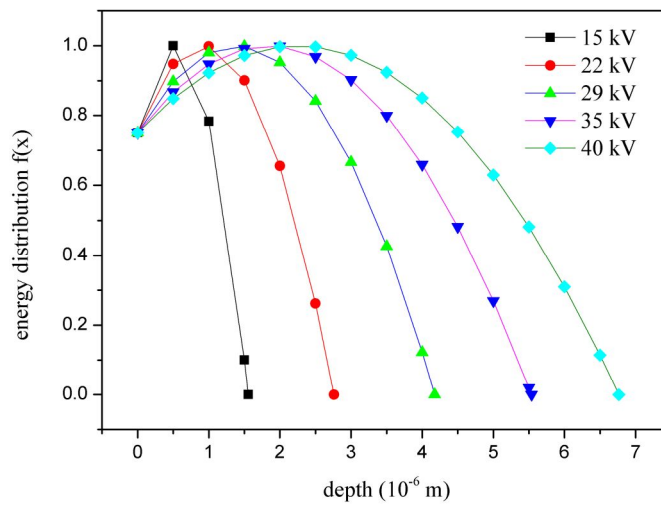


**Figure 7-26 Distribution function of the electron energy under different cathode voltages.**

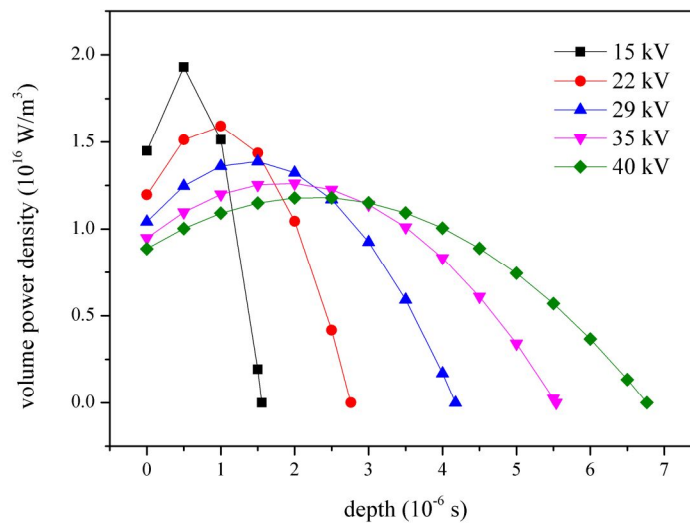


**Figure 7-27 Volume power density of the heat source versus depth under different cathode voltages.**

## 7.4.2 Thickness of the remelted layer and the homogenised layer

### 7.4.2.1 Thickness and initial temperature

In this modelling work, the thickness of the irradiated layer which underwent melting and solidification was defined as the remelted layer thickness. The thickness of the remelted layer for the single pulse treated alloy was found to be relatively stable although the initial temperature was slightly different (**Figure 7-7** and **Figure 7-14**). This is thought to be due to the constant energy input brought by the same cathode voltage, which finally determines the electron penetration depth. Due to the same energy deposition depth, the thickness of the remelted layer (the layer with the temperature above the melting time) is also constant.

**Figure 7-28** and **Figure 7-29** show the comparison of the modelled remelted layer thickness in the LAEB treated sample with different initial temperatures (pulse sequence numbers) and the experimental homogenised layer thickness of the samples treated with different numbers of LAEB pulses at 35 kV for Al-Cu and Al-Co-Ce alloy, respectively. The modelled thickness of the remelted layer for both 1 pulse LAEB treated Al-Cu alloy (12  $\mu\text{m}$ ) and Al-Co-Ce alloy (7  $\mu\text{m}$ ) under 35 kV cathode voltage was much higher than the experimental homogenised layer thickness (0.7  $\mu\text{m}$  and 2.8  $\mu\text{m}$  for Al-Cu and Al-Co-Ce alloy, respectively). This suggests that the calculated thickness of the remelted layer is not equivalent to the homogenised layer thickness. This difference in thickness between the remelted layer and homogenised layer is due to the insufficient melting and element diffusion.

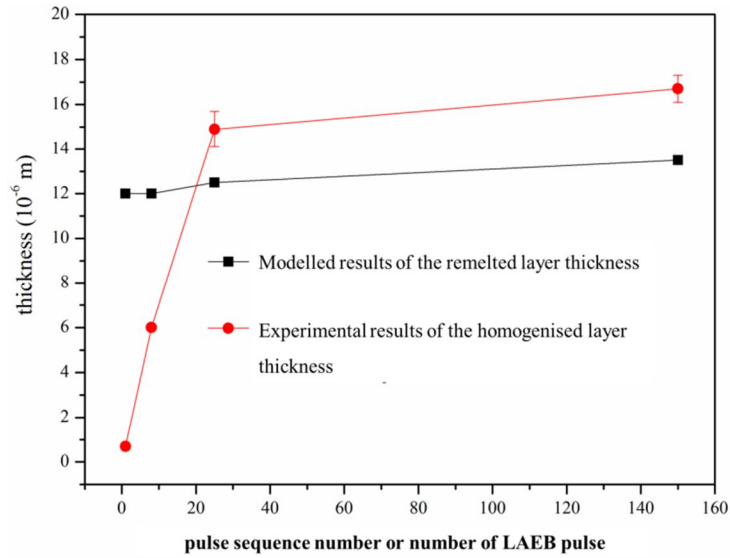


**Figure 7-28 Comparison of the modelled remelted layer thickness (in black) of the LAEB treated alloy with different initial temperatures (pulse sequence numbers), and experimental homogenised layer thickness (in red) of the LAEB treated alloy with different numbers of LAEB pulses (Al-Cu alloy, 35 kV).**

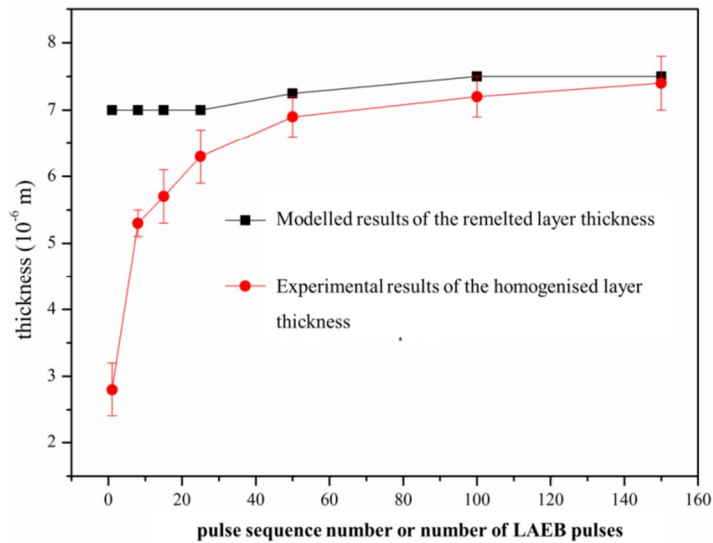


**Figure 7-29 Comparison of the modelled remelted layer thickness (in black) of the LAEB treated alloy with different initial temperatures (pulse sequence numbers), and experimental homogenised layer thickness (in red) of the LAEB treated alloy with different numbers of LAEB pulses (Al-Co-Ce alloy, 35 kV).**

When the temperature of the irradiated layer reaches the melting point, the irradiated layer will begin to melt. However, this kind of hot layer also needs sufficient time for the element diffusion to acquire the homogeneous composition.

In the experiments, when 1 pulse of LAEB irradiation was applied onto the sample

surface, the sample surface only experienced a short-time remelting which cannot support adequate element diffusion. Therefore, the sample surface did not exhibit a large thickness of homogenised layer.

However, when the number of LAEB pulses was increased to 25 and 150, the difference in thickness between the experimental homogenised layer and modelled remelted layer was greatly reduced (**Figure 7-28** and **Figure 7-29**). This is due to the relatively sufficient melting time brought by the accumulated LAEB pulse for the homogenisation of the remelted layer. Therefore, it can be proposed that the modelled remelted layer thickness describes the potential homogenised layer thickness when sufficient pulses of treatment are applied.

#### **7.4.2.2 Thickness and cathode voltage**

The remelted layer thickness was also found to vary greatly with the cathode voltage (**Figure 7-20**). It is known that the electron range i.e. the electron penetration depth is determined by the cathode voltage of the electron beam (**Eq. 7-23**). Higher cathode voltage will cause the larger electron range, and hence results in the larger thickness of modelled remelted layer. This is consistent with the experimental results (**Figure 6-9**).

**Figure 7-30** shows that the experimental homogenised layer thickness in 100 pulses of LAEB treated Al-Co-Ce alloy also increased with increasing cathode voltage. However, the experimental homogenised layer thickness was still smaller than the modelled remelted layer thickness except for the case of 40 kV cathode voltage. This is thought to be due to the insufficient number of LAEB pulses at lower cathode voltage.

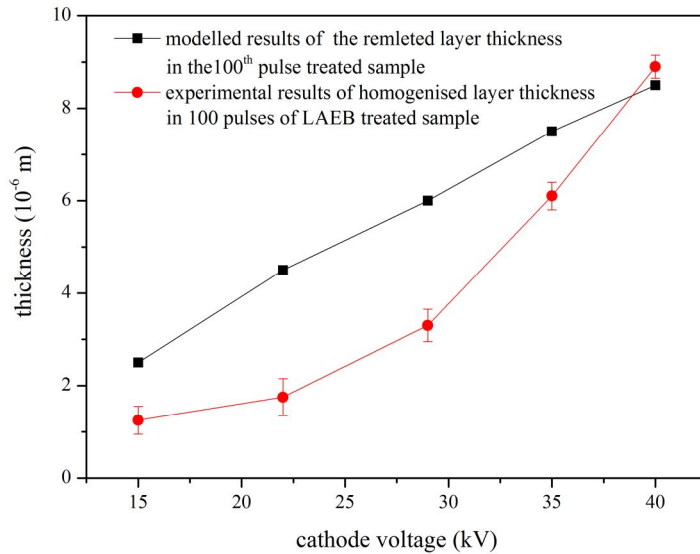


**Figure 7-30 Comparison of the modelled remelted layer thickness in the 100<sup>th</sup> pulse treated alloy and experimental homogenised layer thickness in the 100 pulses of LAEB treated alloy under different cathode voltages (Al-Co-Ce alloy).**

### 7.4.3 Melting time and homogenisation

In the previous discussion in **Section 7.4.2**, the homogenised layer thickness was generally smaller than the modelled remelted layer thickness for the samples which were subjected to few pulses of LAEB irradiation. In addition, in the experimental results shown in **Chapter 6**, the extent of homogenisation in chemical composition of the LAEB treated Al-Co-Ce alloy layer was determined by both cathode voltage and the number of pulses in the LAEB treatment. Higher cathode voltage and more pulses of LAEB treatment make the sample have an apparent homogenisation in composition. This indicates that the homogenised layer thickness is strongly correlated with the melting time.

The homogenisation of the multiphase microstructure is a process of element diffusion between different phases. It is well known that the element diffusion rate is strongly dependent on the temperature. For simplicity, in this work, only high temperature diffusion above the melting point was considered. In addition, the

diffusion coefficient is assumed to be constant within the temperature change above the melting point. Based on the above assumptions, the extent of diffusion in the LAEB irradiated layer in this work is therefore only dependent on the time duration of the material being at the temperature above the melting point, i.e. the melting time previously defined (Section 7.3.4.2).

### 7.4.3.1 Melting time and general uniformity

Although the relationship between the melting time and homogenised layer thickness is not quantified, a longer melting time will definitely enhance the homogenisation and increase the homogenised layer thickness. In order to increase the melting time, increasing the number of LAEB pulses is a direct way. For both Al-Cu and Al-Co-Ce alloys, the melting time linearly increased with the initial temperature, i.e. the pulse sequence number, which was shown in **Figure 7-9** and **Figure 7-16**, respectively.

It should be noted that all the melting time mentioned above is for the individual pulse of LAEB treatment. In this work, the multi-pulse LAEB treatment was conducted. The total melting time ( $t_{N_p}$ ) of the sample treated with a specific number of pulses of LAEB irradiation is thereby necessary. Based on the fitting function of the melting time of the irradiated layer generated by the single-pulse treatment and the pulse sequence number shown in **Figure 7-9** and **Figure 7-16**, the total melting time,  $t_{N_p}$ , can be calculated as follows:

$$t_{N_p} = \sum_{n=1}^{n=N_p} t_0^n \quad \text{Eq. 7-45}$$

where  $t_0^n$  is the melting time from the single-pulse treatment (with different pulse sequence numbers),  $N_p$  is the number of LAEB pulses. The relationship of the

total melting time and the number of pulses for Al-Cu and Al-Co-Ce alloy is shown in **Figure 7-31** and **Figure 7-32**, respectively. Total melting time is seen to increase linearly with the number of LAEB pulses.

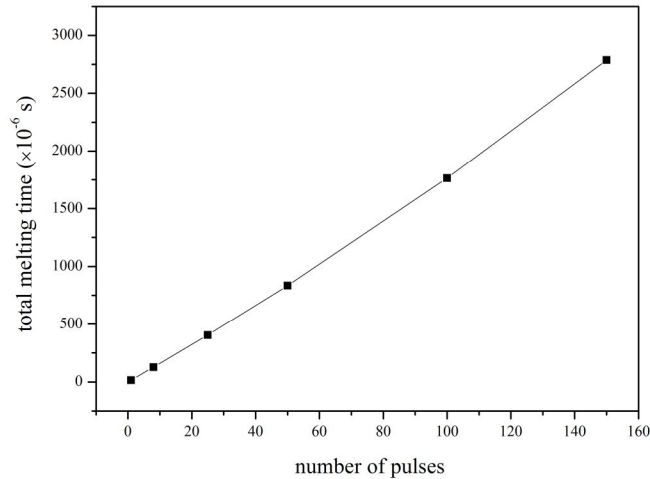


**Figure 7-31 Total melting time ( $t_{N_p}$ ) of the top surface in the LAEB treated Al-Cu alloy versus number of pulse ( $N_p$ ) at 35 kV cathode voltage.**

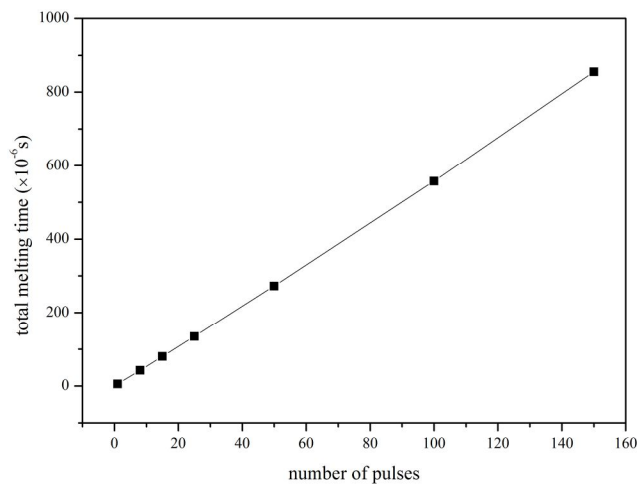


**Figure 7-32 Total melting time ( $t_{N_p}$ ) of the top surface in the LAEB treated Al-Co-Ce alloy versus number of pulses ( $N_p$ ) at 35 kV cathode voltage.**

In addition, **Figure 7-21** has also shown that the melting time of the treated layer increased with increasing cathode voltage at the same depth for Al-Co-Ce alloy. Based on the above discussion, the effect of both number of pulses and cathode voltage of LAEB treatment on the melting time is consistent with the experimental results, i.e. to increase the homogenised layer thickness.

### **7.4.3.2 Melting time at different depths and extent of uniformity of the treated layer**

Melting time of the top surface was found to be longer than that of the deeper treated layer, as seen in **Figure 7-8**, **Figure 7-15** and **Figure 7-21**. This is consistent with the morphology of the treated layer shown in **Chapter 6**. The experimental results have shown that the top surface of the remelted layer was more uniform in composition than the interface between the remelted layer and the substrate. This interface always fluctuated with the underlying crystalline phase profile, especially in the LAEB treated as-cast material.

The melting time of the remelted layer varied with depth. This is thought to be determined by the energy distribution and volume power density of the electron beam in the irradiated alloy. Overall, the energy distribution and volume power density of the deeper remelted layer are smaller than that of the top surface (**Figure 7-26** and **Figure 7-27**), which will result in the difference of melting time at different depths of the remelted layer. In addition, the deeper remelted material is closer to the heat transfer interface, the heat can be conducted away more quickly than that in the top surface.

### **7.4.4 Solidification velocity/cooling rate and initial temperature**

Given the constant energy input of the single-pulse treatment under the same cathode voltage, the temperature increase from the LAEB treatment is also constant (**Eq. 7-27**). The maximum temperature of the treated sample is therefore determined by the initial temperature. In this modelling work, the difference in the initial temperature was very small. Therefore, it has been seen that the maximum

temperature of the samples irradiated with different initial temperatures ( $T_{max}$  shown in **Figure 7-10**) was very similar for both Al-Cu and Al-Co-Ce alloy.

However, this slight variation in initial temperature caused apparently different cooling behaviour. From **Figure 7-12** and **Figure 7-19**, the solidification velocity/cooling rate of the LAEB treated layer was found to decrease with increasing initial temperature for both Al-Cu alloy and Al-Co-Ce alloy. The sample irradiated with a higher initial temperature was found to take an apparently longer time to solidify from the maximum temperature to the solidification temperature ( $t_{solid}-t_{max}$  shown in **Figure 7-10**), which resulted in a decrease in the average cooling rate.

#### 7.4.4.1 Al-Cu alloy

In the experimental work, the solidification velocity and cooling rate for the Al-Cu alloy treated with different numbers of pulses of LAEB irradiation also decreased with increasing number of LAEB pulses (**Chapter 4**), which is consistent with the modelling results. However, it should be mentioned that in the experimental work, the top surface of the Al-Cu alloy treated by 1 pulse LAEB irradiation did not suffer sufficient remelting and diffusion (**Chapter 4**). Also, the samples treated with 8, 25 and 150 pulses of LAEB irradiation did not exhibit the regular eutectic structure seen in the as-cast material. Therefore, the solidification velocity and cooling rate cannot be directly calculated according to  $\lambda^2 v = K_0$  equation.

According to the limit of steady eutectic growth, the solidification velocity and cooling rate of the 150 pulses of LAEB treated Al-Cu alloy are 1.539 m/s and  $4.44 \times 10^7$  K/s, respectively. Compared with the modelled results shown in **Figure 7-11** and **Figure 7-12**, the modelled solidification velocity (0.57 m/s) is smaller

than the experimental value, while the modelled cooling rate ( $5.3 \times 10^7$  K/s) is slightly higher than the experimental one. However, the modelled value and the experimental value are generally at the same order of magnitude. In addition, cooling rate values from two methods must be considered with caution because they are from two different processes i.e. eutectic crystallisation at a fixed temperature (solidification temperature) and solidification of melt over a relatively wide range of temperature (from maximum temperature to solidification temperature).

#### 7.4.4.2 Al-Co-Ce alloy

In the case of the LAEB treated Al-Co-Ce alloy, there is no direct quantitative result of cooling rates under different numbers of pulses. However, the cooling rate can be reflected by the amorphisation extent of the LAEB irradiated layer. First of all, the modelled solidification velocity (**Figure 7-18**) and cooling rate (**Figure 7-19**) of the LAEB treated Al-Co-Ce alloy were 2.05 - 2.30 m/s and  $2.15 \times 10^8$  -  $2.45 \times 10^8$  K/s, respectively. In particular, the modelled cooling rate is sufficiently high for the generation of amorphous alloy. This is consistent with the experimental findings from the glancing angle XRD showing the different extents of amorphisation in the LAEB treated Al-Co-Ce alloys (**Figure 6-6**, **Figure 6-11**, **Figure 6-15** and **Figure 6-21**).

The modelling results also show that the solidification velocity/cooling rate decreased with increasing number of pulses. In our experimental work, the sample irradiated by 1, 8 and 15 pulses of LAEB did not obtain very uniform composition. In other words, the samples have not obtained the same initial microstructure. Therefore, the effect of the number of pulses on the extent of amorphisation cannot

be used to evaluate the cooling rate. For the samples irradiated by 25 or more pulses of LAEB irradiation, they were found to be greatly homogenised in the chemical composition (**Figure 6-1**). This suggests these irradiated layers have obtained similar uniform microstructure. Under this condition, the cooling rate will be the determinative factor to the amorphisation extent.

It has been found that when the number of LAEB pulses was between 25 and 50, the amorphisation extent of the LAEB irradiated Al-Co-Ce alloy was greatest. However, when the number of LAEB pulses was increased to 100 and 150, the amorphisation extent of the treated layer decreased due to the local crystallisation (**Figure 6-6** and **Figure 6-7**). Therefore, the same conclusion that the cooling rate decreases with the number of pulses can be made as that in the modelling work.

#### **7.4.5 Solidification velocity/cooling rate and cathode votage**

According to the modelling results of LAEB treated Al-Co-Ce alloy at different cathode voltages, the solidification velocity and cooling rate were seen to decrease with increasing cathode voltage when the same number of pulses of LAEB irradiation was applied (**Figure 7-24**). Similarly as the effect of initial temperature, higher cathode voltage will bring higher energy input and temperature increase compared with lower cathode voltage, which has been calculated as that in **Table 7-3**. Under the same initial temperature, the maximum temperature of the sample treated with high cathode voltage is hence higher (**Figure 7-24**). Accompanied by the increased maximum temperature, the high cathode voltage more apparently extends the time of cooling and solidification (**Figure 7-24**), which eventually decreases the cooling rate.

In our experimental work, the 100 pulses of LAEB treated Al-Co-Ce alloys under different cathode voltages exhibit different extents of amorphisation. The alloys treated under 15 and 22 kV cathode voltage did not obtain a uniform composition distribution (**Figure 6-8** and **Figure 6-9**). 29 kV treated sample exhibited the largest extent of amorphisation. With increasing cathode voltage, the localised crystallisation occurred in 35 and 40 kV treated samples (**Figure 6-11** and **Figure 6-12**). It has been discussed that the amorphisation extent of the treated layer with similar original microstructure (uniform chemical composition in this work) will be determined by cooling rate. Therefore, it can be suggested that the experimental cooling rate of LAEB treated Al-Co-Ce alloy is consistent with the results from the simulation.

## 7.5 Summary

- A nonstationary heat transfer model with an external pulsed heat source (electron beam) was built, and a finite difference method was used to numerically solve the heat transfer equation with an external heat source. The code written by Matlab compiler language was validated by calculating the energy with time under adiabatic boundary conditions.
- Results of temperature labelling measurement on the bottom surface of LAEB treated pure Al were used to estimate the heat transfer coefficient, as well as the equivalent initial temperature for the multi-pulse LAEB process.
- Three different materials including pure Al, Al-Cu eutectic alloy and Al-Co-Ce alloy were modelled. The effect of initial temperature (i.e. pulse sequence number) and cathode voltage on the thickness of LAEB remelted layer, melting time, solidification velocity and cooling rate was investigated.

- The energy deposition in terms of energy distribution and volume energy density reaches the maximum at the depth of  $1/3$  of the electron range i.e. the electron penetration depth. This energy deposition results in the melting of the subsurface prior to the outmost layer. This can well account for the formation of craters and particles observed in the experimental results on the LAEB treated Al-Co-Ce alloy.
- The modelled thickness of the LAEB treated layer does not apparently increase with increasing initial temperature, but apparently increases with increasing cathode voltage, which is due to the energy input determined by different cathode voltages.
- The modelled single pulse melting time i.e. the time duration of the alloy at or above the melting point increases with increasing pulse sequence number and cathode voltage of the LAEB pulse. Increasing the number of LAEB pulses i.e. applying multi-pulse treatment can increase the total melting time, and hence increase the homogenised layer thickness, which is consistent with the experimental results.
- The modelled solidification velocity and cooling rate decrease with the pulse sequence number and cathode voltage of the LAEB pulse. The modelled results are consistent with the experimental results of the amorphisation extent for the LAEB treated layer with the homogenised microstructure in both Al-Cu and Al-Co-Ce alloy.

## **Chapter 8 Corrosion behaviour of Al-Co-Ce alloy with different microstructures**

### **8.1 Introduction**

In **Chapter 5** and **Chapter 6**, the microstructures of Al-Co-Ce alloy generated in different processes have been characterised. For the crystalline Al-Co-Ce alloy cast in the wedge mould, materials at different locations of the wedge cast exhibited different microstructures in phase category and phase size. When the as-cast alloys were treated by laser surface melting, it was found that the alloy microstructure was greatly refined although the alloy was still in the crystalline form. Furthermore, the alloy subjected to the large area electron beam irradiation was transformed from the crystalline state to the amorphous state under some parameters.

In this chapter, the corrosion behaviour of the above different microstructures is investigated by potentiodynamic polarisation corrosion tests. In addition, AA 2024 and alclad 2024 are used as reference materials, as well as pure Al. Corrosion mechanisms of different materials are discussed and schematically illustrated. The possibility of LSM-LAEB treated Al-Co-Ce amorphous layer replacing the cladding layer on AA2024 is also discussed by comparing their corrosion morphology and corrosion rate. All potentiodynamic polarisation corrosion tests in this work were conducted in 3.5 wt.% NaCl solution considering the susceptibility of aluminium alloy to the chloride ion. At least three scans were made on at least three different parallel samples for each type of materials (See **Appendix 5**).

## 8.2 AA2024 and alclad 2024

### 8.2.1 Characterisation of AA 2024 and alclad 2024

#### 8.2.1.1 AA2024

**Figure 8-1** and **Figure 8-2** show the optical and SE image of Keller's reagent etched AA2024 alloy, respectively. It can be seen that the grains are generally equiaxed with a diameter of 50  $\mu\text{m}$ . There are also some black precipitates distributed all over the sample. From **Figure 8-2**, two precipitates at spot A and B were found. In addition, there were also some cavities seen in the sample, such as at spot C.

To investigate the composition of the Al-rich matrix and precipitates, four spots in the AA2024 shown in **Figure 8-2** were analysed by EDS. EDS spectra and chemical compositions of the above four spots are shown in **Figure 8-3** and **Table 8-1**, respectively. EDS results show that both spot A and spot B were consisted of Al, Cu and Mg. In particular, the atomic ratio of Al, Cu and Mg in the spot A was approximately 2:1:1, which suggests that the precipitates at spots A and B were  $\text{Al}_2\text{CuMg}$ . This is consistent with the finding of Buchheit and Grant et al. [171]. There was a gap surrounding the precipitate at spot B. Based on the literature [172], this gap is thought to be resulted from the dissolution of the precipitate in the etching. Spot D and the cavity at spot C were found to have a similar composition, which was consistent with the nominal composition of AA2024 shown in **Table 3-2**.

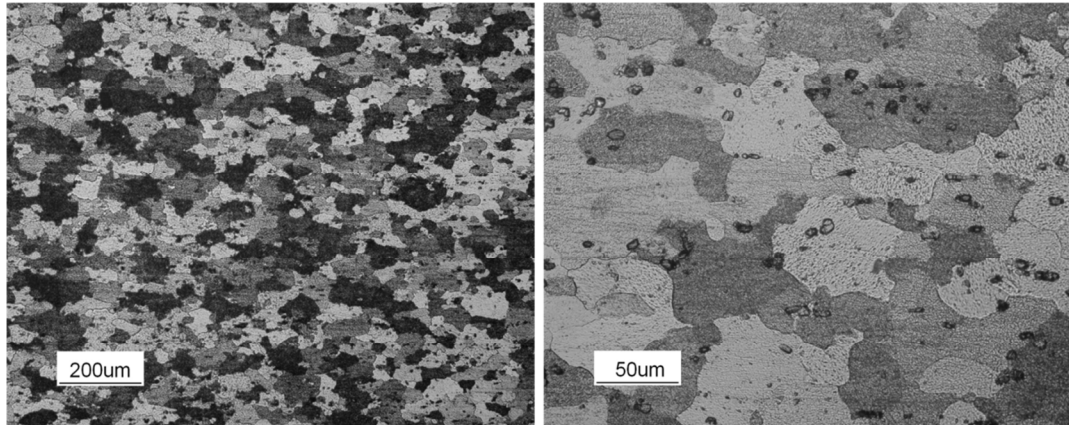


Figure 8-1 Optical micrographs of AA2024 etched by Keller's reagent.

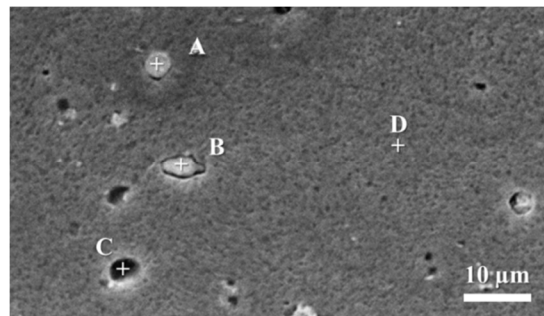


Figure 8-2 SE image of AA2024 sample etched by Keller's reagent.

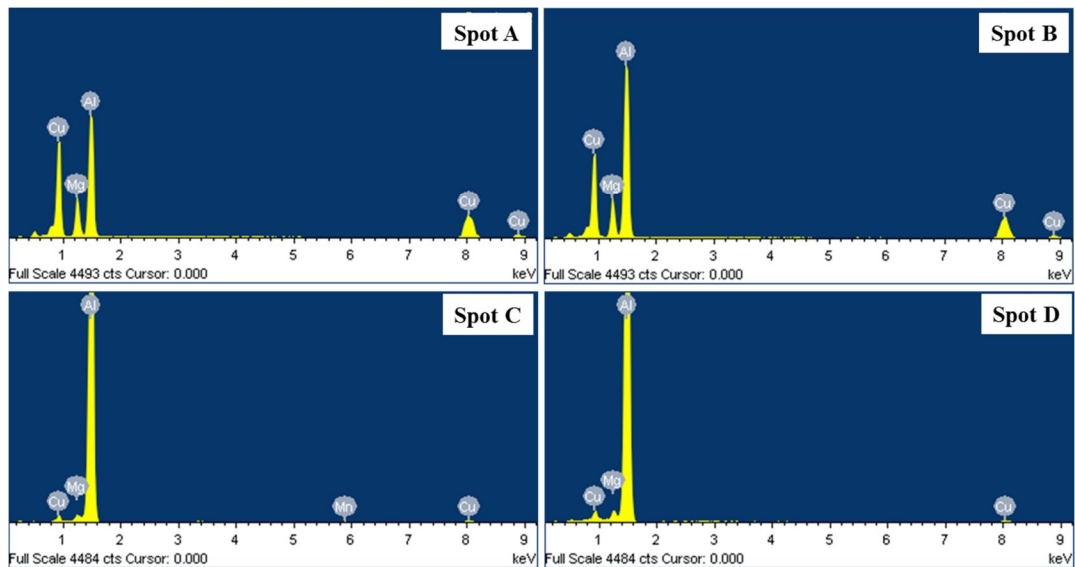


Figure 8-3 EDS spectra of AA2024 at different locations shown in Figure 8-2.

Table 8-1 Chemical composition of AA2024 at different locations shown in Figure 8-2.

Location	Element content (at.%)			
	Al	Cu	Mg	Mn
Spot A	55.6	23.1	21.3	-
Spot B	63.7	19.1	17.2	-
Spot C	95.8	2.3	1.4	0.5
Spot D	96.7	1.6	1.7	-

### 8.2.1.2 Alclad 2024

**Figure 8-4a** is the cross sectional optical micrograph of alclad 2024. The thickness of the cladding was approximately 80  $\mu\text{m}$ . There was a transition layer with the thickness of approximately 15  $\mu\text{m}$  between the cladding layer and the core alloy, exhibiting slight etching effect. The core alloy had a similar microstructure as AA2024. **Figure 8-4b** is the cross sectional BSE image of alclad 2024. It can be seen that there were a number of bright particles exhibited in the core alloy, which was dimensionally consistent with those black spots i.e. the precipitates shown in the optical micrograph (**Figure 8-4a**).

The compositions of the four points shown in the BSE image were analysed by EDS. Point 1, point 2 and point 4 were located in the cladding layer, transition layer and core alloy, respectively, while point 3 was located in the interface of the transition layer and core alloy. **Table 8-2** gives the EDS results of alclad 2024 at different locations. For the point 1 in the cladding layer, there were not any other elements despite Al. However, a small amount of Mg was found at point 2. At point 3 which was close to the core alloy, Cu was found together with Mg and Al. Finally, all four main constituent elements were found at point 4. The composition of point 4 i.e. the core alloy was consistent with the nominal composition of AA2024 shown in **Table 3-2**.

An EDS line scanning analysis was also conducted on the cross section of alclad 2024, as shown in **Figure 8-5**. According to the results, the content of Al decreased along the scanning direction. The contents of Cu and Mg elements showed an opposite tendency compared with Al. Mn also had a slight increase in the core alloy compared with that in the cladding layer. However, no sharp

decrease or increase was seen for any of the above elements, which confirms the existence of the transition layer. Overall, the results of line scanning analysis of alclad 2024 were consistent with the observation of microstructure (**Figure 8-4**) and EDS spot analysis (**Table 8-2**).

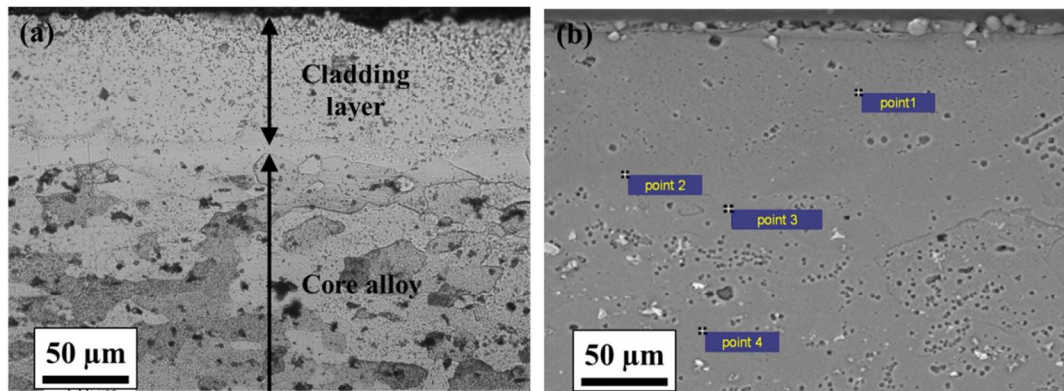


**Figure 8-4** Cross section of alclad 2024 etched by Keller's reagent. (a) and (b) are optical and BSE image, respectively.

**Table 8-2** Composition of alclad 2024 at different locations of the cross section as shown in Figure 8-4b.

Location	Element content (at.%)			
	Al	Cu	Mg	Mn
Point 1	100	-	-	-
Point 2	99.5	-	0.5	-
Point 3	97.7	1.2	1.1	-
Point 4	96.2	2.0	1.5	0.3

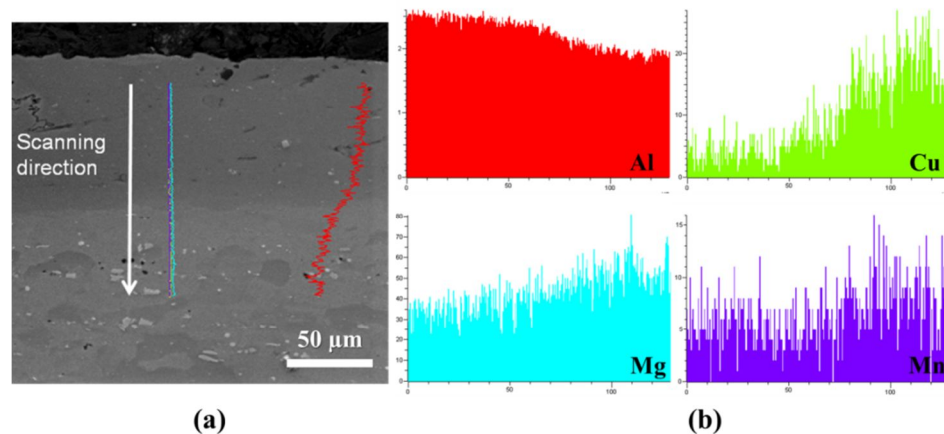


**Figure 8-5** Line scanning analysis of alclad 2024 in the cross-sectional view. (a) BSE image, (b) EDS spectra of four elements.

## 8.2.2 Potentiodynamic polarisation tests

**Figure 8-6** shows the comparison of pure Al, AA2024 and alclad 2024 in potentiodynamic polarisation curves. The definitions of some characteristic electrochemical parameters for the example of pure Al are also shown in this figure. **Table 8-3** summarises the characteristic parameters of three materials shown in **Figure 8-6**. In the comparison of potentiodynamic polarisation curves of the three materials, the materials can be arranged in the decreasing order of corrosion potential ( $E_{corr}$ ) as follows: AA2024 (-647 mV), alclad 2024 (-840 mV) and pure Al (-935 mV). The corrosion current density ( $I_{corr}$ ) corresponding to above  $E_{corr}$  for AA2024, pure Al and alclad 2024 was  $0.5 \times 10^{-4}$  mA/cm<sup>2</sup>,  $1.0 \times 10^{-4}$  mA/cm<sup>2</sup> and  $0.7 \times 10^{-4}$  mA/cm<sup>2</sup>, respectively.

In addition, pure Al and alclad 2024 exhibited slow anodic dissolutions when the polarisation potential was below the pitting potential ( $E_{pit}$ ) of -728 mV. Once the above pitting potential was surpassed, the current density had a rapid growth with the further increase of polarisation potential. The potential difference between  $E_{corr}$  and  $E_{pit}$ , i.e.  $E_{pit} - E_{corr}$  was defined as passivation range which was 206 mV and 112 mV for pure Al and alclad 2024, respectively. In the case of AA2024, the current density in the anodic polarisation increased directly without experiencing any slow increase at the early stage of anodic polarisation. Therefore, no apparent  $E_{pit}$  and  $E_{pit} - E_{corr}$  were identified for AA2024. In terms of  $E_{pit} - E_{corr}$ , pure Al showed a wider passivation potential range than alclad 2024.

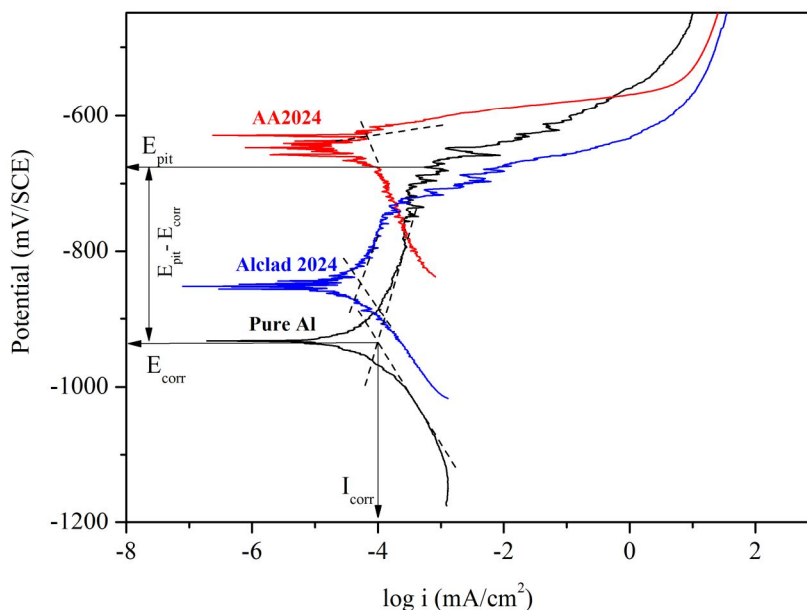


**Figure 8-6 Potentiodynamic polarisation curves of pure Al, AA2024 and Alclad 2024 in deaerated 3.5 wt.% NaCl solution.**

**Table 8-3 Characteristic parameters of pure Al, AA2024 and Alclad 2024 in potentiodynamic polarisation test in deaerated 3.5 wt.% NaCl solution. The shown values are the average of at least three repeated tests shown in Appendix 5. The errors are standard deviation.**

Alloy	$E_{\text{corr}}$ (mV/SCE)	$I_{\text{corr}}$ ( $\times 10^{-4}$ mA/cm <sup>2</sup> )	$E_{\text{pit}}$ (mV/SCE)	$E_{\text{pit}} - E_{\text{corr}}$ (mV)
AA2024	-647±32	0.5±0.1	-	-
Pure Al	-935±3	1.0±0.1	-728±20	206±18
Alclad 2024	-840±15	0.7±0.1	-728±7	112±20

## 8.2.3 Corrosion morphologies

### 8.2.3.1 AA2024

**Figure 8-7** and **Figure 8-8** show the optical and SEM images of AA2024 after a potentiodynamic polarisation corrosion test in deaerated 3.5 wt.% NaCl solution (from -200 mV to 600 mV relative to OCP). It can be seen that AA2024 suffered apparent pitting corrosion. Localised dark corrosion pits were seen all over the sample surface (**Figure 8-7a and b**). From SEM images shown in **Figure 8-8**, the pitting corrosion was found to be related to the presence of the white precipitates.

Overall, there was always a gap surrounding the white precipitates. As that seen in etched AA2024 (**Figure 8-2**), the gap is thought to be due to the dissolution of the precipitate. The cracks crossing the white precipitates were also found (**Figure 8-8c and d**). In addition, a large amount of corrosion products were seen, especially around the corrosion pits (**Figure 8-8c and d**).

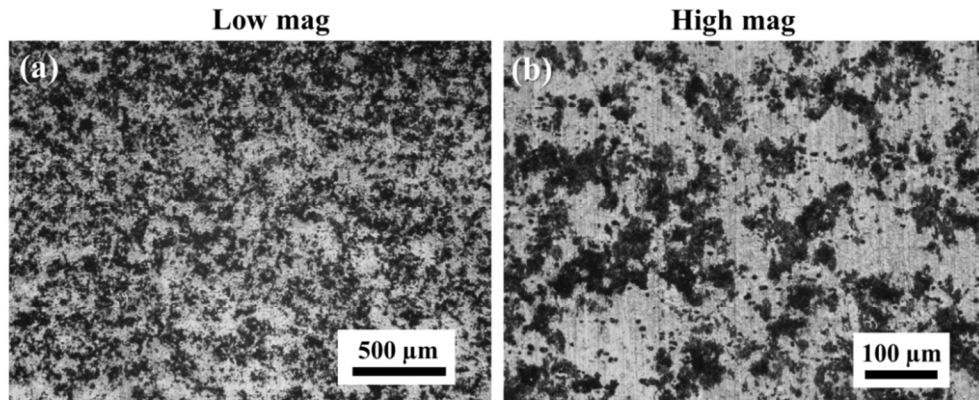


**Figure 8-7** Corrosion morphologies (optical images) of AA2024 in plan view and cross sectional view after a potentiodynamic polarisation corrosion test in deaerated 3.5 wt.% NaCl solution (-200 mV~600 mV relative to OCP).

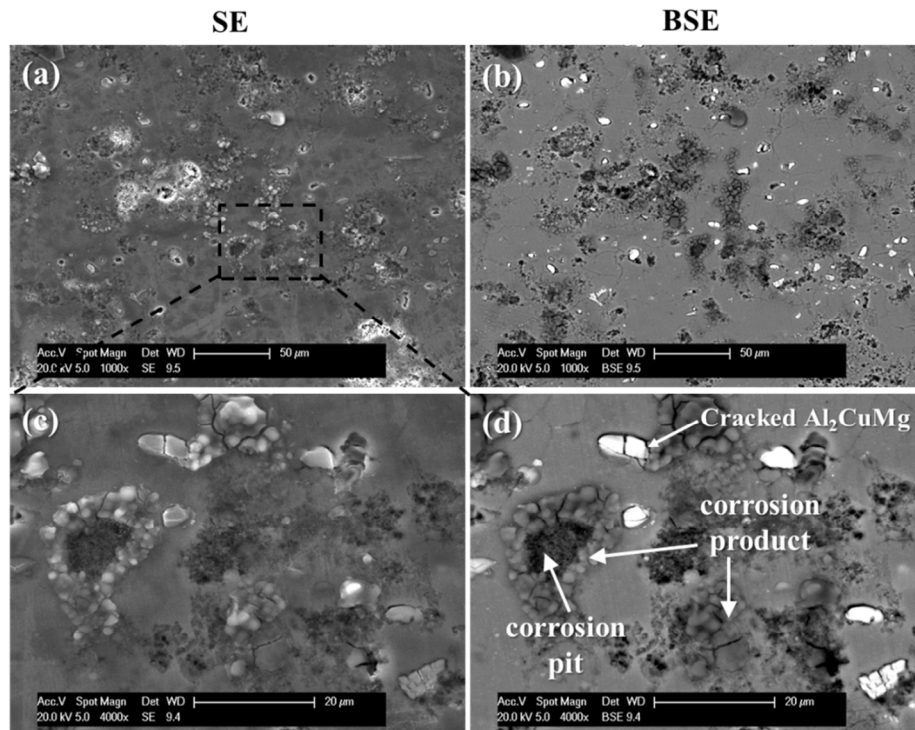


**Figure 8-8** Corrosion morphologies (SEM images) of AA2024 in plan view after a potentiodynamic polarisation corrosion test in deaerated 3.5 wt.% NaCl solution (-200 mV~600 mV relative to OCP).

**Figure 8-9** shows the EDS results of AA2024 at different spots after a polarisation corrosion test. EDS results show that spot A and spot B contained a great amount of Al, O and Cu. The content of Mg had a great decrease at these two spots compared with that in the alloy before corrosion (**Figure 8-3** and **Table 8-1**). The compositions of spot C and spot D which were located at the Al-rich matrix of AA2024 were consistent with that in the sample before corrosion. For the spot E, there was a great amount of O and Al. The content of Cu was also slightly higher than that at spot C and spot D. The elemental mapping of a white precipitate in AA2024 is shown in **Figure 8-10**. A large amount of Cu was seen in the white precipitate compared with the surrounding Al-rich matrix. In addition, there was also slightly more O found in the same location than the Al-rich matrix. This is consistent with the findings that the precipitates act as the anode in the galvanic corrosion reported by Schmut and Frankle et al. [172].

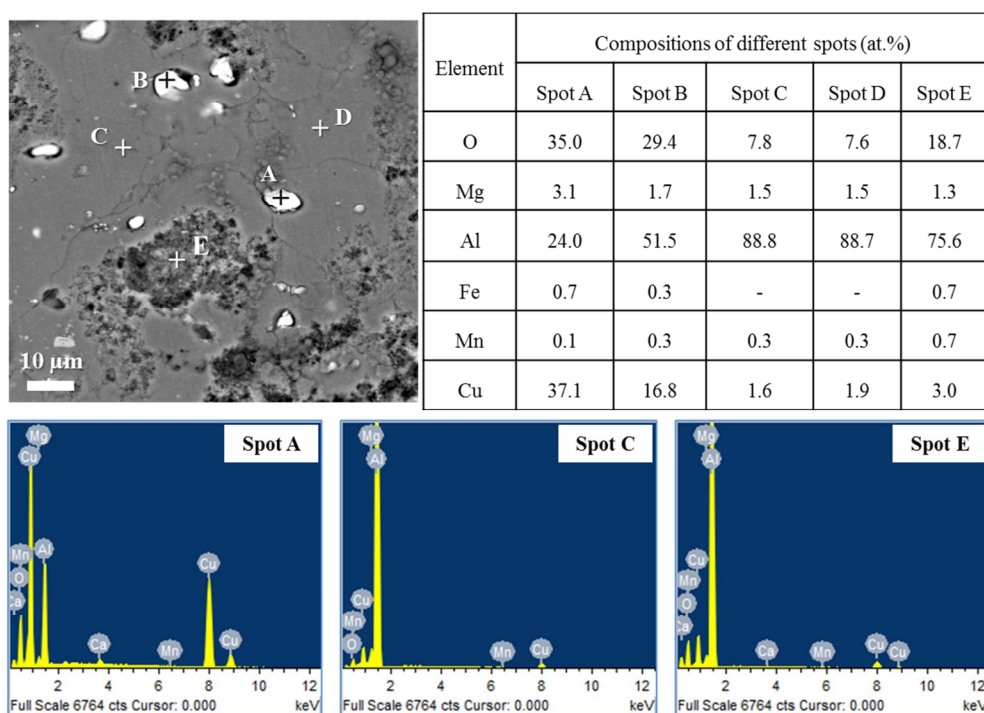


**Figure 8-9** EDS results of AA2024 after a potentiodynamic polarisation corrosion test in deaerated 3.5 wt.% NaCl solution (-200 mV~600 mV relative to OCP).

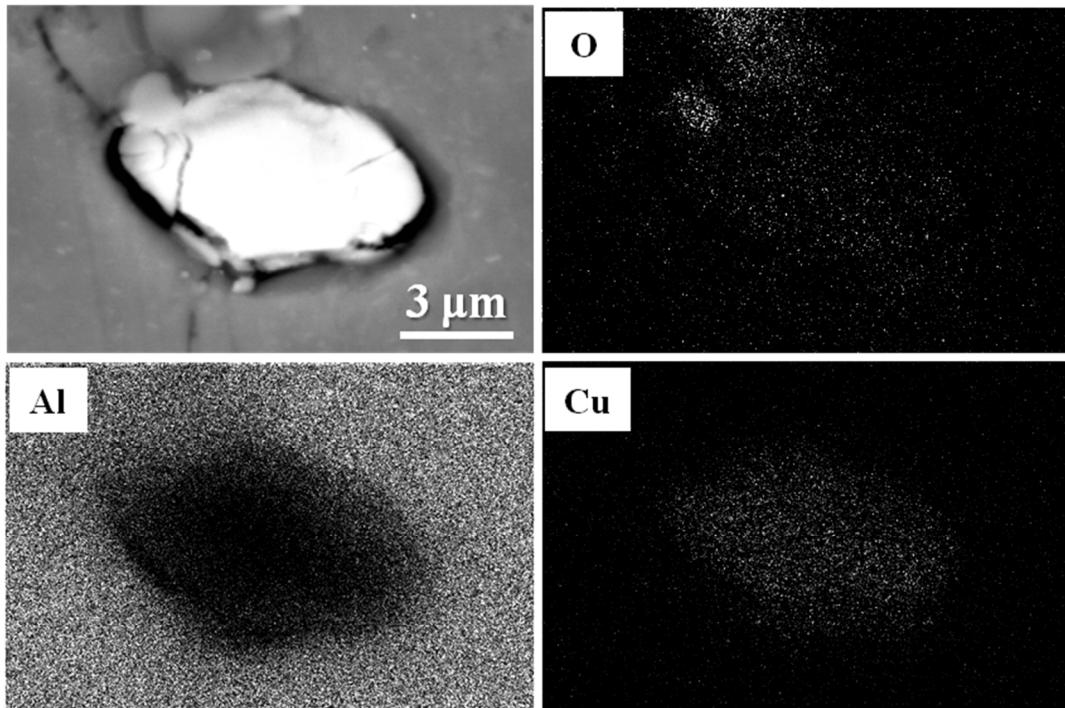


**Figure 8-10 EDS mapping of a precipitate in AA2024 after a potentiodynamic polarisation corrosion test in deaerated 3.5 wt.% NaCl solution (-200 mV~600 mV relative to OCP).**

### 8.2.3.2 Pure Al

**Figure 8-11** shows the BSE images of pure Al in plan view after a potentiodynamic polarisation corrosion test in deaerated 3.5 wt.% NaCl solution (-200 mV~425 mV relative to OCP). Overall, pure Al suffered typical pitting corrosion (**Figure 8-11a and b**). The wall of the corrosion pit was very rough. From the magnified images, the pit consisted of a great number of sharp lattice plane walls. The adjacent lattice plane walls exhibited an angle of  $90^\circ$ , which formed a three-dimensional topography in the corrosion pit (**Figure 8-11c and d**).

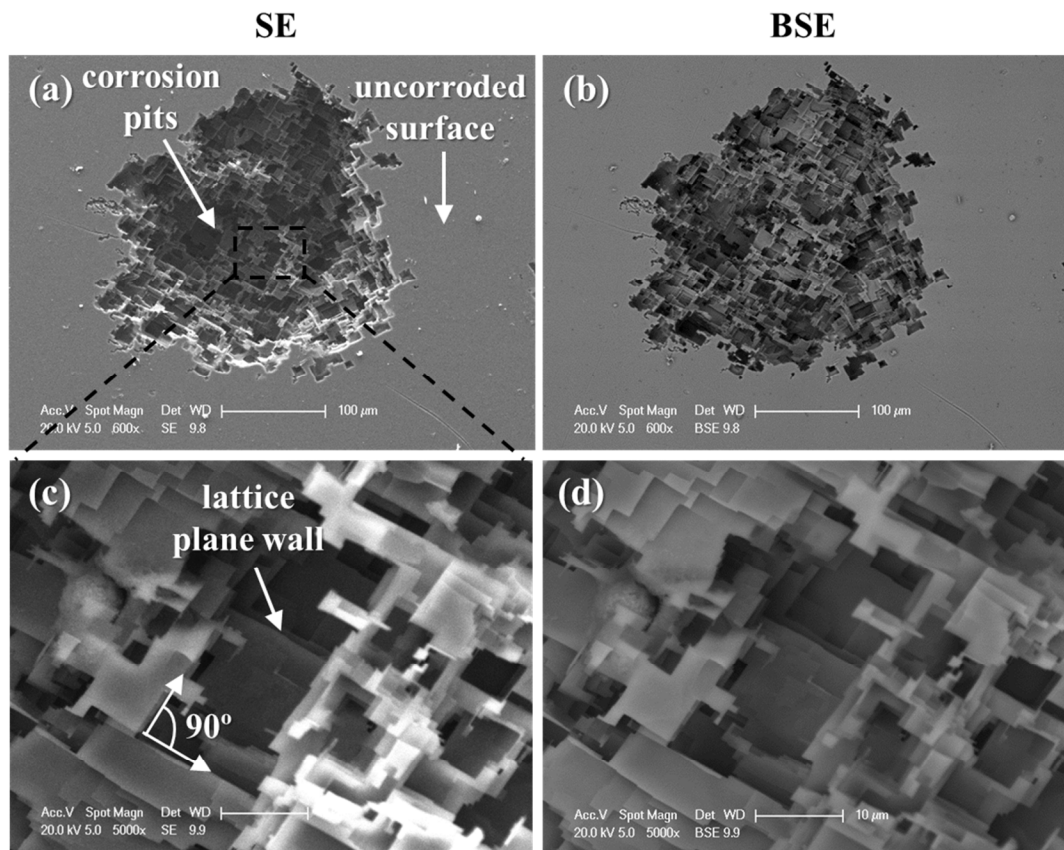


**Figure 8-11** BSE images showing pitting corrosion morphologies of pure Al in plan view after a potentiodynamic polarisation corrosion test in deaerated 3.5 wt.% NaCl solution (-200 mV~425 mV relative to OCP).

### 8.2.3.3 Alclad 2024

**Figure 8-12** shows the corrosion morphologies (optical images) of alclad 2024 after a potentiodynamic polarisation corrosion test in deaerated 3.5 wt.% NaCl solution (-200 mV~425 mV relative to OCP). Pitting corrosion occurred on the surface of alclad 2024 (**Figure 8-12a and b**). In the magnified images of the pit (**Figure 8-12c and d**), it can be seen that there were a great number of sharp pit walls at the edge of the large pit, which was consistent with that seen in the corrosion morphology of pure aluminium. However, some curved pit walls were also seen in the centre of the large pit (**Figure 8-12c and d**). In addition, the bottom of these large pits were found to be very flat (**Figure 8-12a and c**).

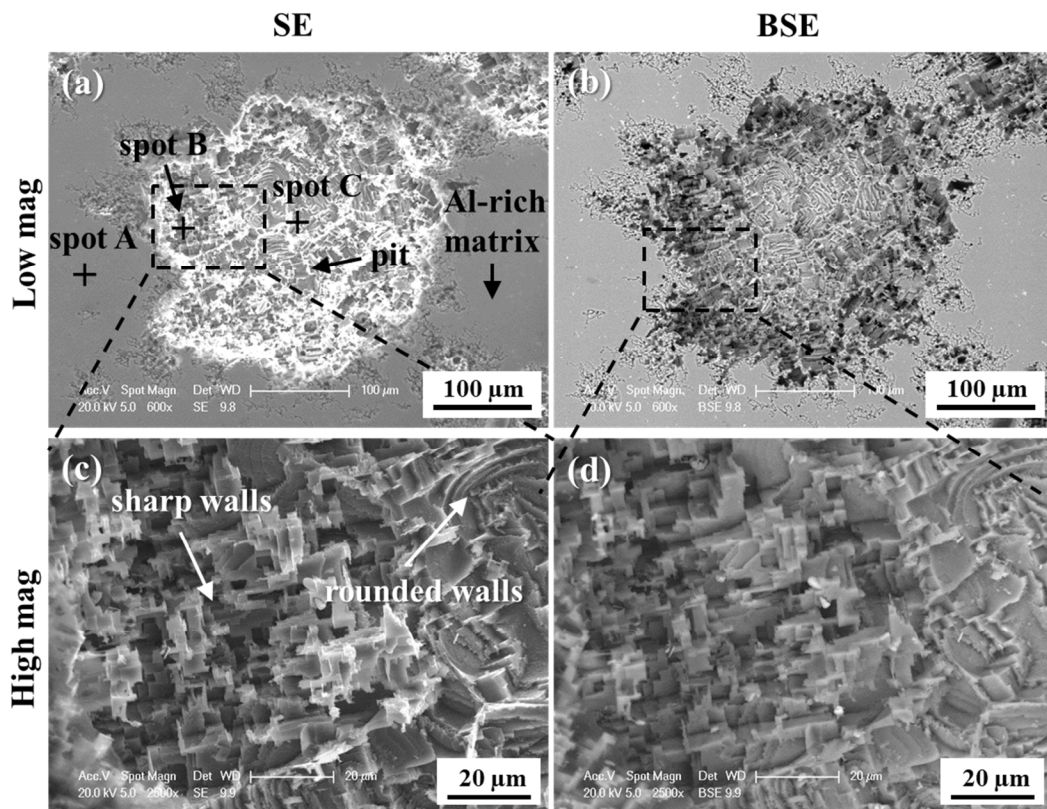


**Figure 8-12** Corrosion morphologies (SEM images) of alclad 2024 in plan view after a potentiodynamic polarisation corrosion test in deaerated 3.5 wt.% NaCl solution (-200 mV~425 mV relative to OCP).

The flat bottom of the corrosion pit can be more clearly seen in the cross sectional corrosion morphologies (Figure 8-13). From Figure 8-13, the corrosion was found to horizontally extend into the surrounding cladding material and formed a large and flat-bottomed corrosion pit (Figure 8-13a). After the corrosion test conducted in this work, a thin layer of cladding material with the thickness of  $\sim 15 \mu\text{m}$  still existed on the top of the substrate AA2024 (Figure 8-13b). The thickness of this uncorroded cladding layer is found to be consistent with that of the transition layer which was seen in the etched sample before corrosion testing (Figure 8-4a). The substrate underlying the corrosion pits did not suffer a corrosion attack under the protection of the cladding material.

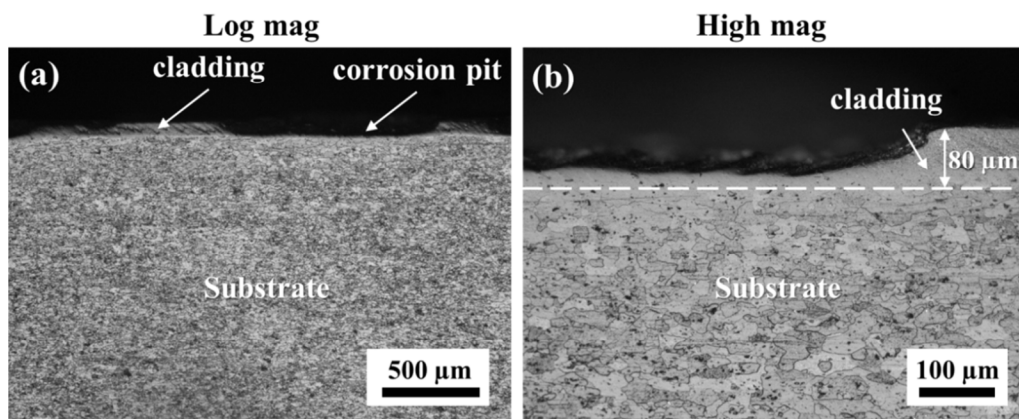


Figure 8-13 Corrosion morphologies (optical images) of alclad 2024 in plan view after a potentiodynamic polarisation corrosion test in deaerated 3.5 wt.% NaCl solution ( $-200 \text{ mV} \sim 425 \text{ mV}$  relative to OCP).

### 8.3 Al-Co-Ce alloy with different microstructures

#### 8.3.1 Potentiodynamic polarisation test

The potentiodynamic polarisation curves of Al-Co-Ce alloy 3 with different microstructures are shown in Figure 8-14. Table 8-4 summarises the characteristic parameters of different materials (defined by the same method shown in Figure

**8-6).** In the four types of microstructures, LSM-LAEB treated layers 1 and 2 had the lower  $E_{corr}$  (-878 and -873 mV, respectively) compared with other samples. As-cast, LSM and LAEB treated samples had the  $E_{corr}$  of -790 mV, -810 mV and 825 mV, respectively. In addition to the different  $E_{corr}$ , samples also differed in the anodic polarisation behaviour. For the as-cast alloy, the current density showed a straightforward increase with potential. However, the other three types of alloys exhibited different degrees of passivation. The  $E_{pit}$  of LSM, LAEB and two LSM-LAEB treated alloys were -704 mV, -711 mV, -606 mV and -736 mV, respectively. In addition, the above three types of alloys can be arranged by the decreasing order of  $E_{pit}-E_{corr}$  as follows: LSM-LAEB (272 mV and 137 mV for treated layers 1 and 2, respectively), LAEB (113 mV) and LSM (106 mV). The current density  $I_{corr}$  at corresponding  $E_{corr}$  of different samples was  $16.2 \times 10^{-4}$  mA/cm<sup>2</sup> (as-cast),  $6.5 \times 10^{-4}$  mA/cm<sup>2</sup> (LSM treated),  $3.8 \times 10^{-4}$  mA/cm<sup>2</sup> (LAEB treated),  $23.4 \times 10^{-4}$  mA/cm<sup>2</sup> (LSM-LAEB treated layer 1) and  $18.6 \times 10^{-4}$  mA/cm<sup>2</sup> (LSM-LAEB treated layer 2). The LSM-LAEB treated layer 1 showed a wider passivation potential range than layer 2.

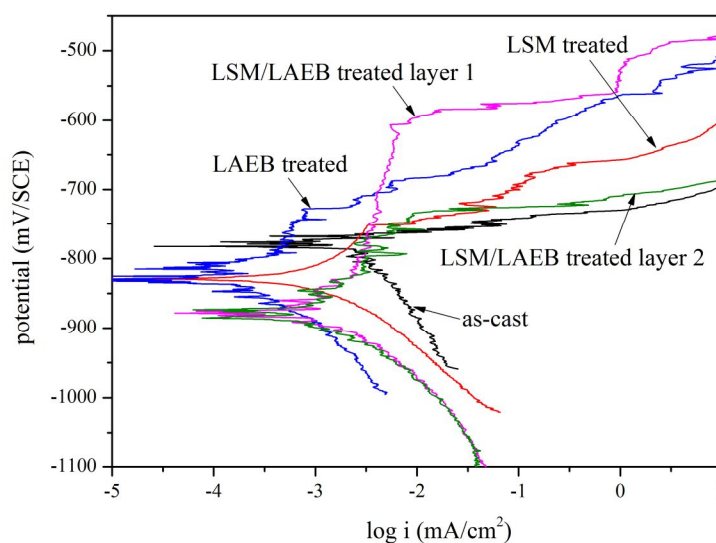


**Figure 8-14 Potentiodynamic polarisation curves of Al-Co-Ce alloy 3 with different microstructures in deaerated 3.5 wt.% NaCl solution.**

**Table 8-4 Characteristic parameters for the polarisation behaviour of various Al-Co-Ce alloys in deaerated 3.5 wt.% NaCl solution. The shown values are the average of at least three repeated tests shown in Appendix 5. The errors are standard deviation. Values without error shown represent the result from only one test.**

Alloy	$E_{\text{corr}}$ (mV/SCE)	$I_{\text{corr}}$ ( $\times 10^{-4}$ mA/cm <sup>2</sup> )	$E_{\text{pit}}$ (mV/SCE)	$E_{\text{pit}} - E_{\text{corr}}$ (mV)
As-cast	-790±17	16.2±0.3	-	-
LSM treated	-810±15	6.5±0.2	-704±44	106±41
LAEB treated	-825±16	3.8±0.2	-711±29	113±44
LSM-LAEB treated layer 1	-878	23.4	-606	272
LSM-LAEB treated layer 2	-873	18.6	-736	137

### 8.3.2 Corrosion morphologies

#### 8.3.2.1 As-cast material

**Figure 8-15** and **Figure 8-16** show the corrosion morphologies of the as-cast Al-Co-Ce alloy 3 in plan view and cross sectional view, respectively, when the sample was subjected to a polarisation ranging from -200 mV to 250 mV relative to OCP. It can be seen that the exposed sample surface suffered severe corrosion compared with the lacquered region. The dark Al-rich phase i.e. Al/Al<sub>11</sub>Ce<sub>3</sub> eutectic and bright primary Al<sub>11</sub>Ce<sub>3</sub> phase were preferentially attacked. A great amount of corrosion products can be found at the corrosion sites. However, there was no apparent corrosion found at the grey Al<sub>8</sub>Co<sub>2</sub>Ce phase particles, which exhibited the same brightness contrast as that shown in the uncorroded lacquered region. These grey Al<sub>8</sub>Co<sub>2</sub>Ce phase particles also retained the original shape and distinct boundaries.

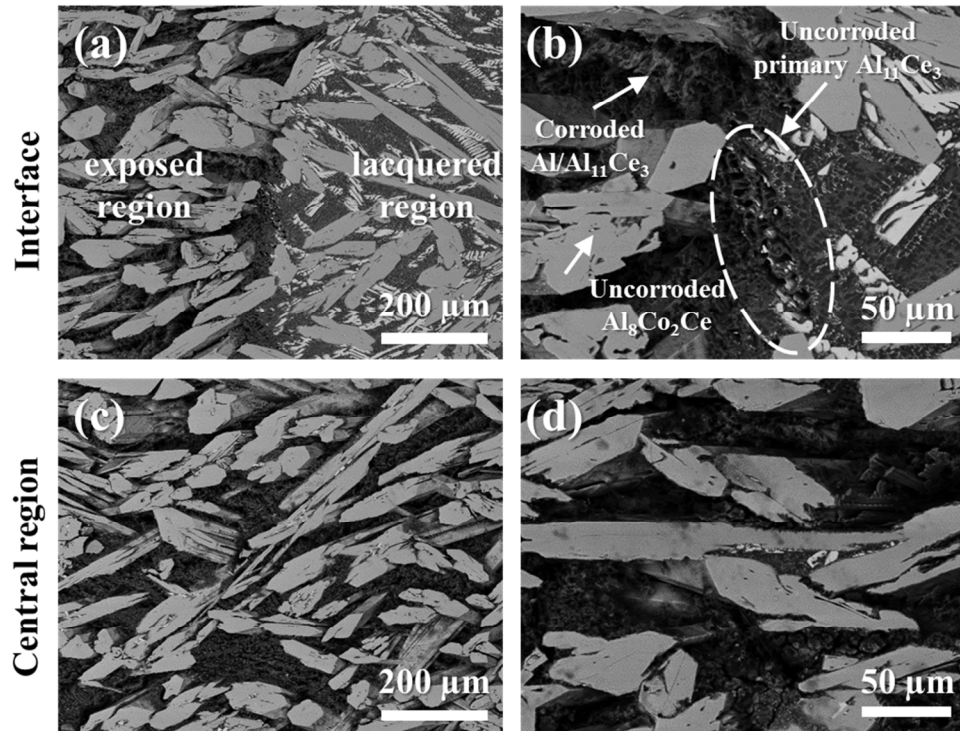


Figure 8-15 BSE images showing the corrosion morphologies in plan view of as-cast Al-Co-Ce alloy 3 after a potentiodynamic polarisation corrosion test in deaerated 3.5 wt.% NaCl solution (-200 mV~250 mV relative to OCP). The ellipse region in (b) shows uncorroded primary  $\text{Al}_{11}\text{Ce}_3$  phases at the interface between the exposed region and the lacquered region.

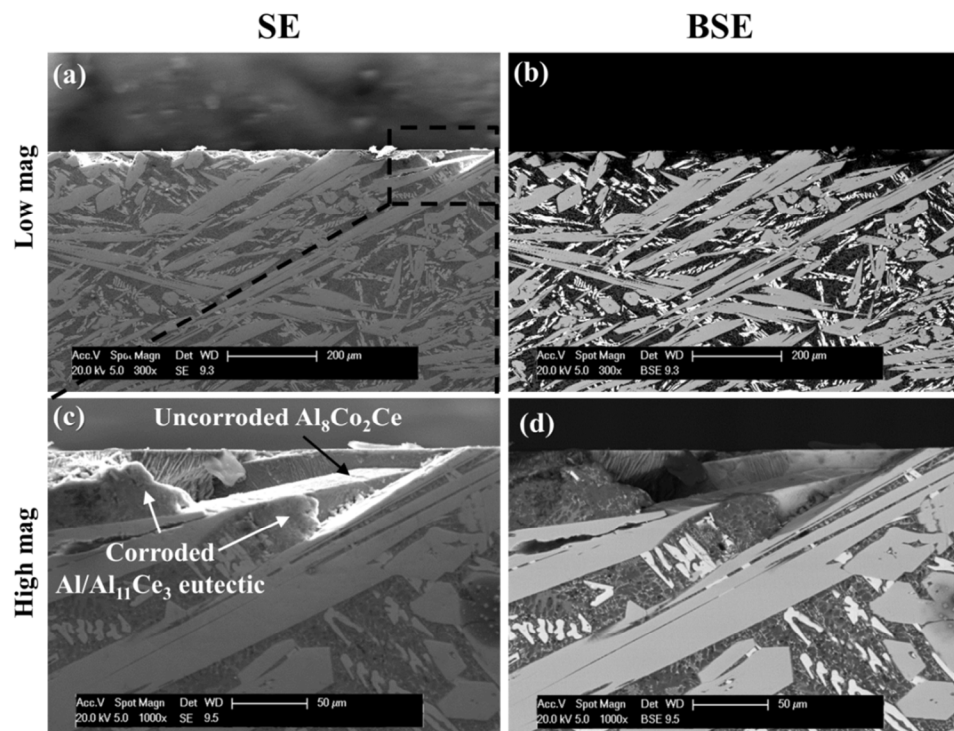
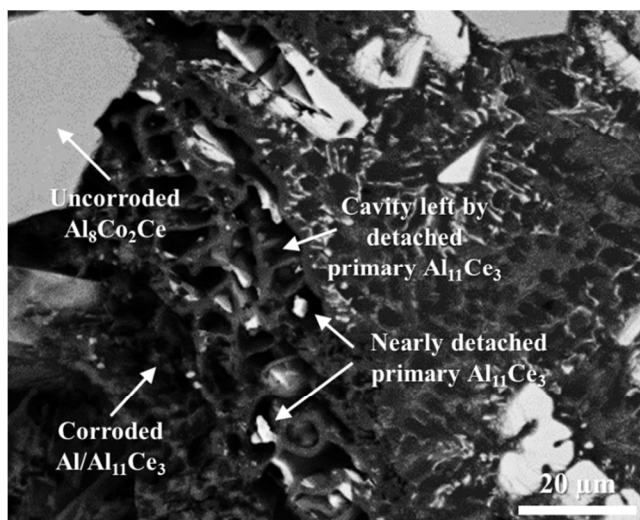


Figure 8-16 Corrosion morphologies in cross sectional view of as-cast Al-Co-Ce alloy 3 after a potentiodynamic polarisation corrosion test in deaerated 3.5 wt.% NaCl solution (-200 mV~250 mV relative to OCP).

**Figure 8-17** shows the magnified corrosion morphologies of as-cast Al-Co-Ce alloy 3 after a corrosion test in the dashed ellipse region as shown in **Figure 8-15b**. It can be seen that there were some nearly detached  $\text{Al}_{11}\text{Ce}_3$  phase particles and a few cavities distributed in the corroded eutectic region. This suggests that under the same polarisation potential the primary  $\text{Al}_{11}\text{Ce}_3$  phase is more corrosion resistant compared with the pure Al phase. In other words, the primary  $\text{Al}_{11}\text{Ce}_3$  phase is more noble than the pure Al phase. However, the primary  $\text{Al}_{11}\text{Ce}_3$  phase can detach from the eutectic matrix when the Al matrix was preferentially dissolved, which is consistent with the existence of the cavities. In the case of the lamellar  $\text{Al}_{11}\text{Ce}_3$  with the small size in the eutectic region, it was easier for these small  $\text{Al}_{11}\text{Ce}_3$  phases to detach with the dissolution of the pure Al matrix compared with primary  $\text{Al}_{11}\text{Ce}_3$  phases with a larger size. Therefore, there was no lamellar  $\text{Al}_{11}\text{Ce}_3$  left in the corroded region although some bright dots were seen.



**Figure 8-17** Magnified BSE image of the region in dashed ellipse as shown in **Figure 8-15b**.

The magnified local region of the as-cast Al-Co-Ce alloy after corrosion testing is shown in **Figure 8-18**. A great number of corrosion products between Al-Co-Ce phases can be seen. The corrosion products located in spot A were analysed using

EDS, showing the existence of a high content of oxygen. However, for the spot B, there was much less oxygen, but a great amount of Al, Co and Ce with the ratio of 8:2:1. This again confirms that the  $\text{Al}_8\text{Co}_2\text{Ce}$  phase did not suffer apparent corrosion.

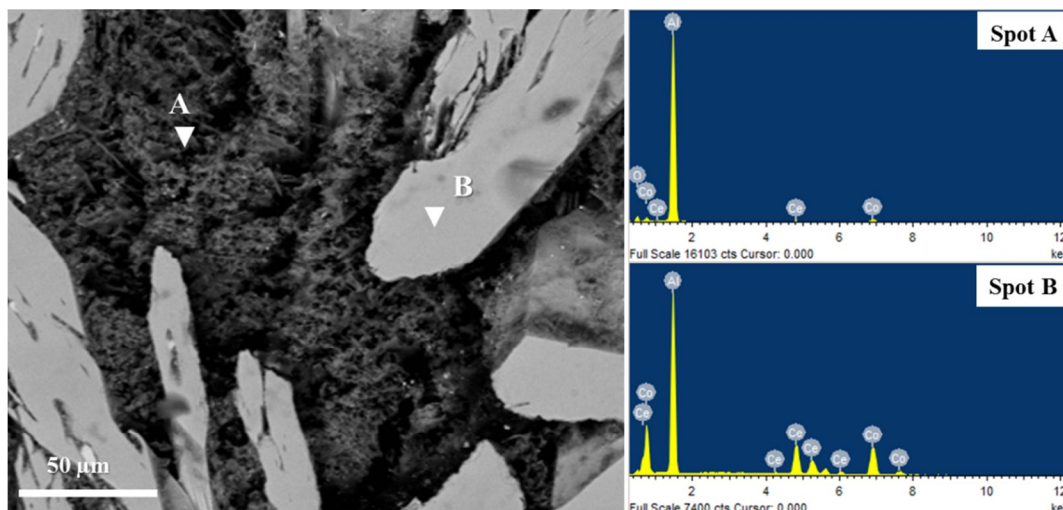


**Figure 8-18** EDS analysis of as-cast Al-Co-Ce alloy 3 after polarisation testing. The details of experiment are same to that shown in Figure 8-15.

### 8.3.2.2 LSM treated alloy

**Figure 8-19** shows the corrosion morphologies of LSM treated Al-Co-Ce alloy 3 in plan view after a potentiodynamic polarisation test in deaerated 3.5 wt.% NaCl solution (-200 mV~250 mV relative to OCP). From the interface between the exposed region and the lacquered region, it can be seen that the exposed region suffered corrosion, which exhibited darker brightness contrast (**Figure 8-19a and b**). The corrosion that occurred in the exposed region was also found to be the preferential corrosion of Al-rich region i.e. eutectic region. The grey  $\text{Al}_8\text{Co}_2\text{Ce}$  phase still retained the original brightness contrast as that before corrosion testing. Additionally, corrosion products were also seen to be accumulated at the interface from the magnified image (**Figure 8-19a and b**). Cracking also occurred in the centre of the exposed region (**Figure 8-19c and d**). Especially, a number of cracks

were seen in the corroded exposed region (**Figure 8-19d**). Similar corrosion was also seen from the corrosion morphology in cross sectional view (**Figure 8-20**). Corroded regions also exhibited darker brightness contrast compared with uncorroded regions. Corrosion also occurred in the Al-rich region i.e. the eutectic region, but not in the  $\text{Al}_8\text{Co}_2\text{Ce}$  phase.

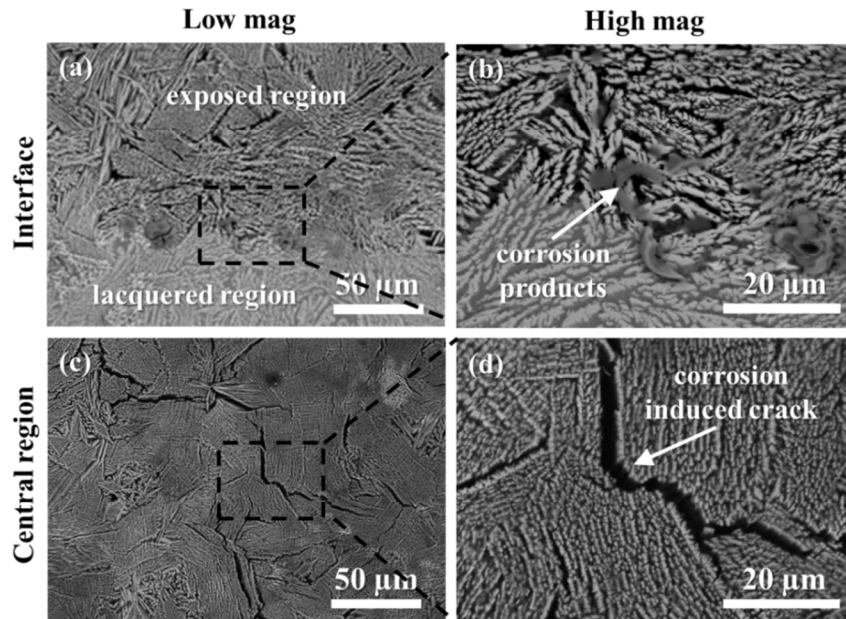


**Figure 8-19** BSE images showing corrosion morphologies of the laser treated Al-Co-Ce alloy 3 in plan view after a potentiodynamic polarisation corrosion test in deaerated 3.5 wt.% NaCl solution (-200 mV~250 mV relative to OCP).

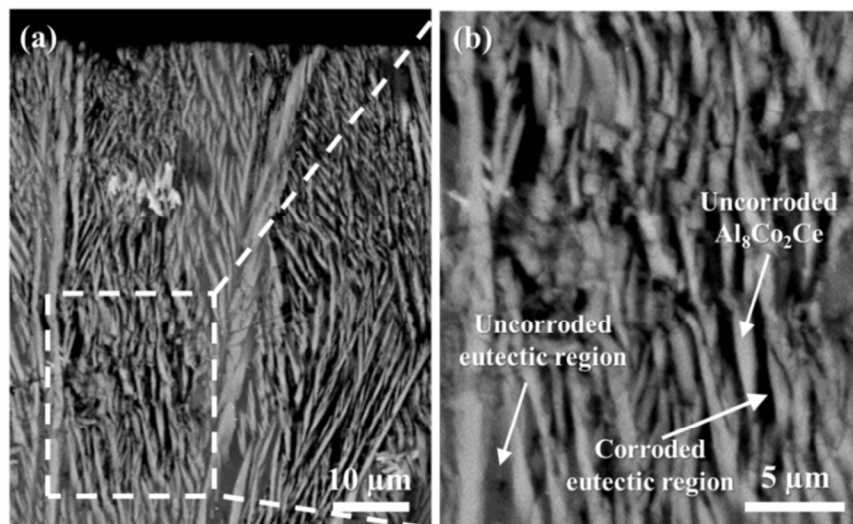


**Figure 8-20** BSE images showing corrosion morphologies of the laser treated Al-Co-Ce alloy 3 in cross sectional view after a potentiodynamic polarisation corrosion test in deaerated 3.5 wt.% NaCl solution (-200 mV~250 mV relative to OCP).

### 8.3.2.3 LAEB treated alloy

**Figure 8-21** and **Figure 8-22** show the corrosion morphologies of the LAEB treated Al-Co-Ce alloy 3 after a potentiodynamic polarisation corrosion test in deaerated 3.5 wt.% NaCl solution (-200 mV~250 mV relative to OCP) in plan view and cross sectional view, respectively. Overall, the surface of the treated sample did not suffer apparent corrosion (**Figure 8-21**). However, a localised corrosion pit was found in the treated layer surface, which was located on a crack (**Figure 8-21c and d**). It also can be seen that the amorphous layer on this corrosion site has been removed. There was a great amount of corrosion products inside the corrosion pit, which exhibited a dark contrast compared with the surrounding uncorroded amorphous layer under back scattered electron imaging mode (**Figure 8-21d**).

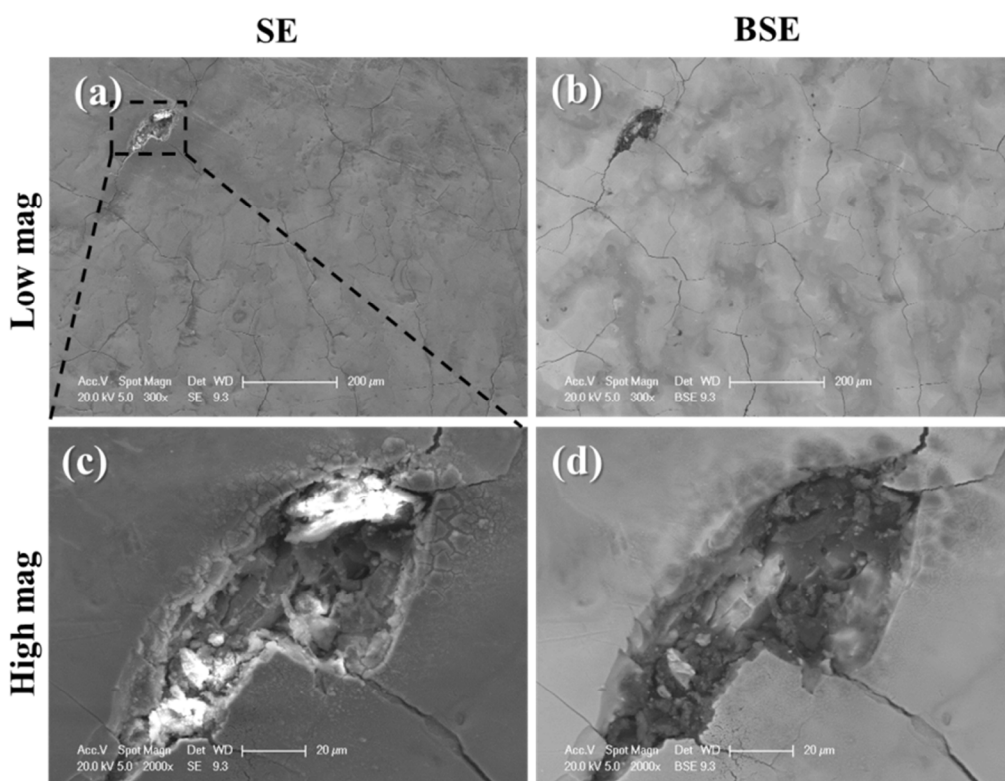


**Figure 8-21** Corrosion morphologies of the LAEB treated Al-Co-Ce alloy 3 (35 kV, 25 pulses) in plan view after a potentiodynamic polarisation corrosion test in deaerated 3.5 wt.% NaCl solution (-200 mV~250 mV relative to OCP).

Underneath the amorphous layer, the substrate surrounding the crack was also corroded from the observation in the cross sectional view (**Figure 8-22**). Although the corrosion of Al/Al<sub>11</sub>Ce<sub>3</sub> region has spread to a distance of approximately 50  $\mu\text{m}$  in depth, the top amorphous layer was still intact even in the region close to the crack. Generally, the surface of the amorphous layer was still smooth, and the thickness was also consistent with that before corrosion testing.

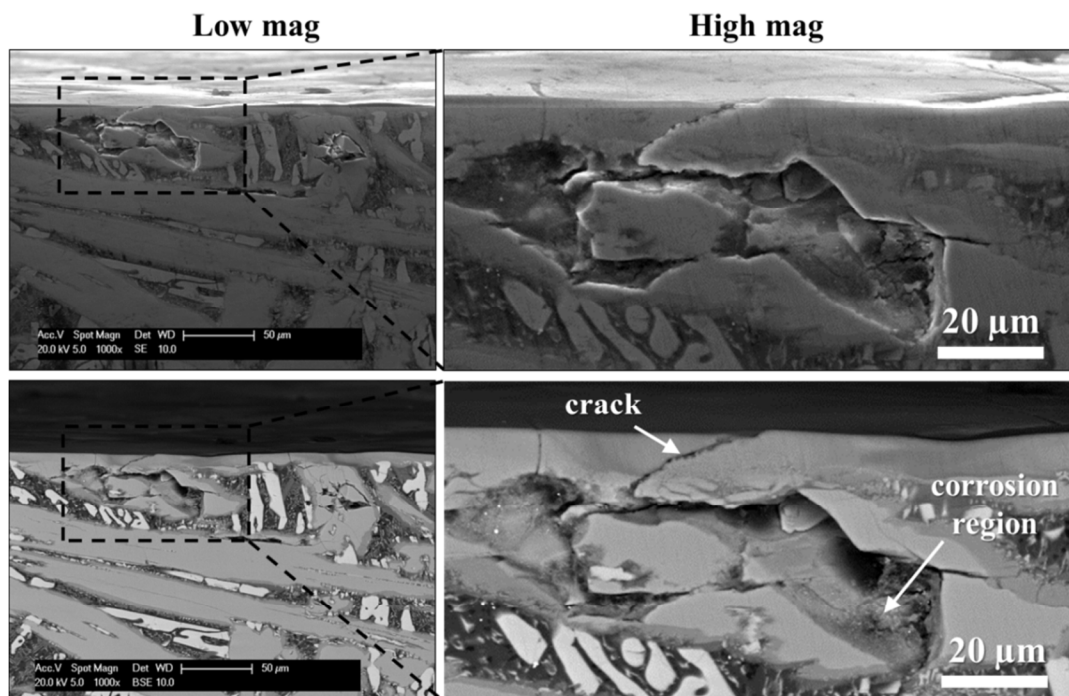


**Figure 8-22** Corrosion morphologies of the LAEB treated Al-Co-Ce alloy 3 (35 kV, 25 pulses) in cross sectional view after a potentiodynamic polarisation corrosion test in deaerated 3.5 wt.% NaCl solution (-200 mV~250 mV relative to OCP).

#### 8.3.2.4 LSM-LAEB treated alloy

Potentiodynamic polarisation corrosion tests were also performed on two LSM-LAEB treated layers. Two layers were generated by the same LSM pre-treatment and LAEB cathode voltage, but different numbers of LAEB pulses. For the treated layer 1 and layer 2, the number of LAEB pulses was 25 and 8, respectively. Based on the microstructural characterisation of the above two layers,

treated layer 1 with higher LAEB pulses was found to be more uniform in the compositional distribution (**Figure 6-18**). After similar corrosion testing, two LSM-LAEB treated layers exhibited different corrosion morphologies as below.

**(1) Layer 1 (LSM: L3, LAEB: 35 kV, 25 pulses)**

**Figure 8-23** is the comparison in plan view of LSM-LAEB Al-Co-Ce alloy 3 (treated layer 1) before and after a potentiodynamic polarisation corrosion test in deaerated 3.5 wt.% NaCl solution (-200 mV~425 mV relative to OCP). It can be seen that the sample did not suffer apparent local corrosion as that shown in the as-cast or LSM treated samples, although the edge of the exposed region exhibited a darker contrast than the centre of the exposed region.

**Figure 8-24** shows the magnified image in plan view of the interface between the exposed and the lacquered region of LSM-LAEB treated sample. The corroded exposed region was apparently lower than the neighbored lacquered region, which formed a step over the interface between them.

This height difference between the exposed region and the lacquered region can be seen more clearly in **Figure 8-25**. In this figure, the sample was sectioned along the plane A-A' as shown in **Figure 8-23** and then slightly tilted under SEM observation. The exposed region was seen to be lower than the lacquered region in height (**Figure 8-25a**). The uniform corrosion in the exposed region also can be confirmed by the straight surface profile of amorphous layer after corrosion testing seen in the cross section observation (**Figure 8-25b**). However, due to the small depth of corrosion attack, the height difference between the lacquered region and the exposed region was not observed in the cross sectional view (**Figure 8-25b**).

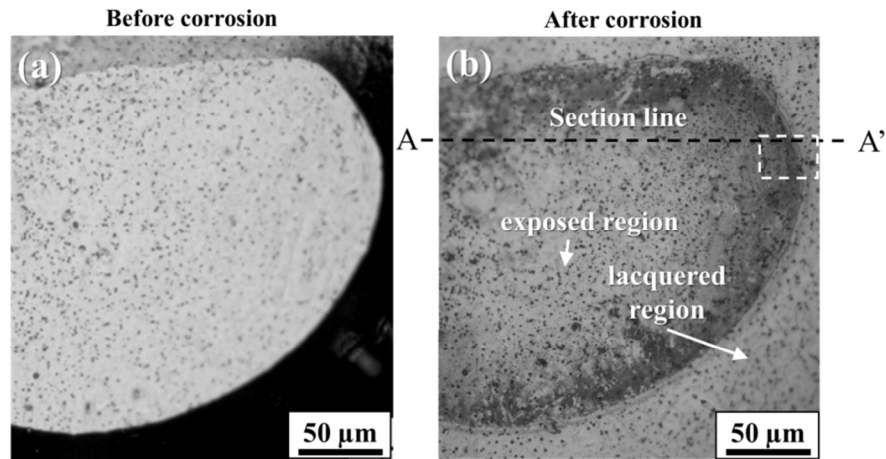


**Figure 8-23** Optical images of the LSM-LAEB treated Al-Co-Ce alloy 3 (treated layer 1) in plan view before (a) and after (b) a potentiodynamic polarisation corrosion test in deaerated 3.5 wt.% NaCl solution (-200 mV~425 mV relative to OCP). The sample was sectioned along the plane A-A' for the cross sectional observation.

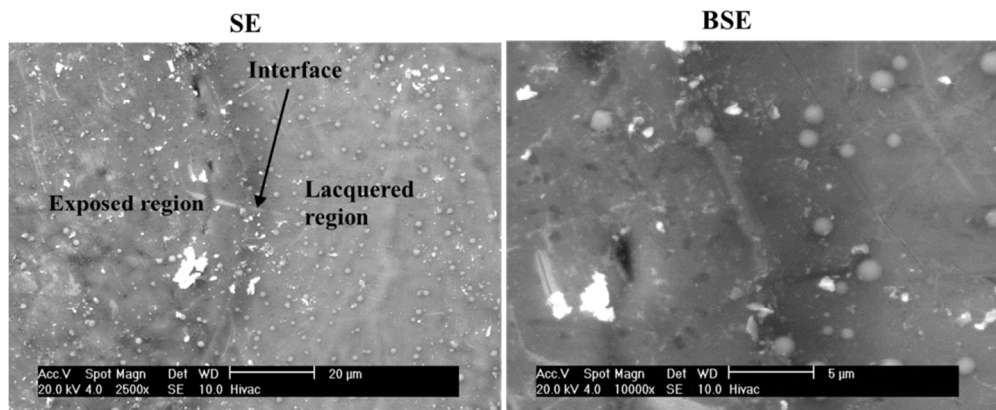


**Figure 8-24** Magnified region in the dashed box of Figure 8-23b.

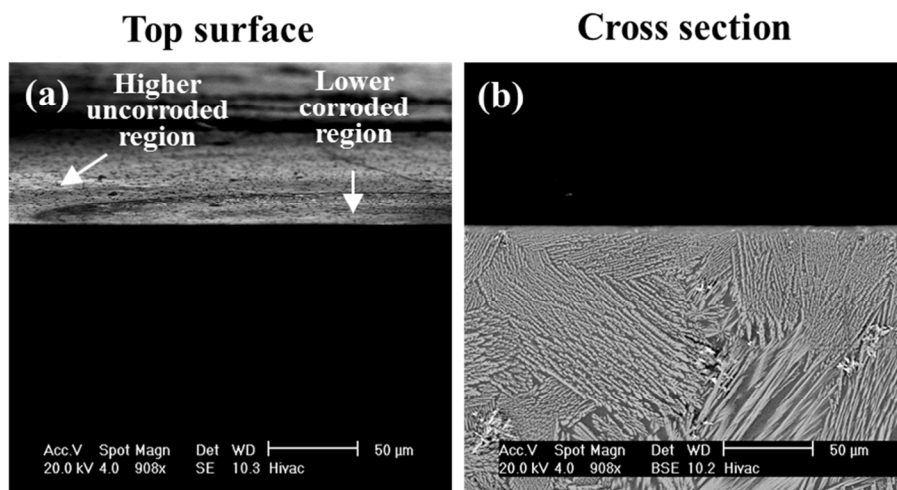


**Figure 8-25** SEM images of the sample cut along the plane A-A' shown in Figure 8-23b. The cross section in this figure is the plane A-A'. The top surface are the view of the same, but tilted sample as that for the cross sectional view.

**Figure 8-26** shows a magnified region shown in **Figure 8-23b** in plan view. There was no apparent local corrosion seen on the sample surface. This again indicates the corrosion which occurred on the LSM-LAEB treated layer is uniform corrosion. In addition, it should be noted that the particles on all over the sample surface after corrosion testing were found to retain the original size and distribution as that shown in the as-treated sample before corrosion. In addition, no apparent corrosion which is related to the existence of these particles was seen for both the amorphous layer and particles themselves.

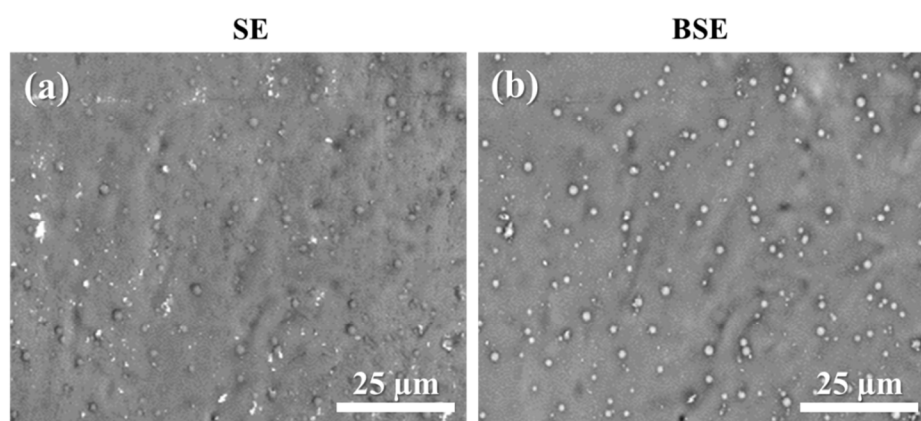


**Figure 8-26** Corrosion morphologies in the central region of the LSM-LAEB treated Al-Co-Ce alloy 3 (treated layer 1) in plan view of a magnified region in **Figure 8-23b** after a potentiodynamic polarisation corrosion test in deaerated 3.5 wt.% NaCl solution (-200 mV~425 mV relative to OCP).

(2) Layer 2 (LSM: L3, LAEB: 35 kV, 8 pulses)

**Figure 8-27** and **Figure 8-28** show the corrosion morphologies of LSM-LAEB treated Al-Co-Ce alloy 3 (treated layer 2) in plan view after a potentiodynamic polarisation corrosion test in deaerated 3.5 wt.% NaCl solution (-200 mV~425 mV relative to OCP). After corrosion testing, the entire exposed region became darker compared with that before corrosion testing and the lacquered region. The corrosion occurred on the exposed region can be confirmed from the observation of the interface (**Figure 8-28**). It can be seen that a step formed between the

exposed region and the lacquered region, which is similar to that shown in **Figure 8-24**. A number of cracks were also found in the exposed region (**Figure 8-27b**). It should be also noted that the cracking seems to be related to the Al-rich region in the exposed region (**Figure 8-28**). This Al-rich region was darker and lower than the surrounding surface in the exposed region under back scattered electron and secondary electron imaging mode, respectively. EDS analyses of the Al-rich region showed that it contained a great amount of aluminium and oxygen, as well as a small amount of cerium and a trace of cobalt.

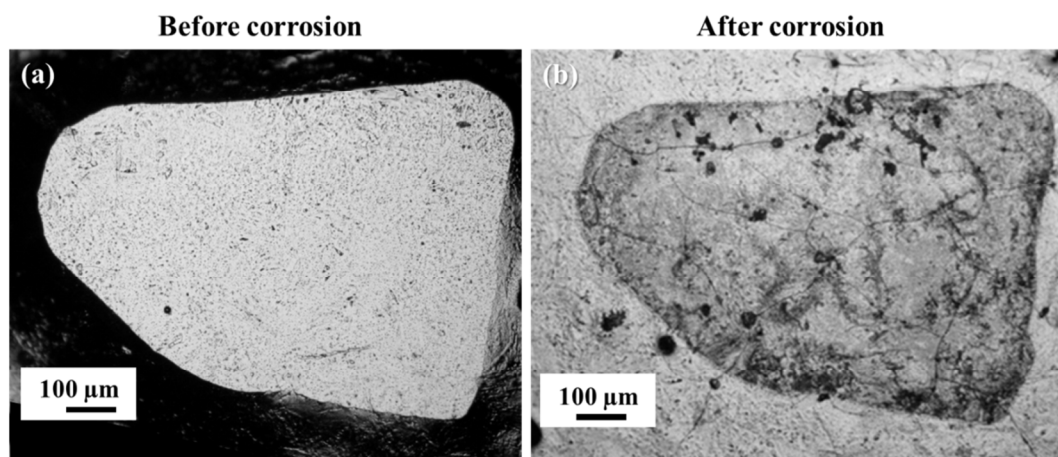


**Figure 8-27** Optical images of the LSM-LAEB treated Al-Co-Ce alloy 3 (treated layer 2) in plan view before and after a potentiodynamic polarisation corrosion test in deaerated 3.5 wt.% NaCl solution (-200 mV~425 mV relative to OCP).

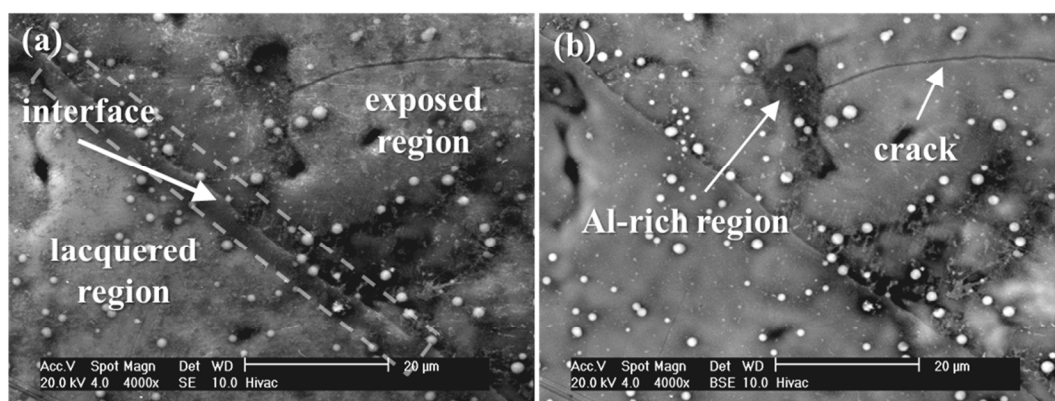


**Figure 8-28** Corrosion morphologies at the interface of the LSM-LAEB treated Al-Co-Ce alloy 3 (treated layer 2) in plan view after a potentiodynamic polarisation corrosion test in deaerated 3.5 wt.% NaCl solution (-200 mV~425 mV relative to OCP).

**Figure 8-29** shows the corrosion morphology in the central region of the LSM-LAEB treated Al-Co-Ce alloy 3 (treated layer 2) in plan view after a potentiodynamic polarisation corrosion test in deaerated 3.5 wt.% NaCl solution. It can be seen that due to the local heterogeneity, local corrosion occurred on the treated layer surface. However, the relatively homogeneous region was covered with uniform corrosion products, which suggest the occurrence of uniform corrosion. In addition, the bright particle also remained on the surface of the amorphous layer as that seen in **Figure 8-26**. There was also no apparent corrosion related to these particles.

The corrosion underneath the cracks and pores in the treated layer as shown in **Figure 8-27b** can be examined in **Figure 8-30**. It can be seen that the corrosion sites in the substrate were closely related to the existence of cracks and pores in the LSM-LAEB treated layer. However, the top amorphous layer did not suffer apparent corrosion as that seen in the underlying material.

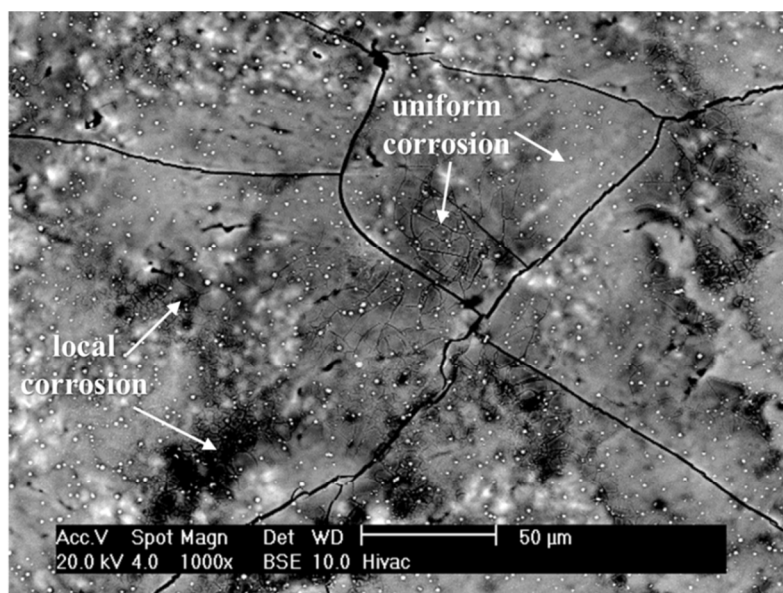


**Figure 8-29** Corrosion morphology in the central region of the LSM-LAEB treated Al-Co-Ce alloy 3 (treated layer 2) in plan view after a potentiodynamic polarisation corrosion test in deaerated 3.5 wt.% NaCl solution (-200 mV~425 mV relative to OCP).

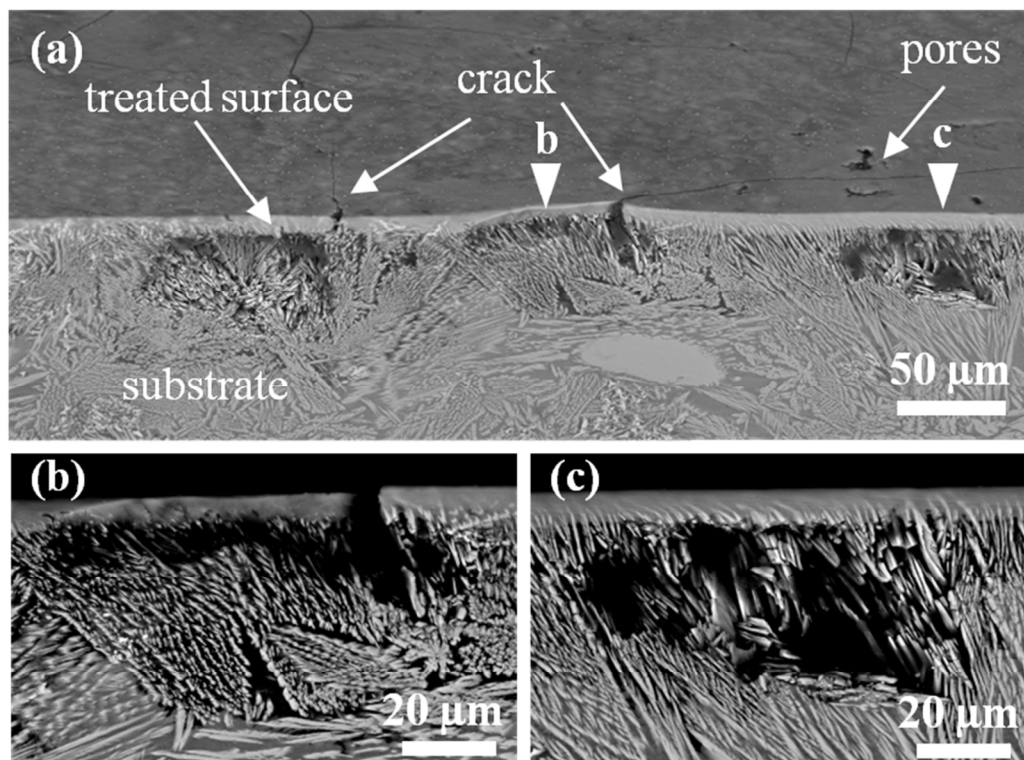


**Figure 8-30** BSE image of tilted sample as shown in Figure 8-28, showing the defects in the treated layer and corresponding underlying corrosion. (a) is the whole image, (b) is the magnified image of region b shown in (a), (c) is the magnified image of region c shown in (a).

## 8.4 Discussion

### 8.4.1 Corrosion behaviour of AA2024, pure Al and alclad 2024

#### 8.4.1.1 AA2024

For the high strength aluminium alloy, corrosion is mainly attributed to the existence of some second phases, such as  $\text{Al}_2\text{CuMg}$  [171, 173-175]. In our work,  $\text{Al}_2\text{CuMg}$  phase particles have been found in the AA2024 alloy before corrosion testing (Figure 8-1, Figure 8-2, Figure 8-3 and Table 8-1). It has been reported that this second phase has lower corrosion potential than the Al-rich matrix [176]. Therefore, during the potentiodynamic corrosion test, this phase will begin to corrode earlier than Al-rich matrix. The increase of Cu content after corrosion

testing shown in **Figure 8-9** can account for the decreased contents of Al and Mg i.e. the dealloying of the precipitate. The above mentioned dealloying of precipitate resulted in the presence of a gap between the precipitate and the matrix (**Figure 8-10**), which also caused the detachment of  $\text{Al}_2\text{CuMg}$  from the matrix, i.e. appearance of the corrosion pit shown in **Figure 8-8**. In addition, the cracking of the precipitate particles (**Figure 8-8 and Figure 8-10**) after corrosion testing might be also due to the dealloying.

#### **8.4.1.2 Pure Al**

Pitting corrosion of aluminium usually initiates at the defects of the naturally formed passive film. In the NaCl solution, chloride ions can preferentially adsorb on these sites. The interaction of  $\text{Cl}^-$  and passive film results in the localised breakdown of the passive film, which finally causes the dissolution of underlying metal [177]. Pitting of aluminium induced by chloride ions at room temperature is the crystallographic form of attack, the pit always bounds by the lattice plane of (100) [178]. In this crystallographic form of attack, the corrosion pit is the product of single short-life tunnelling events. These single tunnels always tend to reach stable crystallographic wall i.e. the (100) plane in the aluminium.

In this work, pure Al suffered typical pitting corrosion (**Figure 8-11a**), which is consistent with the literature [178]. Corrosion pit exhibited a very rough wall which consisted of a great number of sharp lattice plane walls. Two neighbouring lattice plane walls usually exhibited the angle of  $90^\circ$ . These plane were supposed to be the (100) surface in the faced centred cubic aluminium lattice.

### 8.4.1.3 Alclad 2024

For the cladding layer in the alclad 2024, the corrosion behaviour is similar to pure Al. However, due to the difference in chemical composition shown in **Table 3-2**, cladding layer of alclad 2024 had slightly higher  $E_{corr}$  but narrower passivation range than pure Al (**Figure 8-6**). In our work, the tunnelling corrosion occurred in the cladding layer of alclad 2024 (**Figure 8-12**) was seen to be very similar to that shown in pure Al (**Figure 8-11**). However, some curved pit walls were also seen in the centre of the large pit in the corrosion morphology of alclad 2024 (**Figure 8-12c and d**). These curved and finely stepped fronts are thought to be the transient state of pitting of aluminium [178].

In addition, it is seen that the substrate AA2024 did not suffer corrosion attack, although the localised cladding layer has been largely depleted by the pitting dissolution. A thin cladding layer with the thickness of  $\sim 15 \mu\text{m}$  was found to be retained above the substrate. The large pits spread to the rest of the uncorroded cladding layer rather than extended into the substrate AA2024 along with the direction of depth (**Figure 8-13**). This indicates that the transition layer is more resistant to corrosion than cladding layer. Sun et al. [179] also found this phenomenon in their investigation on atmospheric corrosion behaviour of alclad 7075 in long-term field testing. They proposed that when a small amount of Mg is present in pure Al in the form of solid solution, or partially precipitated as  $\text{Al}_8\text{Mg}_5$  particles dispersed uniformly throughout the matrix, the material shows better corrosion resistance than commercially pure aluminium in salt water and some alkaline solutions. In this work, the transition layer was also found to contain a minor amount of Mg (**Figure 8-4 and Table 8-2**).

## 8.4.2 Corrosion behaviour of as-cast, LSM and LAEB treated Al-Co-Ce alloy

### 8.4.2.1 As-cast material

From the corrosion morphologies of as-cast Al-Co-Ce alloy 3, the  $\text{Al}_8\text{Co}_2\text{Ce}$  phase did not suffer obvious corrosion compared to the other two main phases present in the alloy, including the Al and  $\text{Al}_{11}\text{Ce}_3$  phase. Nevertheless, the pure Al phase has been mostly removed due to the dissolution. Therefore, although there was insufficient information to determine the electrode potential of different phases, it can be said that for the conditions used in this work  $\text{Al}_8\text{Co}_2\text{Ce}$  was more noble compared with Al and  $\text{Al}_{11}\text{Ce}_3$ .

In the potentiodynamic polarisation test, oxidation reaction firstly occurs on the Al phase with increasing polarisation potential, which results in the active dissolution of this phase. The dissolution of Al phase caused a great number of cavities among the  $\text{Al}_8\text{Co}_2\text{Ce}$  (**Figure 8-15**). There was also no  $\text{Al}_{11}\text{Ce}_3$  phase left in the corroded region of as-cast sample. For the disappearance of  $\text{Al}_{11}\text{Ce}_3$  phase either in the eutectic or in the form of primary phase,  $\text{Al}_{11}\text{Ce}_3$  might have fallen out as a result of the dissolution of the surrounding pure Al matrix. From **Figure 8-17**, some cavities have been seen due to the detachment of primary  $\text{Al}_{11}\text{Ce}_3$  phase particles. As for the lamellar  $\text{Al}_{11}\text{Ce}_3$  in the eutectic, the small size can ease their detachment. However, at the edge of the exposed area in the test sample, primary  $\text{Al}_{11}\text{Ce}_3$  phase was found to have not been corroded (**Figure 8-17**). This suggests that this phase is relatively noble compared with pure Al. The schematic of the corrosion in the as-cast Al-Co-Ce alloy 3 is shown in **Figure 8-31**.

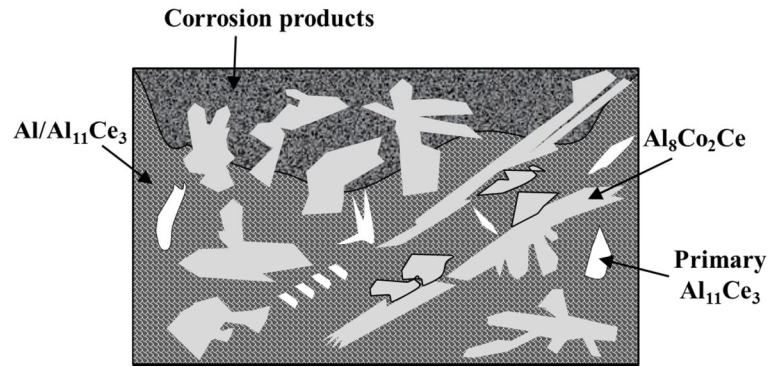


**Figure 8-31 Schematic of the corrosion in the as-cast Al-Co-Ce alloy 3. Al/Al<sub>11</sub>Ce<sub>3</sub> eutectic matrix was preferentially corroded.**

#### 8.4.2.2 LSM treated Al-Co-Ce alloy

The LSM refined microstructure consisted of Al/Al<sub>11</sub>Ce<sub>3</sub> eutectic and greatly refined Al<sub>8</sub>Co<sub>2</sub>Ce phase. In the Al-Co-Ce alloy 3, the primary Al<sub>11</sub>Ce<sub>3</sub> phase was eliminated. Overall, the microstructure treated by LSM in this work suffered similar corrosion to that which occurred in the as-cast alloy. **Figure 8-19** and **Figure 8-20** show the preferential corrosion of Al/Al<sub>11</sub>Ce<sub>3</sub>.

Another phenomenon is interesting to discuss. **Table 8-4** shows that the LSM treated alloy had a slightly lower  $E_{corr}$  compared with the as-cast alloy. Lower  $E_{corr}$  of the LSM treated microstructure is due to the high energy state compared with the as-cast alloy with the same chemical composition. LSM microstructural refinement brings the rapid solidification of the treated alloy. Refined microstructure with excessive energy brought by the LSM treatment is thereby unequilibrium and unstable. It can be proposed that the transformation from the alloy at high-energy state to the metallic ions will cause larger free energy change, compared to that from the relatively equilibrium as-cast alloy to the same metallic ions. The relationship between the energy change and corresponding electrode potential i.e. OCP can be expressed by the equation below.

$$\Delta G = -nFE \quad \text{Eq. 8-1}$$

where  $\Delta G$  is the free energy change when the alloy transformed in the form of metal into ion,  $n$  is the number of electrons transferred in the corrosion reaction,  $F$  is Faraday's constant with the value of 96485 coulombs/mole which represents the charge transported by one mole of electrons,  $E$  is the electrode potential. According to **Eq. 8-1**, LSM treated alloy with larger energy change during the transformation between metallic and ion form will have a more negative electrode potential. This electrode potential is equivalent to OCP, when it is measured in absence of external applied potential. The schematic of the corrosion in the LSM treated sample is shown in **Figure 8-32**.

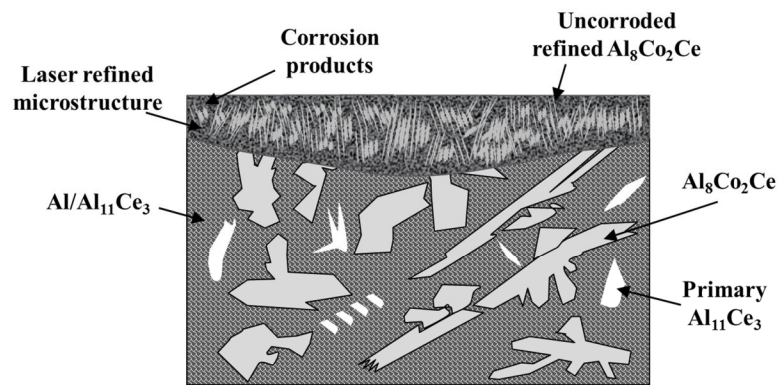


**Figure 8-32 Schematic of the corrosion in the LSM treated Al-Co-Ce alloy 3. Al/Al<sub>11</sub>Ce<sub>3</sub> eutectic in the laser refined microstructure was preferentially corroded. Refined Al<sub>8</sub>Co<sub>2</sub>Ce phase particles were still retained.**

#### **8.4.2.3 Corrosion behaviour of LAEB treated Al-Co-Ce alloy 3 (with cracks)**

In this work, LAEB successfully generated an amorphous layer with the thickness of several microns on the bulk multiphase crystalline Al-Co-Ce alloy. However, the rapid cooling also induced the cracking of the amorphous layer. In the amorphous layer with cracks, cracks in the amorphous layer provided a penetration path for the electrolyte to attack the underlying materials. When the electrolyte reached the crystalline substrate, the multiphase microstructure suffered similar

corrosion as that in the as-cast material, i.e. the preferential dissolution of the pure Al matrix. Both the  $\text{Al}_8\text{Co}_2\text{Ce}$  phase and the amorphous layer did not suffer apparent corrosion attack for the LAEB treated Al-Co-Ce alloy 3 (**Figure 8-21 and Figure 8-22**). The intact amorphous layer indicates that in the same environment, Al-Co-Ce amorphous layer has better corrosion resistance compared with the underlying multiphase crystalline alloy. This can be explained by the higher  $E_{corr}$  and  $E_{pit}$  of amorphous layer compared with pure Al shown in **Figure 8-6 and Figure 8-14**. The schematic of the corrosion in the LAEB treated layer with cracks is shown in **Figure 8-33**.

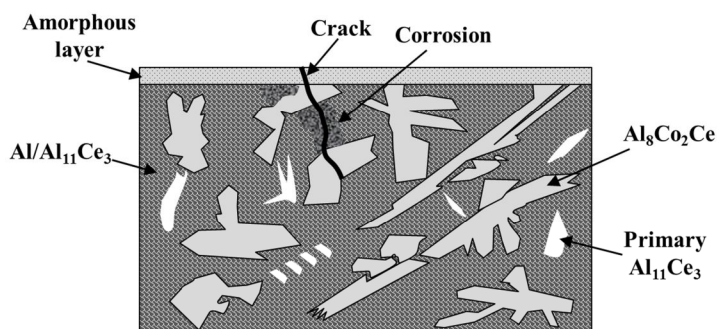


**Figure 8-33 Schematic of the corrosion in the LAEB treated amorphous layer with cracking. Electrolyte penetrated into crystalline substrate through the cracks. The  $\text{Al}/\text{Al}_{11}\text{Ce}_3$  eutectic suffered preferential corrosion.**

### 8.4.3 Corrosion behaviour of LSM-LAEB treated amorphous alloys (crack-free)

#### 8.4.3.1 Corrosion behaviour

In order to eliminate the cracking, LSM pre-treatment was used prior to the LAEB treatment. It has been found that cracking was greatly reduced in the microstructural refined alloy. In the case of LSM-LAEB treated samples, potentiodynamic polarisation corrosion tests were performed on the carefully selected, small crack-free regions (the area of the exposed region in the electrolyte

was always less than  $1 \text{ mm}^2$ ), in order to determine the corrosion behaviour of the crack-free amorphous alloy.

Similar corrosion tests were conducted on two types of LSM-LAEB treated layers differing in the homogeneity of the composition. Results showed that both treated layers suffered uniform corrosion (**Figure 8-24**, **Figure 8-25** and **Figure 8-28**). However, due to the more homogeneous chemical composition, the treated layer 1 was more corrosion resistant, exhibiting higher  $E_{pit}$ , larger passivation potential range  $E_{pit}-E_{corr}$  (**Figure 8-14**) and less distinct corrosion damage. The corrosion only occurred in the top amorphous layer, the underlying crystalline substrate was thereby completely protected (**Figure 8-25**). The schematic of the corrosion in the LSM-LAEB treated layer 1 is shown in **Figure 8-34**.



**Figure 8-34 Schematic of the corrosion in the LSM-LAEB treated layer 1. Uniform corrosion occurred in the crack-free and compositionally homogeneous LSM-LAEB treated amorphous layer.**

In the case of the treated layer 2, localised Al-rich regions also suffered corrosion in addition to the uniform corrosion of the normal amorphous layer. The corrosion of Al-rich regions also induced the cracking of the neighbouring amorphous layer due to the in-situ expansion of corrosion products (**Figure 8-28**). The underlying LSM refined microstructure was therefore corroded by the electrolyte penetrating through the above cracks (**Figure 8-30**). The schematic of the corrosion in the LSM-LAEB treated layer 2 is shown in **Figure 8-35**.

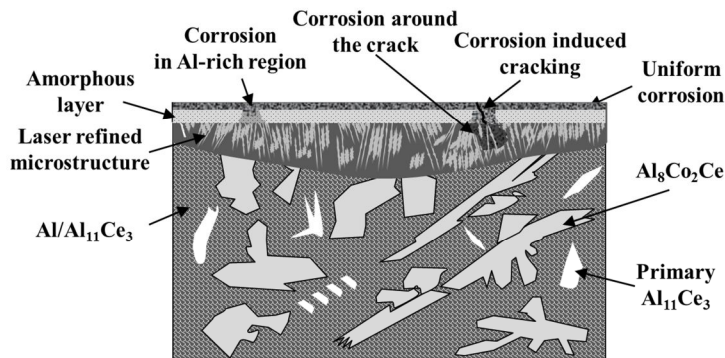


**Figure 8-35 Schematic of the corrosion in the LSM-LAEB treated layer 2. Localised Al-rich region suffered corrosion in addition to the general uniform corrosion in the amorphous layer, which also induced the cracking of amorphous layer. Cracking provided the penetration path for the electrolyte to corrode the underlying LSM refined microstructure.**

#### 8.4.3.2 Comparison with AA2024, pure Al and alclad 2024

**Figure 8-36a** shows the electrochemical polarisation behaviour of the LSM-LAEB treated Al-Co-Ce amorphous layer compared with pure Al, alclad 2024 and AA2024. Combining **Table 8-3** and **Table 8-4**, amorphous layer has a much more negative  $E_{corr}$  compared with AA2024 (the difference between them in  $E_{corr}$  was approximately 220 mV), which means that this amorphous layer can act as the anode once they present in the same environment. It is also seen that the  $E_{corr}$  of amorphous layer was higher than that of pure Al, which suggests that the amorphous layer has a better corrosion barrier property. This has been confirmed by the preferential corrosion of Al-rich region but not amorphous layer in LAEB treated layer with cracks shown in **Figure 8-21** and **Figure 8-22**. Compared with Al cladding, another advantage of amorphous layer is the higher  $E_{pit}$ , and wider passivation range ( $E_{pit}-E_{corr}$ ). However, it should be noted that the passivation range of pure Al is slightly wider than that of the amorphous layer.

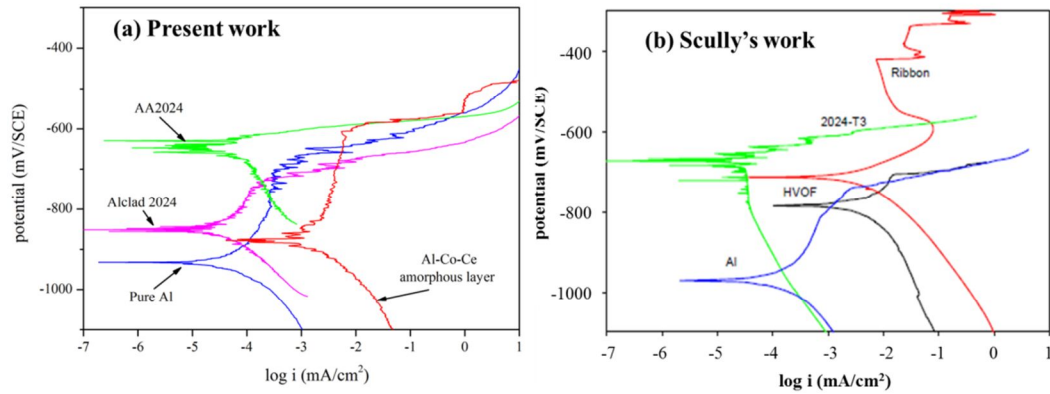


**Figure 8-36** Polarisation behaviour of the LSM-LAEB treated Al-Co-Ce amorphous layer compared with pure Al, alclad 2024, AA2024 and related materials investigated by Scully et al.[14]. Ribbon represents the melt spun bulk fully amorphous alloy with the composition of Al-7.5Co-8.5Ce (at.%).

HVOF represents the high velocity oxygen flame sprayed partially amorphised coating with the composition of Al-8.3Co-7Ce (at.%). Al has the purity of 99.99%. All corrosion tests were performed in deaerated 3.5 wt.% NaCl solution.

#### 8.4.3.3 Comparison with literature

**Figure 8-36b** shows the polarisation curves of related materials investigated by Scully et al. [14]. Overall, the results obtained in the present work are in good agreement with Scully's work. The LSM-LAEB treated Al-Co-Ce alloy with the composition of Al-7.6Co-6.4Ce (at.%) in the present work exhibited a lower  $E_{corr}$  compared with the bulk fully amorphous melt spun ribbon with the composition of Al-7.5Co-8.5Ce (at.%). However, the HVOF coating reported in Scully's work showed the smaller difference in  $E_{corr}$ . Therefore, it is suggested that the above difference might be due to the extent of amorphisation. It has been mentioned the melt spun ribbon had the fully amorphous structure, but both the amorphous layer in this work and the HVOF coating not. The chemical composition difference might also affect  $E_{corr}$ . In addition to  $E_{corr}$ , from the comparison shown in **Figure 8-36a** and **b**, the HVOF coating did not exhibit similar passivation as that seen in the LSM-LAEB treated alloy in this work and melt spun ribbon. This suggests the microstructure of the alloy also influenced the polarisation behaviour.

#### **8.4.3.4 Corrosion current density**

Both in the present work and in Scully's work,  $I_{pit}$  of the amorphous alloy (LAEB treated amorphous layer, HVOF sprayed coating or melt spun ribbon) was bigger than that of AA2024, alclad 2024 or pure Al. This might be partially due to the nature of local corrosion occurred on AA2024, alclad 2024 and pure Al. In above three materials, the measured current consisted of passivation current at uncorroded regions and the dissolution current in the pits growth. The passivated regions have a much lower current but a larger area than the region which suffered pitting. However, the total area exposed in the electrolyte was adopted in the calculation of current density. Therefore, the current density measured in this work is lower than the actual dissolution current density in the pits growth [180]. In addition, the pitted area of the sample surface also varied with time.

In the case of the alloy in the amorphous state, the corrosion mechanism is macroscopic uniform corrosion, which makes the measured current density in the polarisation curve consistent with the reality. Due to this inconsistency of the measured current density and actual current density for pure Al and Al cladding which mainly suffered pitting corrosion, it is not suitable to compare the current density to assess the corrosion rate for the amorphous alloy and the above pitted materials. Therefore, in the next section, the nominal uniform corrosion depth (the volume of the dissolved material divided by the total exposed area of the sample) of three materials will be compared.

#### **8.4.3.5 Corrosion rate**

To directly compare the corrosion rate i.e. dissolution rate of the three materials (crack free amorphous layer, pure Al and Al clad), the nominal uniform corrosion

depth is calculated in this section. For the above three materials, the data used for the calculation was taken from the same polarisation potential range (0 mV to 425 mV relative to OCP) in the potentiodynamic polarisation test. To simplify the analyses, the corrosion occurred on above three materials is assumed to be only resulted from the anodic dissolution of Al. The anodic reaction is shown below:



### (1) Calculation of the dissolved volume

**Figure 8-37** plots the corrosion current versus time over the potential range from 0 to 425 mV (relative to OCP) in the potentiodynamic polarisation test with the same scanning rate of 10 mV/min for pure Al, Alclad 2024 and LSM-LAEB treated layer 1 (the crack free amorphous layer). Therefore, the total electric charge ( $Q$ ) resulted from the dissolution of Al in the polarisation test is the electric current ( $I$ ) integrated over time ( $t$ ):

$$Q = \int_0^t Idt \quad \text{Eq. 8-3}$$

According to Faraday's law,

$$m = \frac{M}{zF} Q \quad \text{Eq. 8-4}$$

where  $m$  is the mass of the substance liberated at an electrode (g),  $F$  is the Faraday constant (96485 C/mol),  $M$  is the molar mass of the substance, and  $z$  is the valency number of ions of the substance (electrons transferred per ion). Combining **Eq. 8-3** and **Eq. 8-4**, the mass ( $m$ ) and volume ( $V$ ) of the substance liberated were written as follows:

$$m = \frac{M}{zF} \int_0^t Idt \quad \text{Eq. 8-5}$$

$$V = m / \rho = \frac{M}{zF\rho} \int_0^t Idt \quad \text{Eq. 8-6}$$

where  $\rho$  is the density of Al (2.7 g/cm<sup>3</sup>). The constants used in above calculation and calculated  $V$  for different materials are listed in **Table 8-5**.

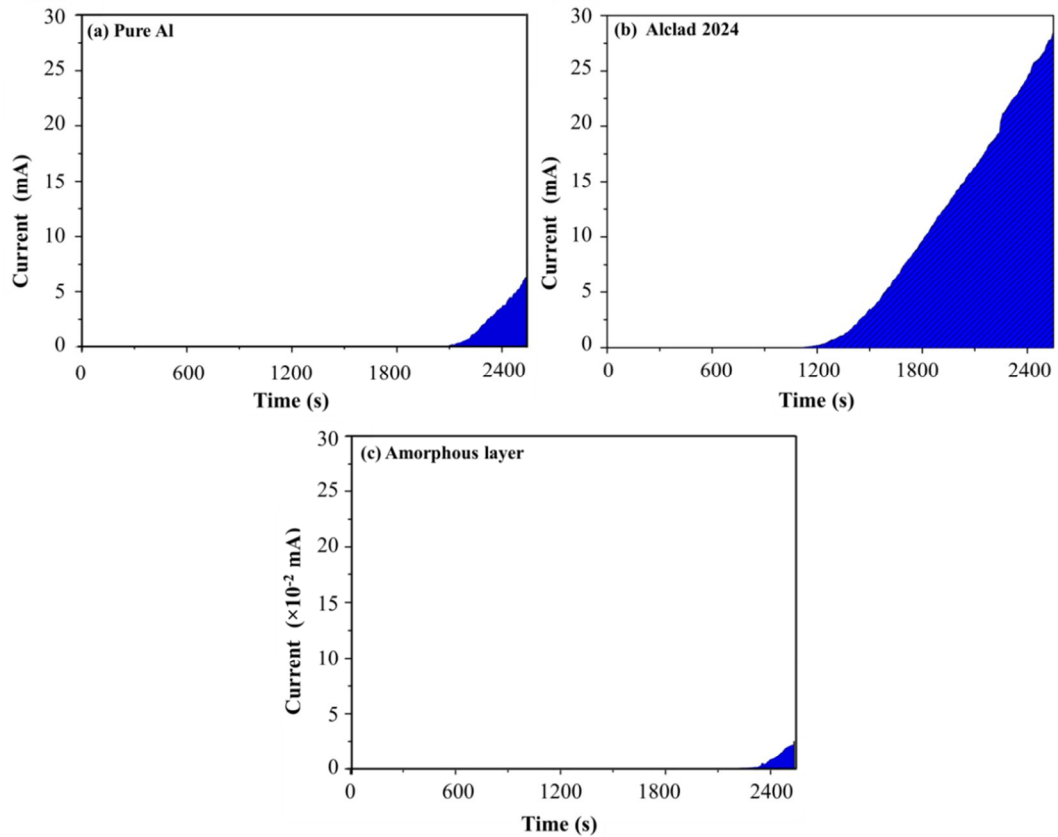


**Figure 8-37** Plots of corrosion current versus time over the potential range from 0 to 425 mV relative to OCP in the potentiodynamic polarisation for pure Al, alclad 2024 and amorphous layer. The scanning rate was 10 mV/min. The scale of x axis in Figure 8-37c is smaller than that in the other two figures.

The smaller current is partially because of the small exposed area of the amorphous layer compared with that of pure Al and alclad 2024.

**Table 8-5** Calculated  $D_{uniform}$  and related constants used in calculations for different materials after the same range of potentiodynamic polarisation in deaerated 3.5 wt.% NaCl solution (-200 mV to 425 mV relative to OCP).

Material	Pure Al	alclad	Amorphous layer
Exposed area, $A_{total}$ (cm <sup>2</sup> )	1.380	0.693	0.00065
Molar mass, $M$ (g/mol)	27	27	36.7
Valency number, $z$ (number)	3	3	3
Electric charge, $Q$ (C)	1.401	16.301	0.0031595
Nominal uniform corrosion depth, $D_{uniform}$ ( $\mu$ m)	0.4	8.2	2.3

## (2) Nominal uniform corrosion depth

The above calculated  $V$  is dependent on the exposed area of the materials. To directly compare the corrosion rate of the three materials, the nominal uniform corrosion depth was calculated based on an assumption that the corrosion that occurred in pure Al and alclad 2024 is uniform. In other words, the corroded area is assumed to be the total exposed area ( $A_{total}$ ) of the test sample. Therefore, the nominal uniform corrosion depth ( $D_{uniform}$ ) can be calculated as follows:

$$D_{uniform} = \frac{V}{A_{total}} \quad \text{Eq. 8-7}$$

For Al-Co-Ce amorphous layer, the corrosion depth can be calculated as well based on the above equation. Calculated results of  $D_{uniform}$  are listed in **Table 8-5**. The nominal uniform corrosion depth for pure Al and alclad was 0.35 and 8.2  $\mu\text{m}$ , respectively. In the case of the amorphous alloy layer, the average depth of uniform corrosion was 2.3  $\mu\text{m}$ , which was generally consistent with the small height difference observed in the corrosion morphology at the interface of the exposed area (**Figure 8-24** and **Figure 8-28**). It can be seen that the depth of the uniform corrosion occurring on amorphous alloy layer was much smaller than that of alclad, and comparable with that on pure Al. Therefore, the crack-free amorphous layer generated by LSM-LAEB process is suggested to be able to replace the alclad in the protection of AA2024 in terms of the corrosion rate.

## 8.5 Summary

- AA2024, pure Al and alclad 2024 suffered pitting corrosion in the potentiodynamic polarisation corrosion test, which is consistent with literature.

- Corrosion behaviour of Al-Co-Ce glass forming alloys is microstructure dependent. Rapid solidified Al-Co-Ce alloys in LSM and LAEB surface melting processes exhibited different extents of passivation compared to the as-cast alloy in the potentiodynamic polarisation corrosion test.
- As-cast and LSM treated Al-Co-Ce alloy suffered localised corrosion. The corrosion occurred in the Al/Al<sub>11</sub>Ce<sub>3</sub> eutectic region. However, the Al<sub>8</sub>Co<sub>2</sub>Ce phase still had the original shape and composition as that seen before corrosion testing.
- Under the conditions used in this work, Al<sub>8</sub>Co<sub>2</sub>Ce is most noble, then Al<sub>11</sub>Ce<sub>3</sub> and then pure Al.
- The amorphous Al-Co-Ce alloy layer generated by LAEB treatment had superior corrosion resistance compared with the crystalline alloy.
- Cracking in the amorphous layer greatly affected the effectiveness of amorphous layer in the protection of the underlying substrate.
- A crack-free amorphous layer generated by combined processing of LSM and LAEB exhibited uniform corrosion. The corrosion rate of crack-free amorphous layer was smaller than alclad and comparable with pure Al in terms of the nominal uniform corrosion depth.

## Chapter 9 Conclusions

### 1. Characterisation of solidification conditions

In this work, Al-Cu eutectic alloy was used to characterise the solidification conditions of the processes, including wedge mould casting, laser surface melting (LSM) and large area electron beam (LAEB) surface melting. In the process of wedge mould casting and laser surface melting, Al-Cu eutectic alloys exhibit lamellar structures consisting of Al and Al<sub>2</sub>Cu phases with different sizes of interlamellar spacing. Based on the well-known  $v\lambda^2 = K_0$  relationship [158], the solidification velocity of the wedge mould cast alloys ranged from 0.0014 to 0.0059 m/s, varying with the position in the wedge mould. In the LSM process, the solidification velocity of the alloys was 0.0104, 0.0370 and 0.0657 m/s, which varied with the sample traverse speed.

In the LAEB process, Al-Cu eutectic alloys did not show a steady eutectic growth. The eutectic structure of Al-Cu alloy seen in wedge mould casting and LSM treatment was transformed into a compositionally uniform structure after LAEB irradiation. There was also an additional phase (cubic close packed supersaturated solid solution) presented in the irradiated alloy (AlCuEB8). Based on TMK theory [164], the estimated solidification velocity was 1.539 m/s. The corresponding cooling rate of the LAEB irradiated Al-Cu alloy was  $4.44 \times 10^7$  K/s. The solidification velocity in the LAEB process decreased with increasing number of pulses. Therefore, the above solidification velocity/cooling rate were thought to be closer to that of the 150 pulses treated sample. In particular, the cooling rate is comparable with the normal critical cooling rate of Al-based amorphous alloy.

## **2. Crystalline Al-Co-Ce alloys prepared by wedge mould casting and laser surface melting**

Crystalline Al-Co-Ce alloys were prepared with wedge mould casting and laser surface melting. There were three main phases, including Al/Al<sub>11</sub>Ce<sub>3</sub> eutectic, Al<sub>8</sub>Co<sub>2</sub>Ce and primary Al<sub>11</sub>Ce<sub>3</sub> in the as-cast alloys. The phase constituent and phase size were found to largely depend on the cooling rate and alloy composition. In the case of the laser surface melting process, the microstructure of the as-cast Al-Co-Ce alloy was greatly refined from ~100×20 μm to ~20×5, ~20×2 and ~20×0.5 μm in different laser treatment. In addition to the greatly reduced size of the Al<sub>8</sub>Co<sub>2</sub>Ce phase, the Al<sub>9</sub>Co<sub>2</sub> phase and the primary Al<sub>11</sub>Ce<sub>3</sub> phase present in the as-cast alloy were almost eliminated, instead of a fine Al/Al<sub>11</sub>Ce<sub>3</sub> eutectic structure. EDS results show that the LSM process also slightly changed the overall composition of the Al/Al<sub>11</sub>Ce<sub>3</sub> eutectic region by increasing the content of Ce.

## **3. Formation of Al-Co-Ce amorphous alloy layers in the LAEB process**

The high cooling rate ( $4.44 \times 10^7$  K/s) of Al-Cu alloy in LAEB process indicates the favourable cooling condition of this process in the preparation of the amorphous alloy. In this work, Al-Co-Ce amorphous layers with the thickness of a few microns were achieved under some suitable LAEB irradiation conditions, such as 100 pulses at cathode voltage of 29 kV and 25~50 pulses at 35 kV. Results show that more pulses of LAEB irradiation and higher cathode voltage were beneficial to increase the thickness and the elemental uniformity of the remelted layer. However, excessive pulses of LAEB irradiation reduced the amorphicity of the remelted layer due to localised crystallisation.

The energy distribution of the electron beam in the irradiated sample and the heterogeneous microstructure of the starting material brought about the formation of craters in the irradiated sample surface. The high cooling rate of the LAEB process and the heterogeneous microstructure of the starting materials also caused cracking in the treated layer. However, laser pretreatment greatly refined the microstructure of the as-cast materials, which greatly reduced the cracking and decreased the number of pulses required for the formation of homogeneous amorphous layer in the LAEB process.

#### **4. Numerical simulation of thermal history in LAEB treated samples**

Temperature is crucial to the thermophysical property. Parallel with the experimental work in **Chapter 6**, the thickness of the remelted layer, the melting time, the solidification velocity and cooling rate of Al-Cu eutectic alloy and Al-Co-Ce alloy under different initial temperatures and cathode voltages were calculated based on the simulation results.

First, calculation results confirm that volume energy density reaches the maximum at the depth of 1/3 of the electron range i.e. the electron penetration depth. This energy deposition results in the prior melting of the subsurface to the outmost layer and subsequent eruption, and causes the formation of craters and particles as observed in the experimental results on the LAEB treated Al-Co-Ce alloy.

Second, due to the same energy input at the same cathode voltage, the modelled thickness of the LAEB remelted layer did not apparently increase with increasing initial temperature, but apparently increases with increasing cathode voltage. However, the modelled thickness of the LAEB remelted layer was higher than the experimental homogenised layer thickness. To explain this difference, melting

time (the time duration of the alloy at or above the melting point) was calculated. It was found that modelled melting time increased with increasing both pulse sequence number and cathode voltage of the LAEB irradiation. Therefore, it can be concluded that the formation of the homogenised layer requires sufficient melting time. Extended melting time will increase homogenised layer thickness, which is consistent with the experimental results.

Third, the modelled solidification velocity and cooling rate of the Al-Cu eutectic alloy were comparable with the experimental ones. For Al-Co-Ce alloy, the modelled solidification velocity and cooling rate were sufficiently high for the generation of amorphous phase. In addition, both solidification velocity and cooling rate decreased with the initial temperature and cathode voltage of the LAEB pulse, which is consistent with the experimental results on the amorphisation extent of the LAEB treated layer with the homogenised microstructure.

### **5. Corrosion behaviour of Al-Co-Ce glass forming alloys with different microstructure**

Corrosion experiments show that the corrosion behaviour of Al-Co-Ce glass forming alloy is microstructure dependent. Potentiodynamic polarisation results indicate rapidly solidified Al-Co-Ce alloys in the LSM, LAEB and LSM-LAEB processes exhibited passivation in different extents compared to the as-cast alloy. Among different rapidly solidified microstructures, LSM-LAEB treated samples showed higher pitting potential ( $E_{pit}$ ) and wider passivation range ( $E_{pit}-E_{corr}$ ) compared with as-cast and LSM treated samples.

Corrosion morphologies show that the crystalline Al-Co-Ce alloy suffered localised corrosion in 3.5 wt.% NaCl solution. Under the conditions used in this work, the Al/Al<sub>11</sub>Ce<sub>3</sub> eutectic region was preferentially corroded rather than Al<sub>8</sub>Co<sub>2</sub>Ce. This suggests Al<sub>8</sub>Co<sub>2</sub>Ce is more noble than Al<sub>11</sub>Ce<sub>3</sub> and pure Al. In addition, the Al-Co-Ce amorphous layer generated by the LAEB process had a better corrosion resistance compared with the crystalline counterpart. However, due to the existence of cracks in the amorphous layer, the effectiveness of the amorphous layer in preventing the underlying substrate was greatly affected.

LSM-LAEB samples as the representative of the crack-free amorphous layer exhibited lower corrosion potential ( $E_{corr}$ ) than AA2024, which indicates a cathodic protection property. Compared with pure Al and alclad, the crack-free amorphous layer had a higher  $E_{pit}$  and wider ( $E_{pit}-E_{corr}$ ). In addition, based on the estimation of the nominal uniform corrosion depth, the corrosion rate of the crack-free amorphous layer generated by the LSM-LAEB process was much smaller than alclad and comparable to pure Al. Therefore, it can be proposed that the crack-free amorphous layer generated by the LSM-LAEB process is promising to replace the alclad.

## Chapter 10 Future work

1. Al-Cu alloy exhibited a largely different microstructure in the LAEB process compared with that in other processes. Further investigation on the microstructure and performance of Al-Cu alloy in the process with high solidification rates is of interest.
2. Al/Al<sub>11</sub>Ce<sub>3</sub> eutectic also has a lamellar structure. Al-Ce eutectic alloy might be useful to characterise the solidification conditions of different processes. It is also necessary to compare the microstructure of Al/Al<sub>11</sub>Ce<sub>3</sub> eutectic region and Al-Ce eutectic alloy under the same process.
3. Cheap misch metal elements can be used to replace pure rare earth in Al based glass forming alloy in order to reduce the cost of the amorphous alloy. However, the corrosion resistance of the new amorphous alloy should also be examined. In addition, LAEB process parameters and pretreatment can be further optimised to generate the large area crack-free amorphous layer. Alternatively, any method to heal the existing cracks should be developed.
4. A two or three dimensional temperature field of the irradiated alloy in LAEB process can be developed. In this thesis, the heat source power was assumed to be constant. However, in practice it might be time dependent. In addition, most thermophysical properties (density, specific heat, thermal conductivity, etc.) of the alloys used in this thesis were assumed to be constant as well. However, in practice they are temperature dependent. The thermal stress field is useful to directly understand cracking formation in the treated layer. Therefore, there also exists interest in the simulation of thermal stress field.

5. Corrosion behaviour of the crack-free amorphous layer was studied in this thesis, however, the exposed area was extremely small. The corrosion behaviour of an amorphous layer with such a small exposed area should be compared with large area ones which are originally crack-free or crack-sealed by any sealing technique.

---

## References

- [1] A. Inoue, M. Yamamoto, H. Kimura, T. Masumoto, Ductile aluminium-base amorphous alloys with two separate phases, *Journal of Materials Science Letters*, 6 (1987) 194-196.
- [2] A.P. Tsai, A. Inoue, T. Masumoto, Formation of metal-metal type aluminum-based amorphous alloys, *Metallurgical and Materials Transactions A*, 19 (1988) 1369-1371.
- [3] Y. He, S.J. Poon, G.J. Shiflet, Synthesis and properties of metallic glasses that contain aluminum, *Science*, 241 (1988) 1640-1642.
- [4] A. Inoue, K. Ohtera, K. Kita, T. Masumoto, New amorphous alloys with good ductility in Al-Ce-M (M=Nb, Fe, Co, Ni or Cu) systems, *Japanese Journal of Applied Physics*, 27 (1988) L1796-L1799.
- [5] A. Inoue, K. Ohtera, A.P. Tsai, T. Masumoto, New amorphous-alloys with good ductility in Al-Y-M and Al-La-M (M=Fe, Co, Ni or Cu) systems, *Japanese Journal of Applied Physics*, 27 (1988) L280-L282.
- [6] C.S. Kiminami, N.D. Bassim, M.J. Kaufman, M.F. Amateau, T.J. Eden, J.M. Galbraith, Challenges in the development of aluminium-based bulk amorphous alloys, *Key Engineering Materials*, 189 (2001) 503-508.
- [7] B.J. Yang, J.H. Yao, J. Zhang, H.W. Yang, J.Q. Wang, E. Ma, Al-rich bulk metallic glasses with plasticity and ultrahigh specific strength, *Scripta Materialia*, 61 (2009) 423-426.
- [8] M.E. Goldman, N. Ünlü, G.J. Shiflet, J.R. Scully, Selected corrosion properties of a novel amorphous Al-Co-Ce alloy system, *Electrochemical and solid-state letters*, 8 (2005) B1-B5.
- [9] M.E. Goldman, N. Ünlü, F.M. Presuel, G.J. Shiflet, J.R. Scully, Amorphous metallic coatings with tunable corrosion properties based on Al-Co-Ce-(Mo) alloy compositions, in: *Corrosion*, NACE International, Huston, TX, 2004.
- [10] M.A. Jakab, J.R. Scully, On-demand release of corrosion-inhibiting ions from amorphous Al-Co-Ce alloys, *Nature Materials*, 4 (2005) 667-670.
- [11] P. Campestrini, E.P.M. Van Westing, H.W. Van Rooijen, J.H.W. De Wit, Relation between microstructural aspects of AA2024 and its corrosion behaviour investigated using AFM scanning potential technique, *Corrosion Science*, 42 (2000) 1853-1861.
- [12] V. Guillaumin, G. Mankowski, Localized corrosion of 2024 T351 aluminium alloy in chloride media, *Corrosion Science*, 41 (1998) 421-438.
- [13] M. Kendig, S. Jeanjaquet, R. Addison, J. Waldrop, Role of hexavalent chromium in the inhibition of corrosion of aluminum alloys, *Surface and Coatings Technology*, 140 (2001) 58-66.

- [14] Q. Meng, A.L. Moran, N. Tailleart, M.A. Jakab, J.R. Scully, Characterization and Mechanical/Corrosion Properties of Amorphous Al-Co-Ce Coatings, in: The 2005 Tri-Service Corrosion Conference, NACE, Orlando, FL., 2005.
- [15] N.R. Tailleart, B. Gauthier, S. Eidelman, J.R. Scully, Metallurgical and Physical Factors Controlling the Multi-Functional Corrosion Properties of Pulsed Thermal-Sprayed Al-Co-Ce Coatings, *Corrosion*, 68 (2012) 035006.
- [16] R. Twite, G. Bierwagen, Review of alternatives to chromate for corrosion protection of aluminum aerospace alloys, *Progress in Organic Coatings*, 33 (1998) 91-100.
- [17] J.R. Davis, *Corrosion of aluminum and aluminum alloys*, ASM International, OH, 1999.
- [18] F. Presuel-Moreno, M.A. Jakab, N. Tailleart, M.E. Goldman, J.R. Scully, Corrosion-resistant metallic coatings, *Materials Today*, 11 (2008) 14-23.
- [19] R.H. Brown, Aluminum alloy laminates-Alclad and clad aluminum alloy products, *Composite Engineering Laminates*, (1969) 227-239.
- [20] S. Wernick, R. Pinner, P.G. Sheasby, *The Surface Treatment and Finishing of Aluminum and its Alloys*, ASM International Finishing Publications Ltd., England, 1987.
- [21] M.W. Kendig, R.G. Buchheit, Corrosion inhibition of aluminum and aluminum alloys by soluble chromates, chromate coatings, and chromate-free coatings, *Corrosion*, 59 (2003) 379-400.
- [22] P. Campestrini, G. Goeminne, H. Terryn, J. Vereecken, J.H.W. de Wit, Chromate conversion coating on aluminum alloys I. Formation Mechanism, *Journal of the Electrochemical Society*, 151 (2004) B59-B70.
- [23] P. O'Brien, A. Kortenkamp, The chemistry underlying chromate toxicity, *Transition Metal Chemistry*, 20 (1995) 636-642.
- [24] D.M. Stearns, K.E. Wetterhahn, Intermediates produced in the reaction of chromium (VI) with dehydroascorbate cause single-strand breaks in plasmid DNA, *Chemical Research in Toxicology*, 10 (1997) 271-278.
- [25] K. Wippermann, J.W. Schultze, R. Kessel, J. Penninger, The inhibition of zinc corrosion by bisaminotriazole and other triazole derivatives, *Corrosion Science*, 32 (1991) 205-230.
- [26] K.A. Yasakau, M.L. Zheludkevich, S.V. Lamaka, M.G. Ferreira, Mechanism of corrosion inhibition of AA2024 by rare-earth compounds, *The Journal of Physical Chemistry B*, 110 (2006) 5515-5528.
- [27] D. Chidambaram, C.R. Clayton, M.W. Kendig, G.P. Halada, Surface pretreatments of aluminum alloy AA2024-T3 and formation of chromate conversion coatings II. Composition and electrochemical behavior of the chromate conversion coating, *Journal of the Electrochemical Society*, 151 (2004) B613-B620.
- [28] G.P. Bierwagen, D.E. Tallman, Choice and measurement of crucial aircraft coatings system properties, *Progress in Organic Coatings*, 41 (2001) 201-216.

- [29] C. Monticelli, G. Brunoro, A. Frignani, G. Trabanelli, Evaluation of corrosion inhibitors by electrochemical noise analysis, *Journal of the Electrochemical Society*, 139 (1992) 706.
- [30] C. Breslin, G. Treacy, W. Carroll, Studies on the passivation of aluminium in chromate and molybdate solutions, *Corrosion Science*, 36 (1994) 1143-1154.
- [31] I.A. Raspini, Influence of sodium salts of organic acids as additives on localized corrosion of aluminum and its alloys, *Corrosion*, 49 (1993).
- [32] L. Garrigues, N. Pebere, F. Dabosi, An investigation of the corrosion inhibition of pure aluminum in neutral and acidic chloride solutions, *Electrochimica Acta*, 41 (1996) 1209-1215.
- [33] S.V. Lamaka, M.L. Zheludkevich, K.A. Yasakau, M.F. Montemor, M.G.S. Ferreira, High effective organic corrosion inhibitors for 2024 aluminium alloy, *Electrochimica Acta*, 52 (2007) 7231-7247.
- [34] B.R.W. Hinton, D.R. Arnott, N.E. Ryan, The inhibition of aluminum corrosion by cerium cations, *Materials Forum*, 7 (1984) 211-217.
- [35] B.R.W. Hinton, The inhibition of aluminum alloy corrosion by rare earth metal cations, *Corrosion Australas*, 210 (1985) 12-17.
- [36] A.J. Aldykewicz Jr, H.S. Isaacs, A.J. Davenport, The investigation of cerium as a cathodic inhibitor for aluminum copper alloys, *Journal of the Electrochemical Society*, 142 (1995) 3342-3350.
- [37] F. Mansfeld, V. Wang, H. Shih, Development of "stainless aluminum", *Journal of the Electrochemical Society*, 138 (1991) L74-L75.
- [38] D. Ho, N. Brack, J. Scully, T. Markley, M. Forsyth, B. Hinton, Cerium dibutylphosphate as a corrosion inhibitor for AA2024-T3 aluminum alloys, *Journal of the Electrochemical Society*, 153 (2006) B392.
- [39] J. Mardel, S.J. Garcia, P.A. Corrigan, T. Markley, A.E. Hughes, T.H. Muster, D. Lau, T.G. Harvey, A.M. Glenn, P.A. White, S.G. Hardin, C. Luo, X. Zhou, G.E. Thompson, J.M.C. Mol, The characterisation and performance of Ce(dbp)<sub>3</sub>-inhibited epoxy coatings, *Progress in Organic Coatings*, 70 (2011) 91-101.
- [40] A.K. Mishra, R. Balasubramaniam, Corrosion inhibition of aluminum alloy AA 2014 by rare earth chlorides, *Corrosion Science*, 49 (2007) 1027-1044.
- [41] T.A. Markley, M. Forsyth, A.E. Hughes, Corrosion protection of AA2024-T3 using rare earth diphenyl phosphates, *Electrochimica Acta*, 52 (2007) 4024-4031.
- [42] T. Muster, D. Lau, H. Wrubel, N. Sherman, A. Hughes, T. Harvey, T. Markley, D. Alexander, P. Corrigan, P. White, An investigation of rare earth chloride mixtures: combinatorial optimisation for AA2024-T3 corrosion inhibition, *Surface and Interface Analysis*, 42 (2010) 170-174.
- [43] M. Khobaib, L.B. Reynolds, M.S. Donley, A comparative evaluation of corrosion protection of sol-gel based coatings systems, *Surface and Coatings Technology*, 140 (2001) 16-23.
- [44] M. Guglielmi, Sol-gel coatings on metals, *Journal of Sol-Gel Science and Technology*, 8 (1997) 443-449.

- [45] A. Conde, A. Duran, J.J. De Damborenea, Polymeric sol-gel coatings as protective layers of aluminium alloys, *Progress in Organic Coatings*, 46 (2003) 288-296.
- [46] R.L. Parkhill, E.T. Knobbe, M.S. Donley, Application and evaluation of environmentally compliant spray-coated ormosil films as corrosion resistant treatments for aluminum 2024-T3, *Progress in Organic Coatings*, 41 (2001) 261-265.
- [47] M.L. Zheludkevich, R. Serra, M.F. Montemor, I.M.M. Salvado, M.G.S. Ferreira, Corrosion protective properties of nanostructured sol-gel hybrid coatings to AA2024-T3, *Surface and Coatings Technology*, 200 (2006) 3084-3094.
- [48] A.S. Hamdy, Advanced nano-particles anti-corrosion ceria based sol gel coatings for aluminum alloys, *Materials Letters*, 60 (2006) 2633-2637.
- [49] H. Yasuda, *Plasma Polymerization*, Academic Press, Orlando, 1985.
- [50] H.P. Schreiber, M.R. Wertheimer, A.M. Wrobel, Corrosion protection by plasma-polymerized coatings, *Thin Solid Films*, 72 (1980) 487-494.
- [51] Y. Momose, M. Tomii, T. Maruyama, T. Shimoda, Y. Motohashi, Potentiodynamic study of the corrosion protection of aluminium by plasma-polymerized coatings, *Surface and Coatings Technology*, 169 (2003) 682-685.
- [52] Q. Yu, J. Deffeyes, H. Yasuda, Engineering the surface and interface of Parylene C coatings by low-temperature plasmas, *Progress in Organic Coatings*, 41 (2001) 247-253.
- [53] H. Yasuda, Y. Matsuzawa, Economical advantages of low pressure plasma polymerization coating, *Plasma Processes and Polymers*, 2 (2005) 507-512.
- [54] D. Zander, U. Köster, Corrosion of amorphous and nanocrystalline Zr-based alloys, *Materials Science and Engineering A*, 375 (2004) 53-59.
- [55] C. Qin, W. Zhang, K. Asami, H. Kimura, X.M. Wang, A. Inoue, A novel Cu-based BMG composite with high corrosion resistance and excellent mechanical properties, *Acta Materialia*, 54 (2006) 3713-3719.
- [56] A. Kawashima, H. Habazaki, K. Hashimoto, Highly corrosion-resistant Ni-based bulk amorphous alloys, *Materials Science and Engineering A*, 304 (2001) 753-757.
- [57] F.J. Presuel-Moreno, H. Wang, M.A. Jakab, R.G. Kelly, J.R. Scully, Computational modeling of active corrosion inhibitor release from an Al-Co-Ce metallic coating-Protection of exposed AA2024-T3, *Journal of the Electrochemical Society*, 153 (2006) B486-B498.
- [58] B.M. Gauthier, I. Vidensky, S. Eidelman, N. Tailleart, J.R. Scully, PTS Al-Co-Ce coatings for aluminum cladding replacement or in-field scratch repair, in: 2009 Department of Defense Corrosion Conference, NACE International, Washington DC, 2009.
- [59] J.R. Scully, F. Presuel-Moreno, M. Goldman, R.G. Kelly, N. Tailleart, User-selectable barrier, sacrificial anode, and active corrosion inhibiting properties of Al-Co-Ce alloys for coating applications, *Corrosion*, 64 (2008) 210-229.

- [60] Y. Kato, D.C. Van Aken, Salt fog corrosion testing of Al-Y-Co based nanocrystalline and amorphous coatings produced by atmospheric plasma spray, in: 3<sup>rd</sup> International Surfaced Engineering Congress, ASM International Inc, Orlando, 2004.
- [61] Y. Kato, Plasma spraying of aluminum-based glass forming alloys, University of Missouri-Rolla, PhD thesis (2005).
- [62] Z.P. Lu, C.T. Liu, A new glass-forming ability criterion for bulk metallic glasses, *Acta Materialia*, 50 (2002) 3501-3512.
- [63] D. Turnbull, Under what conditions can a glass be formed?, *Contemporary Physics*, 10 (1969) 473-488.
- [64] X. Bian, B. Sun, L. Hu, Y. Jia, Fragility of superheated melts and glass-forming ability in Al-based alloys, *Physics Letters A*, 335 (2005) 61-67.
- [65] Q. Meng, S. Zhang, M. Xia, J. Li, J. Zhou, Superheated liquid fragility and thermodynamic refinement for evaluation of metallic glass-forming ability, *Applied Physics Letters*, 90 (2007) 031910.
- [66] M.C. Gao, N. Ünlü, M. Mihalkovic, M. Widom, G. Shiflet, Glass formation, phase equilibria, and thermodynamic assessment of the Al-Ce-Co system assisted by first-principles energy calculations, *Metallurgical and Materials Transactions A*, 38 (2007) 2540-2551.
- [67] E. Posan, G. Ujj, A. Kiss, B. Telek, K. Rak, M. Udvardy, A. Inoue, Amorphous, nanoquasicrystalline and nanocrystalline alloys in Al-based systems, *Progress in Materials Science*, 43 (1998) 365-520.
- [68] A.N. Mansour, C.P. Wong, R.A. Brizzolara, Atomic structure of amorphous  $\text{Al}_{100-2x}\text{Co}_x\text{Ce}_x$  ( $x= 8, 9, \text{ and } 10$ ) and  $\text{Al}_{80}\text{Fe}_{10}\text{Ce}_{10}$  alloys: An XAFS study, *Physical Review B*, 50 (1994) 74753-12412.
- [69] S.R. Taylor, G.J. Shiflet, J.R. Scully, R.G. Buchheit, W.J. van Ooij, K. Sieradzki, R.E. Diaz, C.J. Brinker, A.L. Moran, The development of an environmentally compliant, multi-functional aerospace coating using molecular- and nano-engineering methods, Project Report, The University of Virginia, (2006).
- [70] T.H. Nguyen, R.T. Foley, On the mechanism of pitting of aluminum, *Journal of the Electrochemical Society*, 126 (1979) 1855.
- [71] J.R. Scully, A. Gebert, J.H. Payer, Corrosion and related mechanical properties of bulk metallic glasses, *Journal of Materials Research*, 22 (2007) 302-313.
- [72] M.A. Jakab, Corrosion inhibition by metal ions delivered from amorphous alloys, The University of Virginia, PhD Thesis (2006).
- [73] A.M. Lucente, Effects of aluminum nanocrystals on the corrosion resistance of aluminum-based metallic glasses, The University of Virginia, PhD thesis (2008).
- [74] X.Q. Wu, C.Q. Xie, Influence of crystallization on corrosion resistance of  $\text{Al}_{86}\text{Ni}_6\text{La}_6\text{Cu}_2$  amorphous alloy, *Journal of Rare Earths*, 26 (2008) 745-748.
- [75] J.G. Lin, W.W. Wang, X.Q. Wu, J.H. Lei, S. Yin, Crystallization and corrosion resistance of as-spun  $(\text{Al}_{86}\text{Ni}_9\text{La}_5)_{98}\text{Zr}_2$  amorphous alloy, *Journal of Alloys and Compounds*, 478 (2009) 763-766.

- [76] B.A. Green, P.K. Liaw, R.A. Buchanan, Corrosion behavior, in: M.K. Miller, P.K. Liaw (Eds.) *Bulk metallic glasses: An overview*, Springer-Verlag New York Inc., 2008.
- [77] A.L. Greer, *Metallic Glasses*, *Science*, 267 (1995) 1947-1953.
- [78] H.H. Liebermann, The dependence of the Geometry of glassy alloy ribbons on the chill block melt-spinning process parameters, *Materials Science and Engineering*, 43 (1980) 203-210.
- [79] A. Inoue, Y. Shinohara, Y. Yokoyama, T. Masumoto, Solidification Analyses of Bulky  $Zr_{60}Al_{10}Ni_{10}Cu_{15}Pd_5$  Glass Produced by Casting into Wedge-Shape Copper Mold, *Materials Transactions-JIM*, 36 (1995) 1276-1281.
- [80] K. Hildal, N. Sekido, J.H. Perepezko, Critical cooling rate for  $Fe_{48}Cr_{15}Mo_{14}Y_2C_{15}B_6$  bulk metallic glass formation, *Intermetallics*, 14 (2006) 898-902.
- [81] O.N. Senkov, J.M. Scott, D.B. Miracle, Composition range and glass forming ability of ternary Ca–Mg–Cu bulk metallic glasses, *Journal of alloys and compounds*, 424 (2006) 394-399.
- [82] H.J. Kim, K.M. Lim, B.G. Seong, C.G. Park, Amorphous phase formation of Zr-based alloy coating by HVOF spraying process, *Journal of Materials Science*, 36 (2001) 49-54.
- [83] K. Kishitake, H. Era, F. Otsubo, Thermal-sprayed Fe-10Cr-13P-7C amorphous coatings possessing excellent corrosion resistance, *Journal of Thermal Spray Technology*, 5 (1996) 476-482.
- [84] F. Otsubo, H. Era, K. Kishitake, Formation of amorphous Fe-Cr-Mo-8P-2C coatings by the high velocity oxy-fuel process, *Journal of Thermal Spray Technology*, 9 (2000) 494-498.
- [85] K. Kishitake, H. Era, F. Otsubo, Characterization of plasma sprayed Fe-17Cr-38Mo-4C amorphous coatings crystallizing at extremely high temperature, *Journal of Thermal Spray Technology*, 5 (1996) 283-288.
- [86] K. Kishitake, H. Era, F. Otsubo, Characterization of plasma sprayed Fe-10Cr-10Mo-(C,B) amorphous coatings, *Journal of Thermal Spray Technology*, 5 (1996) 145-153.
- [87] S. Lee, H. Choi, C. Lee, Y. Kim, Characteristics of Ni-Ti-Zr-Si-Sn Bulk Amorphous HVOF Coating, *Materials Science Forum*, 449-452 (2004) 929-932.
- [88] H.S. Choi, S.H. Yoon, G.Y. Kim, H.H. Jo, C.H. Lee, Phase evolutions of bulk amorphous NiTiZrSiSn feedstock during thermal and kinetic spraying processes, *Scripta Materialia*, 53 (2005) 125-130.
- [89] A.P. Wang, Z.M. Wang, J. Zhang, J.Q. Wang, Deposition of HVAF-sprayed Ni-based amorphous metallic coatings, *Journal of Alloys and Compounds*, 440 (2007) 225-228.
- [90] R.Q. Guo, C. Zhang, Q. Chen, Y. Yang, N. Li, L. Liu, Study of structure and corrosion resistance of Fe-based amorphous coatings prepared by HVAF and HVOF, *Corrosion Science*, 53 (2011) 2351-2356.

- [91] Y. Kharlamov, Detonation spraying of protective coatings, *Materials Science and Engineering*, 93 (1987) 1-37.
- [92] Z. Zhou, L. Wang, F.-C. Wang, Y.-B. Liu, Formation and corrosion behavior of Fe-based amorphous metallic coatings prepared by detonation gun spraying, *Transactions of Nonferrous Metals Society of China*, 19 (2009) s634-s638.
- [93] B. Gauthier, N. Tailleart, S. Eidelman, D. Book, J.R. Scully, Spray applied amorphous/nanocrystalline aluminum alloy coatings as a replacement for aluminum cladding, in: *The 2007 Tri-Service Corrosion Conference*, NACE, Denver, Colorado, 2007.
- [94] R.S. Lima, J. Karthikeyan, C.M. Kay, J. Lindemann, C.C. Berndt, Microstructural characteristics of cold-sprayed nanostructured WC-Co coatings, *Thin Solid Films*, 416 (2002) 129-135.
- [95] K.A. Lee, D.J. Jung, D.Y. Park, W.G. Kang, J.K. Lee, H.J. Kim, Study on the fabrication and physical properties of cold-sprayed, Cu-based amorphous coating, in: *13<sup>th</sup> International Conference on Rapidly Quenched and Metastable Materials*, IoP Publishing Ltd, Bristol, 2009.
- [96] D.J. Jung, D.Y. Park, J.K. Lee, H.J. Kim, K.A. Lee, Fabrication and characterization of Cu-based amorphous coatings by cold spray process, *Journal of the Korean Institute of Metals and Materials*, 46 (2008) 321-327.
- [97] A.P. Wang, T. Zhang, J.Q. Wang, Ni-based fully amorphous metallic coating with high corrosion resistance, *Philosophical Magazine Letters*, 86 (2006) 5 - 11.
- [98] A.P. Wang, X.C. Chang, W.L. Hou, J.Q. Wang, Preparation and corrosion behaviour of amorphous Ni-based alloy coatings, *Materials Science and Engineering: A*, 449 (2007) 277-280.
- [99] L. Ajdelsztajn, E.J. Lavernia, B. Jodoin, P. Richer, E. Sansoucy, Cold gas dynamic spraying of iron-base amorphous alloy, *Journal of Thermal Spray Technology*, 15 (2006) 495-500.
- [100] E. Irissou, J.G. Legoux, A.N. Ryabinin, B. Jodoin, C. Moreau, Review on cold spray process and technology: Part I-Intellectual property, *Journal of Thermal Spray Technology*, 17 (2008) 495-516.
- [101] A.L. Moran, Deposition routes for the development of multi-functional coatings for naval application via nano-engineering methods, *Yearly Report*, Department of mechanical engineering, Naval Academy, U. S., (2007).
- [102] P. Sigmund, Mechanisms and theory of physical sputtering by particle impact, *Nuclear Instruments and Methods in Physics Research Section B*, 27 (1987) 1-20.
- [103] H. Yoshioka, Q. Yan, H. Habazaki, A. Kawashima, K. Asami, K. Hashimoto, Passivity and its breakdown on sputter-deposited amorphous Al-early transition metal alloys in 1 M HCl at 30 °C, *Corrosion Science*, 31 (1990) 349-354.
- [104] H. Yoshioka, Q. Yan, K. Asami, K. Hashimoto, Pitting potential and structure of sputter-deposited Al-Ti alloys, *Materials Science and Engineering: A*, 134 (1991) 1054-1057.

- [105] Q. Yan, H. Yoshioka, H. Habazaki, A. Kawashima, K. Asami, K. Hashimoto, Passivity and its breakdown on sputter-deposited amorphous Al-Ti alloys in a neutral aqueous solution with Cl<sup>-</sup>, *Corrosion science*, 31 (1990) 401-406.
- [106] E. Akiyama, H. Yoshioka, J. Kim, H. Habazaki, A. Kawashima, K. Asami, K. Hashimoto, The effect of magnesium on the corrosion behavior of sputter-deposited amorphous Al-Mg-Ti ternary alloys in a neutral chloride solution, *Corrosion science*, 34 (1993) 27-40.
- [107] H. Yoshioka, H. Habazaki, A. Kawashima, K. Asami, K. Hashimoto, Anodic polarization behaviour of sputter-deposited Al-Zr alloys in a neutral chloride-containing buffer solution, *Electrochimica acta*, 36 (1991) 1227-1233.
- [108] F. Sanchette, A. Billard, C. Frantz, Mechanically reinforced and corrosion-resistant sputtered amorphous aluminium alloy coatings, *Surface and Coatings Technology*, 98 (1998) 1162-1168.
- [109] K. Hashimoto, N. Kumagai, H. Yoshioka, K. Asami, Laser and electron beam processing of amorphous surface alloys on conventional crystalline metals, *Materials and Manufacturing Processes*, 5 (1990) 567 - 590.
- [110] E. Breinan, C. Banas, B. Kear, Processing materials with lasers, *Physics Today*, 29 (1976) 44-48.
- [111] F. Audebert, R. Colaço, R. Vilar, H. Sirkin, Production of glassy metallic layers by laser surface treatment, *Scripta Materialia*, 48 (2003) 281-286.
- [112] D. Carvalho, S. Cardoso, R. Vilar, Amorphisation of Zr<sub>60</sub>Al<sub>15</sub>Ni<sub>25</sub> surface layers by laser processing for corrosion resistance, *Scripta Materialia*, 37 (1997) 523-527.
- [113] M. Svéda, A. Roósz, Development of Amorphous and Microstructured Surface Layer by Laser Surface Treatment, *Materials Science Forum*, 752 (2013) 175-182.
- [114] H. Yoshioka, K. Asami, A. Kawashima, K. Hashimoto, Laser-processed corrosion-resistant amorphous Ni-Cr-P-B surface alloys on a mild steel, *Corrosion Science*, 27 (1987) 981-995.
- [115] K. Hashimoto, N. Kumagai, H. Yoshioka, J. Kim, E. Akiyama, H. Habazaki, S. Mrowec, A. Kawashima, K. Asami, Corrosion-resistant amorphous surface alloys, *Corrosion Science*, 35 (1993) 363-370.
- [116] F. Hirose, M. Takagi, H. Mori, Y. Kitoh, T. Imura, Microstructure of Fe-B-Si alloy surface layers produced by laser-quenching, *Japanese Journal of Applied Physics*, 31 (1992) 3940-3945.
- [117] X. Wu, Y. Hong, Fe-based thick amorphous-alloy coating by laser cladding, *Surface and Coatings Technology*, 141 (2001) 141-144.
- [118] J.G. Hoekstra, S.B. Qadri, J.R. Scully, J.M. Fitz-Gerald, Laser surface modification of a crystalline Al-Co-Ce alloy for enhanced corrosion resistance, *Advanced Engineering Materials*, 7 (2005) 805-809.
- [119] K. Lee, E. Yun, S. Lee, N.J. Kim, Fabrication of Zr-and Cu-base bulk metallic glass/Cu surface composites by high-energy electron-beam irradiation, *Materials Science and Engineering A*, 408 (2005) 92-101.

## References

---

- [120] P. Fauchais, G. Montavon, G. Bertrand, From powders to thermally sprayed coatings, *Journal of Thermal Spray Technology*, 19 (2010) 56-80.
- [121] A. Inoue, K. Kita, K. Ohtera, H. Kimura, T. Masumoto, Al-Y-Ni amorphous powders prepared by high-pressure gas atomization, *Journal of Materials Science Letters*, 7 (1988) 1287-1290.
- [122] K.R. Cardoso, A.G. Escorial, M. Liebllich, W.J. Botta, Amorphous and nanostructured Al-Fe-Nd powders obtained by gas atomization, *Materials Science and Engineering A*, 315 (2001) 89-97.
- [123] Z.H. Zhang, N. Yang, Y.Z. Zhou, E.J. Lavernia, Nanocrystal formation in gas-atomized amorphous Al<sub>85</sub>Ni<sub>10</sub>La<sub>5</sub> alloy, *Philosophical Magazine*, 88 (2008) 737-753.
- [124] B.L. Zheng, Y.J. Lin, Y.Z. Zhou, E.J. Lavernia, Gas atomization of amorphous aluminum powder: Part II. Experimental Investigation, *Metallurgical and Materials Transactions B*, 40 (2009) 995-1004.
- [125] S.W. He, Y. Liu, S. Guo, Cooling rate calculation of non-equilibrium aluminum alloy powders prepared by gas atomization, *Rare Metal Materials and Engineering*, 38 (2009) 353-356.
- [126] P. Dong, W.L. Hou, X.C. Chang, M.X. Quan, J.Q. Wang, Amorphous and nanostructured Al<sub>85</sub>Ni<sub>5</sub>Y<sub>6</sub>Co<sub>2</sub>Fe<sub>2</sub> powder prepared by nitrogen gas-atomization, *Journal of Alloys and Compounds*, 436 (2007) 118-123.
- [127] Y. Liu, Z.M. Liu, S. Guo, Y. Du, B.Y. Huang, J.S. Huang, S.Q. Chen, F.X. Liu, Amorphous and nanocrystalline Al<sub>82</sub>Ni<sub>10</sub>Y<sub>8</sub> alloy powder prepared by gas atomization, *Intermetallics*, 13 (2005) 393-398.
- [128] S.J. Hong, T.S. Kim, H.S. Kim, W.T. Kim, B.S. Chun, Microstructural behavior of rapidly solidified and extruded Al-14wt% Ni-14wt% Mm (Mm, misch metal) alloy powders, *Materials Science and Engineering A*, 271 (1999) 469-476.
- [129] B.L. Zheng, Y.J. Lin, Y.Z. Zhou, E.J. Lavernia, Gas atomization of amorphous aluminum: Part I. Thermal behavior calculations, *Metallurgical and Materials Transactions B*, 40 (2009) 768-778.
- [130] J. Benjamin, Dispersion strengthened superalloys by mechanical alloying, *Metallurgical and Materials Transactions B*, 1 (1970) 2943-2951.
- [131] C.C. Koch, O.B. Cavin, C.G. McKamey, J.O. Scarbrough, Preparation of "amorphous" Ni<sub>60</sub>Nb<sub>40</sub> by mechanical alloying, *Applied Physics Letters*, 43 (1983) 1017-1019.
- [132] P. Choi, J. Kim, O. Nguyen, D. Kwon, Y. Kwon, J. Kim, Al-La-Ni-Fe bulk metallic glasses produced by mechanical alloying and spark-plasma sintering, *Materials Science and Engineering: A*, 449 (2007) 1119-1122.
- [133] X. Wei, F. Han, X. Wang, C. Wen, Fabrication of Al-based bulk metallic glass by mechanical alloying and vacuum hot consolidation, *Journal of Alloys and Compounds*, 501 (2010) 164-167.
- [134] J.S. Kim, I.V. Povstugar, P. Choi, E.P. Yelsukov, Y.S. Kwon, Synthesis of Al-Y-Ni-Co composites by mechanical alloying and consecutive spark-plasma sintering, *Journal of Alloys and Compounds*, 486 (2009) 511-514.

- [135] S. Mula, S. Ghosh, S.K. Pabi, Synthesis of an Al-based Al-Cr-Co-Ce alloy by mechanical alloying and its thermal stability, *Materials Science and Engineering: A*, 472 (2008) 208-213.
- [136] A.R. Yavari, P.J. Desre, Thermodynamic and kinetic justification for amorphization by mechanical alloying of A-B metal couples with zero heat of mixing  $\Delta H_{\text{mix}}$ , *Physical Review Letters*, 65 (1990) 2571-2574.
- [137] R. Sundaresan, A.G. Jackson, S. Krishnamurthy, F.H. Froes, Study of the formation of the amorphous phase in metallic systems by mechanical alloying, *Materials Science and Engineering*, 97 (1988) 115-119.
- [138] D.I. Proskurovsky, V.P. Rotshtein, G.E. Ozur, A.B. Markov, D.S. Nazarov, V.A. Shulov, Y.F. Ivanov, R.G. Buchheit, Pulsed electron-beam technology for surface modification of metallic materials, *Journal of Vacuum Science and Technology A*, 16 (1998) 2480-2488.
- [139] Y. Uno, A. Okada, K. Uemura, P. Raharjo, T. Furukawa, K. Karato, High-efficiency finishing process for metal mold by large-area electron beam irradiation, *Precision Engineering*, 29 (2005) 449-455.
- [140] Y. Uno, A. Okada, K. Uemura, P. Raharjo, S. Sano, Z. Yu, S. Mishima, A new polishing method of metal mold with large-area electron beam irradiation, *Journal of Materials Processing Technology*, 187 (2007) 77-80.
- [141] J.W. Murray, P.K. Kinnell, A.H. Cannon, B. Bailey, A.T. Clare, Surface finishing of intricate metal mould structures by large-area electron beam irradiation, *Precision Engineering*, 37 (2013) 443-450.
- [142] D.I. Proskurovsky, V.P. Rotshtein, G.E. Ozur, Y.F. Ivanov, A.B. Markov, Physical foundations for surface treatment of materials with low energy, high current electron beams, *Surface and Coatings Technology*, 125 (2000) 49-56.
- [143] Q.F. Guan, H. Zou, G.T. Zou, A.M. Wu, S.Z. Hao, J.X. Zou, Y. Qin, C. Dong, Q.Y. Zhang, Surface nanostructure and amorphous state of a low carbon steel induced by high-current pulsed electron beam, *Surface and Coatings Technology*, 196 (2005) 145-149.
- [144] S. Hao, B. Gao, A. Wu, J. Zou, Y. Qin, C. Dong, J. An, Q. Guan, Surface modification of steels and magnesium alloy by high current pulsed electron beam, *Nuclear Instruments and Methods in Physics Research Section B*, 240 (2005) 646-652.
- [145] Y. Hao, B. Gao, G.F. Tu, S.W. Li, S.Z. Hao, C. Dong, Surface modification of Al-20Si alloy by high current pulsed electron beam, *Applied Surface Science*, 257 (2011) 3913-3919.
- [146] J.C. Walker, J. Murray, S. Narania, A.T. Clare, Dry sliding friction and wear behaviour of an electron beam melted hypereutectic Al-Si alloy, *Tribology Letters*, 45 (2012) 49-58.
- [147] A. Okada, Y. Uno, N. Yabushita, K. Uemura, P. Raharjo, High efficient surface finishing of bio-titanium alloy by large-area electron beam irradiation, *Journal of materials processing technology*, 149 (2004) 506-511.

- [148] A. Okada, Y. Uno, K. Uemura, P. Raharjo, J. McGeough, Surface modification for orthopaedic titanium alloy by wide-area electron beam, *Proceedings of the Institution of Mechanical Engineers, Part B: Journal of Engineering Manufacture*, 221 (2007) 173-178.
- [149] A. Markov, V. Rotshtein, Calculation and experimental determination of dimensions of hardening and tempering zones in quenched U7A steel irradiated with a pulsed electron beam, *Nuclear Instruments and Methods in Physics Research Section B*, 132 (1997) 79-86.
- [150] J. Zou, Y. Qin, C. Dong, X. Wang, A. Wu, S. Hao, Numerical simulation of the thermal-mechanical process of high current pulsed electron beam treatment, *Journal of Vacuum Science & Technology A*, 22 (2004) 545-552.
- [151] Y. Qin, C. Dong, X. Wang, S. Hao, A. Wu, J. Zou, Y. Liu, Temperature profile and crater formation induced in high-current pulsed electron beam processing, *Journal of Vacuum Science & Technology A*, 21 (2003) 1934-1938.
- [152] Y. Qin, J. Zou, C. Dong, X. Wang, A. Wu, Y. Liu, S. Hao, Q. Guan, Temperature-stress fields and related phenomena induced by a high current pulsed electron beam, *Nuclear Instruments and Methods in Physics Research Section B*, 225 (2004) 544-554.
- [153] A. Inoue, K. Ohtera, T. Masumoto, New amorphous Al-Y, Al-La and Al-Ce alloys prepared by melt spinning, *Japanese Journal of Applied Physics*, 27 (1988) L736-L739.
- [154] A. Inoue, K. Ohtera, A. Tsai, T. Masumoto, Aluminum-based amorphous alloys with tensile strength above 980 MPa (100 kg/mm<sup>2</sup>), *Japanese Journal of Applied Physics*, 27 (1988) L479-L482.
- [155] Z. Lu, C. Liu, Role of minor alloying additions in formation of bulk metallic glasses: A Review, *Journal of Materials Science*, 39 (2004) 3965-3974.
- [156] N.R. Tailleart, B. Gauthier, S. Eidelman, J.R. Scully, Metallurgical and physical factors in improving the corrosion resistance of thermally sprayed semi-amorphous Al-Co-Ce coatings, *ECS Transactions*, 16 (2009) 39-63.
- [157] W. Kurz, D.J. Fisher, *Fundamentals of solidification*, Fourth revised ed., Trans Tech Publications Ltd., Aedermannsdorf, Switzerland, 1998.
- [158] K.A. Jackson, J.D. Hunt, Lamellar and rod eutectic growth, *Transactions of the Metallurgical Society of AIME*, 236 (1966) 1129-1142.
- [159] R.M. Srivastava, J. Eckert, W. Loser, B.K. Dhindaw, L. Schultz, Cooling rate evaluation for bulk amorphous alloys from eutectic microstructures in casting processes, *Materials Transactions-JIM*, 43 (2002) 1670-1675.
- [160] P. Predecki, A.W. Mullendore, N.J. Grant, A study of the splat cooling technique, *Transactions of the Metallurgical Society of AIME*, 233 (1965) 1581-1586.
- [161] M.G. Scott, J.A. Leake, The formation and decomposition of an aluminium 17.3 at.% copper solid solution, *Acta Metallurgica*, 23 (1975) 503-511.

- [162] R.M. Jordan, J.D. Hunt, The growth of lamellar eutectic structures in the Pb–Sn and Al–CuAl<sub>2</sub> systems, *Metallurgical and Materials Transactions B*, 2 (1971) 3401-3410.
- [163] M. Zimmermann, M. Carrard, W. Kurz, Rapid solidification of Al-Cu eutectic alloy by laser remelting, *Acta Metallurgica*, 37 (1989) 3305-3313.
- [164] N. Wang, R. Trivedi, Limit of steady-state lamellar eutectic growth, *Scripta Materialia*, 64 (2011) 848-851.
- [165] M.H. Burden, H. Jones, Determination of cooling rate in splat-cooling from scale of microstructure, *Journal of the Institute of Metals*, 98 (1970) 249-252.
- [166] R. Trivedi, P. Magnin, W. Kurz, Theory of eutectic growth under rapid solidification conditions, *Acta Metallurgica*, 35 (1987) 971-980.
- [167] A. Juarez-Hernandez, H. Jones, Growth temperatures and microstructure selection during Bridgman solidification of hypereutectic Al–La and Al–Ce alloys, *Journal of crystal growth*, 208 (2000) 442-448.
- [168] Y. Qin, C. Dong, X. Wang, S. Hao, A. Wu, J. Zou, Y. Liu, Temperature profile and crater formation induced in high-current pulsed electron beam processing, *Journal of Vacuum Science & Technology A: Vacuum, Surfaces, and Films*, 21 (2003) 1934-1938.
- [169] S. Hao, S. Yao, J. Guan, A. Wu, P. Zhong, C. Dong, Surface treatment of aluminum by high current pulsed electron beam, *Current Applied Physics*, 1 (2001) 203-208.
- [170] A. Kumar, S. Ghosh, B. Dhindaw, Simulation of Cooling of Double-Layered Splat and its Experimental Validation Using Jackson–Hunt Theory, *Metallurgical and Materials Transactions B*, 42 (2011) 269-273.
- [171] R. Buchheit, R. Grant, P. Hlava, B. McKenzie, G. Zender, Local Dissolution Phenomena Associated with S Phase (Al<sub>2</sub>CuMg) Particles in Aluminum Alloy 2024-T3, *Journal of the Electrochemical Society*, 144 (1997) 2621-2628.
- [172] P. Schmutz, G.S. Frankel, Corrosion study of AA2024-T3 by scanning Kelvin probe force microscopy and in situ atomic force microscopy scratching, *Journal of the Electrochemical Society*, 145 (1998) 2295-2306.
- [173] A. Boag, A. Hughes, A. Glenn, T. Muster, D. McCulloch, Corrosion of AA2024-T3 Part I: Localised corrosion of isolated IM particles, *Corrosion Science*, 53 (2011) 17-26.
- [174] A. Hughes, A. Boag, A. Glenn, D. McCulloch, T. Muster, C. Ryan, C. Luo, X. Zhou, G. Thompson, Corrosion of AA2024-T3 Part II: Co-operative corrosion, *Corrosion Science*, 53 (2011) 27-39.
- [175] A. Glenn, T. Muster, C. Luo, X. Zhou, G. Thompson, A. Boag, A. Hughes, Corrosion of AA2024-T3 Part III: propagation, *Corrosion Science*, 53 (2011) 40-50.
- [176] N. Birbilis, R. Buchheit, Electrochemical characteristics of intermetallic phases in aluminum alloys an experimental survey and discussion, *Journal of the Electrochemical Society*, 152 (2005) B140-B151.

## References

---

- [177] Z. Szklarska-Smialowska, Pitting corrosion of aluminum, *Corrosion Science*, 41 (1999) 1743-1767.
- [178] M. Baumgaertner, H. Kaesche, Aluminum pitting in chloride solutions: morphology and pit growth kinetics, *Corrosion Science*, 31 (1990) 231-236.
- [179] S. Sun, Q. Zheng, D. Li, J. Wen, Long-term atmospheric corrosion behaviour of aluminium alloys 2024 and 7075 in urban, coastal and industrial environments, *Corrosion Science*, 51 (2009) 719-727.
- [180] G. Knörnschild, Mechanism of Pit Growth in Homogeneous Aluminum Alloys in: N. Bensalah (Ed.) *Pitting Corrosion*, InTech, Rijeka, 2012.

# Appendixes

## Appendix 1 ICP-OES results of as-cast Al-Co-Ce alloys



**SHEFFIELD ANALYTICAL SERVICES**  
A Division of Sheffield Assay Office

To : Department Of Mechanical  
Materials And Manufacturing Engineering  
University Of Nottingham  
Nottingham

Order No. PAY BY VISA

NG7 2RD

Report No. 05000/01 Issued: 18/10/12 Page 01

DATE-S/N	REFERENCE	ELEMENT	RESULT		METHOD
23/08/12 0058	CASTING 1	Aluminium	66.5%	mean	ICP-OES
			66.2%	low	
			66.8%	high	
		Cerium	23.7%	mean	ICP-OES
			23.4%	low	
			23.9%	high	
		Cobalt	9.85%	mean	ICP-OES
			9.77%	low	
			9.91%	high	
				Oxygen	<0.1%
23/08/12 0059	CASTING 3	Aluminium	67.6%	mean	ICP-OES
			67.4%	low	
			67.7%	high	
		Cerium	19.0%	mean	ICP-OES
			18.9%	low	
			19.2%	high	
		Cobalt	13.4%	mean	ICP-OES
			13.3%	low	
			13.4%	high	
				Oxygen	<0.1%

Signature: Lab Manager - F M Hudson *F.M. Hudson*  
A.S. Team Leader - M Wood



SHEFFIELD ASSAY OFFICE - Guardians' Hall - Drouth Road - Hillsborough - Sheffield S6 2AK  
Telephone +44 (0)114 231 8160 Fax +44 (0)114 231 8161 Email info@assayoffice.co.uk  
www.assayoffice.co.uk

This issue replaces all previous issues. Standard conditions and tolerances apply. cont...page 2



SHEFFIELD ANALYTICAL SERVICES  
A Division of Sheffield Assay Office

To: Department Of Mechanical  
Materials And Manufacturing Engineering

Order No. PAY BY VISA

University Of Nottingham  
Nottingham

NG7 2RD

Report No. 05000/01 Issued: 18/10/12

Page 02

DATE-S/N	REFERENCE	ELEMENT	RESULT	METHOD			
23/08/12 0060	CASTING 4	Aluminium	63.3%	mean	ICP-OES		
			63.1%	low			
			63.6%	high			
		Cerium	24.4%	mean	ICP-OES		
			24.2%	low			
			24.5%	high			
		Cobalt	12.3%	mean	ICP-OES		
			12.1%	low			
			12.5%	high			
				Oxygen	<0.1%		Fusion (Non UKAS)
		23/08/12 0061	MM ED	Aluminium	65.0%	mean	ICP-OES
					64.7%	low	
65.1%	high						
Cerium	16.2%			mean	ICP-OES		
	16.1%			low			
	16.3%			high			
Cobalt	11.2%			mean	ICP-OES		
	11.1%			low			
	11.3%			high			
Lanthanum	7.68%			mean	ICP-OES		
	7.65%			low			
	7.70%			high			

Signature: Lab Manager - F M Hudson

*F.M. Hudson*

A.S. Team Leader - M Wood



SHEFFIELD ASSAY OFFICE - Guardians' Hall - Buxton Road - Hillsborough - Sheffield S6 2AN  
Telephone: +44 (0)114 231 8190 Fax: +44 (0)114 231 8161 Email: info@assayoffice.co.uk  
www.assayoffice.co.uk

This issue replaces all previous issues. Standard conditions and tolerances apply. cont...page 3

## Appendix 2      DSC measurement

DSC is a thermoanalytical technique which is extensively applied in the fields of materials, chemistry and drug analysis, etc. In DSC analysis, sample and reference are designed to be heated at a constant heating rate. However, due to their different heat capacities, different amounts of heat flow are required by the sample and reference to maintain that they are at the same temperature. The difference in the amount of heat flow required by the sample and reference is recorded and plotted with temperature or time. In this work, the melting point and latent heat of fusion of Al-Co-Ce alloys were determined by DSC, which was carried out by a SDT 600 analyser with a heating rate of 20 °C/min. The heating process is conducted under Ar atmosphere, while the cooling gas is air. A well characterised reference material (sapphire) was used in the measurement.

**Figure A2-1** shows the DSC curve of Al-Co-Ce alloy 3. The area of three endothermic peaks was integrated. There are two phase transitions at 650.36 °C and 815.35 °C during the heating process. The melting peak at 1035.31 °C was also identified, which is consistent with the reported results [66]. It also can be seen that the above three peaks have the peak area of 62.88 J/g, 63.53 J/g and 33.91 J/g, respectively. For simplicity, the latent heat of phase transitions at 650.36 °C and 815.35 °C was combined into the latent heat of fusion. Therefore, the total latent heat of fusion for Al-Co-Ce alloy is 160.32 J/g. The temperature compensation for the latent heat of fusion and solidification was also calculated according to **Eq. 7-22**, which was 182.8 K.

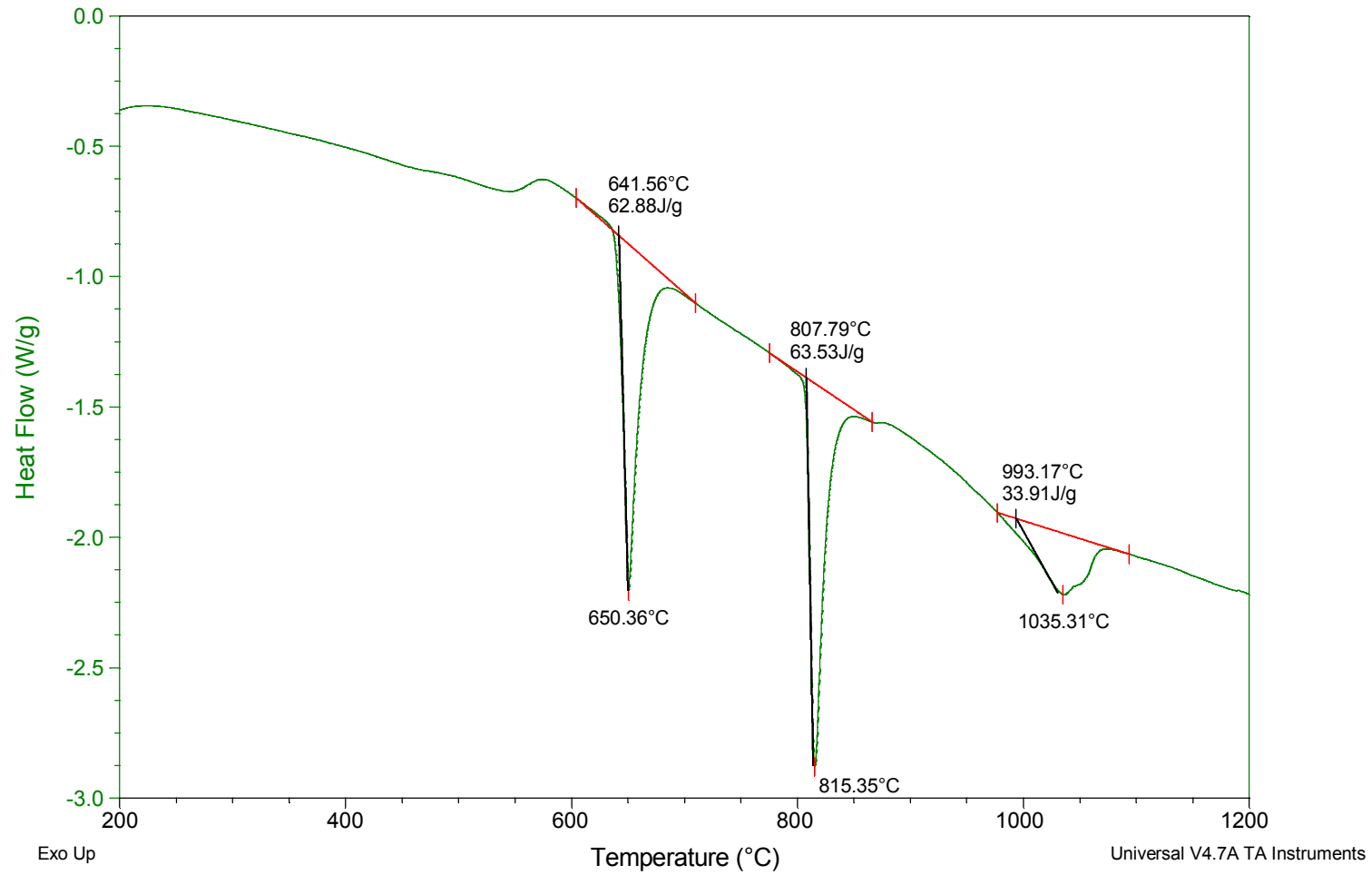


Figure A2-1 DSC curve of Al-Co-Ce alloy 3.

### Appendix 3 Laser flash measurement

In this work, the thermal diffusivity and specific heat of Al-Co-Ce alloy were measured by a laser flash apparatus (LFA 472, NETZSCH), and then the thermal conductivity was calculated by the equation below.

$$\kappa = \alpha \rho c \quad \text{Eq. A3-1}$$

where  $\kappa$  is the thermal conductivity (W/m·K),  $\alpha$  is the thermal diffusivity (m<sup>2</sup>/s),  $\rho$  is the density (kg/m<sup>3</sup>) and  $c$  is the specific heat (J/kg·K).

The laser flash test was conducted under a dynamic Ar gas atmosphere with a flow rate of 100 mL/min. A pulsed Nd: YAG laser was used to heat the sample with a wave length of 1064 nm and a duration time of 0.8 ms. Laser voltage was 450 V. The IR detector is made of InSb (Indium-Antimony) alloy. The sample size is 10×10×2.59 mm. All measurements were carried out by the Advanced Materials Research Laboratory at the University of Strathclyde, UK. Results are listed in **Table A3-1**.

**Table A3-1 Diffusivity, specific heat and conductivity of Al-Co-Ce alloy 3 at room temperature.**

Shot number	Temperature/ °C	Diffusivity/ (mm <sup>2</sup> /s)	Specific heat/ (J/g/K)	Conductivity/ (W/m/K)
1	18.2	19.966	0.877	60.754
2	18.6	19.661	0.877	59.831
3	19.1	19.979	0.877	60.813
Mean	18.6	19.868	0.877	60.466
Standard deviation	0.5	0.18	0	0.551

## Appendix 4      Programme code of numerical simulation

The code below is an example for the simulation of pure Al in the LAEB process (cathode voltage is 35 kV, initial temperature is 293 K.).

```

clear;clc;
curr=2e6;%current density (A/m2)
E0=35000;%acceleration voltage (V)
pd=1e-6;%pulse duration (s)
p0=2710;%density (kg/m3)
r0=1e-4*(E0/1000)^(3/2)/p0;%electron range (m)
%grid setting time step size
deltat0=1e-9;%time step size (s)
nt0=1e5;%total running time steps
nj=pd/deltat0;%heating time
nj=1e3;%total steps for heating
nt=6000;%total steps
%grid setting distance step size
deltax1=5e-7;%grid spacing (m)
nx0=6000;%total nodes
c=884.8;%specific heat (J/Kg/K)
k=239.871;%thermal conductivity (W/m/K)
h=13000;%heat transfer coefficient (W/m2 K)
sigma=5.67e-8;%stefan-boltzamann coeffecient (W/m2 K4)
emiss=0.06;%emissivity coefficient
Bi=h*deltax1/k;
F0=k*deltat0/(deltax1^2*c*p0);
ss=1-2*Bi*F0-2*F0;
mu01=k*deltat0/(deltax1^2*c*p0);%F0
mu02=deltat0/c/p0;%coefficient for heat source
mu03=deltat0*sigma*emiss/c/p0/deltax1;%coefficient for radiation
mu04=h*deltat0/c/p0/deltax1;%coefficient for conduction
mp=933;%melting point 933 K
ti=293;%initial temperature 293 K
ts=293;%surrounding temperature 293 K
deltamv0=362;%temperature compensation for the latent heat of fusion (K)
deltasv0=362;%temperature compensation for the latent heat of solidification (K)
mv=zeros(1,nx0);
sv=zeros(1,nx0);
deltamv=zeros(1,nx0);
deltasv=zeros(1,nx0);
%grid setting finished
x=0:deltax1:r0;

```

```

nLv=fix(r0/deltax1)+1;%number of nodes with heat source
fx=zeros(1,nLv);%energy distribution function
lv=zeros(1,nx0);%volumetric power density of heat source(W/m3)
%lv setting finished
u=zeros(2,nx0);%temperature(K)
for j=1:nx0
u(1,j)=ti;%setting initial temperature
end
for i=2:nt0
    if i>=2&&i<=nj%heat source on
        for j=1:nLv%within the electron range
            fx(1,j)=1-(9/4)*(x(1,j)/r0-1/3).^2;
            lv(1,j)=curr*E0*fx(1,j)/r0;
        end
        for j=nLv+1:nx0%beyond the electron range
            lv(1,j)=0;
        end
        for j=1:nx0
            lvv(1,j)=lv(1,j);
        end
    elseif i>nj&&i<=nt0%heat source turned off
        for j=1:nx0
            lv(1,j)=0;
        end
    end
    %boundary 1 top surface of sample
    if u(1,1)<mp%temperature<melting point
        u(2,1)=mu01*2*u(1,2)+(1-2*mu01)*u(1,1)+mu02*lv(1,1)-2*mu03*(u(1,1)^4-
ts^4);
        s=u(2,1)-u(1,1);
        if s>0
            u(2,1)=mu01*2*u(1,2)+(1-2*mu01)*u(1,1)+mu02*lv(1,1)-
2*mu03*(u(1,1)^4-ts^4);
        elseif s<=0
            if mv(1,1)>0
                if sv(1,1)<=deltasv0
                    deltasv(1,1)=abs(s);
                    sv(1,1)=sv(1,1)+deltasv(1,1);
                    u(1,1)=mp;
                    u(2,1)=mp-1e-12;
                elseif sv(1,1)>deltasv0
                    u(2,1)=mu01*2*u(1,2)+(1-2*mu01)*u(1,1)+mu02*lv(1,1)-
2*mu03*(u(1,1)^4-ts^4);
                end
            elseif mv(1,1)==0

```

```

        u(2,1)=mu01*2*u(1,2)+(1-2*mu01)*u(1,1)+mu02*lv(1,1)-
2*mu03*(u(1,1)^4-ts^4);
    end
    end
    elseif u(1,1)>=mp%temperature is between the melting point and boiling point
        u(2,1)=mu01*2*u(1,2)+(1-2*mu01)*u(1,1)+mu02*lv(1,1)-2*mu03*(u(1,1)^4-
ts^4);
        m=u(2,1)-u(1,1);
        if m>=0
            if mv(1,1)<=deltamv0
                u(2,1)=mu01*2*u(1,2)+(1-2*mu01)*u(1,1)+mu02*lv(1,1)-
2*mu03*(u(1,1)^4-ts^4);
                m=u(2,1)-u(1,1);
                deltamv(1,1)=abs(m);
                mv(1,1)=mv(1,1)+deltamv(1,1);
                u(1,1)=mp;
                u(2,1)=mp;
            elseif mv(1,1)>deltamv0
                u(2,1)=mu01*2*u(1,2)+(1-2*mu01)*u(1,1)+mu02*lv(1,1)-
2*mu03*(u(1,1)^4-ts^4);
            end
            elseif m<0
                u(2,1)=mu01*2*u(1,2)+(1-2*mu01)*u(1,1)+mu02*lv(1,1)-
2*mu03*(u(1,1)^4-ts^4);
            end
        end
    end
    %normal nodes
    for j=2:nx0-1
        if u(1,j)<mp
            u(2,j)=mu01*(u(1,j-1)+u(1,j+1))+(1-2*mu01)*u(1,j)+mu02*lv(1,j);
            s=u(2,j)-u(1,j);
            if s>0
                u(2,j)=mu01*(u(1,j-1)+u(1,j+1))+(1-2*mu01)*u(1,j)+mu02*lv(1,j);
            elseif s<=0
                if mv(1,j)>0
                    if sv(1,j)<=deltasv0
                        deltasv(1,j)=abs(s);
                        sv(1,j)=sv(1,j)+deltasv(1,j);
                        u(1,j)=mp;
                        u(2,j)=mp-1e-12;
                    elseif sv(1,j)>deltasv0
                        u(2,j)=mu01*(u(1,j-1)+u(1,j+1))+(1-2*mu01)*u(1,j)+mu02*lv(1,j);
                    end
                elseif mv(1,j)==0
                    u(2,j)=mu01*(u(1,j-1)+u(1,j+1))+(1-2*mu01)*u(1,j)+mu02*lv(1,j);
                end
            end
        end
    end

```

```

end
elseif u(1,j)>=mp
u(2,j)=mu01*(u(1,j-1)+u(1,j+1))+(1-2*mu01)*u(1,j)+mu02*lv(1,j);
m=u(2,j)-u(1,j);
if m>=0
if mv(1,j)<=deltamv0
u(2,j)=mu01*(u(1,j-1)+u(1,j+1))+(1-2*mu01)*u(1,j)+mu02*lv(1,j);
m=u(2,j)-u(1,j);
deltamv(1,j)=abs(m);
mv(1,j)=mv(1,j)+deltamv(1,j);
u(1,j)=mp;
u(2,j)=mp;
elseif mv(1,j)>deltamv0
u(2,j)=mu01*(u(1,j-1)+u(1,j+1))+(1-2*mu01)*u(1,j)+mu02*lv(1,j);
end
elseif m<0
u(2,j)=mu01*(u(1,j-1)+u(1,j+1))+(1-2*mu01)*u(1,j)+mu02*lv(1,j);
end
end
end
end
%boundary 2 the bottom of the sample
if u(1,nx0)<mp
u(2,nx0)=mu01*2*u(1,nx0-1)+(1-
2*mu01)*u(1,nx0)+mu02*lv(1,nx0)+2*mu04*(ts-u(1,nx0));
s=u(2,nx0)-u(1,nx0);
if s>0
u(2,nx0)=mu01*2*u(1,nx0-1)+(1-
2*mu01)*u(1,nx0)+mu02*lv(1,nx0)+2*mu04*(ts-u(1,nx0));
elseif s<=0
if mv(1,nx0)>0
if sv(1,nx0)<=deltasv0
deltasv(1,nx0)=abs(s);
sv(1,nx0)=sv(1,nx0)+deltasv(1,nx0);
u(1,nx0)=mp;
u(2,nx0)=mp-1e-12;
elseif sv(1,nx0)>deltasv0
u(2,nx0)=mu01*2*u(1,nx0-1)+(1-
2*mu01)*u(1,nx0)+mu02*lv(1,nx0)+2*mu04*(ts-u(1,nx0));
end
elseif mv(1,nx0)==0
u(2,nx0)=mu01*2*u(1,nx0-1)+(1-
2*mu01)*u(1,nx0)+mu02*lv(1,nx0)+2*mu04*(ts-u(1,nx0));
end
end
end
elseif u(1,nx0)>=mp

```

```

    u(2,nx0)=mu01*2*u(1,nx0-1)+(1-
2*mu01)*u(1,nx0)+mu02*lv(1,nx0)+2*mu04*(ts-u(1,nx0));
    m=u(2,nx0)-u(1,nx0);
    if m>=0
        if mv(1,nx0)<=deltamv0
            u(2,nx0)=mu01*2*u(1,nx0-1)+(1-
2*mu01)*u(1,nx0)+mu02*lv(1,nx0)+2*mu04*(ts-u(1,nx0));
            m=u(2,nx0)-u(1,nx0);
            deltamv(1,nx0)=abs(m);
            mv(1,nx0)=mv(1,nx0)+deltamv(1,nx0);
            u(1,nx0)=mp;
            u(2,nx0)=mp;
        elseif mv(1,nx0)>deltamv0
            u(2,nx0)=mu01*2*u(1,nx0-1)+(1-
2*mu01)*u(1,nx0)+mu02*lv(1,nx0)+2*mu04*(ts-u(1,nx0));
            end
        elseif m<0
            u(2,nx0)=mu01*2*u(1,nx0-1)+(1-
2*mu01)*u(1,nx0)+mu02*lv(1,nx0)+2*mu04*(ts-u(1,nx0));
            end
        end
    for j=1:nx0
        u(1,j)=u(2,j);
    end
    for j=1:nx0
        if i>=2&&i<nj
            if j>=1&&j<=500;
                v1(i-1,j)=u(2,j);
            elseif j>=501&&j<=nx0&&mod(j,10)==0
                v1(i-1,500+fix(j/10)-50)=u(2,j);
            end
        elseif i>=nj&&i<5000&&mod(i,10)==0
            if j>=1&&j<=500;
                v2(fix(i/10)-99,j)=u(2,j);
            elseif j>=501&&j<=nx0&&mod(j,10)==0
                v2(fix(i/10)-99,500+fix(j/10)-50)=u(2,j);
            end
        elseif i>=5000&&i<1e4&&mod(i,1e3)==0
            if j>=1&&j<=500;
                v3(fix(i/1e3)-4,j)=u(2,j);
            elseif j>=501&&j<=nx0&&mod(j,10)==0
                v3(fix(i/1e3)-4,500+fix(j/10)-50)=u(2,j);
            end
        elseif i>=1e4&&i<1e5&&mod(i,1e4)==0
            if j>=1&&j<=500;
                v4(fix(i/1e4),j)=u(2,j);
            end
        end
    end

```

```
elseif j>=501&&j<=nx0&&mod(j,10)==0
    v4(fix(i/1e4),500+fix(j/10)-50)=u(2,j);
end
elseif i>=1e5&&i<1e6&&mod(i,1e5)==0
    if j>=1&&j<=500;
        v5(fix(i/1e5),j)=u(2,j);
    elseif j>=501&&j<=nx0&&mod(j,10)==0
        v5(fix(i/1e5),500+fix(j/10)-50)=u(2,j);
    end
elseif i>=1e6&&i<1e7&&mod(i,1e6)==0
    if j>=1&&j<=500;
        v6(fix(i/1e6),j)=u(2,j);
    elseif j>=501&&j<=nx0&&mod(j,10)==0
        v6(fix(i/1e6),500+fix(j/10)-50)=u(2,j);
    end
elseif i>=1e7&&i<1e8&&mod(i,1e7)==0
    if j>=1&&j<=500;
        v7(fix(i/1e7),j)=u(2,j);
    elseif j>=501&&j<=nx0&&mod(j,10)==0
        v7(fix(i/1e7),500+fix(j/10)-50)=u(2,j);
    end
elseif i>=1e8&&i<=1e9&&mod(i,1e8)==0
    if j>=1&&j<=500;
        v8(fix(i/1e8),j)=u(2,j);
    elseif j>=501&&j<=nx0&&mod(j,10)==0
        v8(fix(i/1e8),500+fix(j/10)-50)=u(2,j);
    end
end
end
end
end
```

## Appendix 5 Repeated scans of OCP and potentiodynamic polarisation tests

### Pure Al

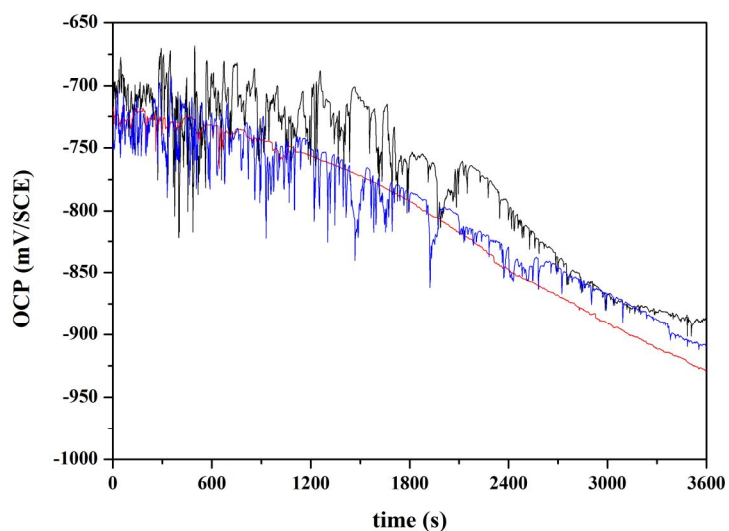


Figure A5-1 OCP scans of three pure Al samples in 3.5 wt.% NaCl solution.

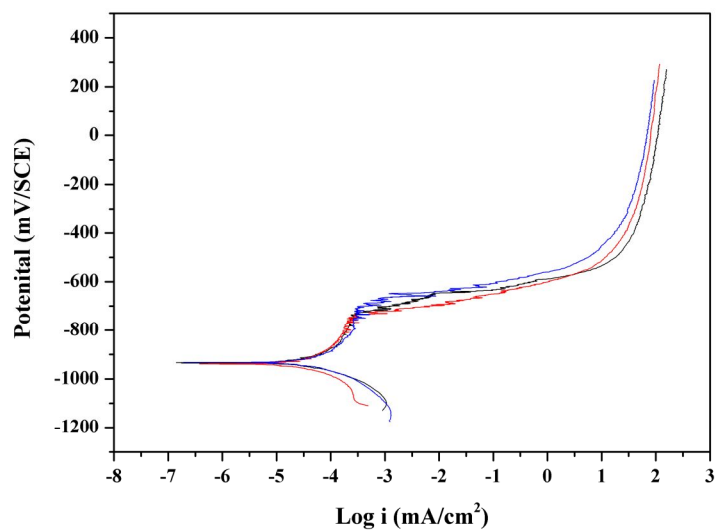


Figure A5-2 Potentiodynamic polarisation scans of three pure Al samples in 3.5 wt.% NaCl solution.

AA2024

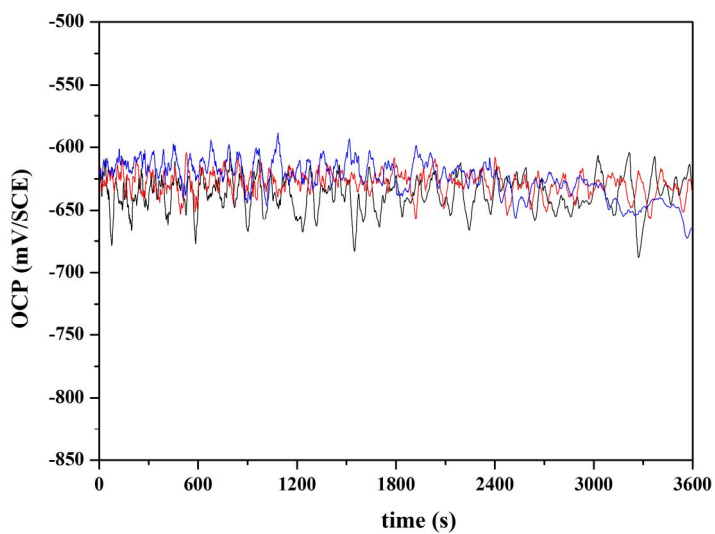


Figure A5-3 OCP scans of three AA2024 samples in 3.5 wt.% NaCl solution.

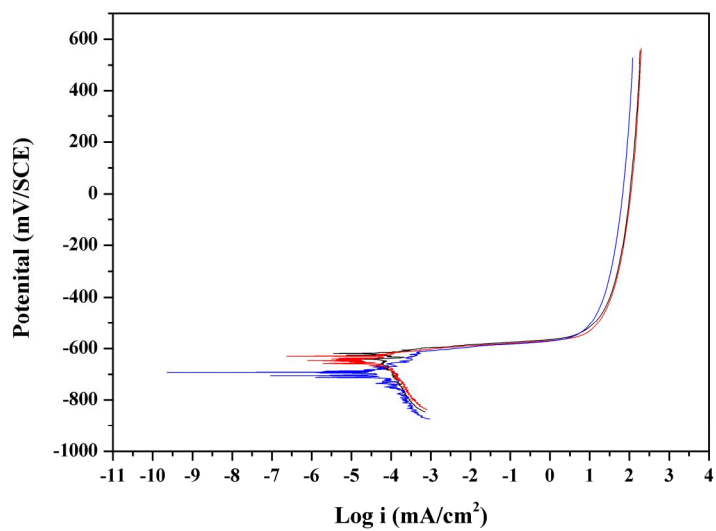
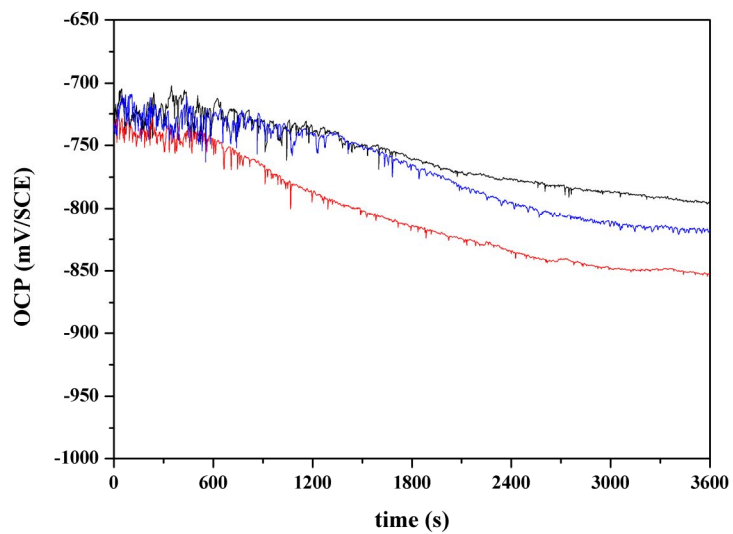
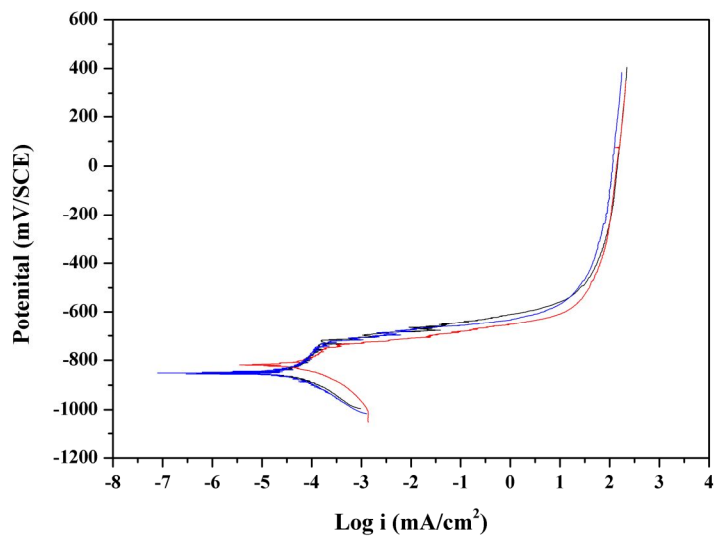


Figure A5-4 Potentiodynamic polarisation scans of three AA2024 samples in 3.5 wt.% NaCl solution.

## Alclad 2024



**Figure A5-5 OCP scans of three alclad 2024 samples in 3.5 wt.% NaCl solution.**



**Figure A5-6 Potentiodynamic polarisation scans of three alclad 2024 samples in 3.5 wt.% NaCl solution.**

### As-cast Al-Co-Ce alloy 3

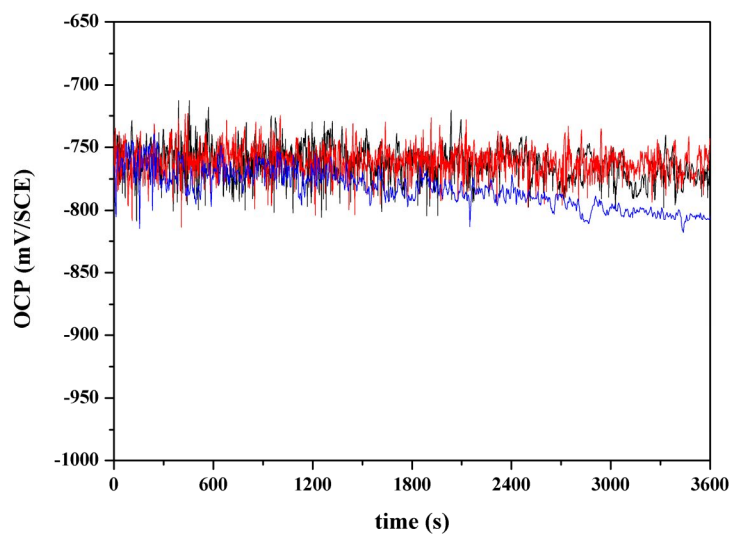


**Figure A5-7 OCP scans of three as-cast Al-Co-Ce alloy 3 samples in 3.5 wt.% NaCl solution.**

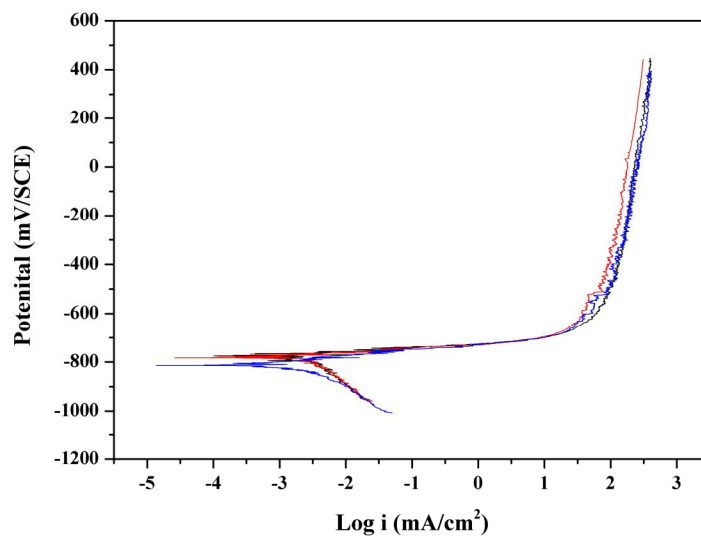


**Figure A5-8 Potentiodynamic polarisation scans of three as-cast Al-Co-Ce alloy 3 samples in 3.5 wt.% NaCl solution.**

### LSM treated Al-Co-Ce alloy 3

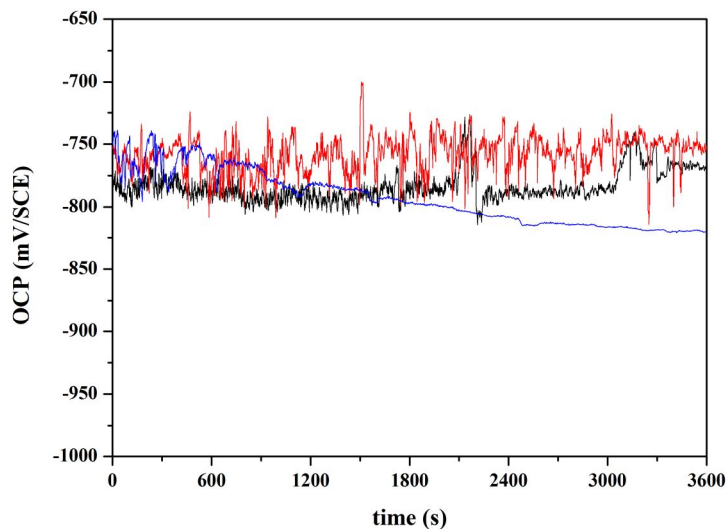


**Figure A5-9 OCP scans of three LSM treated Al-Co-Ce alloy 3 samples in 3.5 wt.% NaCl solution.**

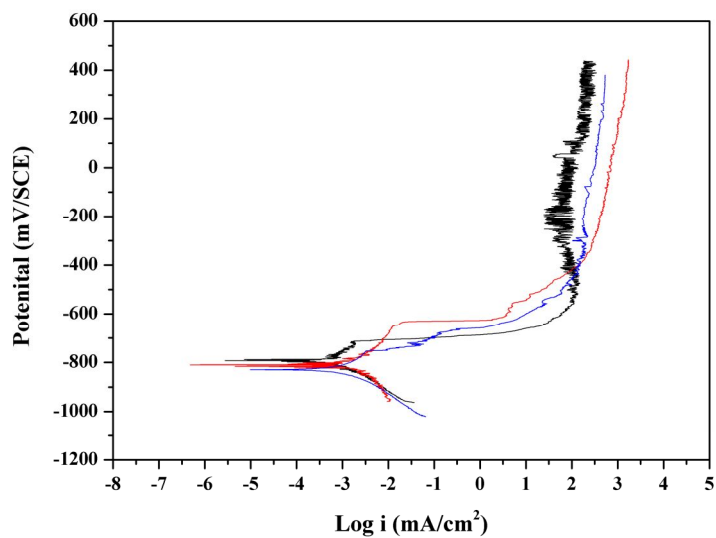


**Figure A5-10 Potentiodynamic polarisation scans of three LSM treated Al-Co-Ce alloy 3 samples in 3.5 wt.% NaCl solution.**

## LAEB treated Al-Co-Ce alloy 3

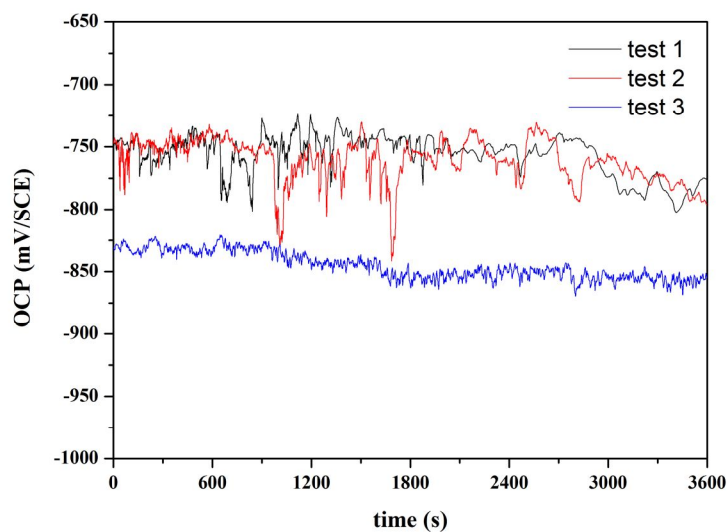


Figure A5-11 OCP scans of three LAEB treated Al-Co-Co alloy 3 samples in 3.5 wt.% NaCl solution.

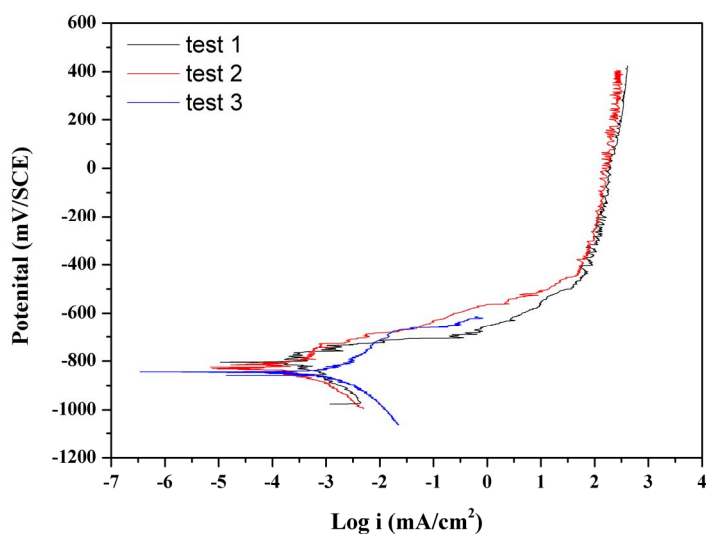
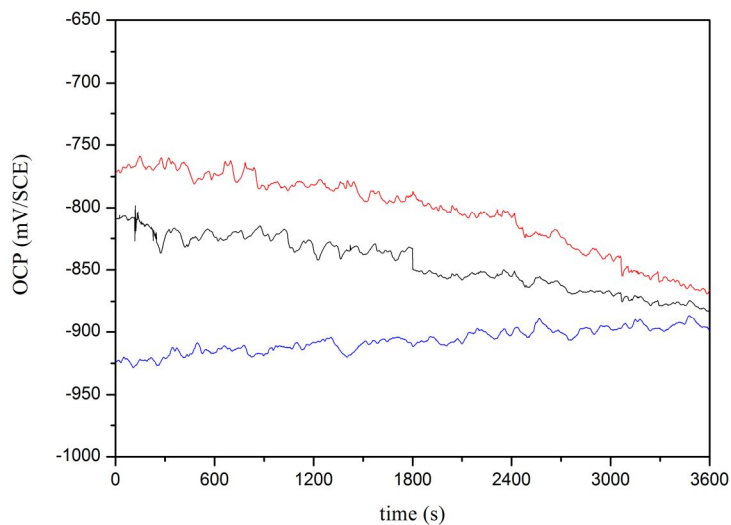
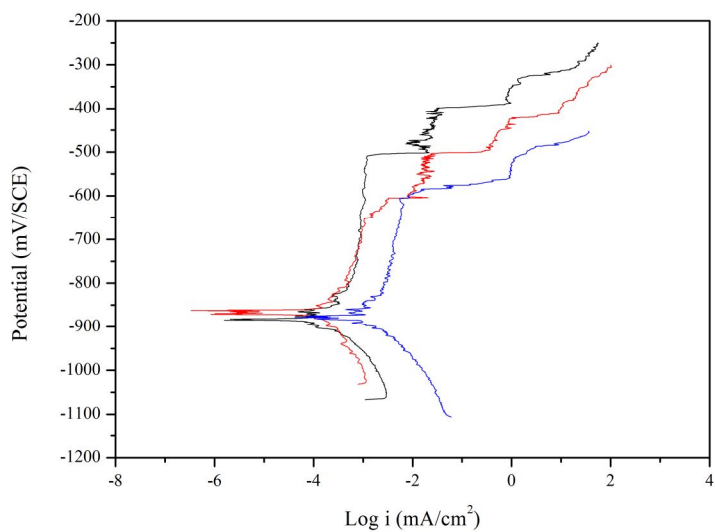


Figure A5-12 Potentiodynamic polarisation scans of three LAEB treated Al-Co-Co alloy 3 samples in 3.5 wt.% NaCl solution. Tests 1 and 2 have the higher final polarisation potential, while test 3 has the lower one.

**LSM-LAEB treated Al-Co-Ce alloy 3 (layer 1)**



**Figure A5-13 OCP scans of three LSM-LAEB treated Al-Co-Co alloy 3 (layer 1) samples in 3.5 wt.% NaCl solution.**



**Figure A5-14 Potentiodynamic polarisation scans of three LSM-LAEB treated Al-Co-Co alloy 3 (layer 1) samples in 3.5 wt.% NaCl solution.**

**LSM-LAEB treated Al-Co-Ce alloy 3 (layer 2)**

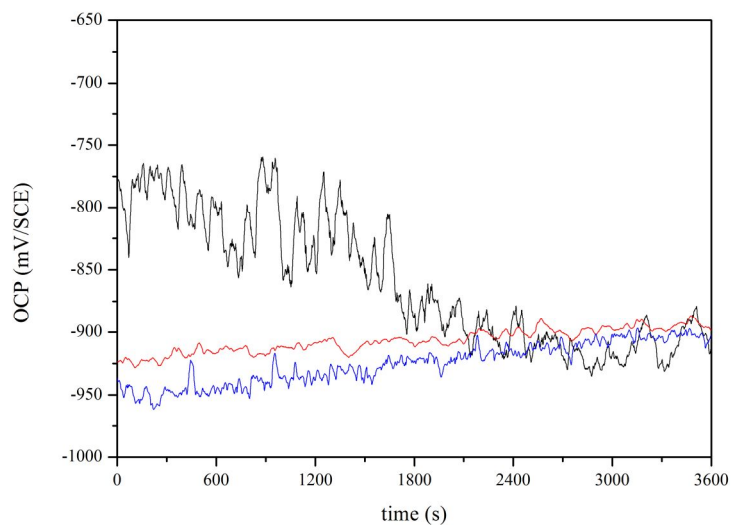


**Figure A5-15 OCP scans of three LSM-LAEB treated Al-Co-Co alloy 3 (layer 2) samples in 3.5 wt.% NaCl solution.**

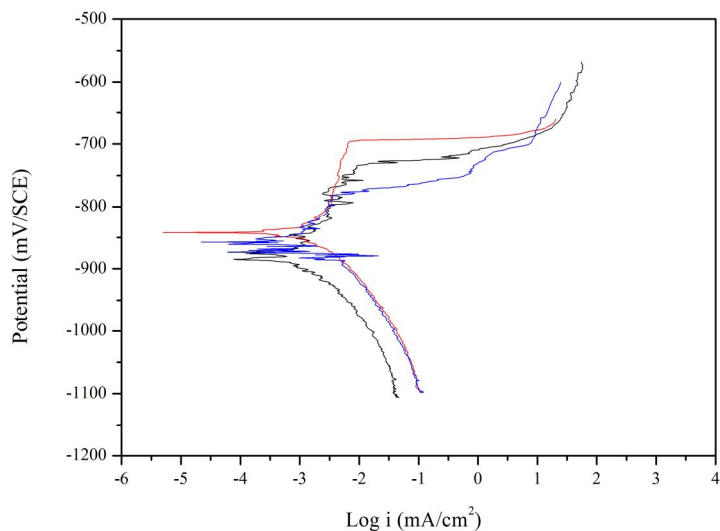


**Figure A5-16 Potentiodynamic polarisation scans of three LSM-LAEB treated Al-Co-Co alloy 3 (layer 2) samples in 3.5 wt.% NaCl solution.**